2012

A study of oxidation and wear on high speed steel roll material

Qiang Zhu
University of Wollongong

A study of oxidation and wear on high speed steel roll material

A thesis submitted for the award of the degree of

Doctor of Philosophy

from

UNIVERSITY OF WOLLONGONG

by

QIANG ZHU

BEng (Mat), MEng (Mat)

School of Mechanical, Materials and Mechatronics Engineering
Faculty of Engineering

2012

Declaration

I, Qiang Zhu, declare that this thesis, submitted in fulfilment of the requirements for the award of Doctor of Philosophy, in the School of Mechanical, Materials and Mechatronics Engineering, University of Wollongong, Australia, is wholly my own work unless otherwise referenced or acknowledged, and has not been submitted for qualifications at any other university or academic institution.

Qiang Zhu

February 2012

Acknowledgements

I wish to express deep gratitude to my supervisors Prof. Kiet Tieu, and Dr. Hongtao Zhu for their support, patience, and guidance throughout all these years.

I also wish to take the opportunity to thank the staff and students within the School of Materials, Mechanical, and Mechatronics Engineering for all the help and assistance given. In particular, I wish to thank Mr. Mark Reid in the Steel Lab, Mr. Greg Tillman in the Metalogy Lab, Mr. Bob de Jong and Mr. Jose Gonzalez on the Gleeble 3500, Mr. Nick Mackie on SEM, and Dr. David Wexler on XRD for their help and attention.

I would like to thank Dr. Charlie Kong from the University of New South Wales, an expert on FIB-SEM and TEM, for his assistance and invaluable advice.

I will always be grateful to the University of Wollongong for providing the HDR and UPA scholarships.

Finally, I give my heartfelt thanks to my wife Ms. Ning Wu for her love, encouragement, patience, and sharing during my doctoral work for without her, it would have been impossible for me to finish this thesis.

Thank you all,

Qiang

List of Publications during the PhD course

1. ***Qiang Zhu***, Hongtao Zhu, Kiet Tieu, Charlie Kong. Three dimensional microstructure study of oxide scale formed on a high-speed steel by means of SEM, FIB and TEM. *Corrosion Science*, 2011 (53): 3603-3611. (IF 3.261)

2. Kiet Tieu, ***Qiang Zhu***, Hongtao Zhu, Cheng Lu. An investigation into the tribological behavior of a work roll material at high temperature. *Wear*, 2011(273): 43-48. (IF: 1.635)

3. ***Qiang Zhu***, Hongtao Zhu, Kiet Tieu, Mark Reid, Laichang Zhang. In-situ investigation of oxidation behaviour in high-speed steel roll material under dry and humid atmospheres. *Corrosion Science*, 2010 (52): 2070-2715. (IF 3.261)

4. ***Qiang Zhu***, Hongtao Zhu, Kiet Tieu, Cheng Lu. High temperature oxidation behavior of a high speed steel material. *Steel Research International*, 2010(81): 134-135. (IF: 0.453)

5. Hongtao Zhu, ***Qiang Zhu***, Cheng Lu, Kiet Tieu. Tribologcial characterization of a high speed steel roll material at elevated temperature. In: *Proceedings of the 10th international conferences on steel rolling*, September 15-17, 2010, Beijing, China, 1806-1811.

6. ***Qiang Zhu***, Hongtao Zhu, A. Kiet Tieu, Bob De Jong. A study on tribological behavior of a hot work roll on a coupled mini-mill and Gleeble system. In: 4th International Conference on Tribology in Manufacturing Process Proceedings (ICTMP 2010), June 13-15, 2010, Nice, France, 869-876.

7. Wan W. Zamri, Buyung Kosasih, Kiet Tieu, ***Qiang Zhu***, Hongtao Zhu, Variation of microstructural and mechanical properties of oxide layers on high speed steel hot Work roll. *Journal of Materials Processing Technology*, 2012. (IF: 1.567, Accepted)

Abstract

The oxidation of high speed steel roll material has been investigated using a high temperature microscope with a CCD camera as a detector, in temperatures ranging from 500 to 700 ^{o}C, in both dry and humid atmospheres (up to 12.5% H_2O). The whole oxidation process was observed in-situ and recorded. In-situ observations indicate that oxide scales from high speed steel first nucleate at the carbides/matrix interfaces, then spread rapidly outward to cover the vanadium rich MC carbides, followed by a continuous growth over the whole surface. The surface morphology of the oxidised high speed steel is not homogenous due to severe selective oxidation. The temperature at which oxidation commences has a significant influence on the oxidation behaviour of the material because as the temperature increases, the rate of oxidation increases dramatically. The sample surface was oxidised far more severely at 700 ^{o}C than at 650 ^{o}C in both a dry and humid atmosphere. These results indicate that water vapour in the atmosphere greatly enhances the oxidation of high speed steel, as well as having a significant influence on the morphology of the oxidised surface. Water vapour in the reacting atmosphere reduces the grain size and increases the porosity of the iron oxide. Different types of carbides in the material show large differences in their resistance to oxidation, for example, chromium rich M_7C_3 carbides strongly resist oxidation while vanadium rich MC carbides oxidise much easier. A TEM investigation of oxide scale formed on the HSS sample indicates that it consists of two sub-layers: a fine grained (Fe,Cr)-rich oxides inner layer and a larger columnar Fe oxide outer layer.

Oxidation tests under a high humidity (46.5% H_2O) atmosphere were carried out in the Gleeble 3500 thermal mechanical simulator. The results show that the water content in the atmosphere not only increases the oxidation rate of high speed steel, but it also influences the microstructure and morphology of the oxide scale. The

formed oxide scale is non-uniform and more porous and fractured than the compact, uniform layer formed with dry air. With an increasing content of water vapour, more porous oxide scales form and more Fe_2O_3 phase is formed in the oxide scale.

Nano-indentation tests were used to characterise the mechanical properties of the oxide scale formed on the HSS sample. A nano-indentation was performed on the cross section of the oxide scale with a matrix (5 by 5 and/or 7 by 7) routine. The tests successfully revealed the different mechanical properties of the inner and outer sub-layer. The results indicate that the outer layer with larger columnar Fe oxides was the hardest (13-16GPa), followed by the inner sub-layer (9-11GPa) with fine grained (Fe,Cr) rich oxides, and then the HSS matrix (approximate 9GPa). The HSS matrix had the highest Young's modulus, around 270GPa, the outer oxide layer was 200-240GPa, and the inner oxide layer was the lowest at 130-180GPa. The mechanical properties of the oxide scale were significantly influenced by the chemical composition and microstructure of the scales. Because these oxides scales have different hardness/modules than the matrix, they contribute significantly to the frictional behaviour and wear resistance.

A high temperature pin-on-disc tribological test was carried out to simulate the contact and tribological behaviours of oxide scale in the roll bite. The pin represents the HSS work roll, and the mild carbon steel disc represents the hot rolled strip. Only the sliding part of the motion was considered, the rolling part was neglected. The results show that a typical tribological test can be sub-divided into three stages: i) stage I corresponds to the start of the friction curve when the coefficient of friction decreases, ii) stage II corresponds to an increase in the coefficient of friction after the minimum value, and iii) stage III is the stabilisation step of the friction. Stage I and stage II can be summarised as a running-in period which lasts less than 300 seconds from the start of the test. A thin, compact, and smooth "glaze" oxide scale around 800-850nm formed on the surface of the pin during the running-in

period. This “glaze” oxide layer in the contact zone helps stabilise the friction and protects the pin from wearing. Adhesive wear is the predominant wear mechanism on the pin during this period. At stage III the wear mechanism on the pin becomes complicated. In addition to oxidation on the HSS pin, the oxides transfer from the disc to the pin, which thickens the oxide scale on the surface of the pin quite significantly. Large cracks and pores could be found inside the oxide scale, which indicates that a severe “banding” phenomenon could occur when the oxide scale reaches a critical value. A large amount of wear debris observed on the pin wear track confirmed that abrasion happens at this stage. It is the balance between adhesion, abrasion, and oxidation.

For the first time a mini-rolling mill was successfully incorporated into the Gleeble 3500 thermal mechanical simulator to simulate stalled hot rolling. Two types of roller surfaces, e.g. a relatively virgin surface and a pre-oxidised surface were investigated. The experimental results show that these two surfaces exhibit quite different tribological behaviours. The rolling force and friction of pre-oxidised rolls is always higher than fresh rolls for different reductions and temperatures. With the pre-oxidised roll, a high rolling temperature can cause the oxide scale to peel off from the strip and stick onto the surface of the roll.

List of tables

List of figures

List of contents

Chapter 1
Introduction

High speed steel (HSS) rolls have been utilized for both early and last finishing stands in hot strip mills, in place of high chromium (HiCr) and indefinite chill iron (IC) rolls due to their superior mechanical properties such as high hardness, strong wear resistance, and high temperature properties [1-3]. The use of HSS rolls has improved the strip surface quality by up to 20% and also extended the length of the rolling campaign [4-6]. HSS roll materials are complex multi-component alloys, with a carbon content ranging from 1.5 to 2.0wt% and a significant amount of alloy elements such as V, W, Cr, Ni and Mo [7, 8]. The typical microstructure of HSS consists of primary carbides (10-20%) distributed in a matrix of tempered martensite and fine secondary carbides, formed from the high concentration of strong carbide forming elements such as V, W, and Mo. The types of carbide in HSS are usually MC, M_2C, M_6C and M_7C_3. As these carbides possess much higher hardness than the matrix, they contribute to the mechanical strength, load bearing capacity, and wear resistance [9-11].

In the hot rolling process, the surface of the roll is initially heated up to approximately 700 ^{o}C while in contact with the hot strip for short periods (10^{-2}-10^{-3}s), and subsequently cooled by water to around 50 ^{o}C during the same cycle [12, 13]. The flash temperature could in fact rise above 800 ^{o}C owing to the heat generated by friction, plastic work and the heat transferred from the strip [13]. Because of this cyclic thermal working environment, hot rolls are exposed to extreme thermal fatigue and oxidation which causes the surface of the roll to deteriorate, for example, a piece of oxide scale may peel off the surface [14-16]. Moreover, hot rolls are subjected to high loading and shear forces when contact between the rolled materials occurs, which causes mechanical fatigue and wear.

These extremely arduous working conditions causes hot rolls to deteriorate very quickly. It is well known that some of the most important segments in the operating costs of a modern hot rolling mill are related to the work rolls because they are expensive and a large stock must be kept on hand to ensure that the mills can operate continually [17]. Therefore the study of oxidation and the wear behaviour of high speed steel rolls has for various reasons, become very important.

Firstly, the thermal cyclic working of rolls in hot rolling causes a superficial oxide scale to form which plays an important role on the wear of work rolls because a hard oxide scale may be very abrasive whereas a ductile oxide scale, acting like a solid lubricant, may decrease the coefficient of friction as well as the wear [14, 15, 18-21]. Secondly, since the quality of the rolled products is closely related to the surface conditions, it is important to understand roll surface topography and the morphology of this surface oxide. Thirdly, numerous work have been carried out to study the wear of the high speed steel work rolls, however, little work focus on the influence of the formation of an oxide scale on the contact behaviour. Whether the change of friction during hot rolling is or is not associated with the formation of oxides on the roll surface remains uncertain [22].

The aim of this present work is to study the oxidation of a high speed steel work roll under dry and humid atmospheric conditions. The morphology and topography of the oxide scale on the sample surface will be investigated in detail because it is important to understanding how the surface of the rolls deteriorates. In addition, the mechanical properties of the oxide will also be characterised using nano-indentation techniques. In order to understand the wear mechanism of HSS and the role of oxides in the tribological behaviour during the hot roll process, a series of high temperature pin-on-disc wear tests and stalled hot rolling simulation on Gleeble 3500 thermo-mechanical simulator will be conducted.

Chapter 2
Literature review

This chapter contains a substantial amount of information on topics considered essential for an understanding of the mechanisms of high temperature oxidation and wear of high speed steel work roll materials for hot rolling, and the role oxides play on the tribological behaviour of high speed steel work rolls.

2.1 High temperature oxidation of iron and steel alloys

2.1.1 Iron oxides

Iron is thermodynamically unstable when exposed to the atmosphere [23]; it forms pure oxide compounds in three main forms, wüstite ($Fe_{1-x}O$), magnetite (Fe_3O_4), and hematite (Fe_2O_3). Wüstite is thermodynamically stable above the eutectoid temperature of 570 ^oC. At temperatures below 570 ^oC the wüstite phase decomposes to magnetite and alpha-iron [20]. Wüstite has a cubic halite structure (NaCl), with anion sites occupied by O^{2-} and most cation sites occupied by divalent Fe^{2+} ions. An alternative description of this structure is that of a ccp array of anions stacked along the [111] direction where planes of anions alternate with planes of cations. Most of the Fe is octahedral with a small proportion of Fe^{3+} on the usually vacant tetrahedral sites. These octahedra share edges (Fig. 2.1a) and Fe^{2+}- and O-layers alternate along the [111] direction (Fig. 2.1b). Wüstite is a p-type metal deficient conductor with a high concentration of lattice defects [20, 24] whose chemical formula may be written as $Fe_{1-\alpha}O$. Depending on the partial pressure of oxygen and its temperature, the metal deficit α in wüstite can vary from 0.04 to 0.17 in the range of 800-1250 ^oC [25-27]. These high cation vacancies result in a high mobility of cations and electrons via metal vacancies and electron holes.

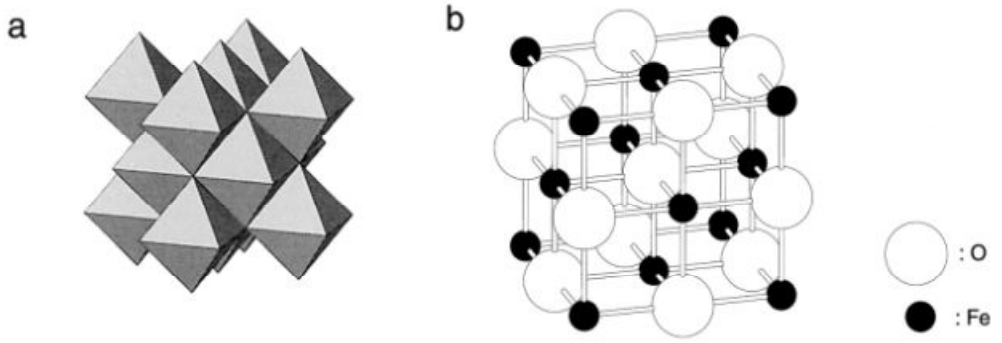

Fig. 2.1 Structure of wüstite, a) arrangement of octahedra, b) ball-and-stick model. [28]

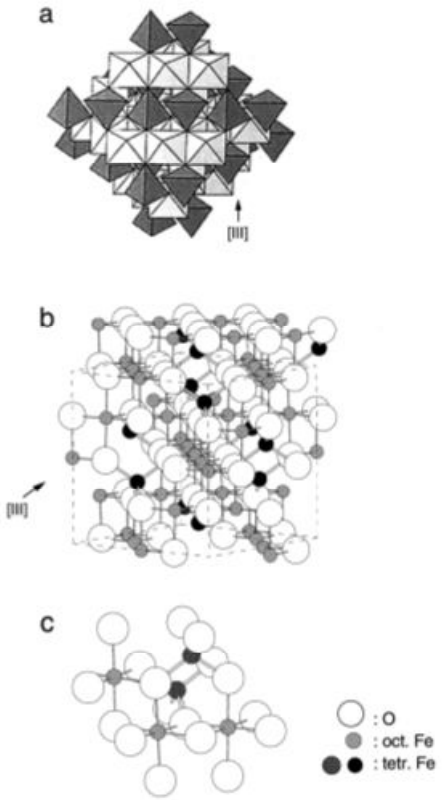

Fig. 2.2 Structure of magnetite. a) Polyhedral model with alternating octahedra and tetrahedral-octahedra layers. b) Ball-and-stick model. c) Ball-and-stick model of the arrangement of octaheda and tetrahedra. [28]

Magnetite (Fe_3O_4 or $FeO.Fe_2O_3$) is an inverse spinel ($MgAl_2O_4$) structure containing both divalent and trivalent iron ions. The unit cell of this spinel structure contains 32 oxygen ions, 32 octahedral sites, and 64 tetrahedral sites. Magnetite has 16 trivalent cations and 8 divalent cations. Its formula is written as $Y[XY]O_4$ where $X=Fe^{2+}$, $Y=Fe^{3+}$ and the brackets denote octahedral sites (M sites). Eight tetrahedral sites (T sites) are distributed between Fe^{2+} and Fe^{3+}, i.e. the trivalent ions occupy

both tetrahedral and octahedral sites. The structure consists of octahedral and mixed tetrahedral/octahedral layers stacked along the [111] direction (Fig.2.2a). Fig. 2.2b shows the sequence of Fe- and O- layers and section of this structure with three octahedra and two tetrahedra being depicted in Fig. 2.2c. Magnetite also exists with an excess of oxygen but this excess is much smaller than with wüstite, and the corresponding defect concentration is less [20]. It is almost stoichiometric below 1000^{o} C, whereas at higher temperatures it contains more oxygen in the solid solution than the stoichiometric composition [26].

Hematite (α-Fe_2O_3) is a stoichiometric chemical compound, which is the oldest known Fe oxide. At high temperatures (above $500\,^{o}$C), magnetite oxidises to form α-Fe_2O_3 [28]. The crystal system of hematite in the form α-Fe_2O_3 is a rhombohedral (α-Al_2O_3) structure (Fig. 2.3) with a low concentration of structural defects [29]. The structure of hematite can be described as consisting of hcp arrays of oxygen ions stacked along the [001] direction, i.e. planes of anions are parallel to the (001) plane (Fig. 2.3a). Two thirds of the sites are filled with Fe^{3+} ions which are arranged regularly with two filled sites, followed by one vacant site in the (001) plane, thereby forming sixfold rings (Fig. 2.3b). The arrangement of cations produces pairs of $Fe(O)_6$ octahedra. Each octahedron shares edges with three neighbouring octahedra in the same plane, and one face with an octahedron in an adjacent plane (Fig. 2.3c). The O-O distances along the shared face of an octahedron are shorter (0.2669 nm) than the distance along the unshared edge (0.3035 nm), hence the octahedron is distorted tri-gonally (Fig. 2.3d). The arrangement of oxygen and Fe around a shared face is depicted in Fig. 2.3e; this Fe-O_3-Fe triplet structure influences the magnetic properties of the oxide [28]. Hematite is an n-type semi-conductor in which anions are largely diffused [20].

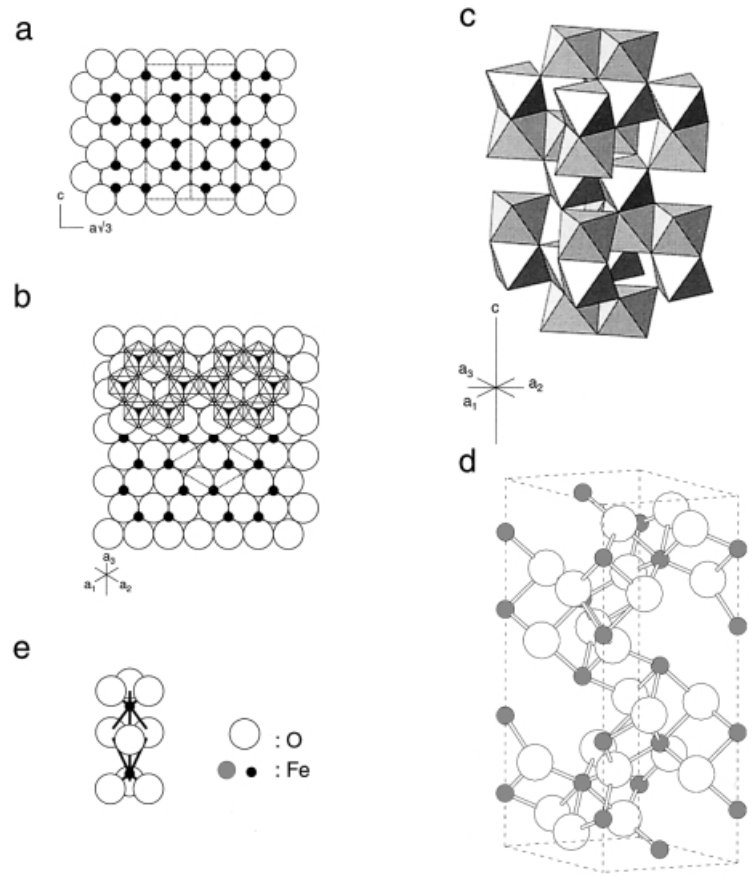

Fig. 2.3 Crystal structure of hematite (α-Fe_2O_3); a) Hexagonal close packing of oxygens with cations distributed in the octahedral interstices. b) View down the c-axis showing the distribution of Fe ions over a given oxygen layer, and the hexagonal arrangement of octahedra. c) Arrangement of octahedra. Note their face sharing. d) Ball-and-stick model. e) O_3-Fe-O_3-Fe-O_3 triplets. [28]

2.1.2 Mechanism of oxide scale formation

Oxidation of iron has been extensively investigated and is well understood [20, 26, 30, 31]. When iron is oxidised in air at elevated temperatures, layers of oxide scale are formed on the top of the metal surface. It has been suggested that the composition of the scale layers is temperature dependent [32, 33]. According to the iron-oxygen phase diagram [20], as shown in Fig. 2.4, wüstite (FeO) is only stable at temperatures greater than 570 ^{o}C. At lower temperatures it has a disproportionate level of Fe and Fe_3O_4 [30]. A two layer scale of magnetite (Fe_3O_4) and hematite (Fe_2O_3) are expected to form below this temperature with magnetite next to the metal. When the oxidation temperature above is 570 ^{o}C, a series of oxide layers will

form and consist of FeO, Fe_3O_4 and Fe_2O_3, with FeO next to the metal.

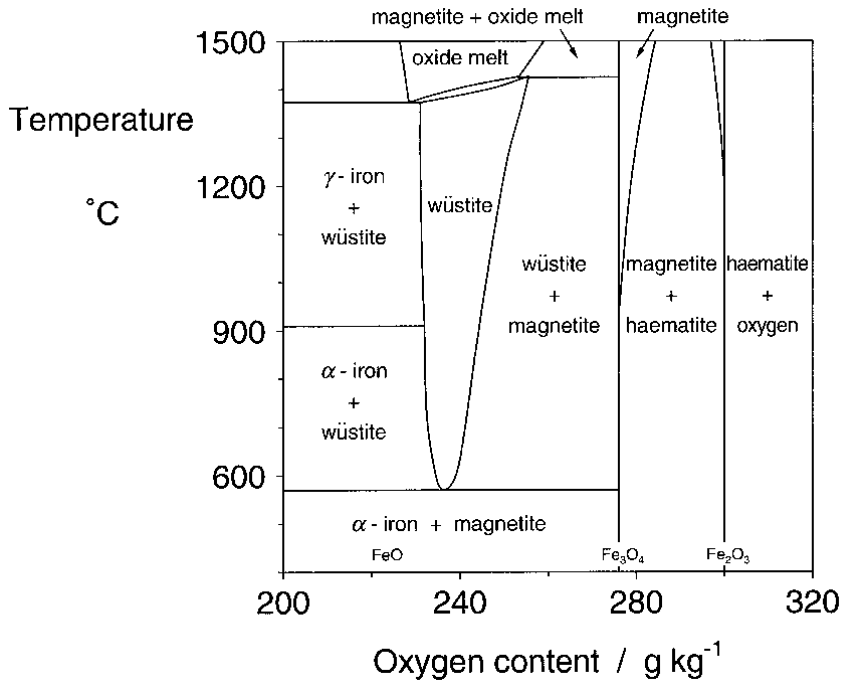

Fig. 2.4 Equilibrium diagram of the iron-oxygen system. [24]

Jonsson et al. [34] carried out oxidation tests on pure iron in dry air at 500 ^{o}C to study the initial growth of iron oxide. The oxide layer was found to consist of a thin layer of hematite, and a double layer of magnetite, as shown in Fig. 2.5. The double layer of magnetite is separated by a straight interface, which is suggested to be the original metal surface. Pujilaksono et al. [35] found in their work on pure iron that hematite, magnetite, and wüstite, make up 5%, 30-35%, and 60-65% of the scale, respectively, after oxidation in dry air at 600 ^{o}C for 24h (Fig. 2.6). Païdassi [31] carried out oxidation tests on pure iron in air, in temperatures from 700-1250 ^{o}C, to examine the growth rate of the scale. He measured the scale thickness and found that the average thickness ratios of wüstite/magnetite/hematite were roughly 95:4:1. The constitution of these three iron oxides in oxide the layer is strongly influenced by the temperature, atmosphere, and even the oxidation period. Tominaga and Yoshimura et al. [36] investigated the mole fraction of the three oxides as a function of temperature (Fig. 2.7), and provided detailed information of compositional changes of the oxides with temperature, when iron oxidises in air.

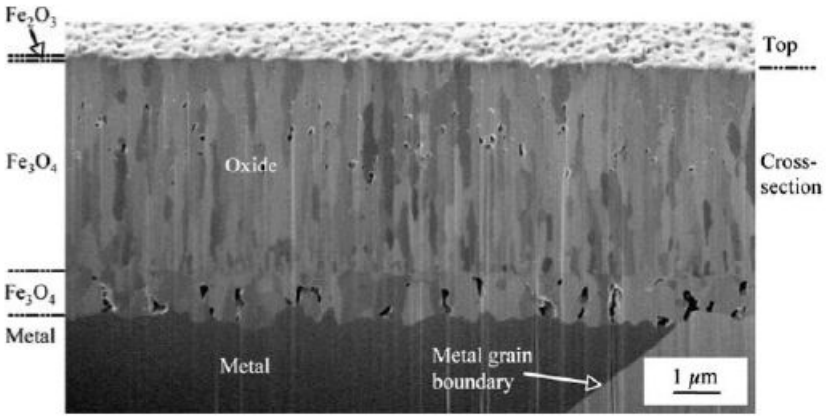

Fig. 2.5 FIB image of the oxide cross section of the sample of pure iron exposed to dry air at 500 °C for 1h. The sample was titled 52°. [34]

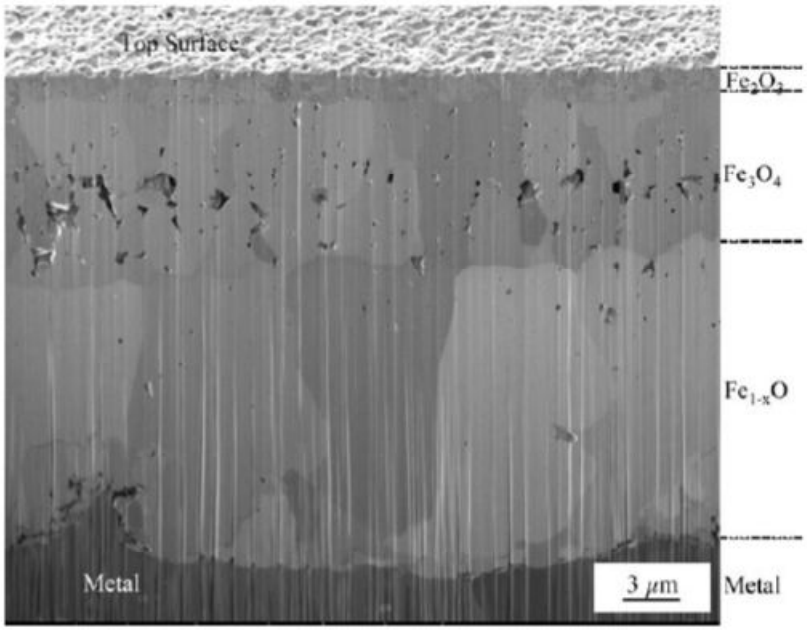

Fig. 2.6 FIB cross section after 24h in dry air at 600 °C. The sample was titled 52°. [35]

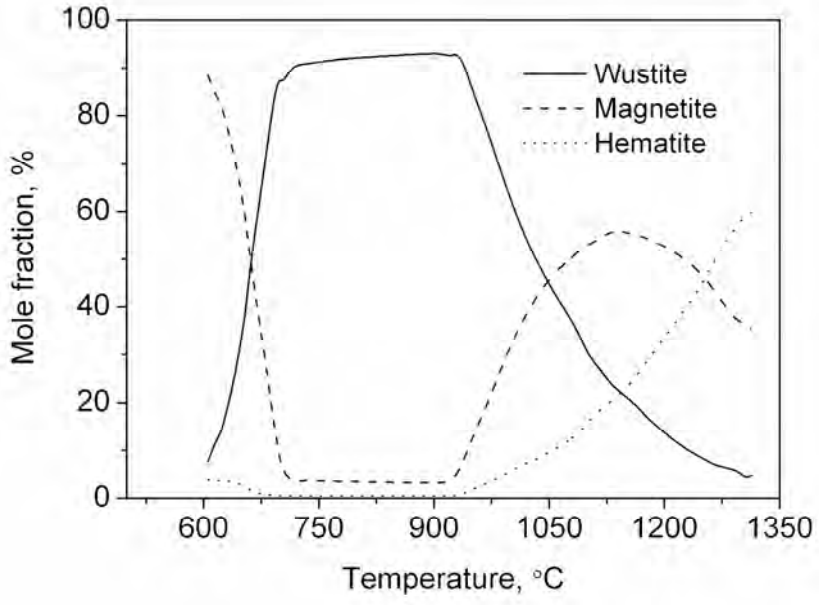

Fig. 2.7 Mole fraction of oxides as a function of temperature. [36]

Birks and Meier [26] proposed a mechanism for the growth of iron oxide scale above 570 ^{o}C (Fig. 2.8). In their model the mechanism of iron oxidation in a multi-layer scale is explained through the following reactions:

Iron ionises at the wüsitite/iron interface according to the reaction:

$$\mathrm{Fe} = \mathrm{Fe}^{2+} + 2e^{-} \tag{2.1}$$

Iron ions and electrons migrate in the wüstite layer via vacancies in the iron and electron holes respectively. At the magnetite/wüstite interface, iron ions and electrons react with magnetic forming wüstite according to the reaction:

$$\mathrm{Fe}^{2+} + 2e^{-} + \mathrm{Fe_3O_4} = 4\mathrm{FeO} \tag{2.2}$$

In the magnetite layer, iron ions migrate via iron ion vacancies in the tetrahedral and octahedral sites, and electrons migrate via electron holes and excess electrons. At the hematite/magnetite interface magnetite is formed through the reactions:

$$\mathrm{Fe}^{2+} + 2e^{-} + 4\mathrm{Fe_2O_3} = 3\mathrm{Fe_3O_4} \tag{2.3}$$

$$\mathrm{Fe}^{3+} + 3e^{-} + 4\mathrm{Fe_2O_3} = 3\mathrm{Fe_3O_4} \tag{2.4}$$

Hematite can be formed by iron ions moving outward or oxygen ions moving inward in the hematite layer. In the outward migration of iron ions in the hematite layer,

the iron ions migrate via iron ion vacancies, together with electrons. The reaction for the formation of hematite at the gas/hematite interface is:

$$2Fe^{3+} + 6e^{-} + \frac{3}{2}O_2 = Fe_2O_3 \quad (2.5)$$

In the case of oxygen ions migrating inward in the hematite layer, the iron ions and electrons (in excess of requirements for reduction of hematite to magnetite) react with oxygen moving via oxygen vacancies. The reactions for the oxygen ionisation and formation of hematite at the hematite/magnetite interface are:

$$\frac{1}{2}O_2 + 2e^{-} = O^{2-} \quad (2.6)$$

$$2Fe^{3+} + 3O^{2-} = Fe_2O_3 \quad (2.7)$$

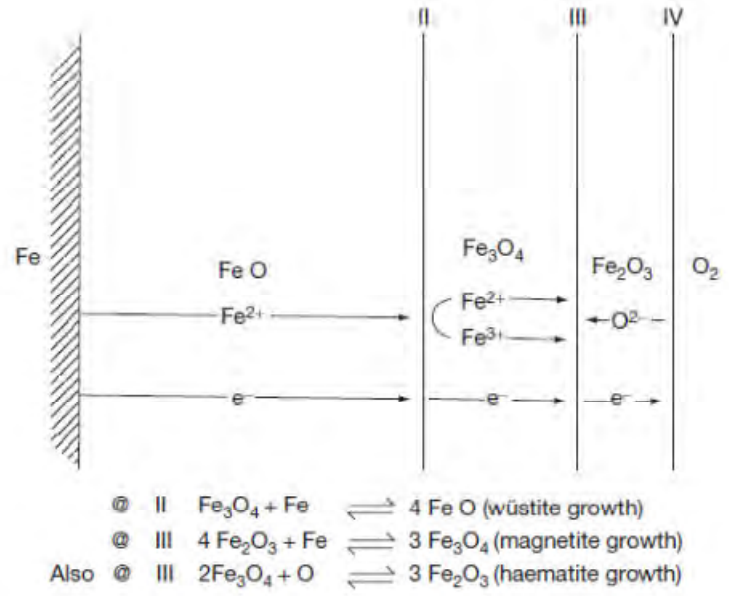

Fig. 2.8 Simplified scheme for the diffusion controlled growth of multi-layered scales on pure iron above 570 °C. [37]

2.1.3 Kinetics of oxide scale growth

Most metals tend to form oxides at high and low temperatures. The mechanism for the oxidation of metals has been well interpreted [26, 30, 38-41]. During the initial stage of oxidation, plenty of iron is available to react with oxygen. Iron diffusion in the thin oxide scale can be so fast that it does not contribute to rate control. However, a transfer of oxygen from the bulk gas to the scale surface will be

relatively slow, occurring at a rate controlled only by the properties of the gas, including temperatures and oxygen partial pressure in the atmosphere [26, 33, 42-52]. As long as these are fixed, the rate of oxygen arriving at the scale surface is constant. Therefore the rate of oxide growth can be considered as linear at this stage.

The linear rate of oxidation can be expressed as:

$$\frac{dX}{dt} = k_l \tag{2.9}$$

which integrates to yield

$$X = k_1 t \tag{2.10}$$

where k_l is the linear rate constant, X the thickness of oxide scale, and t the oxidation time.

As the oxidation time proceeds, a certain thickness of oxide scale has been achieved. Under this condition, the rate of further oxidation becomes limited by solid-state diffusion of iron ions or cation vacancies through the scale. Therefore the oxygen potential at the gas/scale interface becomes significantly higher than at the scale/metal interface. The gradient of concentrated oxygen diminishes as the scale grows and the thickness yields a parabolic growth rate [20, 39, 53-55].

The parabolic rate of oxidation can be expressed as:

$$\frac{dX}{dt} = \frac{k_p}{X} \tag{2.11}$$

$$X^2 = 2k_p t \tag{2.12}$$

where k_p denotes the parabolic rate constant that is expected to obey Arrhenius' relationship [56, 57].

$$K_p = k_0 \cdot e^{-Q/RT} \tag{2.13}$$

where K_0 is a constant, Q the activation energy, R the universal gas constant (8.314 $J \cdot mol^{-1} \cdot K^{-1}$), and T the temperature in Kelvin. Païdassi [58] characterised growth

rates of the oxide layer on pure iron above 700 ^{o}C by micro-graphical work and determined the overall growth of the oxide layer on top of the iron as:

$$k_p = 6.1e^{-40500/RT} \ \ cm^2s^{-1} \tag{2.14}$$

Stanley et al. [59] presented the rate constant equation for pure iron in a temperature range from 500-1100 ^{o}C in terms of scale weight gain:

$$k_p = 0.37e^{-33000/RT} \ \ g^2cm^{-4}s^{-1} \tag{2.15}$$

The above results were substantially confirmed by Païdassi's experimental results [31, 58], which also indicates a much lower parabolic rate constant in a lower temperature range (400-600 ^{o}C). The rate of oxide formation usually increases with temperature, but the rate of oxide growth is often influenced by the purity of the metal, the pressure of the system, and the type and defects present in the oxide layer.

2.2 Work roll materials for hot rolling of steel

The process of hot strip rolling is quite complex, as shown in Fig. 2.9 [59]. Firstly, the slabs are re-heated up to 1250 ^{o}C for several hours in a carbon rich atmosphere. Primary scale formed during the soaking period can reach 2-6mm thick [32, 60, 61]. After being pushed from the reheating furnace, the slab enters a high pressure water spray de-scaling unit where the primary scale is removed. The de-scaled work piece is then subjected to successive reductions in the roughing mill and coiled up in the coil box before entering finishing stands. A secondary scale approximately 10-20μm thick forms at this period. After de-scaling again to remove the secondary scale, the hot strip is sent into the finishing stands for further thinning. During this period a tertiary scale forms while travelling through the finishing stands while the temperature of the hot strip remains between 800-1100 ^{o}C. During rolling, due to contact with the strip, the roll surface heats up from 50-80 ^{o}C (stationary conditions) to very high temperatures (up to 700 ^{o}C in the initial stands) in only one second, with water sprays subsequently cooling it back down to 80 ^{o}C in about 4s [62].

Therefore, hot strip work rolls have to withstand extreme service conditions, i.e., high stress, high temperature, high humidity, and dramatic thermal cycles. Since work rolls are very expensive, around 15% of the production costs in a hot rolling mill, the development of the roll materials, its manufacturing process and wear performance have always been vital [3, 4, 63-65].

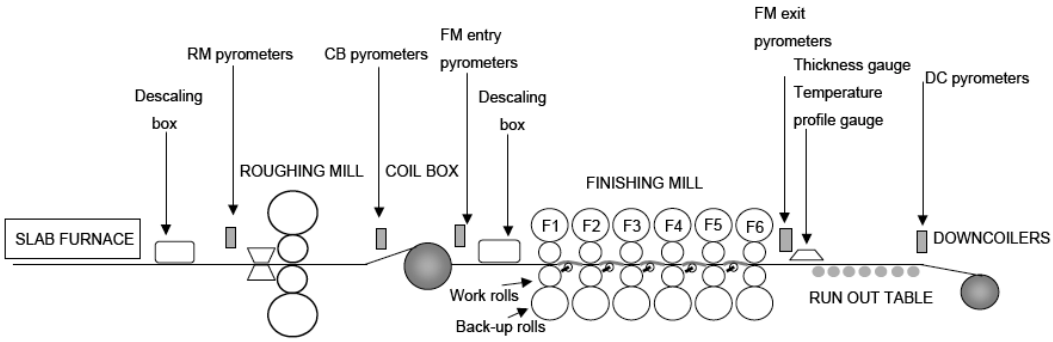

Fig. 2.9 Schematic illustration of the hot strip mill located at the BlueScope Steel Port Kembla works. [59]

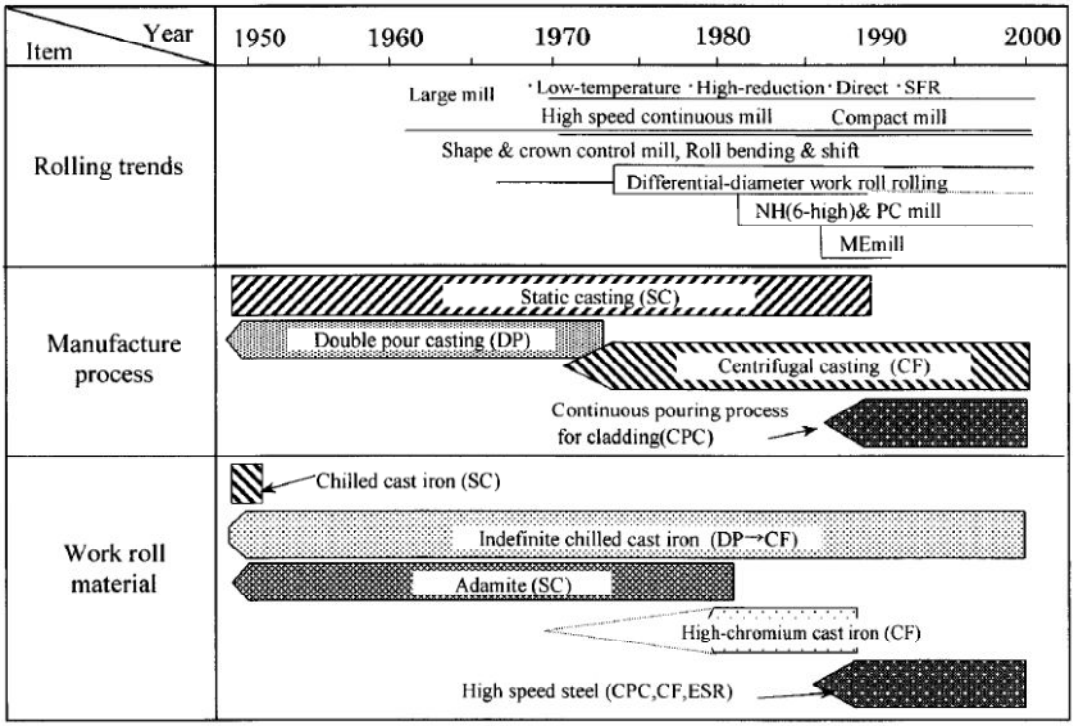

Fig. 2.10 Transitions of roll materials and roll manufactruing process for hot strip finishing work rolls. [63]

Fig. 2.10 illustrates the transition of roll materials and the roll manufacturing process for hot strip finishing work rolls. It can be seen that indefinite chill cast iron

rolls have been the most useful work roll grade for all kinds of hot rolling application since the 1950s [64]. Indefinite chill, also known as “Ni-Hard” or “Ni Grain” was invented in the 1920s. Table 2.1 shows the typical chemical composition of an IC roll. The IC roll is a hypoeutectic white cast iron with inter-dendritic graphite embedded in the ledeburitic matrix [65]. Fig. 2.11 shows the microstructure of an IC roll. Graphite in the roll shell greatly improves the ability of the roll to withstand the thermal shock associated with hot rolling steel strip, decreases friction between the roll and the strip, and greatly reduces the potential of adhesion of the strip to the roll [68]. On the negative side, however, graphite reduces hardness and lowers wear resistance, which shortens the usable life between regrinds compared with other roll types, such as high Cr cast irons and HSS steel types.

Table 2.1 Chemical composition of the IC roll in weight percent. [66]

C	Mn	Si	S	P	Cr	Ni	Mo
3.2-3.3	0.9-1.0	0.9-1.0	<0.015	<0.035	1.7-1.8	4.2-4.4	0.25

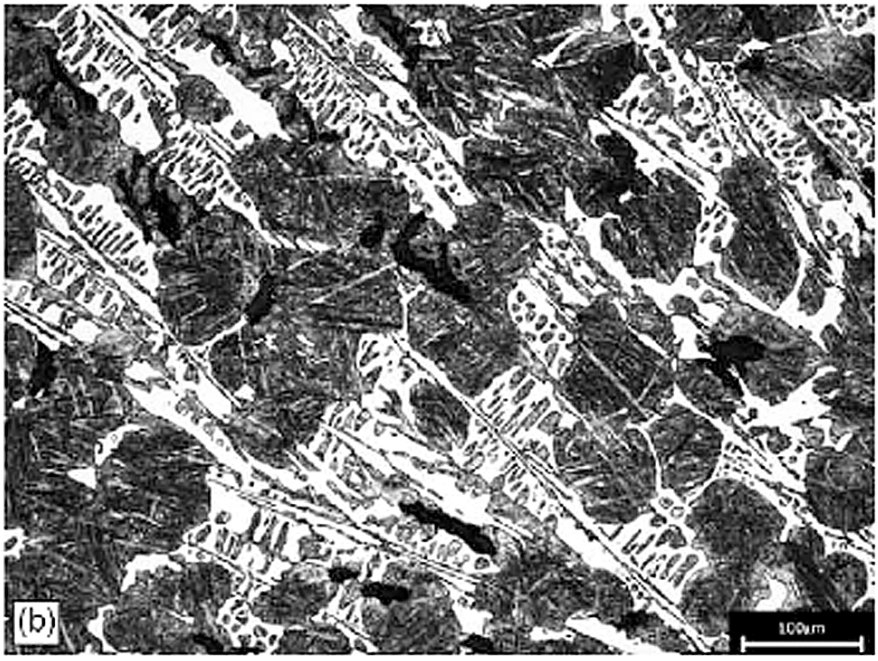

Fig. 2.11 Microstructure of IC iron roll. [67]

High resistance to abrasive wear combined with relatively low production costs make high chromium (HiCr) cast iron rolls particularly attractive for hot work rolls in

hot strip mill since the 1970s [69]. The chemical composition of a high chromium iron is listed in Table 2.2. High chromium iron contains about 2.5-3.0 C_{eq} and a chromium constitution ranging from 15.0 to 18.0 wt%, which gives rise to the formation of a large amount of primary M_7C_3 (M=Cr, Fe) carbides (up to 30 vol.%) during solidification. The microstructure of a HiCr cast iron roll is shown as Fig. 2.12. Compared to IC rolls, HiCr cast iron rolls have a superior performance due to a significant amount of M_7C_3-type carbides distributed in the matrix [70]. A noticeable amount of chromium in the material gives HiCr cast iron rolls a very strong resistance to oxidation at high temperatures.

Table 2.2 Chemical composition of the high chromium iron. [67]

C_{eq} [a]	Ni	Cr	W_{eq} [b]	V+Nb
2.5-3.0	0.3-0.8	15.0-18.0	0.5-2.0	-

[a] Ceq=C+1/3Si.

[b] Weq=W+2Mo.

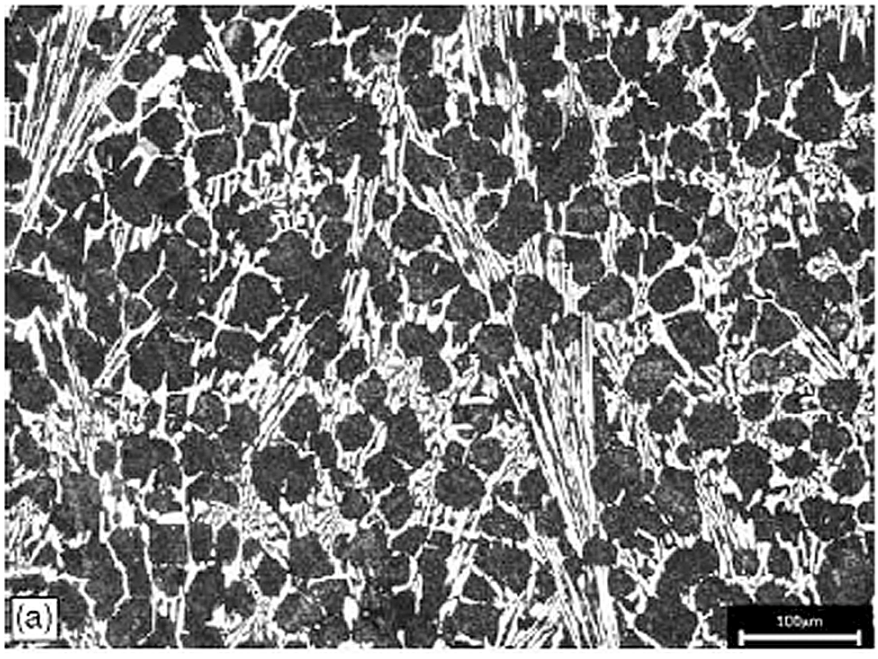

Fig. 2.12 Microstructure of high chromium iron roll. [67]

High speed steel was initially developed for manufacturing cutting tools. It is called high speed steel because this family of alloys are characterised by their capacity to retain a high level of hardness even when submitted to elevated temperatures

resulting from cutting metals at high speed [71]. Because of this advantage, high speed steels have prevailed for early and last finishing stands in hot rolling mills since the 1990s. HSS rolls consist of complex multi-component alloys. The main alloying elements in HSS are carbon, vanadium, chromium, tungsten, and molybdenum. Their role in the structure of HSS is as follows: Carbon is needed for the formation of carbides. Vanadium is a strong carbide forming element. The formula for vanadium carbide is typically V_8C_7, but they are usually called MC. Chromium is also a carbide forming element. Chromium carbides are usually of the M_7C_3 or $M_{23}C_6$ type. Tungsten forms very hard carbides and allows secondary hardening of HSS, but the high specific mass of its carbides is the origin of segregation problems. Molybdenum behaves similar to tungsten but is less sensitive to segregation. Both of those elements form carbides of the M_2C or M_6C type. The unique morphologies of different carbides formed in HSS are shown in Fig. 2.13. The typical microstructure of HSS consists of primary carbides (10-20vol.%) distributed in a matrix of tempered martensite and fine secondary carbides [7, 8]. High speed steel rolls are superior to high chromium and indefinite chill iron rolls because HSS alloys contain a large amount of MC type carbides whose hardness is much greater than M_7C_3 and cementite (Fe_3C). Table 2.3 compares the hardness among different carbides.

Table 2.3 Hardness range for different types of carbide. [67]

Carbide	HV0.02
Cementite (Fe_3C)	800-900
M_6C	1500
M_7C_3	1200-1600
M_2C	2000
MC	3000

Carbide type		Morphology	Chemistry	Localization
MC		•Globular •Thick •Isolated or associated	•Mainly V •Secondary Mo, W, Cr	Centre of grains or grain boundaries (in association with M_7C_3)
M_2C		•Acicular (needles) or lamellar •Associated	•Mainly Mo, W •Secondary Cr, Fe, V	Interdendritic areas
M_6C	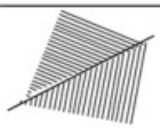	•Thin lamellae (fish bone) •Associated	•Mainly Mo, W •Secondary Cr, Fe, W, V	Areas of strong cooling (first 5 mm from surface)
M_7C_3		•Thick lamellae (fish bone) •Associated	•Mainly Fe, Cr •Secondary Mo, V, W	Interdendritic areas
$M_{23}C_6$		•Small globules •Isolated	•Mainly Cr, Fe •Secondary Mo, W, V	Homogeneously reparted in matrix

Fig. 2.13 Summary of carbide morphology and localization in HSS. [73]

2.3 Oxidation of hot rolling rolls

2.3.1 Energy for oxidation of the hot rolling work rolls

In hot strip mills the slabs are re-heated to around 1250 ^{o}C for several hours before hot rolling commences[32, 62]. Although heat between the rolling passes may be lost through different types of heat transfer such as convection, radiation, etc, the temperature of hot slabs/strips between 800 and 1200 ^{o}C is the result of the surface of the work roll being heated up by the heat transferred from the hotter strip to the work roll when they are in contact [62, 74-76]. The heat transferred from the strip to the work rolls is of great importance because not only does it provide the energy for the surface of the work roll to become oxidised, it also affects the profile of the work rolls. The working temperature of hot rolls can easily exceed 600 ^{o}C indeed the flash temperature could rise above 800 ^{o}C due to heat generated by friction [2, 13]. It is, however, quite difficult for researchers to directly measure the surface temperature of the work rolls by means of contacted thermocouples or other

measurements, therefore, numbers of numerical models have been developed to investigate the thermal response of the work rolls [77-86].

Devadas and Samarasekera [87] used a one dimensional mathematical model to study the heat transfer phenomena in the finishing stands of a hot strip mill. They found that the temperature on the surface of the work rolls varied between 620 and 650 ^{o}C when different lubricants were used, when the rolls were in contact with the strip at 1100 ^{o}C.

Corral et al. [88] studied the thermal and thermo-elastic response of work rolls used for hot rolling steel strip using a hybrid analytic-numerical model. They predicted the maximum temperature of the roll surface of 650 ^{o}C during contact with a hot steel strip and a minimum temperature of about 100 ^{o}C when cooling water was sprayed in one cycle, as shown in Fig. 2.14.

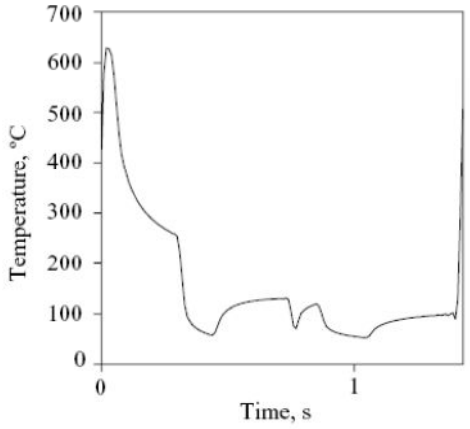

Fig. 2.14 Variation of surface temperature on the work rolls during one cycle. [88]

Sikdar and John [89] developed a mathematical model to predict the temperature profile of the surface and inner depth of the roll, in the finishing stand of a hot strip mill. They divided the work rolls into different angular sectors, depending on the positions of the water cooling headers and the strip, which are depicted in Fig. 2.15 and Table 2.4. The results calculated from the model show that the surface temperature of the work roll, with a 30% reduction, follows a cyclic path increasing up to 620 ^{o}C when it was in contact with the strip, but then it dropped sharply down

to 20 ^{o}C when coolant was sprayed onto the surface of the work roll (Fig. 2.16).

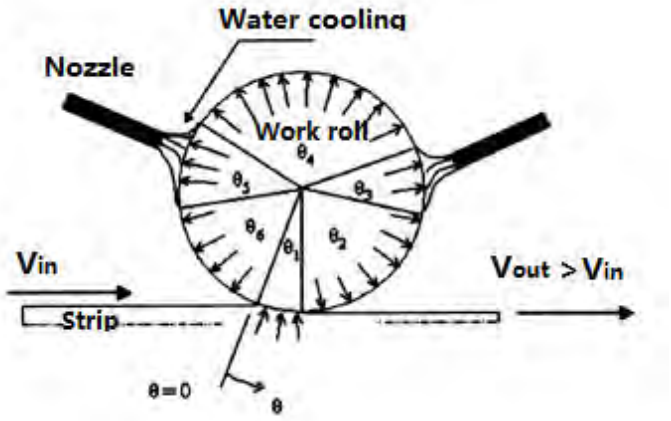

Fig. 2.15 Different angular sectors on work roll. [89]

Table 2.4 Different boundary conditions of work roll. [89]

Angle	Degrees, ^{o}	Zones
θ_1	18	Roll bite
θ_2	78	Air cooling
θ_3	30	Water cooling
θ_4	150	Air cooling
θ_5	24	Water cooling
θ_6	60	Air cooling

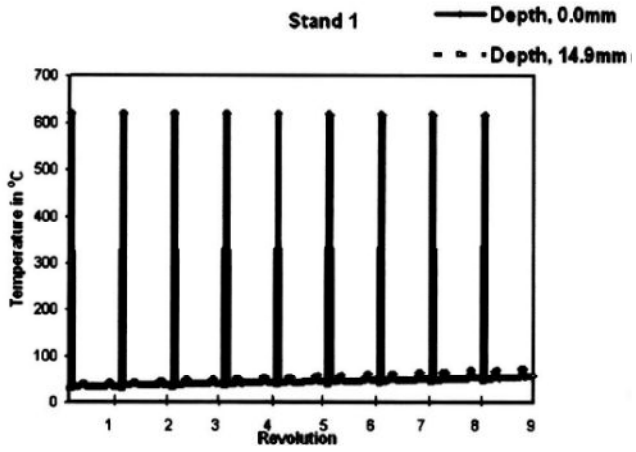

Fig. 2.16 Thermal cycles imposed on the work roll surface per roll revolution.[89]

Li et al. [90] developed an FEM model to simulate the three dimensional (3D) temperature field of a work roll during hot rolling. The results indicate that the highest temperature of the roll surface was 593 ^{o}C during hot rolling when the

temperature of the strip was set as 1000 ^{o}C. It only took 25s for the temperature to increase from 30 to 590 ^{o}C during the first rolling interval, and the temperature of the roll surface decreased to 61 ^{o}C. Then the roll temperature cycled between 61 and 590 ^{o}C.

2.3.2 Oxidation of high speed steel work rolls

As mentioned above, hot rolling work rolls are subjected to a high frequency of thermal cycles so high temperature oxidation of the surface is a common phenomenon in hot strip mills. This build up of oxides on the surface of the work roll affects its performance because these oxides produce a complex friction condition at the strip/roll interface while simultaneously acting as a protective layer minimising roll wear by oxide-to-oxide contact. It can be imagined that metal-to-metal, or metal-to-oxide contact between the work roll and the hot strip will result in a severe wear on the surface of the work roll. However, this surface deterioration possibly occurs when some of the surface comes off with the oxide scale [14, 91]. It is of great importance to understand the topography of the work roll surface, and the nature and morphology of the oxide on this surface.

Kim et al. [2] investigated the oxidation of three different high speed steel roll materials under wet and dry atmospheres at 600 ^{o}C up to 60 min. They found that carbides and the matrix were oxidised in a dry atmosphere but only the matrix in a wet atmosphere. After dry oxidation the M_2C-, M_6C- and M_7C_3-type carbides maintained their original shapes, while the MC-type carbides were oxidised into parallelepiped (orthorhombic) crystals. In the early stage of oxidation, the high speed steels oxidised following the parabolic rate law, as shown in Fig. 2.17. But this parabolic weight change became linear when the oxide was thicker than 1.3 μm due to cracks forming in the oxide layer. While in a humid atmosphere this transformation to a linear weight change was not observed, although it should be noted that the wet atmospheres consisted of argon (Ar) and water vapour, which are different to the industrial conditions.

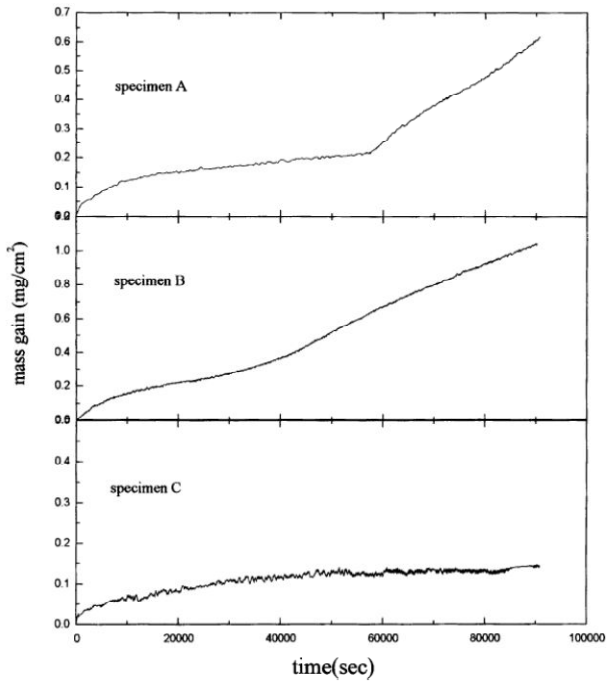

Fig. 2.17 Overall stage in mass gain of HSS by oxidation in O_2 at 600 ^{o}C. Specimen A and specimen B contain similar amount of chromium element, while specimen C contains much more Cr. [2]

Zhou et al. [92, 93] studied the oxidation of a roll grade high speed steel at temperatures between 500 to 800 ^{o}C in both dry and moist atmospheres. They found that selective oxidation occurred during the oxidation tests. The reason for selective oxidation is that high speed steel contains a high amount of oxidation resistance elements such as Cr, Mo, W, V, which form carbides inside the matrix, which leads to the difference of oxidation behaviour between the carbide-free matrix and carbides. They proposed the mechanism of oxide scale growing on a high speed steel surface as shown in Fig. 2.18. The oxidation nucleates first at the carbide/matrix interface due to its high, free energy content. Because the Cr-rich carbides have a high thermal stability and a low oxidation rate, oxide begins to grow mainly on the metal matrix and the V-rich carbides, which results in an uneven oxide scale. With an increasing oxidation temperature, the oxide scale covers the whole surface but it maintains an irregular morphology.

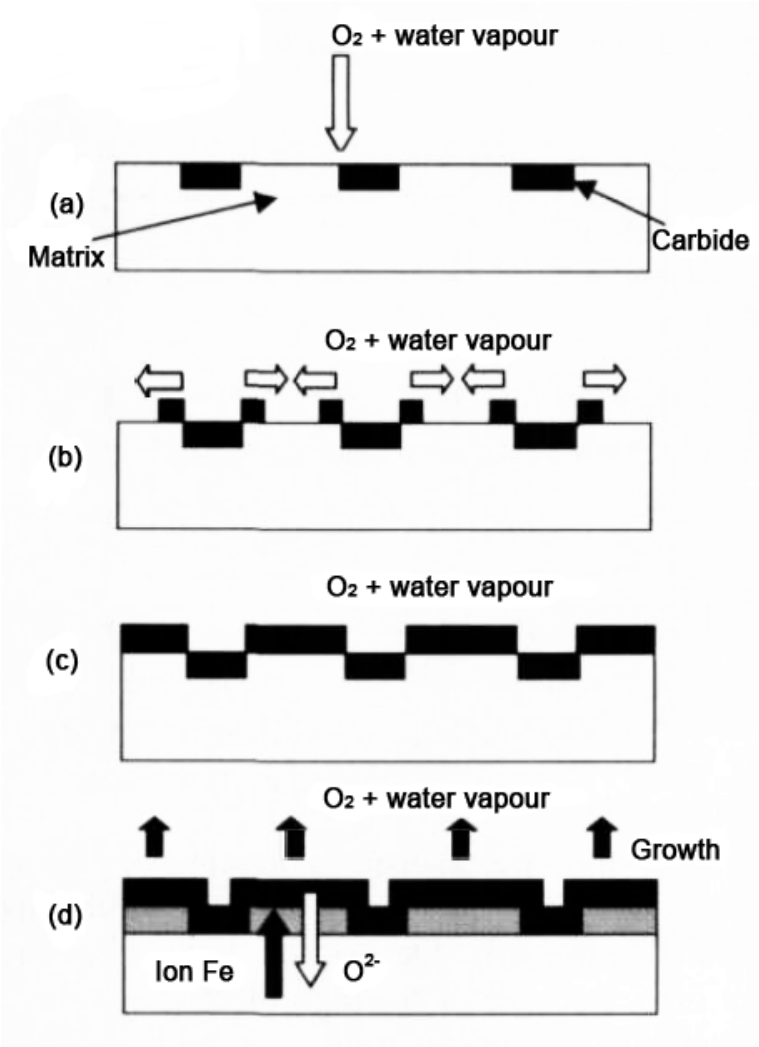

Fig. 2.18 The mechanism of selective oxidation of high speed steel. [92]

Molinari and Pellizzari [94] studied the oxidation of spincast HSS used in hot rolling, in temperatures ranging from 500-700 ^{o}C, by thermal-gravimetric analysis (TGA) and by characterising the oxidised specimens. They pointed out that the ferrous matrix oxidises homogeneously whilst carbides oxidise differently, and therefore have a significant influence on the compactness and homogeneity of the oxide scale. M_7C_3 carbides do not oxidise, whereas MC oxidised severely with a less compact scale, M_2C has an intermediate behaviour, which leans towards that of the M_7C_3 carbides. Oxidation rate follows the parabolic kinetics at both 500 and 700 ^{o}C.

Monteiro and Rizzo [6] studied the oxidation of three high speed steels with different contents of chromium (Table 2.5). They carried out the corrosion

experiments by means of a thermo-balance under dry and moist (12.5% H_2O) environments at 765 ^oC for 240 minutes. They found that variations in the content of chromium were enough to influence oxidation behaviour. Samples with high chromium contents gained the smallest final mass. The results of the weight change measurements for the three high speed steels showed that the mass gain was influenced by the oxidation atmosphere (Fig. 2.19 and 2.20). All the samples gained a higher mass in a moist atmosphere (Table 2.6). The authors argued that the addition of chromium could effectively reduce the oxidation rate of high speed steel in dry air because of the formation of a compact and continuous layer of chromia or a complex chromium based oxide at the scale-base metal interface. However, the study showed that in moist atmospheres an increase in water vapour might cause the formation of a porous and non-protective layer of iron oxide which increases the rate of oxidation.

Table 2.5 Chemical composition of the high-speed steels (wt.%). [6]

Samples	C	Cr	Mo	V
A1	1.5-2.5	3.5	2.0	5.0
A2	1.5-2.5	4.4	2.0	5.0
A3	1.5-2.5	7.5	2.0	5.0

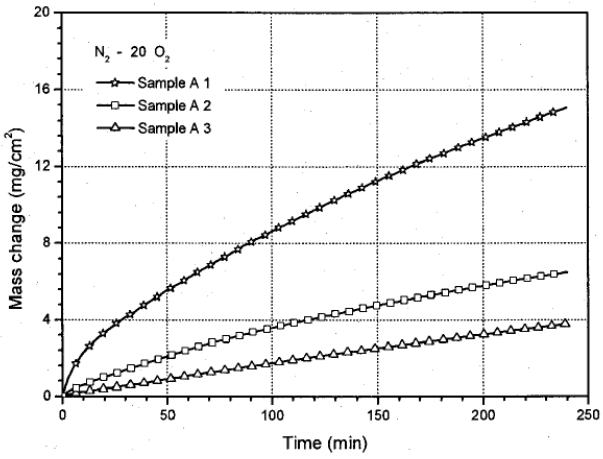

Fig. 2.19 Results of mass change measurement as a function of time for samples A1, A2 and A3 at 765 ^oC in N_2-20O_2 atmosphere. [6]

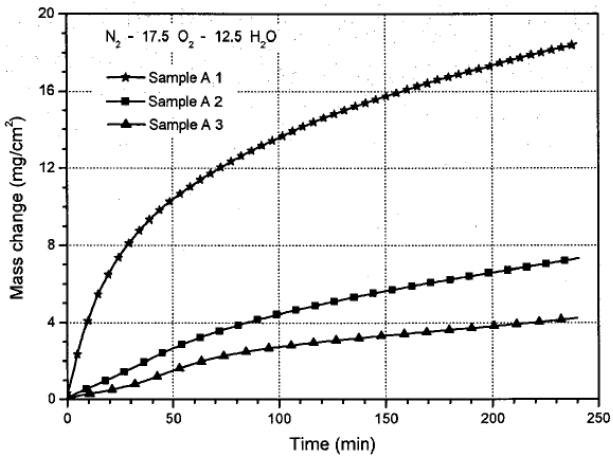

Fig. 2.20 Results of mass change measurement as a function of time for samples A1, A2 and A3 at 765 ^{o}C in N_2-17.5O_2-12.5H_2O atmosphere. [6]

Table 2.6 Summary of kinetic behaviour of samples A1, A2 and A3. [6]

Sample	Atmosphere	Kp (Average) (g^2/cm^4s)	Final grain mass (mg/cm^2)
A1	N_2-20O_2	1.43E-8	15.05
	N_2-17.5O_2-12.5H_2O	2.57E-8	18.49
A2	N_2-20O_2	2.49E-9	6.49
	N_2-17.5O_2-12.5H_2O	3.96E-9	7.33
A3	N_2-20O_2	----	3.78
	N_2-17.5O_2-12.5H_2O	1.65E-9	4.25

Molinari et al. [19] carried out a series of oxidation tests on two HSS steels used to produce hot rolls in order to investigate the oxidation mechanisms and their correlation with a particular microstructure and chemical composition. These two steels have slightly different chromium contents (3 and 5wt%) as well as volume fraction of primary carbides. Isothermal oxidation tests were carried out in a thermo-analytical apparatus in dry air and at temperatures of 500, 600, and 700 ^{o}C for up to 24h. They found that oxidation started at the carbide/matrix interface and involved the matrix only, because carbides have a high resistance to oxidation. They also found that steel containing more chromium and less carbides resisted oxidation better. However, the capability of chromium to reduce the oxidation rate depends on the oxidation temperature; it was almost negligible at 500 ^{o}C, increased at 600 ^{o}C, and even more at 700 ^{o}C, as can be seen from Fig. 2.21.

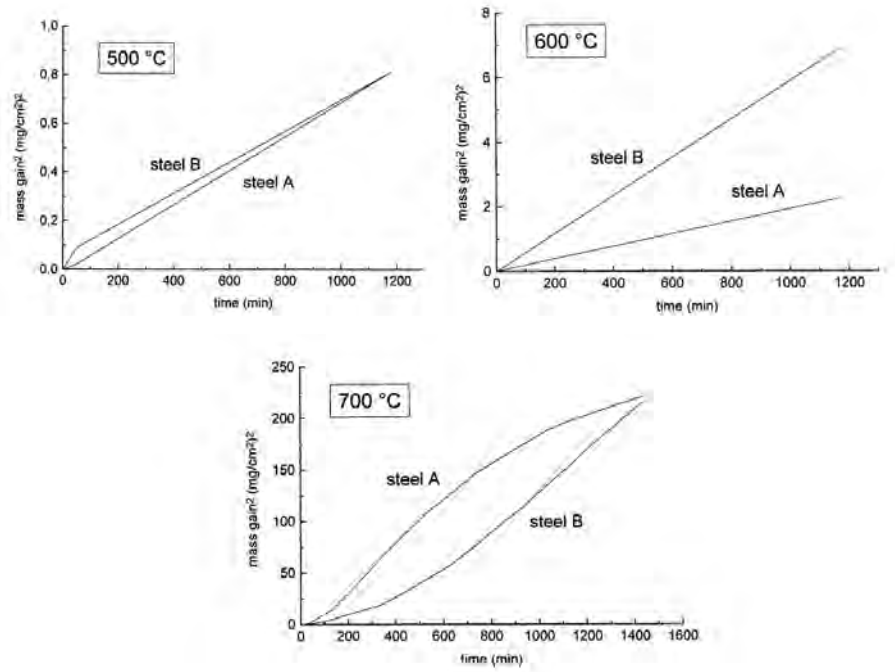

Fig. 2.21 Quantification of the oxidation phenomenon obtained at three temperatures for two high speed steels containing slightly different amounts of chromium (steel A > steel B). Note the differences in the mass gained as a function of the testing temperature. [19]

Monteiro et al. [95] investigated the effect of water vapour on four different high speed steels (Table 2.7). The experiments were carried out at 650 ^{o}C in a mixture of nitrogen and oxygen (volume ratio 4:1) with 4.2, 7.3, and 12.5vol.% water vapour for up to 4h. They found that the oxidation rate reduced with an increase in chromium in dry air, but an increase in the content of V and W had no effect (as see in Table 2.8). In moist conditions the alloys containing a higher volume of Cr and W had the lowest oxidation rates followed by the alloy with increased V levels, although these effects were small. The presence of water vapour in the atmosphere increased the oxidation rate, as can be seen from Fig. 2.22. However, the parabolic kinetics was not obeyed. The content of water vapour not only enhanced the oxidation rate, it also greatly influenced the sample surface morphologies after oxidation. It can be seen from Fig. 2.23 that an exposure to water vapour causes platelets to form and their density increases as the amount of water vapour increases. At the highest level of water vapour, whisker formation was also observed, as shown in Fig. 2.23d.

Table 2.7 Composition of alloys, % mass fraction. [95]

	C	Cr	Mo	W	V	Fe
A1	1.5-2.5	4.06	2.02	1.96	4.79	Bal
A2	1.5-2.5	7.50	2.00	2.00	4.80	Bal
A3	1.5-2.5	4.40	2.30	3.90	4.80	Bal
A4	1.5-2.5	4.19	2.07	2.02	8.09	Bal

Table 2.8 Average mass gain data for alloys investigated after 4 h at 650 ^{o}C in dry and moist air, mg·cm^{-2}. [95]

	0 vol.%	4.2 vol.%	7.3 vol.%	12.2 vol.%
A1	0.55±0.018	0.97±0.057	1.72±0.132	2.54±0.022
A2	0.43±0.000			2.08±0.038
A3	0.64±0.072			2.08±0.051
A4	0.58±0.061			2.33±0.062

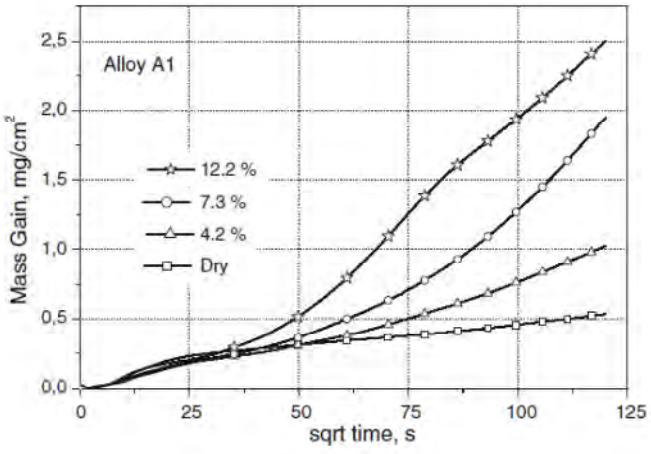

Fig. 2.22 Mass gain versus time curves for alloy A1 at 650 ^{o}C in dry synthetic air and with various water vapour additions (vol%).[95]

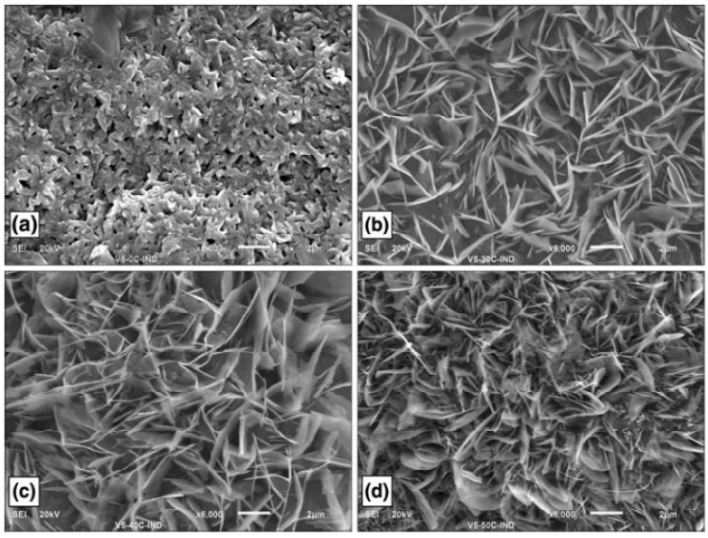

Fig. 2.23 Scanning electron micrographs of the surface of alloy A1 after oxidation in various conditions at 650 ^{o}C, (a) dry air, (b) air plus 4.2vol.% water vapour, (c) air plus 7.3vol.% water vapour and (d) air plus 12.2vol.% water vapour. [95]

Garza-Montes-de-Oca et al. [96] carried out a thermal cycling oxidation experiment to study the behaviour of an oxide scale grown on the surface of a high speed steel in dry air and water vapour. They found that the oxide layer covering the surface of high speed steel work rolls was predominantly a mixture of hematite Fe_2O_3 (outer layer) and M_3O_4 iron-chromium spinel (inner layer). The oxide layer was subjected to thermal stresses generated during either heating or cooling stages. Due to differences in the thermal expansion coefficients of hematite (13×10^{-6} $1/^oC$) and magnetite (12×10^{-6} $1/^oC$), buckling and spallation of the top layer of oxide develop preferentially on the layer of hematite (Fig. 2.24). The authors pointed out that spallation of the hematite layer must be considered as an important mechanism that controls the friction and wear properties of work rolls in hot strip mills.

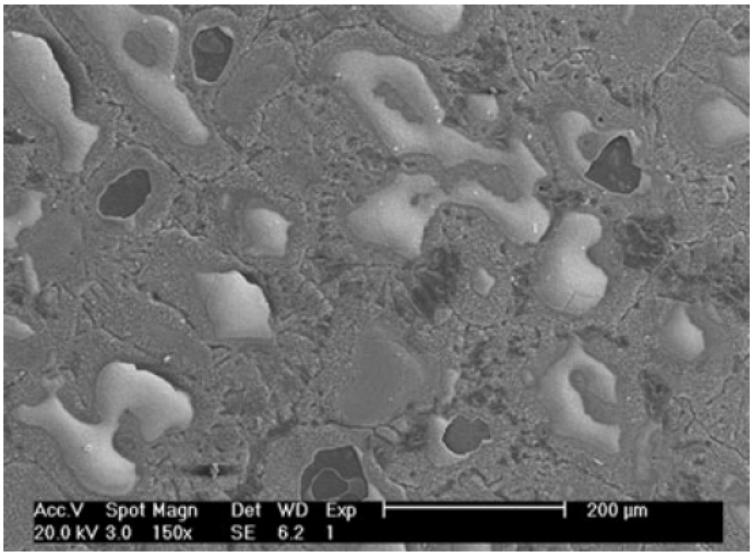

Fig. 2.24 Typical buckles formed in the Fe_2O_3 layer after 7 thermal cycles. [96]

2.4 Wear of work rolls in hot rolling

2.4.1 Wear mechanisms of high speed steel work rolls

During hot rolling work rolls are worn by a combination of various wear mechanisms. It is well accepted that surface abrasion, adhesion, thermal fatigue and high temperature oxidation are the four main wear mechanisms of hot work rolls [4, 10, 12, 68, 97-103]. A number of researchers consider that abrasive wear, in

which micro-cutting, surface plastic deformation, and crack initiation occur simultaneously, depending on the shape and hardness of the abrasive particles, is the major wear mechanism [97-102]. The oxide scale formed on the surface of the hot strip is hard enough to cause abrasion on the rolls [12, 97, 103]. The high temperatures result in a loss of hardness in the roll material, which in turn promotes wear. This is the reason why high speed steels have become the material of choice for hot rolling work rolls because they possess a higher surface hardness than other roll materials. During hot rolling, the abrasive and adhesive wear of the work roll occurs while in contact with oxide scale on hot strip surface; corrosive wear is caused by oxidation and further deterioration at high operating temperatures and humid atmospheres, while thermal fatigue wear is caused by a combination of mechanical loading and thermal cycles.

Although it is still a challenge for researchers to simulate hot rolling conditions in a laboratory, several test configurations have been developed to simulate the operating conditions in the roll bite. Many researchers use a disc-on-disc configuration (as seen in Fig. 2.25), one simulating the hot strip, the other one simulating the roll. The disc simulating the hot strip can usually be heated up to 700-950 ^{o}C by an induction heating system [4, 8, 10, 12, 68, 99, 104-108]. Some researchers refer to a pin-on-disc configuration (as seen in Fig. 2.26). Generally, the disc is simulating the hot strip and can be heated, while the pin (or ball) simulating the roll [109, 110]. But in some cases, the disc is made of roll material (HiCr-HSS plate), while the pin counterpart is alternatively made of bearing steels, WC-Co and silicon nitride (Si_3N_4) [111-113].

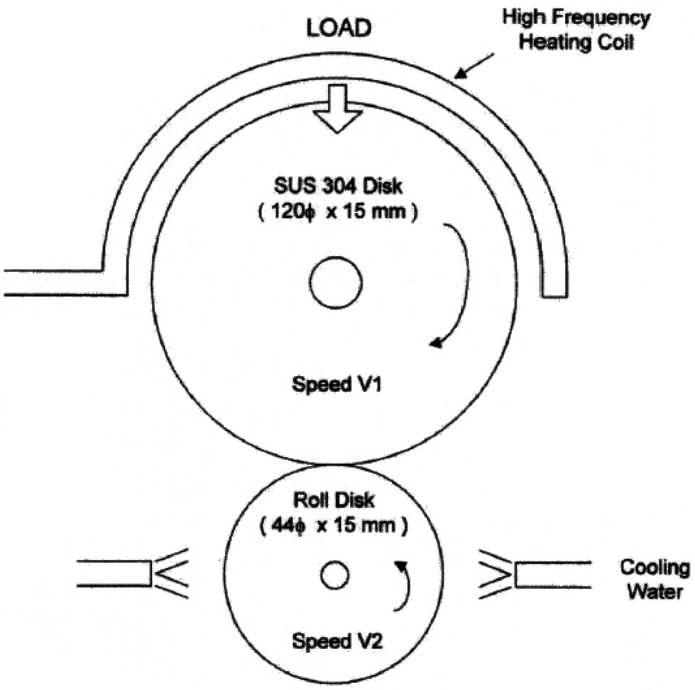

Fig. 2.25 Schematic diagram of a high temperature disc-on-disc wear tester used to simulate hot rolling. [8]

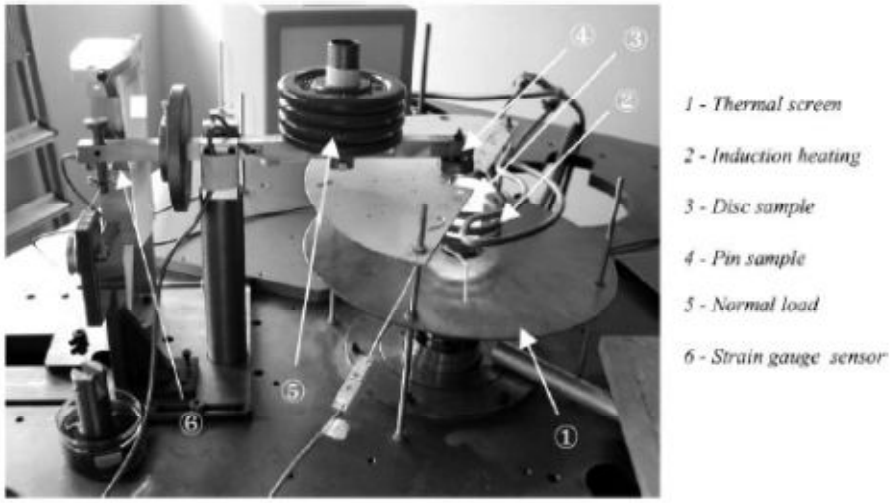

Fig. 2.26 High temperature pin-on-disc tribometer. [14]

Kang et al. [8] studied the effects of carbon and chromium additions on the wear resistance and surface roughness of five high speed steel rolls. High temperature disc–on-disc wear tests were conducted on these rolls to experimentally simulate the wear process during hot rolling. They found that wear resistance increases with the carbon content because of an increased total carbide fraction. In the HSS roll containing a smaller amount of chromium, wear resistance was improved because it

contained a number of very hard MC carbides. However, the roll surface is very rough because of the preferential removal of the matrix and sticking the rolled material onto the roll surface during the wear process. Rolls containing higher chromium contents had very low surface roughness, because of the formation of a larger amount of M_7C_3 carbides of slightly lower hardness and homogeneous wear of the matrix and carbides. The authors suggested that it should increase the chromium content in the HSS rolls in order to improve the wear resistance in terms of surface roughness.

Hanlon and Rainforth [107] studied the wear mechanism of high speed steel rolls by using a high temperature disc-on-disc testing rig. Their results indicated that the surface degradation of rolls occurred preferentially at the carbide/matrix interface, but was particularly prominent in the Fe/M_2C-M_6C eutectic regions and at large primary VC carbides regions, due to the great difference in hardness between carbides and matrix. At the same time, the oxidation of the roll surface occurred during the rolling sliding wear test, which seemed to have no significant influence on the wear rate. However, internal oxidation along with the fractured carbides might lead to substantial zones of weakness on the worn surface and to some depth below. The authors confirmed that controlling the microstructure of HSS is a key issue in improving its mechanical properties. Later on, Rodenburg and Rainforth [7] investigated the influence of carbides size distribution on the wear behaviour of high speed steel. They found that the carbide size distribution was a major controlling factor in the mild oxidational wear of high speed steel based materials. A reduction in carbide size for a constant volume fraction of carbide not only altered the probability of carbide fracture, it also reduced the mean distance between carbides, which reduced the matrix exposure to contact damage.

Pellizzari et al. [108] analysed the wear tribological behaviour of high speed steel and high chromium iron rolls based on their high temperature disc-on-disc tests. The authors indicated that the wear mechanism was given by abrasion, adhesion,

and triboxidation. The higher wear resistance of HSS compared to HiCr irons was due to the former being harder, which resulted in more resistance to abrasion. As far as friction was concerned, the HSS and HiCr displayed different behaviours. It can be seen from Fig. 2.27a that HSS showed an almost steady value of friction while the HiCr showed a step change. In the early stage of wear the friction was quite low but then it suddenly increased to higher values (Fig. 2.27b). The friction of HiCr highlighted the transition from an oxide-metal contact in the early stage to an oxide-oxide contact. On the contrary, the friction of HSS remained almost constant during the whole test, the authors regarded that the contact between the HSS roll and steel strip was always an oxide-metal contact.

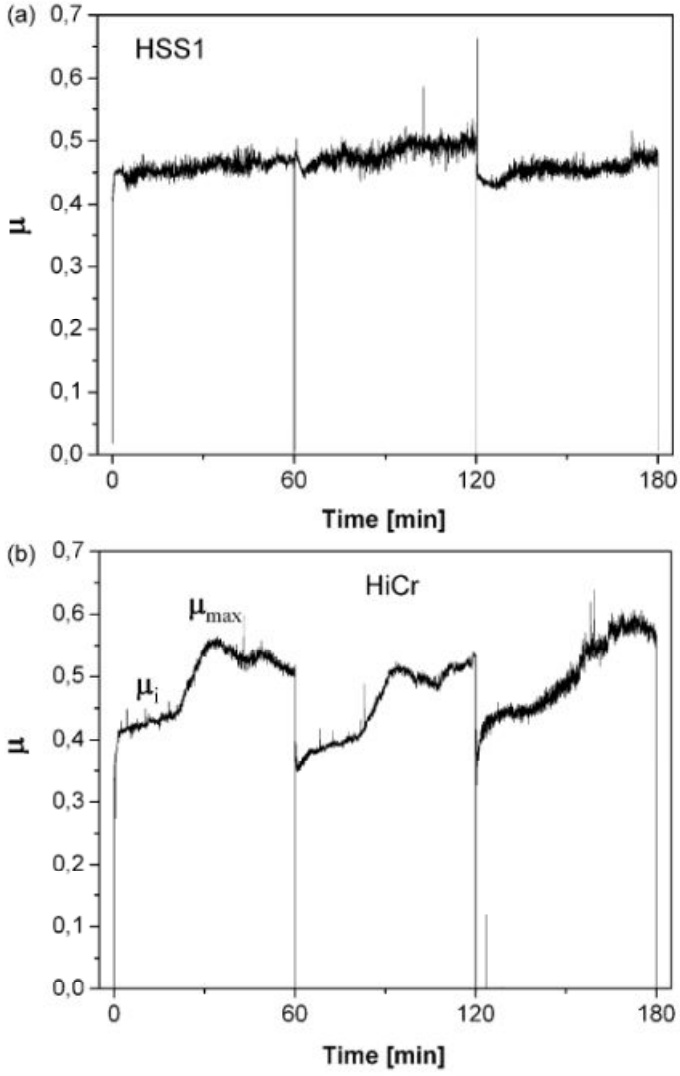

Fig. 2.27 Diagram of friction typically displayed by (a) HSS and (b) HiCr irons. Hourly cycle tests were carried out to determine sample weight loss. [108]

Garaza-Montes-de-Oca and Rainforth [114] studied the wear mechanisms of a high speed steel work roll under different environmental conditions. The experiments were carried out on a high temperature disc-on-disc testing rig, but the rig was modified to allow for the introduction of both water and water vapour during the tests via two nozzles located close to the test disc (Fig. 2.28). An SEM image of the cross section of the worn surface confirmed the previous work results that the cracks generally began at the interface between the carbide and the matrix, especially in the large MC vanadium rich carbides, as shown in Fig. 2.29. The authors proposed that different wear mechanisms occur depending on the temperature range and atmospheric conditions. Under dry conditions the wear mechanism was a mixture of oxidational and metallic ploughing wear, with a proportion of the latter increasing with temperature. Under moist conditions the wear mechanism was essentially oxidational at all temperatures. The coefficient of friction increased in an approximately linear manner with the test temperature. It was noted that the coefficient of friction was higher for the wet tests compared to dry air, however the authors were not able to explain the reasons for this behaviour.

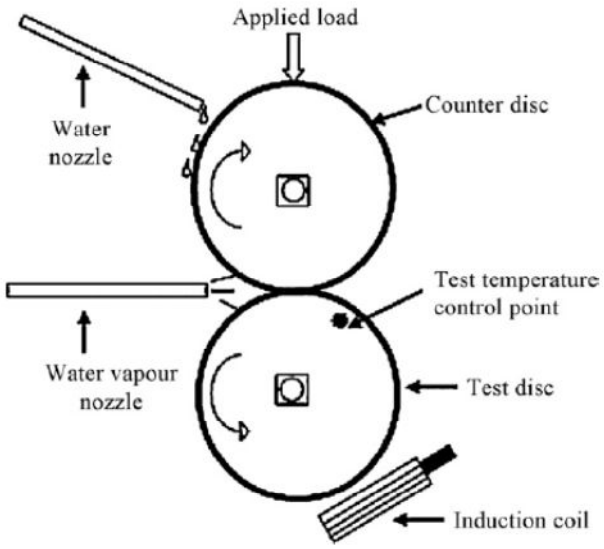

Fig. 2.28 Schematic representation of the rig used for the rolling-sliding experiments. [114]

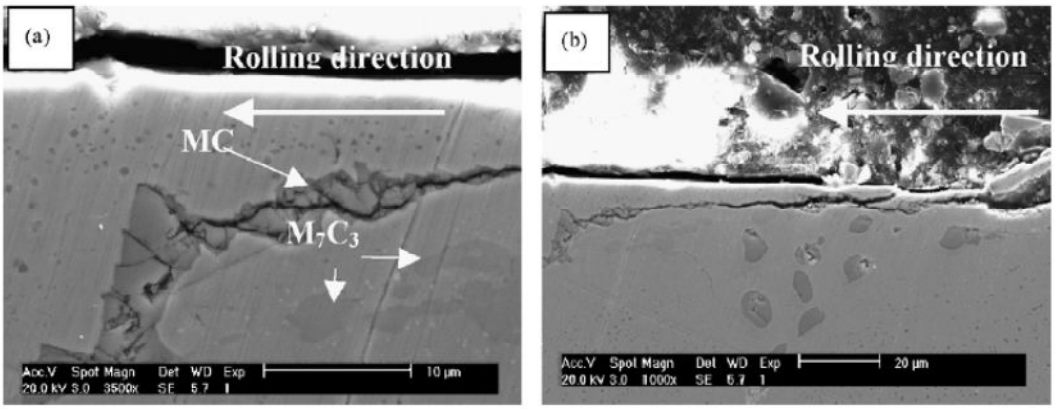

Fig. 2.29 Fracture of MC vanadium rich carbide and subsurface oxide. (a) General surface appearance and (b) detail.

2.4.2 The role of oxides on contact behaviour of work rolls in hot rolling

In hot rolling most attention related to oxidation has always focused on the oxides formed on the surface of the hot strip [85, 115-123], although oxidation of the roll surface is usually considered as one of four main types of damage (i.e. surface abrasion, adhesion, thermal fatigue, and high temperature oxidation) observed in rolling service [13, 32, 100, 123-128]. The contribution and impact of the oxides that form on the surfaces of the work roll on the tribological behaviour between the work rolls and hot strips has barely been studied and is not well understood [129]. The oxide scale formed on the work roll plays an important role during hot rolling [112, 130]. On one hand it can act as a diffusion barrier and protect the metal underneath from rapid degradation, while on the other hand it prevents metal-metal contact or metal-oxide contact between the hot strip and work rolls, which may prevent the sticking phenomena from occurring [98]. This protective effect, however, will be impaired when cracks occur in the scale or spallation happens [131, 132]. However, the tribological behaviour of oxide scale is ambiguous. Milan et al. [101], Molinari et al. [19] and Vergne et al. [14] considered that a compact and adherent oxide scale acts like a solid lubricant by reducing the coefficient of friction between the roll and the rolled material, while a hard and brittle oxide may give abrasive behaviour by increasing coefficient of friction as well as wear. Vergne et al. [14, 109] pointed out that the tribological behaviour of oxide

scale depends on the nature and mechanical properties of the oxide scales, and is also correlated to other aspects and friction conditions for instance.

Vardavoulias [133] carried out a series of pin-on-disc tests to investigate the role of hard second phases in the mild oxidational wear mechanism of high speed steel based materials. With high speed steel materials containing various hard second phases, an α-Fe_2O_3 film is formed during pin-on-disc testing (under mild conditions of load and sliding speed), which reaches a critical thickness of 1-2µm before breaking up into loose wear debris. The author found that the size of the hard second phase particles appear to be the most important parameter determining the possibility for the particles to provide protection against oxidational wear of the matrix. More specifically, when oxidation advances from the oxide-metal interface towards the metallic substrate, like in the case of α-Fe_2O_3, matrix protection depends on the relationship between the second phase mean particle size (d) and critical oxide thickness (ξ). When d is less than or equal to ξ, the second phase particles can be entirely included in the oxide layer (Fig. 2.30a) and removed together with the oxide when the oxide layer breaks up to form wear debris (Fig. 2.30b). The second phase is not capable of directly protecting the metallic matrix and thus positively influencing its wear behaviour. When d is only a few times higher than the critical oxide thickness (i.e. $\xi<d<3\xi$), a transition phase in the wear mechanism takes places (Fig. 2.31). A small quantity of the second phase particles may be removed together with the oxide. However, when the oxide layer breaks up most of the second phase particles remain in the substrate and protrude above the nominal surface (Figs. 2.31a and b). The counter body will slide on these particles. During this stage, which may be called the second stage of the wear mechanism (the first stage is the formation and breaking up of the oxide film), the matrix does not influence wear. This second stage wear may be accompanied by high abrasive wear on the counter body (Fig. 2.31c). If the particles do not resist wear and fail under the loading imposed by the counter body (Fig. 2.31d), the duration of second stage wear is very short and the first stage wear of the metallic matrix repeats itself.

Wear rates are generally higher for this case. Finally, if the metallic matrix/second phase cohesion is not strong enough, the second phase particles can be rapidly detached after the oxide breaks up into debris (Fig. 2.31e). The wear rate of both sliding bodies has probably increased because the detached hard particles can function as third body abrasives. Second phase particles with a mean particle size that is much higher than the critical oxide thickness ($d>>\xi$) are better at providing oxidational wear protection to the material. After the first stage takes place and the oxide breaks up, the coarse second phase particles remain embedded in the metallic matrix (Fig. 2.32). A counter body/second phase interaction takes place in this case also.

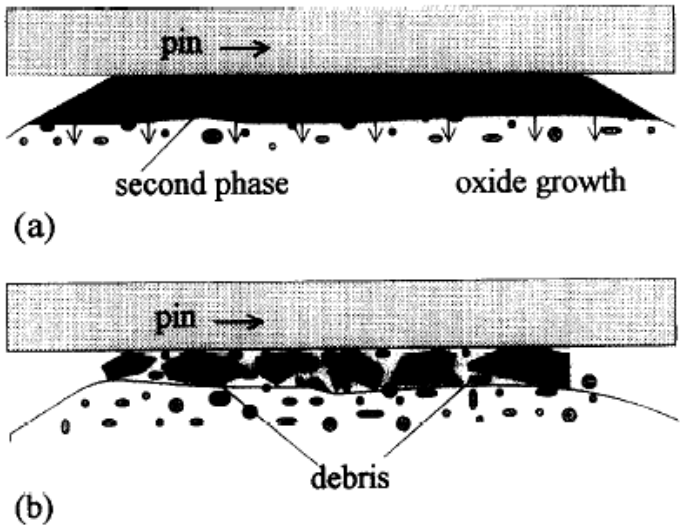

Fig. 2.30 Oxide development in the presence of hard second phases with mean particle size less than or equal to the oxide's critical thickness. (a) Hard particles are surrounded by the oxide; (b) hard particles are drawn by the oxide when it breaks up to form wear debris. [133]

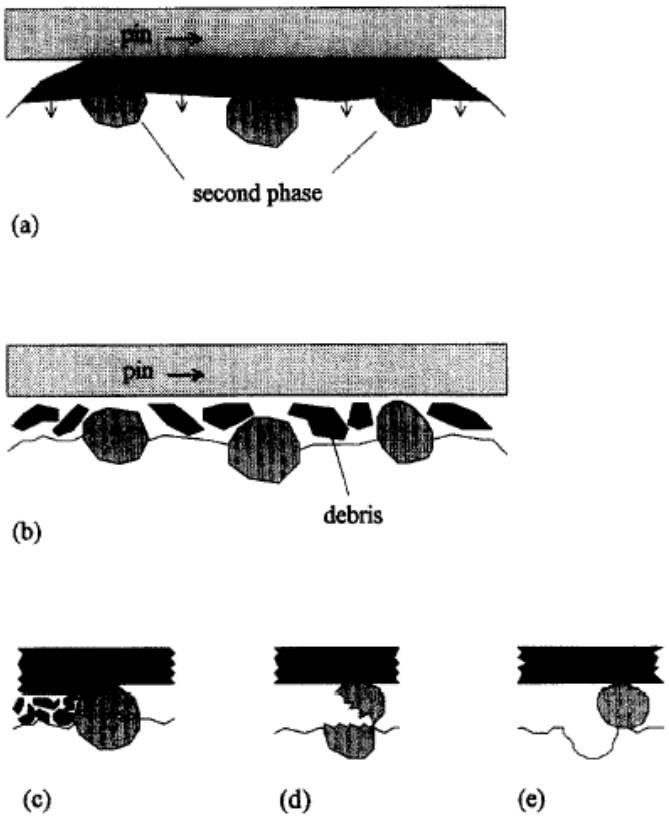

Fig. 2.31 Oxide development in the presence of hard second phases with mean particle size higher than the oxide's critical thickness. (a) Hard particles are partially surrounded by the oxide, (b) hard particles remain in place when the oxide breaks up, (c) abrasion of the counterbody by the hard particle, (d) particle failure, (e) particle detachment. [133]

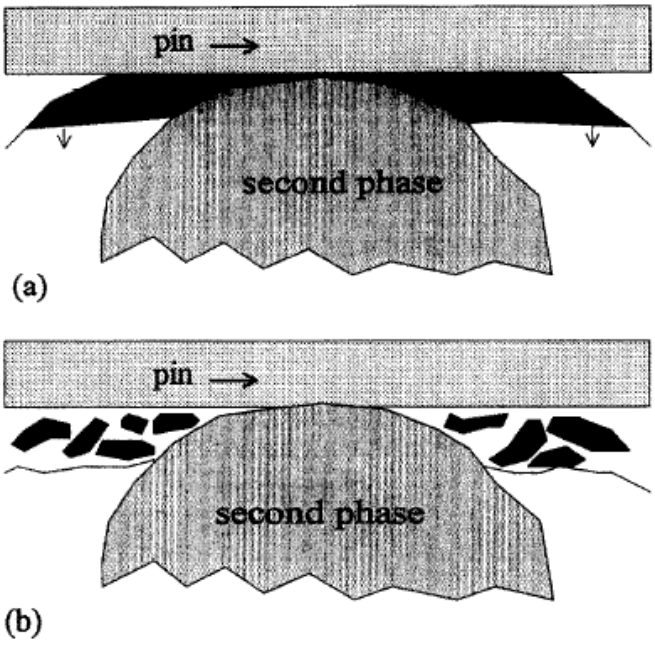

Fig. 2.32 Oxide development in the presence of hard second phase with mean particle size much higher than the oxide's critical thickness. (a) Hard particles remain largely out of the oxide; (b) hard particles are not actually influenced by the oxide's breaking up. [133]

Hokkirigawa et al. [134] developed an in-situ CCD microscope tribosystem to analyse the microscopic sliding wear mechanism of oxide films on hot roll surfaces. Using this system the dynamic wear process of oxide films on hot roll surfaces were observed successively. The authors classified three types of wear modes of oxide films on the hot rolls surfaces based on these observations and summarised a wear mode map, as seen in Fig. 2.33, which indicates a different wear mode. It can be seen that (i) when the normal load $W < W_{c1}$ wear mode of ploughing or powder formation occurs throughout the sliding, (ii) when $W_{c1} \leq W \leq W_{c2}$ wear mode of flake formation occurs after a certain number of repeat passages, (iii) when $W \geq W_{c2}$ spalling of oxide films occurs after a certain number of repeat passages.

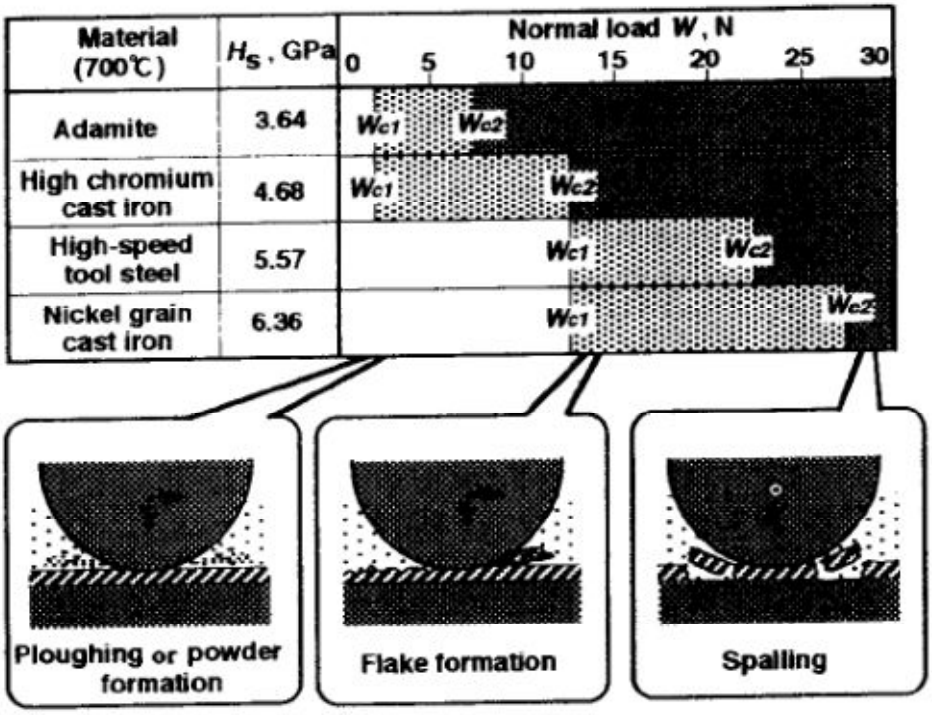

Fig. 2.33 The value of critical normal loads W_{c1} and W_{c2} for four roll materials under the water lubricated condition. [134]

Vergne et al. [109] carried out an extensive investigation of the interaction between the oxides formed on the surface of a work roll and the coefficient of friction established when hot rolling steel, by means of a pin-on-disc configuration rig using alloyed white cast iron as the pin material faced against a disc made of mild steel, under various temperatures, loads, and speeds. The actual operating conditions of

friction tests were rather different from industrial rolling conditions. Nevertheless, the tribological configuration of contact --- a sliding motion at a high temperature close to the rolling temperature with an initial Hertzian pressure close to the contact pressure in a rolling bite – allowed a display of the impact of the chemical composition of a work roll grade on the friction and wear mechanisms.

In their work, the authors explained the friction behaviour in the following manner based on electron microscopy observations and EDX micro-analysis. The initial increment in the coefficient of friction since the beginning of the test was due to an increase in the value of the shear force needed to cut off the oxide excrescences formed on the surface of the pin, and break the junctions formed when the pin entered the oxide layer. A reduction in the values of friction followed because the attrition and rolling of the Nb-oxide grains produced by oxidation of the MC niobium rich carbide acted as a solid lubricant in the contact while simultaneously causing a decrease of the tangential force. And the increase in the value of friction again was attributed to failure of the oxide layer and the generation of wear debris responsible for increasing the superficial area. As the contact area increased, more junctions were subsequently created which increased the value of the shear stress needed to break the newly formed junctions. In the stabilised friction regime, the temperature recorded by the thermocouples in the pin seemed to be stabilised. The trio-system achieved a thermo-mechanical equilibrium where the wear mechanisms had no more notable influence on the evolution of the coefficient of friction.

Joos et al. [99] tried to identify and assess the wear mechanisms involved in the hot tribological behaviour of high speed steel roll grades by carrying out a series of pin-on-disc tests at evaluated temperatures. They argued that the tribological behaviour of roll grades at high temperature was strongly affected by the nature, thickness, and thermo-mechanical properties of their oxide scales involved in the contact (Table 2.9). For a disc temperature of 20 ^{o}C the contact was metal against metal and the wear mechanism was abrasive. The debris attrition phenomena lead

to the formation of oxide debris and the coefficient of friction was high. For a disc temperature of 650 ^{o}C oxidation of the surface of a HSS pin was low and the wear mechanism was still abrasive by disc oxide scale. The decrease in the coefficient of friction could only be attributed to the disc oxide layer that plays the role of a solid lubricant. For a disc temperature of 950 ^{o}C, the low oxidation resistance of HSS leads rapidly to the formation of a continuous oxide scale on the surface of the pin that was thick enough to take in charge the contact. That contributed to the drop of friction in comparison with tests at 650 ^{o}C.

Table 2.9 Contact nature in tribological tests for HSS. [99]

Disc temperature (^{o}C)	First bodies		Third body
	On pins	On discs	
20	Metallic substrate	Metallic substrate	Oxidised debris
650	Continuous oxide scale	Thin and continuous Fe_2O_3/Fe_3O_4 oxide scale	Oxidised debris
950	Thick and continuous glazed oxide scale	Thick and continuous ferrous $Fe_2O_3/Fe_3O_4/FeO$ oxide scale	Oxidised debris

Chapter 3
Experimental instruments and analytical methodology

This chapter includes a detailed description of the experimental instruments and analytical methodology used in the current study.

3.1 Experimental instruments

3.1.1 High temperature microscope (HTM)

In-situ oxidation tests were carried out in a high temperature microscope (HTM) with a CCD camera as a detector. Fig. 3.1 shows a photo of the HTM chamber. The HTM is normally used as a laser scanning confocal of the specimen, but the CCD camera provides a far better resolution in the case of oxidation experiments due to its ability to compensate for differences in light emission and a greater depth of field [60, 135, 136]. Fig. 3.2 shows a schematic illustration of the transverse cross section of the high temperature furnace and experimental configuration of the test. A 1.5 KW-halogen lamp located at one focal point of the ellipsoidal cavity, heats the specimen located at the other focal point by radiation. Images from the heated sample can be captured by the CCD camera and sent directly to a computer at 25 frames per second. By recording continuously during an experiment, the whole oxidation process can be observed in-situ. During oxidation, the sample was placed in a 4-mm diameter alumina crucible with a polished surface on top. The crucible was then put into the sample holder which was inserted into the gold plated ellipsoidal infrared heating furnace. One end of the gas entry tube was placed above and adjacent to the sample, in order to apply the oxidising gas directly onto the surface of the sample.

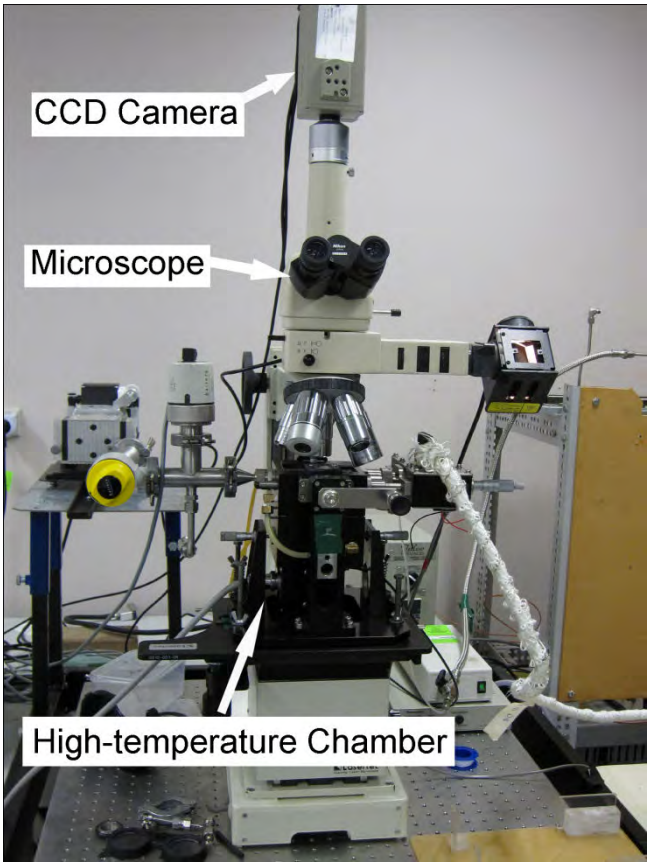

Fig. 3.1 Photo of high temperature microscope chamber.

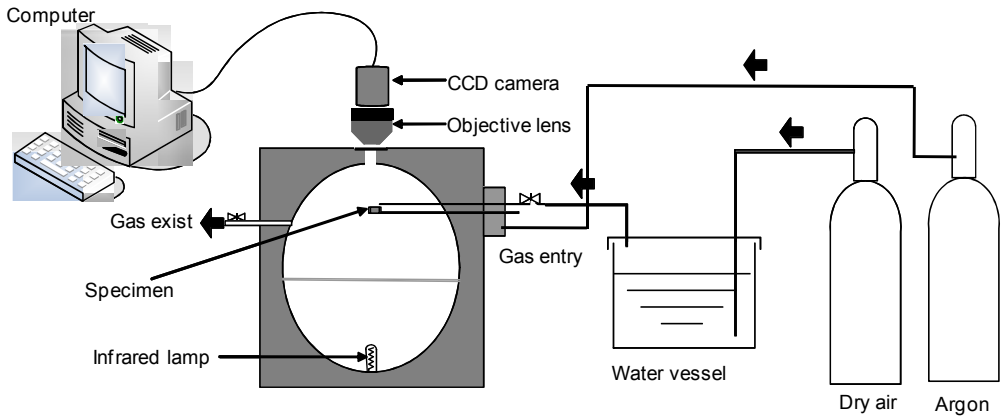

Fig. 3.2 Schematic illustration for in-situ observation oxidation experiments in high temperature microscope.

3.1.2 Gleeble 3500 thermal and mechanical testing system

The Gleeble 3500 is a fully integrated digital closed loop control thermal and mechanical testing system. Fig. 3.3 shows a photo of the Gleebe 3500 thermal mechanical system located at the University of Wollongong. The thermal system is

equipped with a direct resistance heating system that can heat specimens at a rate up to 10,000 ^{o}C/s, or can hold steady-state equilibrium temperatures. The system is also capable of performing a high cooling rate in excess of 10,000 ^{o}C/s at the surface of a specimen with the high thermal conductivity grips holding the specimen. Thermocouples provide signals for accurate feedback control of specimen temperatures. The test chamber is connected to a high vacuum system. Optional protection gas can also be introduced into the chamber as well. The mechanical system is a complete, hydraulic servo capable of exerting up to 10 tons of static force in tension or compression. Displacement rates as fast as 1,000 mm/s can be achieved.

Fig. 3.3 Photo of Gleeble 3500 thermal mechanical system.

3.1.3 CETR multi-specimen test system

The CETR UMT2 multi-specimen test system can be used for tribological testing of ferrous and non-ferrous metals, plastics, ceramics, paper, composites, thick and thin coatings, as well as solid lubricants, lubricating fluids, and oils and greases. Fig. 3.4 shows a photo of the CETR with a high temperature pin-on-disc configuration. Mounted with the high temperature chamber, the CETR multi-specimen test system can conduct high temperature wear tests in a temperature range up to 1000 ^{o}C. Various common tribology test modes are available in the system, including pin on

disc, ball on disc, disc on disc, and so on.

The CETR multi-specimen test system can accommodate upper and lower samples of practically any geometry. The upper specimen is connected to a vertical linear motion system that has a 150mm length of travel. Wear measurements can be performed to an accuracy of 50nm. A precision spindle can rotate the lower specimen at speeds from 0.001 to 5,000rpm. The load cell can precisely control the load in a range from 2-200N. Ultra-accurate strain-gauge sensors perform simultaneous measurements of load and torque in two to six axes. The forces can be measured precisely in ranges from milligrams to kilograms, with a resolution of 0.00003% of full-scale, and very high repeatability.

Fig. 3.4 Photo of CETR multi-specimen test system. (High temperature pin-on-disc configuration)

3.1.4 IBIS/UMIS nano-indentation system

The IBIS/UMIS nano-indentation system was first manufactured in 1984 by CSIRO Division of Applied Physics in Sydney Australia. The instrument arose from a need to

measure the hardness of thin films. The system can be mounted with various types and sizes of indenters, such as Berkovich indenters, sphero-conical indenters, knoop indenters, and cube corner indenters. Fig. 3.5 shows a photo of the IBIS/UMIS nano-indentation system in the tribology laboratory at the University of Wollongong.

For nano-indentation, information is derived from penetration on loading and also from the elastic recovery of the indentation on unloading – the load-displacement curve. This method can characterise bulk materials including metals, ceramics, plastics, crystalline, and amorphous materials, coatings, and modified surface layers. The IBIS/UMIS nano-indentation system can continuously record load vs. depth curves with a resolution of 75 nN in load and 0.05nm in depth. The system can perform an indentation test in a wide load range from 100μN up to 500 mN. A video microscope in the system can be used with precise sample positioning for measuring the mechanical properties of very small volumes of material.

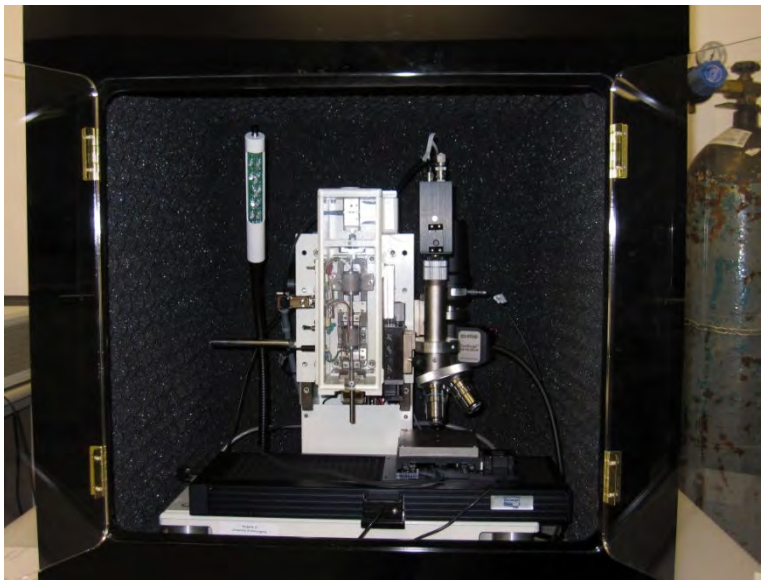

Fig. 3.5 Photo of IBIS/UMIS nano-indentation system.

3.2 Analytical Methodology

3.2.1 Scanning electron microscope

A JEOL JSM 6490 scanning electron microscope (SEM) equipped with energy

dispersive X-ray analysis (EDS) was used to investigate the microstructure of samples of high speed steel and the morphologies of oxide scales. The operation voltage was chosen as 20kV and the working distance was set at 10mm.

3.2.2 Focus ion beam microscope

An XT Nova Nanolab 2000 workstation which combines a dual beam high resolution focused ion beam and a high scanning electron microscope (FIB/SEM) was used to characterise the surface morphology of the specimen after oxidation and prepare thin foil specimens for further TEM observation. The system is equipped with a platinum deposition system and the SEM column with a field emission gun (FEG). The FIB column uses a fine, energetic beam of gallium ions that scan over the surface of a specimen. At high beam currents the gallium beam rapidly sputters away the surface of the specimen to expose the sub-surface cross section. During this FIB cross sectioning, an accelerating voltage of 30KV and high ion currents were used and, lower currents of 1nA and 0.5nA for nano-milling.

3.2.3 Transmission electron microscope

A Philips CM200 field emission gun transmission electron microscope (FEG-TEM) equipped with an energy dispersive X-ray spectroscopy (EDAX) system was used to investigate the detailed microstructure of the FIB cross sections of the oxide scales. The Philips CM200 FEG-TEM allows very high resolution images to be obtained from thin, electron transparent sections of materials. Ultimately, this microscope allows individual atoms to be imaged. The TEM allows not only structural information to be obtained, but also crystallographic studies of materials are routinely possible. This microscope has an EDAX energy dispersive x-ray spectroscopy system interfaced to it, which can allow chemical analysis from regions as small as 10nm in diameter to be obtained. In addition, it has an SIS CCD camera to directly record digital images. In this study the TEM was operated with an accelerating voltage of 200KV.

3.2.4 Atomic force microscope

A Multi-Mode Scanning Probe Microscopy (SPM) from Digital Instruments operating in contact AFM mode (Nanoscope IIIA AFM) was used to obtain topographic images of the surfaces of the samples. This AFM has a lateral resolution of 1-5nm and a vertical resolution of 0.08nm.

The V-shaped nano-probe cantilevers were made of silicon nitride (Si_3N_4) with a nominal tip radius of 20-60nm. The lengths of each cantilever were 100µm and 200µm. The tips are shaped like a pyramid with 35° angles on all four sides. Fig. 3.3 illustrates the design of the probes and the cantilever spring constants. The tip with 0.12m/s spring constant was used in the present study. The Digital Nanoscope software version 5.12b was used to analyse the surface roughness profiles of the samples [137].

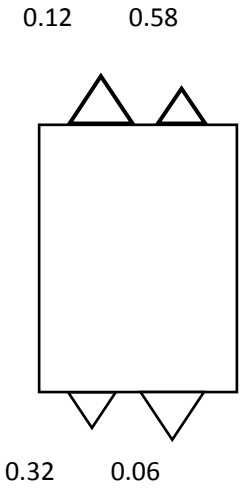

Fig. 3.6 Design of the probe and its four silicon nitride cantilevers showing spring constants (N/m).

3.2.5 X-ray diffractometer

An X-ray diffraction (XRD) using a GBC MMA diffractometer with mono-chromated Cu-Kα radiation was used to detect the phase composition of the samples before and after oxidation. The operating voltage and current of X-ray beam was set as 35kV and 28.6mA, respectively.

Chapter 4
Isothermal oxidation of the HSS material

High speed steel (HSS) has successfully been used to manufacture hot rolls because it retains a higher hardness at high temperature compared to conventional high chromium (Hi-Cr) and indefinite chill iron (IC) rolls. However, oxidation is an ever present problem during hot rolling [27, 109]. The working temperature of hot rolls can exceed 600 ^{o}C and the flash temperature could in fact rise above 800 ^{o}C owing to the friction and plastic work generated heat [2, 13]. Oxidation of the roll surface is considered to be one of four wear mechanisms (i.e. abrasion, adhesion, thermal fatigue, and oxidation) of work rolls which directly affects hot roll performance and the surface quality of rolled materials [2, 130, 112]. Therefore, a number of studies have been carried out to investigate the oxidation behaviour of HSS roll materials.

Kim et al. [2] compared the oxidation behaviour of HSS materials in dry and humid atmospheres, however, the humid atmosphere consisted of distilled water and argon gas which is different from industrial conditions. Monteiro and Rizzo [6] and Zhou et al. [93] reported that the presence of water vapour increased the oxidation rate of HSS. Their work mainly focused on the kinetics of oxide formation or the effect of alloy content on oxidation resistance during long term (up to several hundreds of hours) experiments. However, the total contact time of a roll with a hot strip in one rolling campaign is less than 30 min, and oxide scale formed on the roll surface can be broken by thermal and mechanical fatigue. In addition oxide scales may spall under shearing loading when their thickness is above a critical value [109]. Therefore, understanding the initial oxidation behaviour of HSS rolls is becoming more important and needs to be investigated. As the oxidation behaviour of the carbides and matrix in HSS materials affects the homogeneity of the oxidised surface of a roll, this has an important influence on contact friction and wear. It is therefore instructive to investigate the selective oxidation behaviour and

The content of this chapter has been published in *Corrosion Science 2010 (52): 2070-2715.* and *Corrosion Science 2011 (53): 3603-3611.*

subsequent formation of oxide scales on the carbides and matrix in HSS materials.

In this chapter a series of isothermal oxidation tests were carried out in a high temperature microscope (HTM) with a CCD camera as a detector. This means the initial formation and subsequent growth of oxide scales on the surface of HSS samples in dry and 12.5% H_2O humidity oxidising atmospheres were monitored in-situ and recorded. We also studied the morphology of the scales formed by using a variety of microscopy techniques and the nature of the oxides phases. During this experimentation, we came across interesting finds that we believe contribute to a better understanding of the oxidation behaviour and mechanisms of oxides formed on HSS samples.

4.1 Experimental methods

The oxidation tests were carried out in two oxidising atmospheres (dry and 12.5% H_2O humid air) and at four temperatures, i.e. 550, 600, 650, and 700 ^{o}C, for 30 min and up to 120 min. The following procedure was used for each of the oxidation experiments:

(1) the samples were heated to the desired temperature under a high argon atmosphere (Ar, 99.999% pure) at a rate of 1.7 $^{o}CS^{-1}$ and held for 5 min to allow the system to equilibrate;

(2) the argon flow was switched off concurrently with the introduction of oxidising gas. The samples were then oxidised for the designated testing time at the desired temperatures;

(3) the gas flow was switched back to pure argon to prevent further oxidation and the samples were cooled to room temperature at the rate of 1.7 $^{o}CS^{-1}$.

A compressed industrial air was used as the dry oxidising gas. For a humid atmosphere, a moisture content of 12.5% H_2O vapour was obtained by passing industrial air through a tank of distilled water maintained at a constant temperature of 50 ^{o}C. The gas tube connecting the water tank and the furnace chamber was

pre-heated to 60 ^{o}C to prevent the water from condensing on the inside wall of the tube. This ensured that the gas had the correct humidity while also protecting the furnace from exposure to liquid water. The flow rate of the oxidising gas was set as 96 cm^3min^{-1}, and the gas pressure in the HTM chamber was kept at 1 atm during the tests.

The microstructures of the as-received HSS samples were examined by X-ray diffraction (XRD) using a GBC MMA diffractometer with mono-chromated Cu K_α radiation and a JEOL JSM 6490 scanning electron microscope (SEM) equipped with energy dispersive X-ray analysis (EDX). The oxidised samples were immediately examined in a Nanoscope IIIA atomic force microscope (AFM) after each experiment to prevent the surface of the sample from becoming contaminated. The surface topography and roughness after oxidation were measured in the contact mode with a lateral resolution of 1-5 nm and a vertical resolution of 0.08 nm. The nano-probe cantilevers were made of silicon nitride (Si_3N_4) with a spring constant of 0.06 $N.m^{-1}$.

After oxidation, an FEI XT Nova Nanolab 200 workstation which combines a dual beam of focused ion beams and a field emission scanning electron microscope (FIB/SEM) was used to characterise the surface morphology of the specimen and prepare thin foil specimens for further TEM observation. The system is equipped with a platinum deposition system. The FIB column uses a fine, energetic beam of gallium ions that scan the surface of a specimen for imaging. At high beam currents the ion beam rapidly sputters away the surface of the specimen to expose the sub-surface cross section. Two steps were taken to prepare the TEM samples used in this work. Firstly, the electron beam was used to choose a typical feature, and a protective Pt film was deposited on the selected surface to protect the oxide scale before cutting. Secondly, the ion beam was used to cut the cross sections off at 15µm×5µm×0.5-0.6µm and then mill these thin foils down to less than 100 nm thick for a TEM examination. During the FIB cross sectioning, an accelerating voltage of 30 kV and high ion currents were used and for milling, lower currents of 1nA to

0.1nA were used. A JEOL JSM 6490 scanning electron microscope (SEM) equipped with energy dispersive X-ray analysis (EDAX) was also used to characterise the surface morphology of the specimen before and after oxidation.

A Philips CM200 field emission gun transmission electron microscope (FEGTEM) equipped with a Brucker energy dispersive X-ray spectroscopy (EDAX) system was used to investigate the detailed microstructure of the FIB cross sections of the oxide scales. It was operated with an accelerating voltage of 200kV. Selected oxidised samples were examined by X-ray diffraction (XRD) using a GBC MMA diffractometer with mono-chromated Cu-Kα radiation.

4.2 Results

4.2.1 Microstructure of the studied HSS sample

The high speed steel material of a work roll whose composition is shown in Table 4.1 was selected as the material to be used in all experiments. Fig. 4.1 shows the XRD spectrum of the high speed steel sample. An X-ray analysis indicated that there were two kinds of carbides (V_8C_7 and Cr_7C_3) present in the iron matrix. However, it was difficult to detect all the carbides present by XRD [2]. Fig. 4.2a shows a typical back scattered electron (BSE) image of the polished HSS roll material. The BSE microstructure observed (Fig. 4.2a) was to classify the carbides based on their unique morphologies precipitated in the high speed steel materials [72, 92, 138, 139]. In the HSS roll material, the carbides were identified as follows: the slender petal-like dark zones are V-rich MC (V_8C_7) carbides (Fig. 4.2b), the fibrous bright phases are Mo, W-rich M_2C (Mo_2C) carbides (Fig. 4.2c), which Cr-rich M_7C_3 (Cr_7C_3) carbides appear with a structure that looks like a network (Fig. 4.2d). High magnification observation in TEM (Fig. 4.3) indicated there are many fine Mo, W-rich spherical carbides (M_2C) with sizes ~200nm precipitate in the HSS matrix. Image analysis of BSE images, as shown in Fig. 4.4, determined that the total volume fraction of all three carbides to be 13%, which comprises 9 %MC and 4%

M_2C+M_7C_3. The EDX analysis indicated that although more chromium precipitates with carbides, chromium was evenly distributed in the matrix.

Table 4.1 Chemical composition of the studied high-speed steel (in weight percent, wt%) analysed by X-ray fluorescence spectroscopy.

Fe	C	Ni	Mn	Cr	Mo	V	W	Si	P	S
Balance	1.96	0.78	1.26	4.85	4.47	4.00	3.40	0.99	0.028	0.034

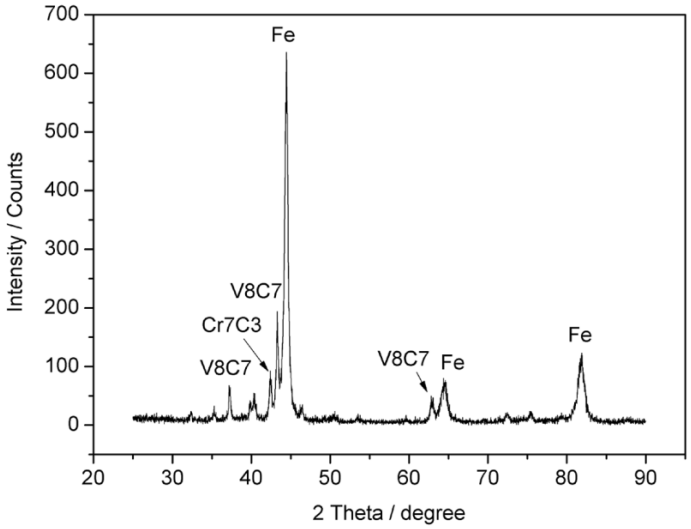

Fig. 4.1 X-ray pattern of HSS sample.

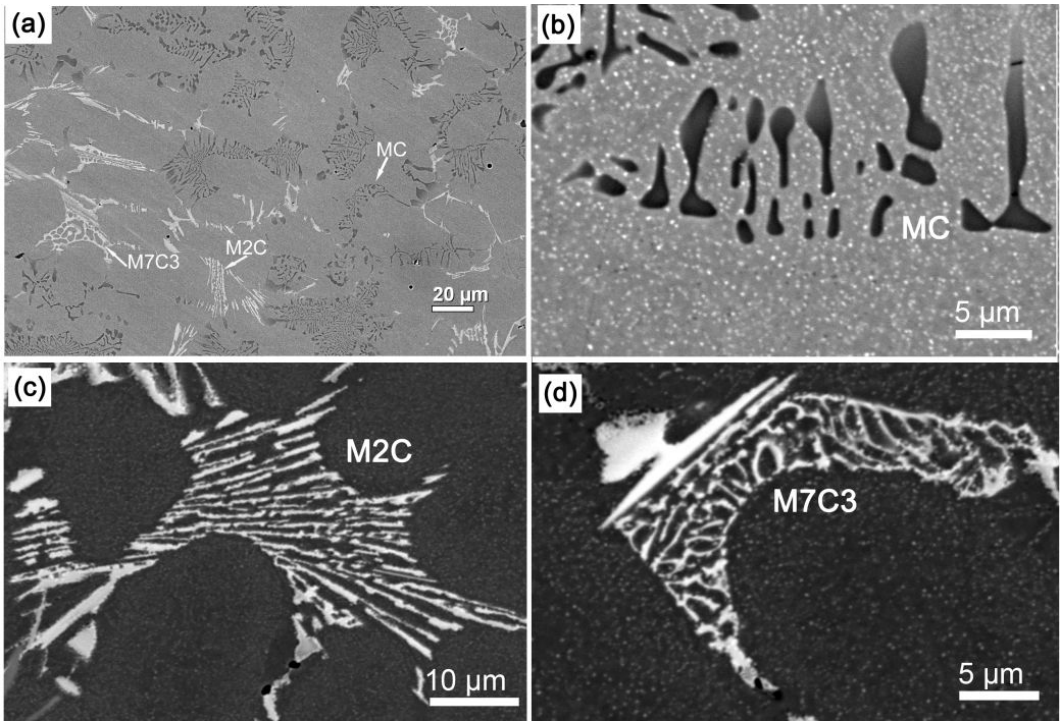

Fig. 4.2 Backscattered electron (BSE) image of microstructure of HSS sample. (a) Over view of the microstructure, (b) morphology of MC carbides, (c) morphology of M_2C carbides, and (d) morphology of M_7C_3 carbides.

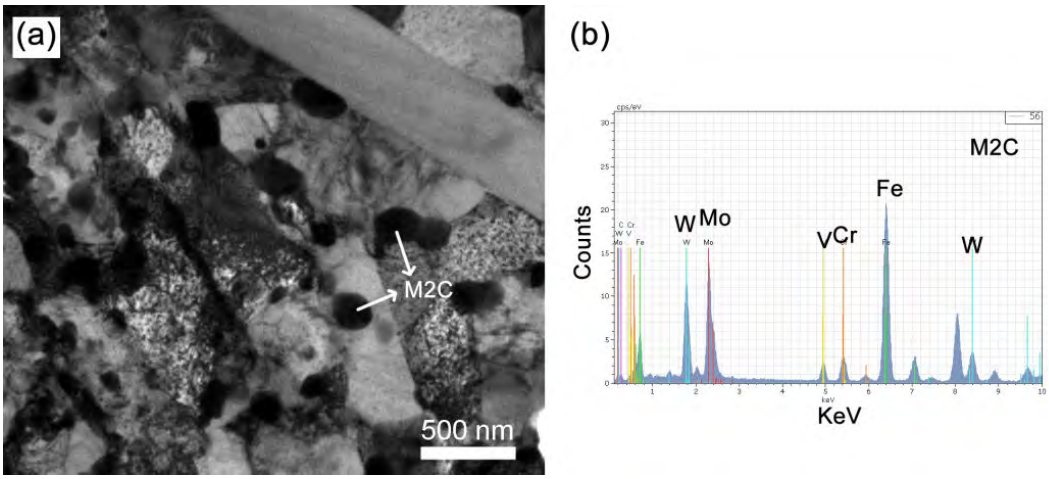

Fig. 4.3 (a) TEM bright field microstructure image of the HSS sample matrix, and (b) EDS spectra of spherical particles.

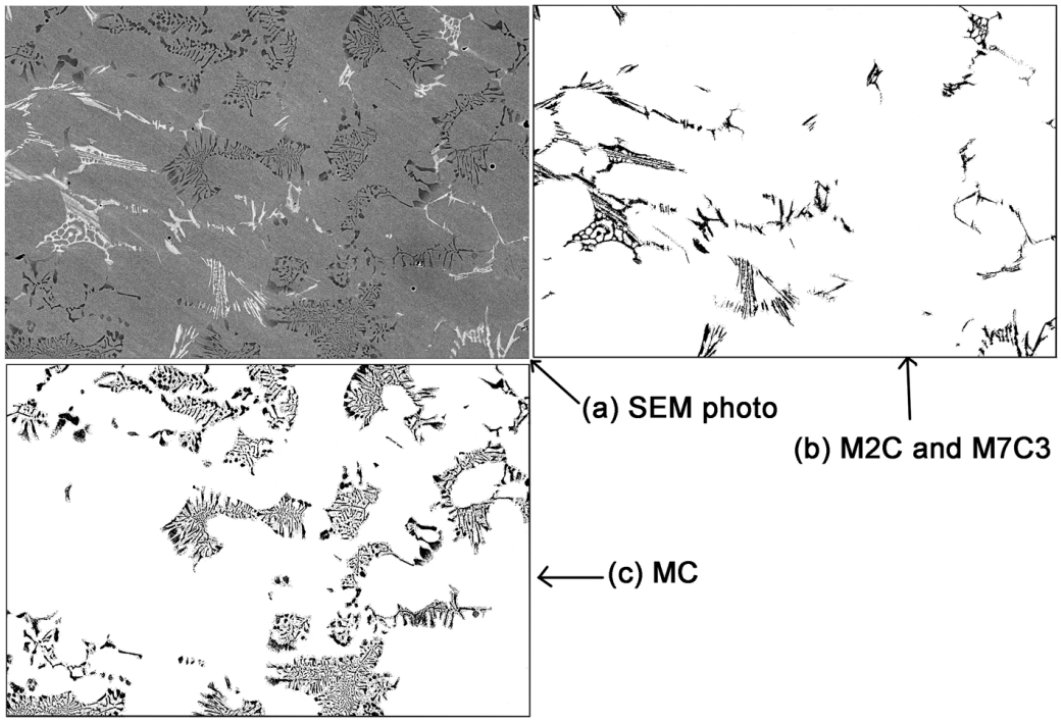

Fig. 4.4 Image analysis of carbides volume fraction in HSS sample. (a) Backscattered electron (BSE) image of microstructure of HSS sample, (b) black areas are referred to areas of M_2C+M_7C_3 carbides, (c) black areas are referred to areas of MC carbides. The volume fraction was determined by means of Image Pro Plus 6.0 software.

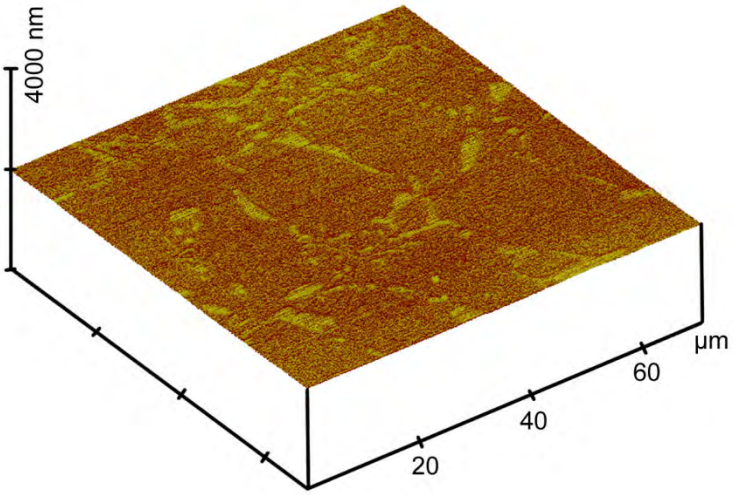

Fig. 4.5 AFM image for surface topography of the HSS sample prior to oxidation tests.

Fig. 4.5 shows an AFM image for surface topography of the sample before oxidation tests. The surface was flat after polishing with a 1μm diamond suspension and the roughness was about 10nm. The carbides are protruding slightly above the surface of the matrix due to their high hardness relative to the matrix, resulting in differential polishing finish.

4.2.2 In-situ observation of the oxidation of the HSS samples

Fig. 4.6 provides a series of in-situ frames from the first 20s of the oxidation experiments in industrial dry air at 700 ^{o}C, showing the initial formation and growth of the oxide scale on the surface of the sample. The colour on the surface of the sample changed as the oxidation time proceeded. This may be due to growth in the thickness of the oxide scale, but other factors can also affect the colour change, such as different oxide phases, surface conditions, and configuration of the optical microscope. Fig. 4.6a shows the microstructure of the HSS sample before dry air was introduced, which shows the carbides distributed in the matrix. It is evident from Fig. 4.6b that the oxidation initially takes place at the carbides/matrix interfaces once the oxidising gas was introduced. After 5s of oxidation the oxide scale spread rapidly over the carbides and then propagated into the matrix, as shown in Fig. 4.6c. As the oxidation time progressed to 10s and 15s (shown in Fig.

4.6d and 4.6e, respectively), the oxide scale continuously grows further over the matrix. It takes about 20 s for a complete oxide scale to form, from initiation at the carbides/matrix interfaces to cover the whole surface at 700 ^{o}C as shown in Fig. 4.6f. The HSS showed similar oxidation behaviour at 650 ^{o}C, as shown in Fig. 4.7. However, the growth rate of oxidation at this temperature was three times slower than at 700 ^{o}C, with more than 60s required for the oxide scale to cover all the surface of the sample. When the oxidation temperature was decreased further to 600 and 550 ^{o}C, the growth rates of the oxide scale on the surface of the sample were reduced significantly, so it was difficult to detect the growth of oxide scale.

In-situ observation of oxidation process in 12.5% H_2O humid air at different temperatures indicated a similar phenomenon to the case of dry air. It was still hard to detect the growth of oxide at 550 ^{o}C in humid air, as in the case with dry air. In contrast, the formation and growth of oxide scale on the sample surface is clearly visible at 600, 650 and 700 ^{o}C.

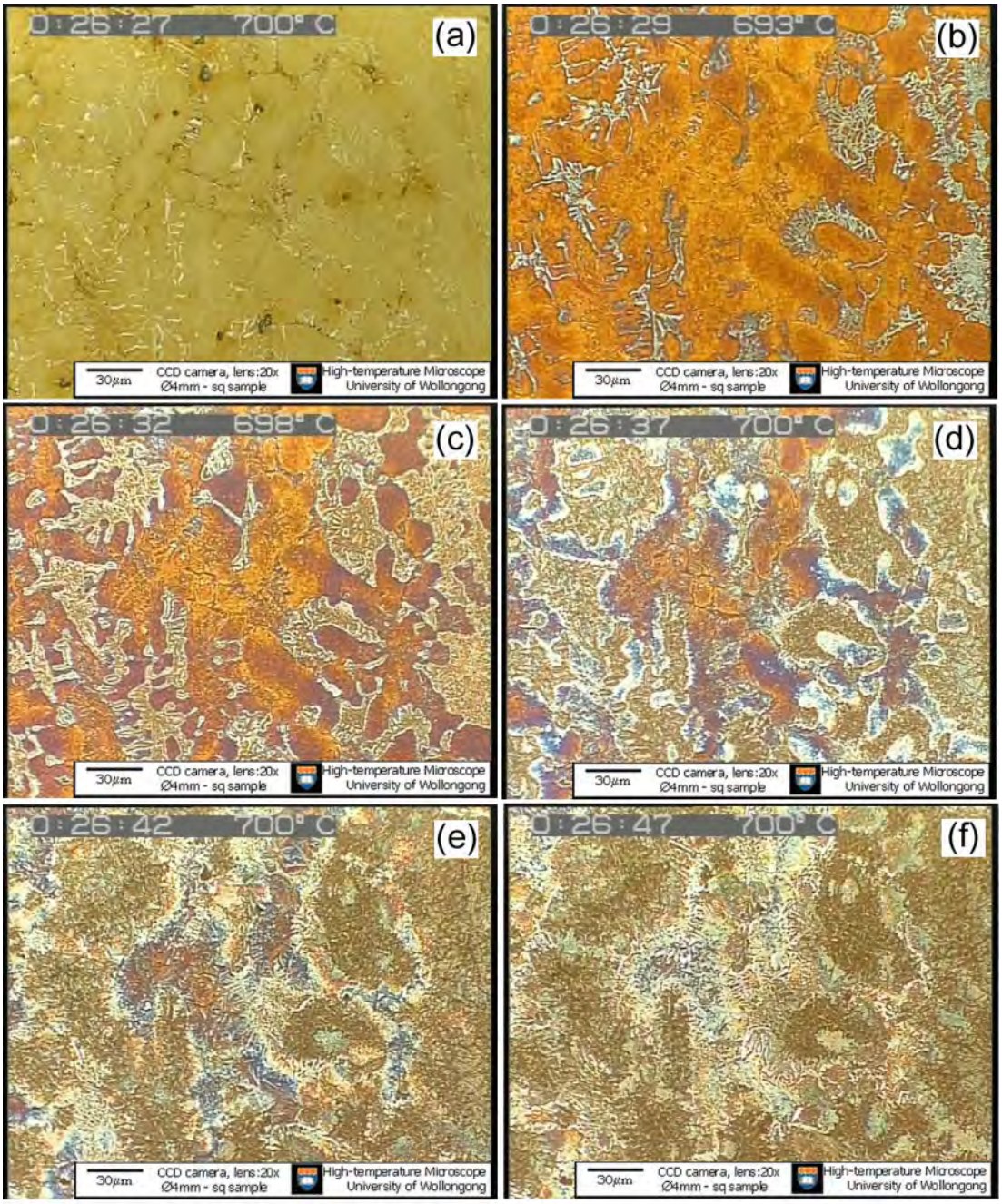

Fig. 4.6 Snapshots from an in-situ recorded video for the formation and growth of oxide scales on the surface of the specimen in dry air at 700 ^{o}C. The time indicated in the figures is the program proceeding time rather than oxidising time: (a) 0s, (b) 2s, (c) 5s, (d) 10s, (e) 15s, and (f) 20s.

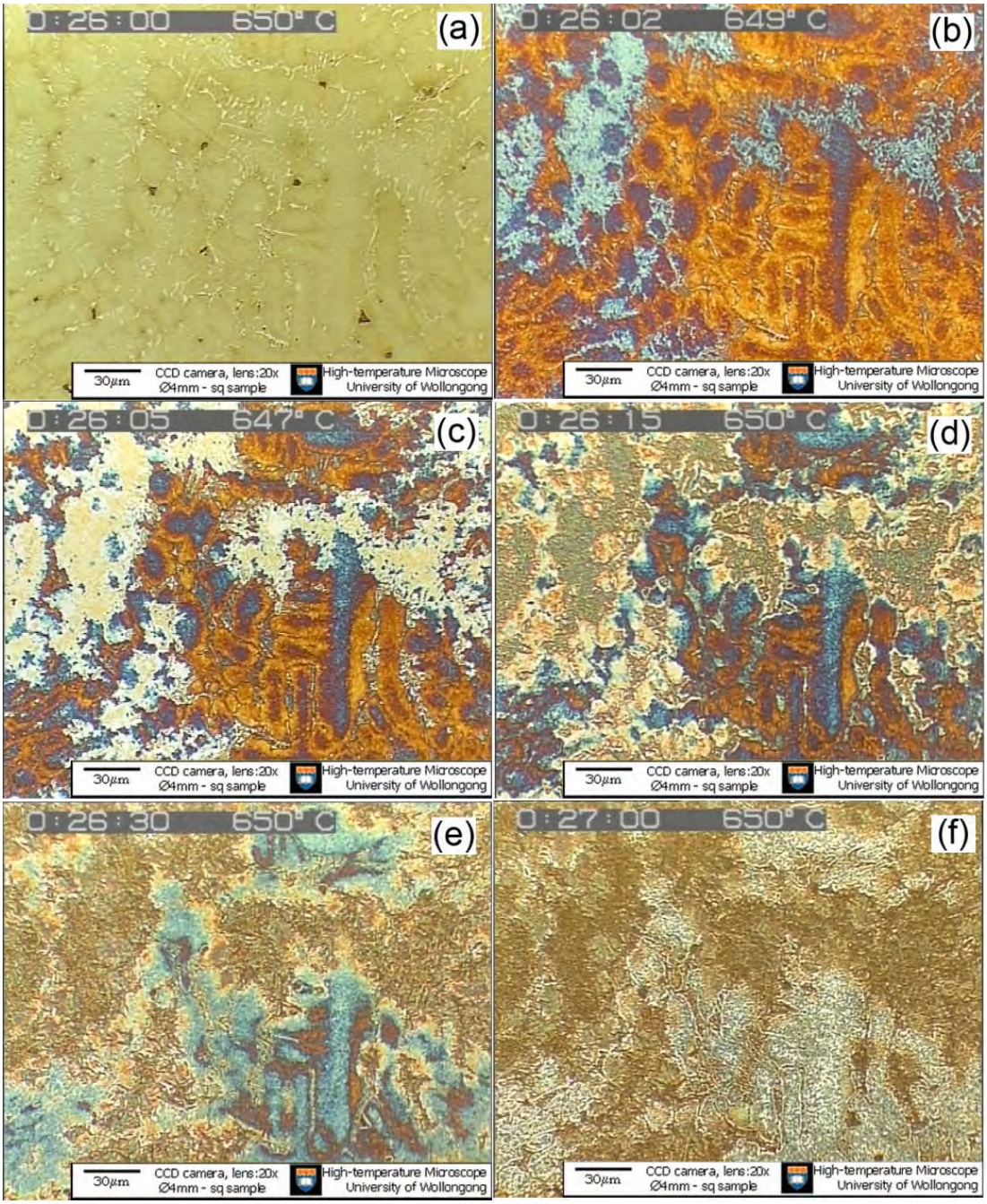

Fig. 4.7 Snapshots from an in-situ recorded video for the formation and growth of oxide scales on the specimen surface in dry air at 650 ^{o}C. The time indicated in the figures is the program proceeding time rather than oxidising time: (a) 0s, (b) 2s, (c) 5s, (d) 15s, (e) 30s, and (f) 60s

4.2.3 Surface morphology after oxidation

4.2.3.1 Oxidation in dry air

Fig. 4.8 shows the secondary electron (SE) images of the surface of the HSS sample after 30 min of oxidation at 550 ^{o}C in dry air. It can be seen that most of the surface

is covered by a thin film of oxide, as shown in Fig. 4.8a. However, the higher magnified image indicates that the oxide scale does not cover the substrate evenly, several cavities are clearly visible and some locations have protrusions of rod-like crystals (Fig. 4.8b). SEM/X-ray mapping analysis of oxidised HSS sample surface shown in Fig. 4.9 confirmed that the cavities correspond to the chromium and molybdenum rich carbides area, and the rod like crystals are rich in vanadium, which indicates that V-rich MC carbides have been oxidised after the test (detailed feature of vanadium oxide as seen in Fig. 4.8c). It can be clearly seen in Figs. 4.8c and 4.8d that fine, iron oxide whiskers and blades are growing on the oxide scale however, the iron oxides do not grow directly from the metal substrate, there is a thin, compact, chromium rich layer of oxide formed that covers the substrate. The fine chromium oxides are more visible at the Cr-rich M_7C_3 carbides/matrix interface due to higher contents of chromium precipitating at these areas than in the matrix (Fig. 4.8d).

Fig. 4.10 shows the secondary electron (SE) images of the HSS sample surface after 30 min oxidation at 600 ^{o}C in dry air. The surface has a unique feature after 30 min of oxidation. A thin oxide layer covers the HSS matrix, and the areas of vanadium rich MC carbides are oxidised and protrude above the surface (Fig. 4.10a). A higher magnified image (Fig. 4.10b) indicates there are some rod-like oxidised products appearing at the vanadium-rich MC carbides area, and the MC carbides/matrix interfaces are oxidised severely where the large iron oxides crystal forms. Fig. 4.11 shows the SE images of the HSS sample surface after 120 min oxidation at 600 ^{o}C in dry air. The surface morphology of the oxidised sample shows no significant difference after 30 min (Fig. 4.11a), although the oxide scale covering the HSS matrix seems to be getting a little thicker and the vanadium-rich MC carbides are oxidised more severely, as shown in Fig. 4.11b, compared to those for 30 min.

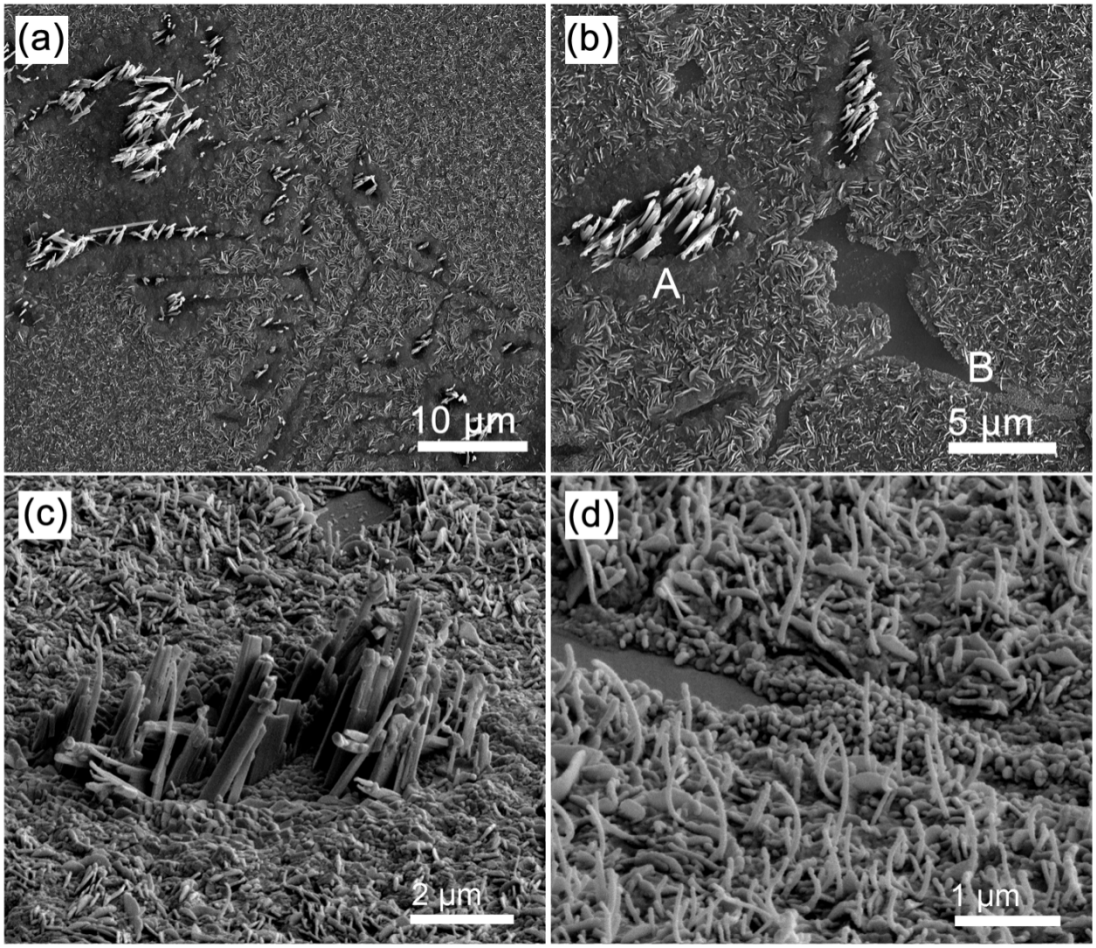

Fig. 4.8 Secondary electron (SE) image of surface morphology of HSS sample oxidised at 550 ^{o}C in dry air for 30 min. (a) overview of the oxidised surface, the sample is titled 52^{o}, (b) higher magnification SE image of the oxidised surface, the sample is titled 52^{o}, (c) higher magnification SE image of area "A" labelled in (b), the sample is titled 52^{o}, and (d) higher magnification SE image of area "B" labelled in (b), the sample is titled 52^{o}.

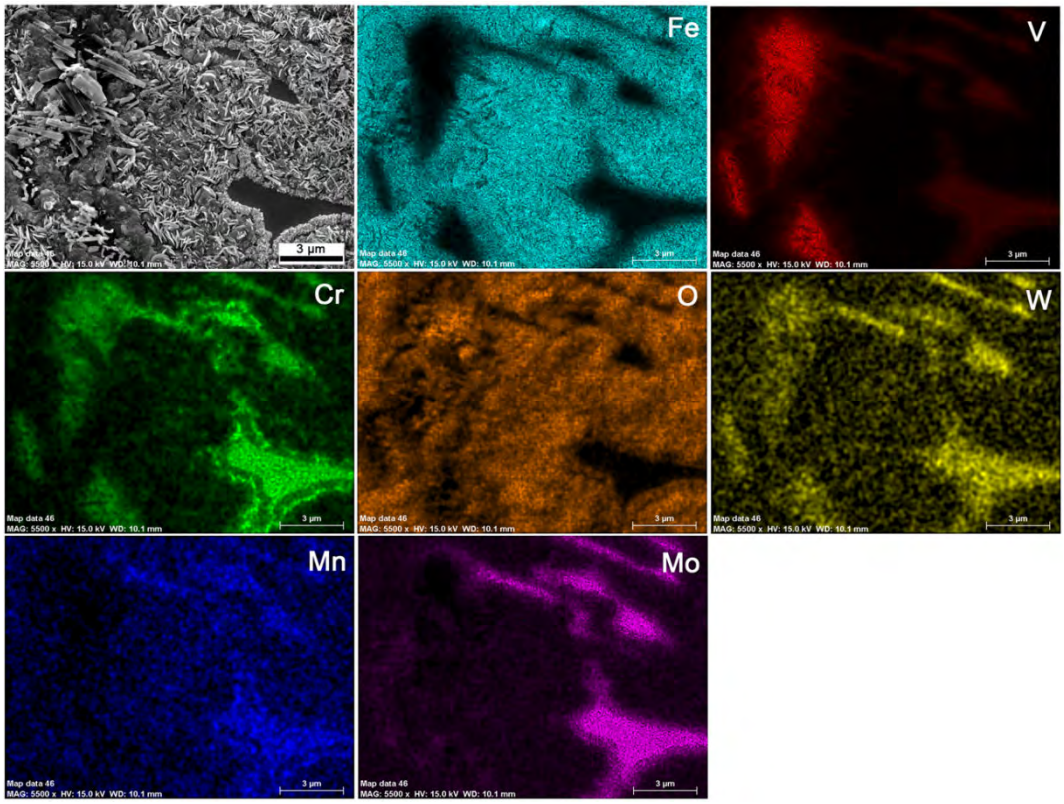

Fig. 4.9 FEG-SEM/X-ray mapping of oxidised HSS sample surface after oxidation at 550 ^{o}C for 30 min in dry air.

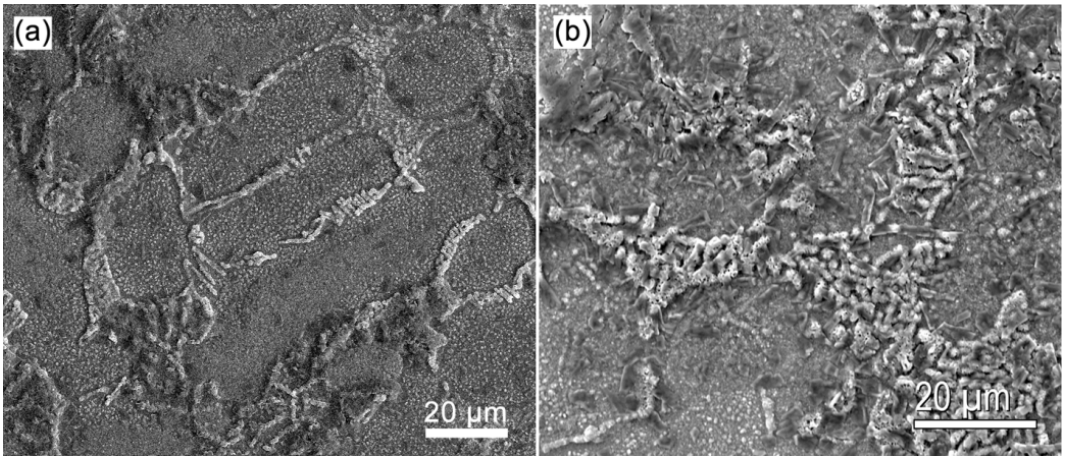

Fig. 4.10 Secondary electron (SE) image of surface morphology of HSS sample oxidised at 600 ^{o}C in dry air for 30 min. (a) Overview of the oxidised surface, and (b) higher magnified SE image of oxidised surface.

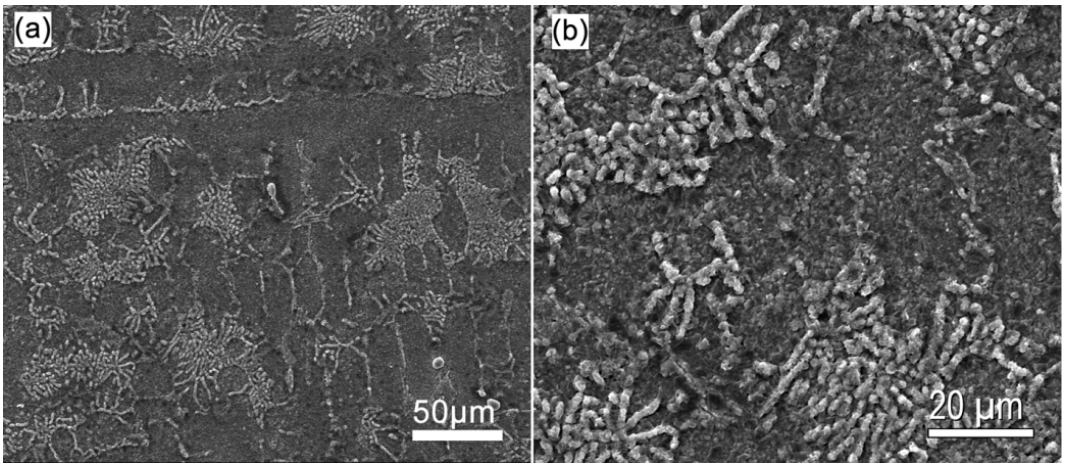

Fig. 4.11 Secondary electron (SE) image of surface morphology of HSS sample oxidised at 600 ^{o}C in dry air for 120 min. (a) Overview of the oxidised surface, and (b) higher magnified SE image of oxidised surface.

Fig. 4.12 shows the SE images of the HSS sample surface after 30 min oxidation at 650 ^{o}C in dry air. It can be seen that the surface is oxidised more severely than the samples at 600 ^{o}C even though the whole surface is still oxidised unevenly (Fig. 4.12a). At a higher magnification, the vanadium-rich MC carbides areas on the surface are severely oxidised while the matrix areas have resisted oxidation very well, albeit they are covered with a thin and compact oxide scale (Fig. 4.12b). This has resulted in an inhomogeneous surface. Fig. 4.13 shows the SEM X-ray mapping of the sample surface after oxidation at 650 ^{o}C for 30 min in dry air. The matrix here is oxidised less than other areas. The vanadium rich MC carbides/matrix interfaces are oxidised most severely, especially in the narrow areas among the vanadium rich MC carbides. Not only are the vanadium rich MC carbides oxidised to form parallelepiped grains, so too are the fine Mo and W-rich M_2C carbides. However, the chromium rich M_7C_3 was not oxidised because its volume fraction is low (M_2C and M_7C_3 is approximate 4 vol.%), and it is preferentially precipitated with Mo and W-rich carbides, as seen in the microstructure of the un-oxidised sample (Fig. 4.2a). After 120 min of oxidation, the vanadium rich MC carbides areas are heavily oxidised and protrude prominently out of the surface (Fig. 4.14a and b). Although the matrix has a strong resistance to oxidation, when the oxidation time increased the area of the matrix was getting smaller due to an expansion of the oxides from the MC carbides.

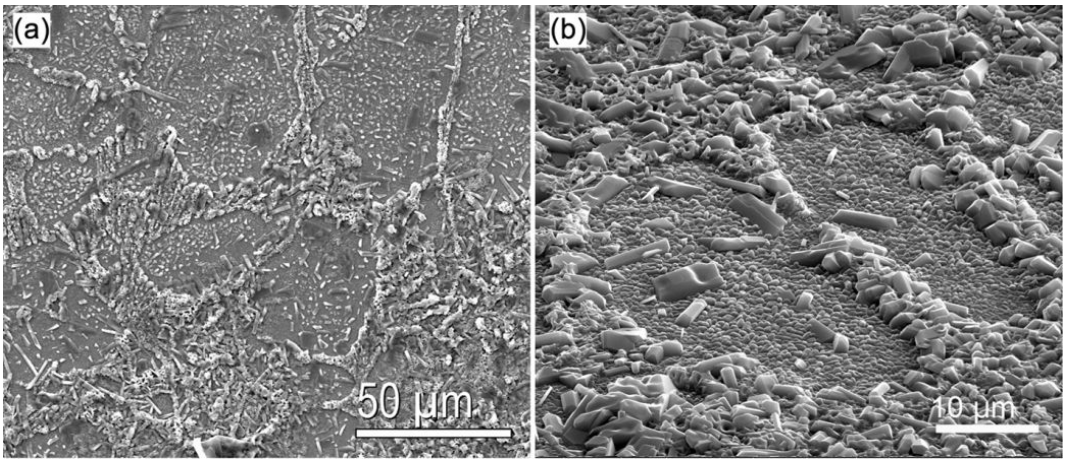

Fig. 4.12 Secondary electron (SE) image of surface morphology of HSS sample oxidised at 650 °C in dry air for 30 min. (a) Overview of the oxidised surface, and (b) higher magnified SE image of oxidised surface.

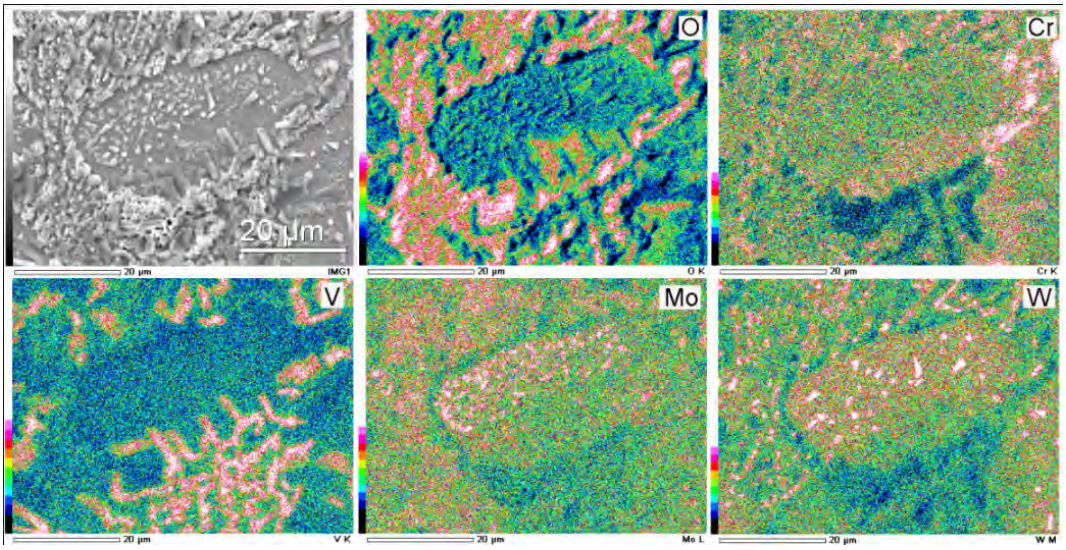

Fig. 4.13 SEM X-ray mapping for sample surface after oxidation at 650 °C for 30 min in dry air.

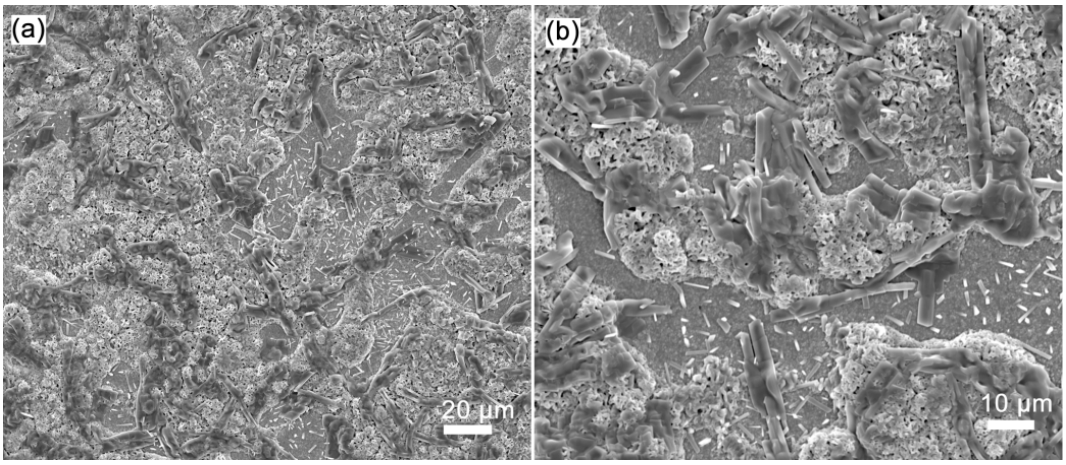

Fig. 4.14 Secondary electron (SE) image of surface morphology of HSS sample oxidised at 650 °C in dry air for 120 min. (a) Overview of the oxidised surface, and (b) higher magnified SE image of oxidised surface.

Fig. 4.15 shows the SE images of the HSS sample surface after 30 min oxidation at 700 ^{o}C in dry air. It can be seen that the whole surface was covered by oxides after oxidation. The surface morphology became more homogeneous than at 650 ^{o}C, as we can see a porous honeycomb like oxide scale growing through the matrix and around the oxidised vanadium-rich MC carbides whose shapes have been changed into parallelepiped grains.

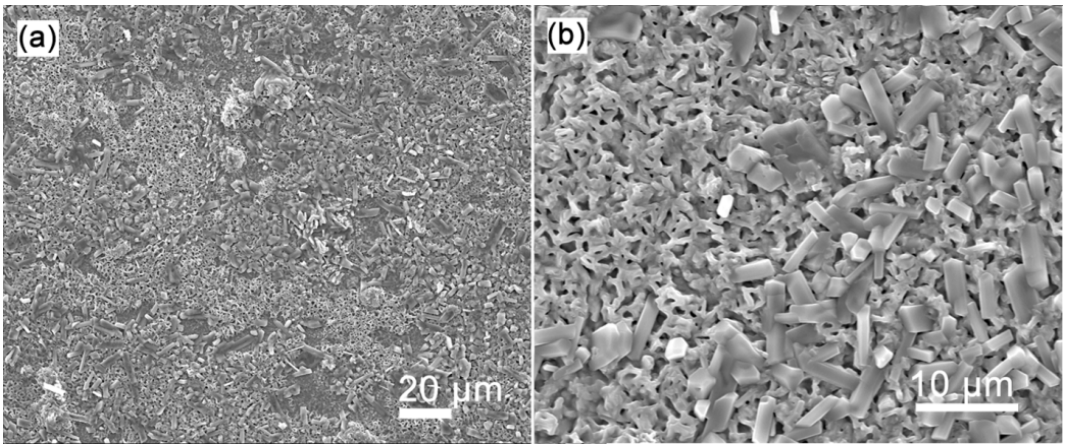

Fig. 4.15 Secondary electron (SE) image of surface morphology of HSS sample oxidised at 700 ^{o}C in dry air for 30 min. (a) Overview of the oxidised surface, and (b) higher magnified SE image of oxidised surface.

4.2.3.2 Oxidation in 12.5% H_2O humid air

Fig. 4.16 shows the SE images of the HSS sample surfaces after 30 min oxidation at 550 ^{o}C in 12.5% H_2O humid air. It can be seen that the morphologies of the oxidised surface in the humid air are significantly different from those in dry air, as shown in Fig. 4.8. After oxidation at 550 ^{o}C, the oxidised surface has dark areas which are the vanadium rich iron oxides around the V-rich MC carbides, and bright areas which are oxidised Mo and W-rich M_2C carbides, as shown in Figs. 4.16a and b. There is no significant difference in the oxide morphology between wet and dry air because the oxidation temperature were low at 550 ^{o}C.

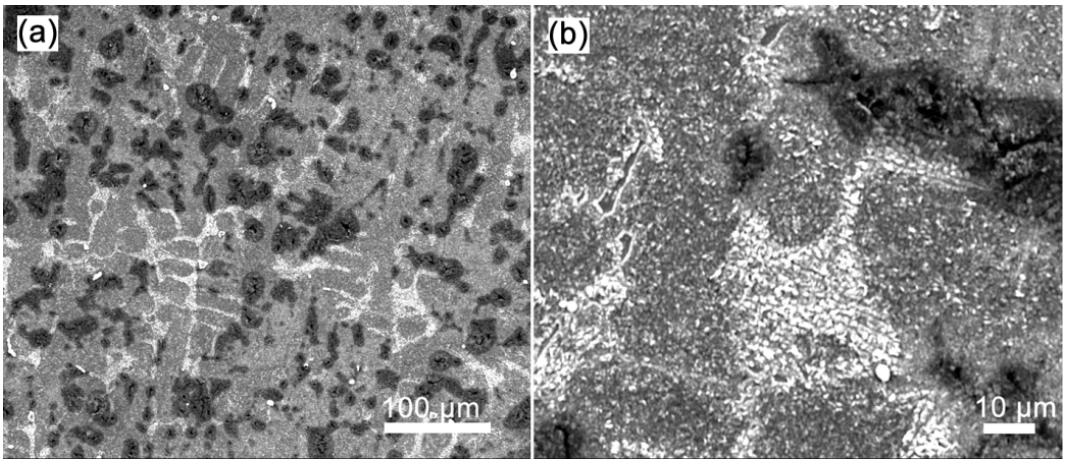

Fig. 4.16 Secondary electron (SE) image of surface morphology of HSS sample oxidised at 550 ^{o}C in 12.5%H_2O humid air for 30 min. (a) Overview of the oxidised surface, and (b) higher magnified SE image of oxidised surface.

Fig. 4.17 shows the SE images of the HSS sample surfaces after 30 min oxidation at 600 ^{o}C in 12.5% H_2O humid air. The surface morphologies are similar to those oxidised in dry air, as shown in Fig. 4.10. However the surface seems coarser which indicates that oxidation in 12.5% H_2O humid air is more severe than in dry air. Fig. 4.18 shows the SEM X-ray mapping of the oxidised surface. It can be seen that vanadium-rich MC carbides are the most severely oxidised and protrude out of the matrix, while the Mo and W-rich M_2C carbides are also oxidised out of the surface. However, Mo, W-rich M_2C carbides, and Cr-rich M_7C_3 carbides precipitated together so in this current investigation it is not easy to distinguish from the surface morphology which one has a better resistance to oxidation.

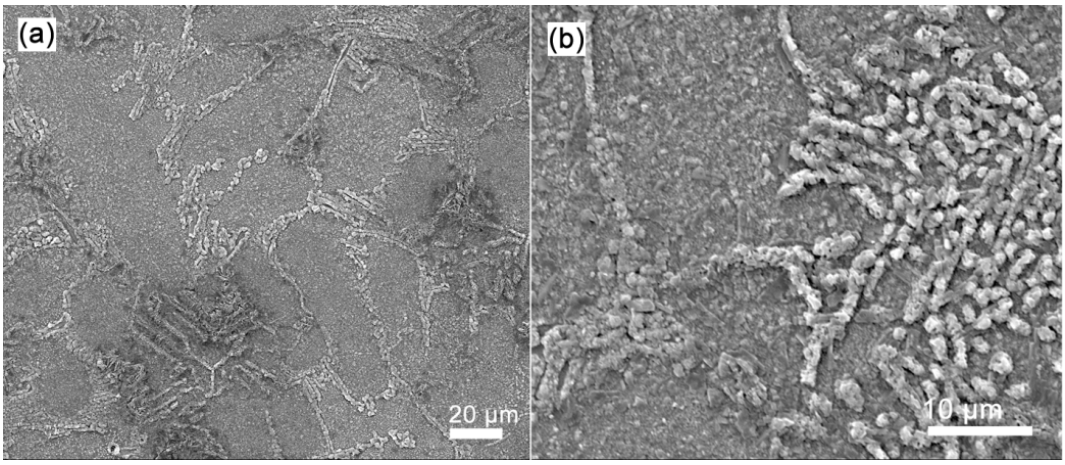

Fig. 4.17 Secondary electron (SE) image of surface morphology of HSS sample oxidised at 600 ^{o}C in 12.5%H_2O humid air for 30 min. (a) Overview of the oxidised surface, and (b) higher magnified SE image of oxidised surface.

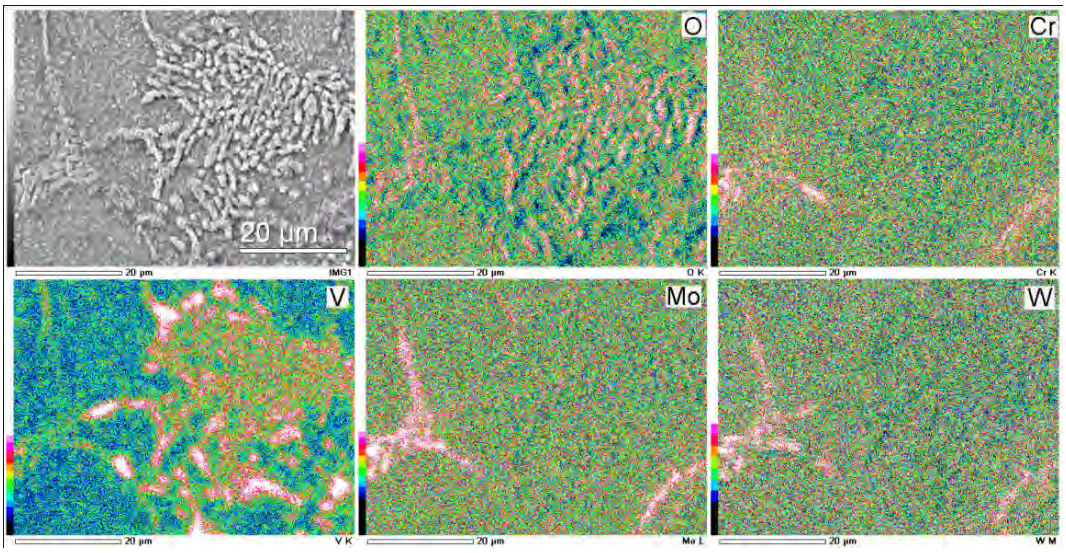

Fig. 4.18 SEM X-ray maps for the sample surface after oxidation at 600 °C for 30 min in 12.5% H_2O humid air.

Fig. 4.19 shows the SE images of the HSS sample surfaces after 30 min oxidation at 650 °C in 12.5% H_2O humid air. The surface morphology indicates that the vanadium-rich MC carbides are significantly oxidised while the oxidised surface of the matrix in 12.5% H_2O humid air is not as even as in dry air. Some locations in the matrix are oxidised more heavily than other areas, leading to large iron oxide grains growing out of the surface.

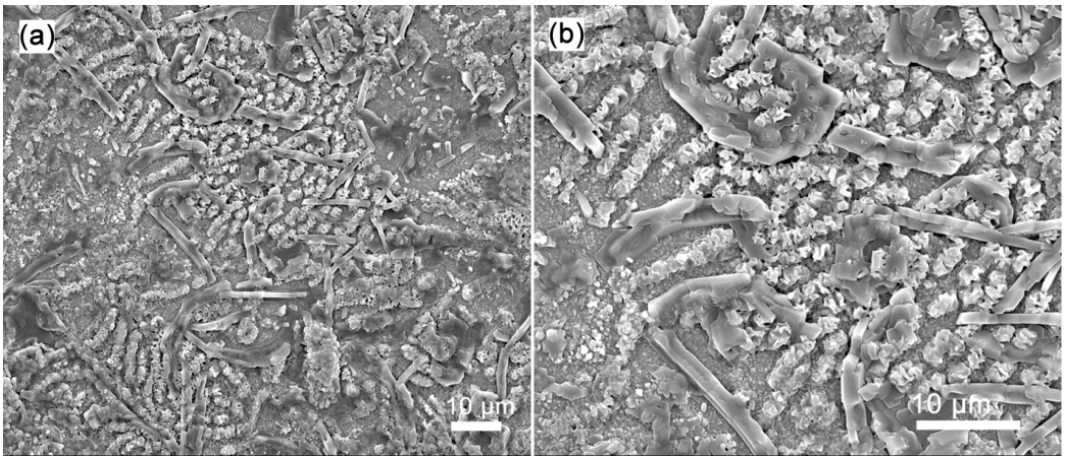

Fig. 4.19 Secondary electron (SE) image of surface morphology of HSS sample oxidised at 650 °C in 12.5%H_2O humid air for 30 min. (a) Overview of the oxidised surface, and (b) high magnified SE image of oxidised surface.

Fig. 4.20 shows the SE images of surface morphology of HSS sample oxidised at 700 °C in 12.5% H_2O humid air for 30 min. It can be seen that a honeycomb-structural

iron oxide scale covers the sample surface. However, the iron scale is thicker and the iron oxide grains are smaller compared to the oxide formed in dry air at 700 ^{o}C. And it is also noted that the oxidised vanadium rich MC carbides are oxidised severely and spread among the iron oxide scale instead of forming parallelepiped grains as is observed in dry air (Fig. 4.15).

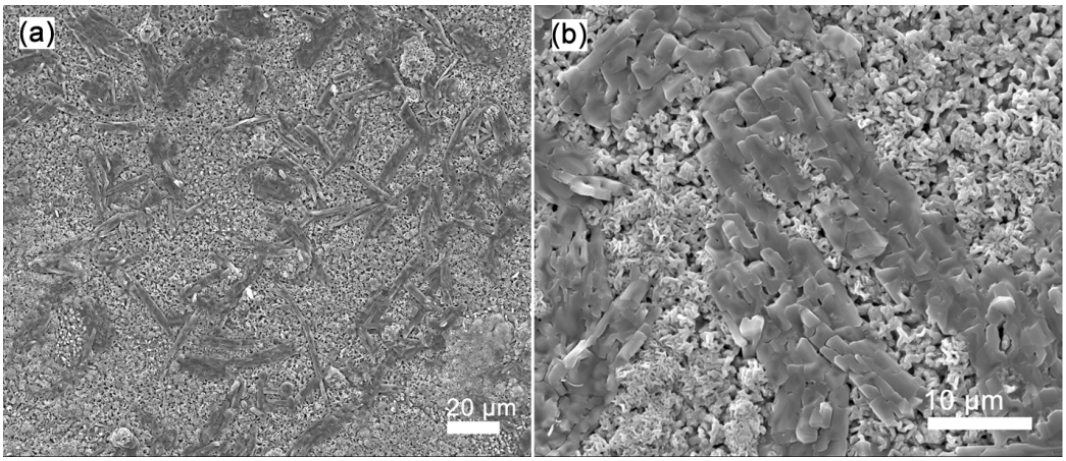

Fig. 4.20 Secondary electron (SE) image of surface morphology of HSS sample oxidised at 700 ^{o}C in 12.5%H_2O humid air for 30 min. (a) Overview of the oxidised surface, and (b) high magnified SE image of oxidised surface.

4.2.4 X-ray structural analysis

Fig. 4.21 and Fig. 4.22 show the XRD patterns of oxidised samples after oxidation in dry air at 650 and 700 ^{o}C, respectively. The reflections of iron substrate present in both spectra indicate that the thickness of oxide scales is less than the depth of the X-ray diffraction. At the same testing condition, more X-ray penetrates into the steel substrate leads to a higher Fe phase peak in the pattern which indicates a thinner oxide layer, and vice versa. Although XRD is used to identify the phase composition in the oxide scale, the XRD pattern can be used to compare the thickness of oxide scale under the current circumstance. The intensity of the Fe phase decreased significantly when the temperatures was increased to 700 ^{o}C indicating that the oxide scale was becoming thicker with a rise in temperature. Fig. 4.23 and Fig. 4.24 show the XRD patterns of oxidised samples after oxidation in 12.5% H_2O humid air at 650 and 700 ^{o}C, respectively. It is evident that the main phases of oxide scale are

Fe_2O_3 (hematite) and Fe_3O_4 (magnetite) in both atmospheres, although the constitution of the Fe_2O_3 phase in the oxide scale formed in 12.5% H_2O humid air is higher than in dry air.

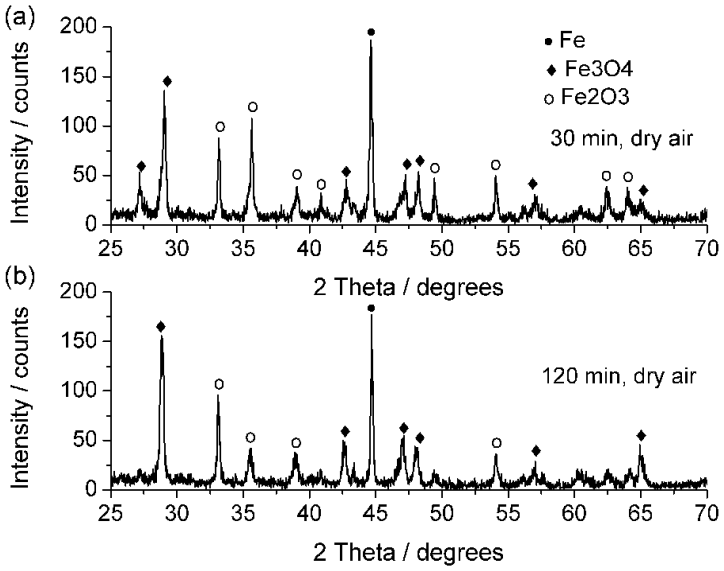

Fig. 4.21 XRD patterns of the oxidised sample after oxidation at 650 °C in dry air: (a) 30 min and (b) 120 min.

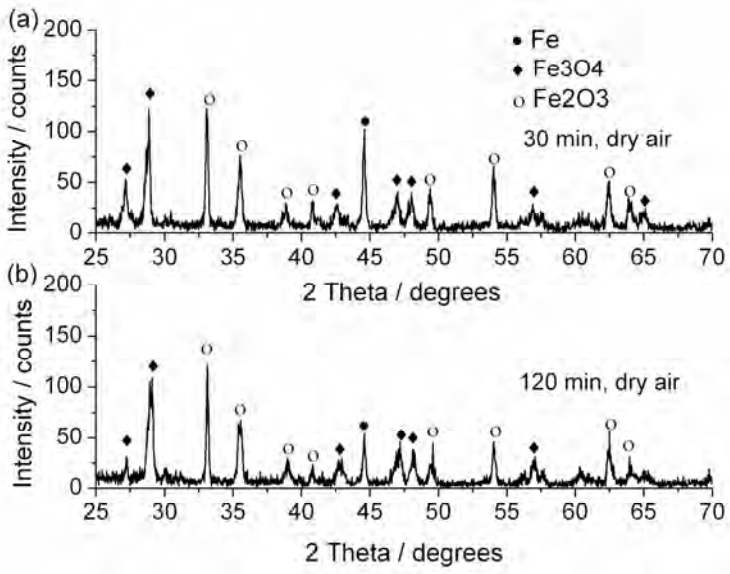

Fig. 4.22 XRD patterns of the oxidised sample after oxidation at 700 °C in dry air: (a) 30 min and (b) 120 min.

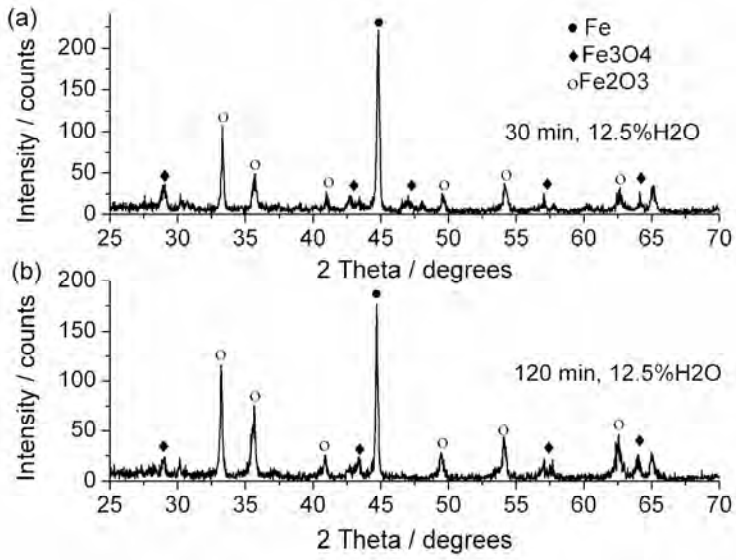

Fig. 4.23 XRD patterns of the oxidised sample after oxidation at 650 ^{o}C in 12.5% H_2O humid air: (a) 30 min and (b) 120 min.

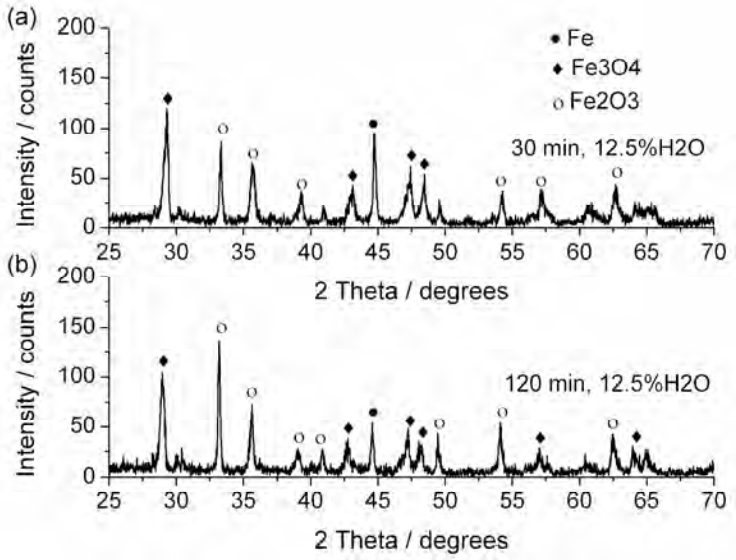

Fig. 4.24 XRD patterns of the oxidised sample after oxidation at 700 ^{o}C in 12.5% H_2O humid air: (a) 30 min and (b) 120 min.

4.2.5 Cross sectional microstructure of oxide scales

4.2.5.1 Oxidation in dry air

Fig. 4.25 shows the TEM bright field image of the cross section of the oxide layer formed at 600 ^{o}C for 30 min in dry air. It can be seen that the oxide layer can clearly be distinguished as two sub-layers which the outer layer is compact while the inner layer is porous. However the thickness of the oxide scale fluctuates significantly

from less than 0.5µm (carbides free matrix) to 1.28µm (vanadium-rich MC carbides region). Fig. 4.26a shows the cross section cut off from the vanadium-rich MC carbides area (Fig. 4.25). The EDS results indicate that the oxides in the outer layer (Fig. 4.26b, "A" in Fig. 4.26a) are rich in vanadium, manganese, and iron, while the oxides in the inner layer consist of chromium and iron oxides (Fig. 4.26c, "B" in Fig. 4.26a). It is noted that the vanadium-rich MC carbides were oxidised and decomposed into small grains (Fig. 4.26d, "C" in Fig. 4.26a) and fine Mo and W-rich spherical carbide was not oxidised after oxidation (Fig. 4.26e, "D" in Fig. 4.26a) in the inner oxide layer. There are no chromium elements appearing in the outer layer, which indicates that chromium oxides only form on the metal surface and remain in the same place during the growth of oxide scale. With a longer oxidation time, the thin layer of chromium oxide becomes the interface between the inner and outer layers of oxide. Fig. 4.27 shows the TEM bright field image of an FIB cross section of oxide scale formed at 600 ^{o}C for 120 min in dry air. It can be seen that the thickness of the oxide scale after oxidation for 120 min on the HSS matrix changed little compared to that for 30 min, but the oxides in the vanadium-rich carbides areas are obviously increasing.

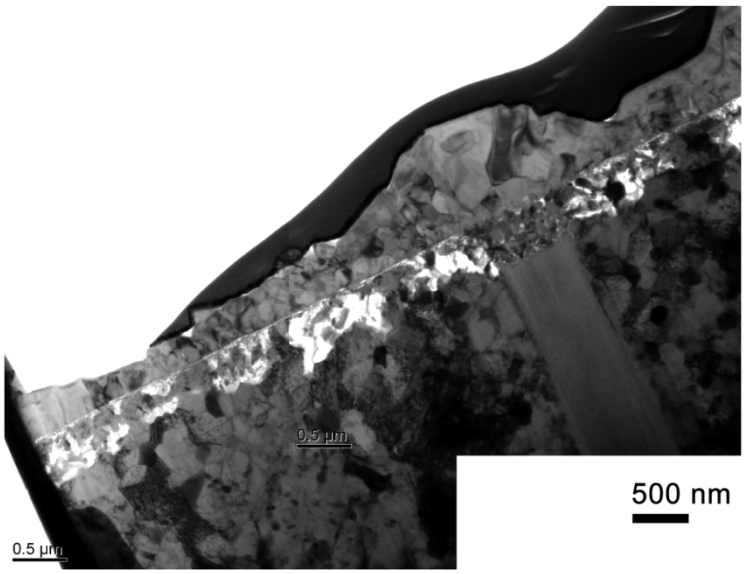

Fig. 4.25 TEM bright field image of an FIB cross section of the oxidised sample at 600 ^{o}C for 30 min in dry air.

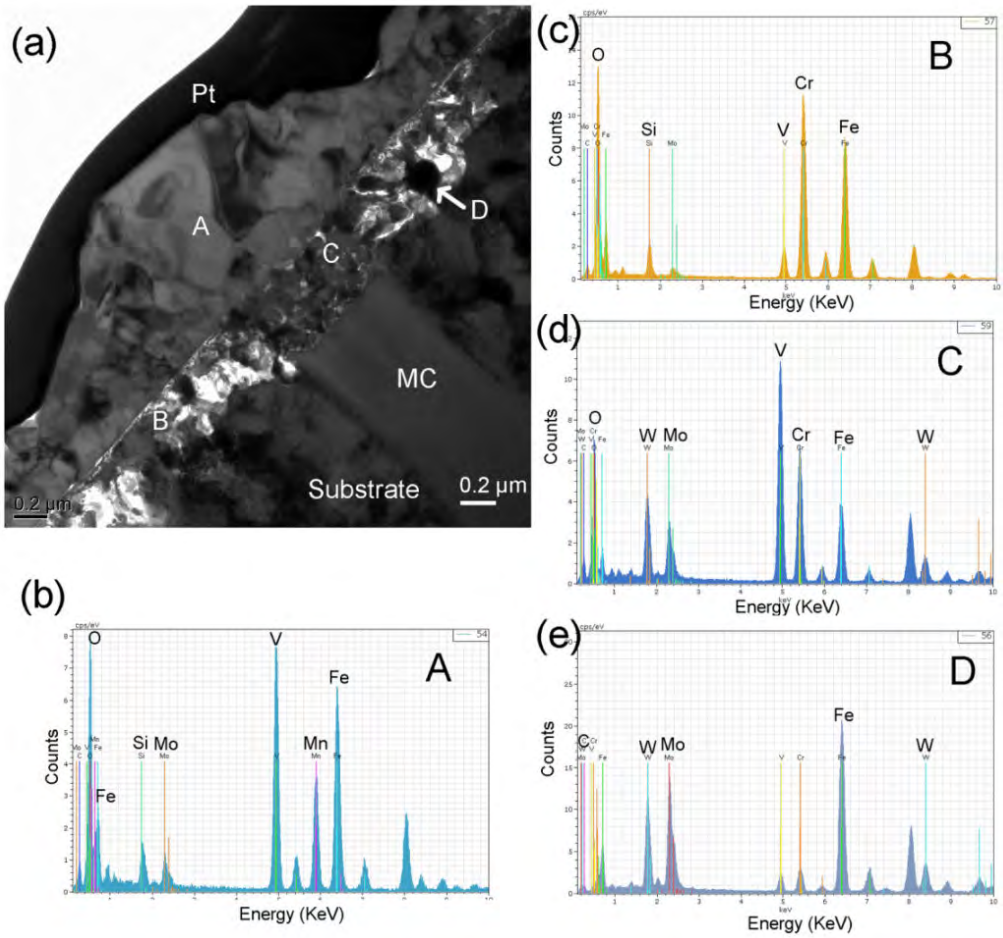

Fig. 4.26 (a) High magnification TEM bright field cross-section image of oxide scale on a vanadium carbides (MC) area formed at 600 °C in dry air after 30 min oxidation, (b) EDS spectra of area "A", (c) EDS spectra of area "B", (d) EDS spectra of area "C", (e) EDS spectra of area "D".

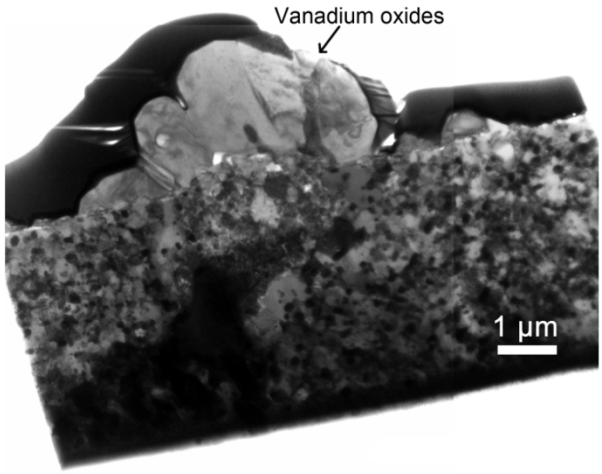

Fig. 4.27 TEM bright field image of an FIB cross section of the oxidised sample at 600 °C for 120 min in dry air.

Fig. 4.27 shows the TEM bright field mage of the cross section of the oxide layer formed at 600 ^{o}C for 120 min in dry air. It can be seen that the oxide scale formed on the HSS sample substrate remained thin while the V-rich MC carbides were oxidised much more severely than the 30 min oxidation at the same temperature (Fig. 4.25).

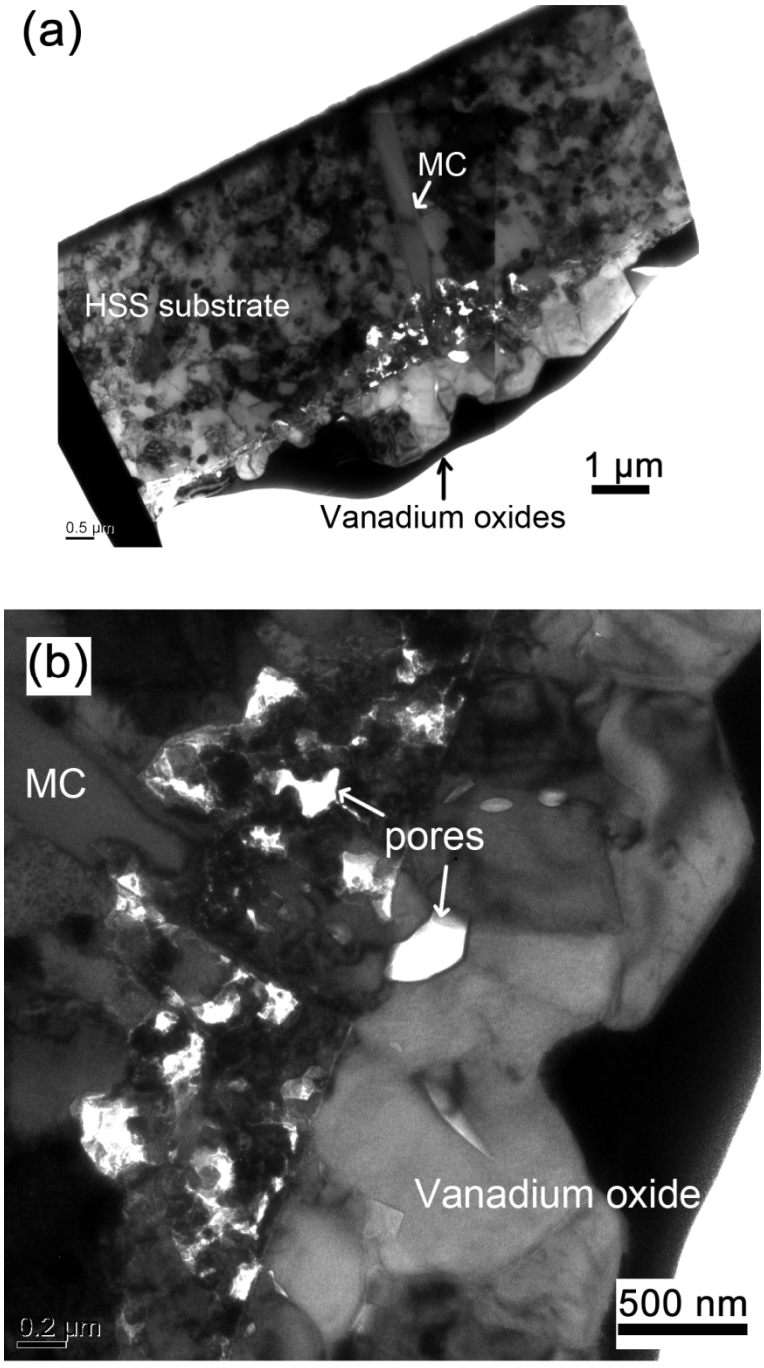

Fig. 4.28 (a) Overview TEM bright field image of FIB cross-section of the oxidized sample at 650 ^{o}C for 30 min in dry air, (b) higher magnified TEM bright field cross-section images of oxide scale.

Fig. 4.28 illustrates the TEM bright field mage of the cross section of the oxide layer formed at 650 ^{o}C for 30 min in dry air. The microstructure of the oxide scale remained the same compared with that formed at 600 ^{o}C. The thickness of the oxide scale at the carbides free areas has no significant change but a thicker oxide scale formed at the vanadium rich carbides area due to more severe oxidation. The maximum thickness of the oxide scale is approximate 2.3µm.

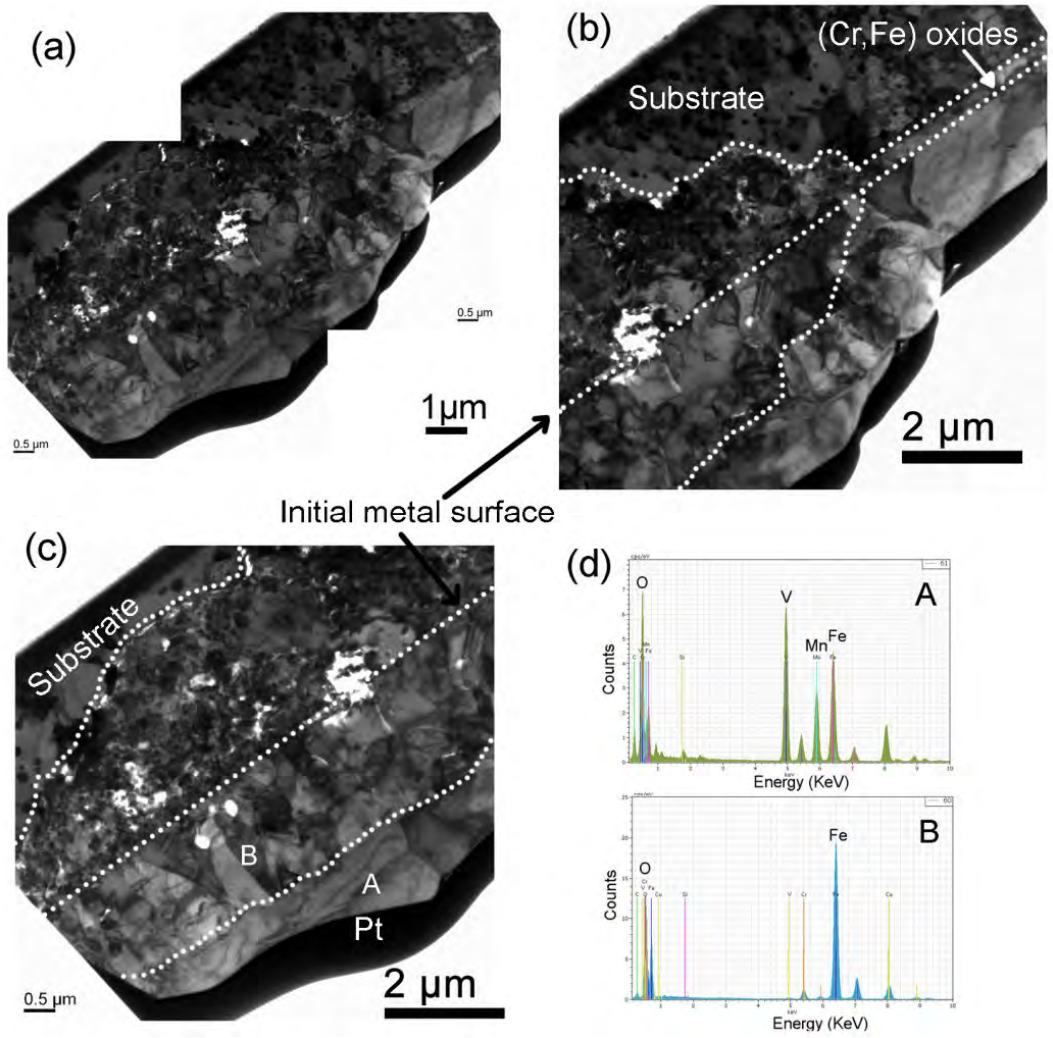

Fig. 4.29 (a) Overview TEM bright field image of an FIB cross section of oxide scale formed at 650 ^{o}C in dry air after 120 min oxidation, (b) and (c) higher magnified TEM bright field cross section images of oxide scale, (d) EDS spectra of areas "A" and "B" labelled in (c).

Fig.4.29a illustrates the cross section of oxide scale after oxidation at 650 ^{o}C for 120 min. The FIB cross section was cut off from the vanadium-rich carbides area. Fig. 4.29b and c show the higher magnification TEM bright field image of this area. It

can be seen that a thin and compact layer of chromium-iron oxide was formed in the carbide free matrix area, and the total thickness of the oxide scale formed in this area is around 1.6μm. However in the vanadium rich MC carbide area, a thick, duplex layer of oxide scale formed (Fig. 4.29b and c) whose maximum thickness is over 6μm. The inner layer consists of fine oxides and a high concentration of porosity and the outer layer has big columnar oxide crystals. An EDS analysis (Fig. 4.29d) indicated that the columnar oxide crystals are pure iron oxide and vanadium oxides that formed on top of the oxide scale. There is a big difference in the thickness of oxide scale which formed at the MC carbides area and carbide free matrix. Fig. 4.30 shows the TEM/X-ray maps of the cross section of the oxide scale. It confirms that vanadium ions diffused to the scale/air interface during the oxidation and oxidised on the top of the oxide scale. Mn was also found on the top of the scale. Chromium accumulated at the substrate/inner oxide layer and inner/outer layer interfaces. Si, Mo, and W elements are mainly distributed in the inner layer, similar to Cr.

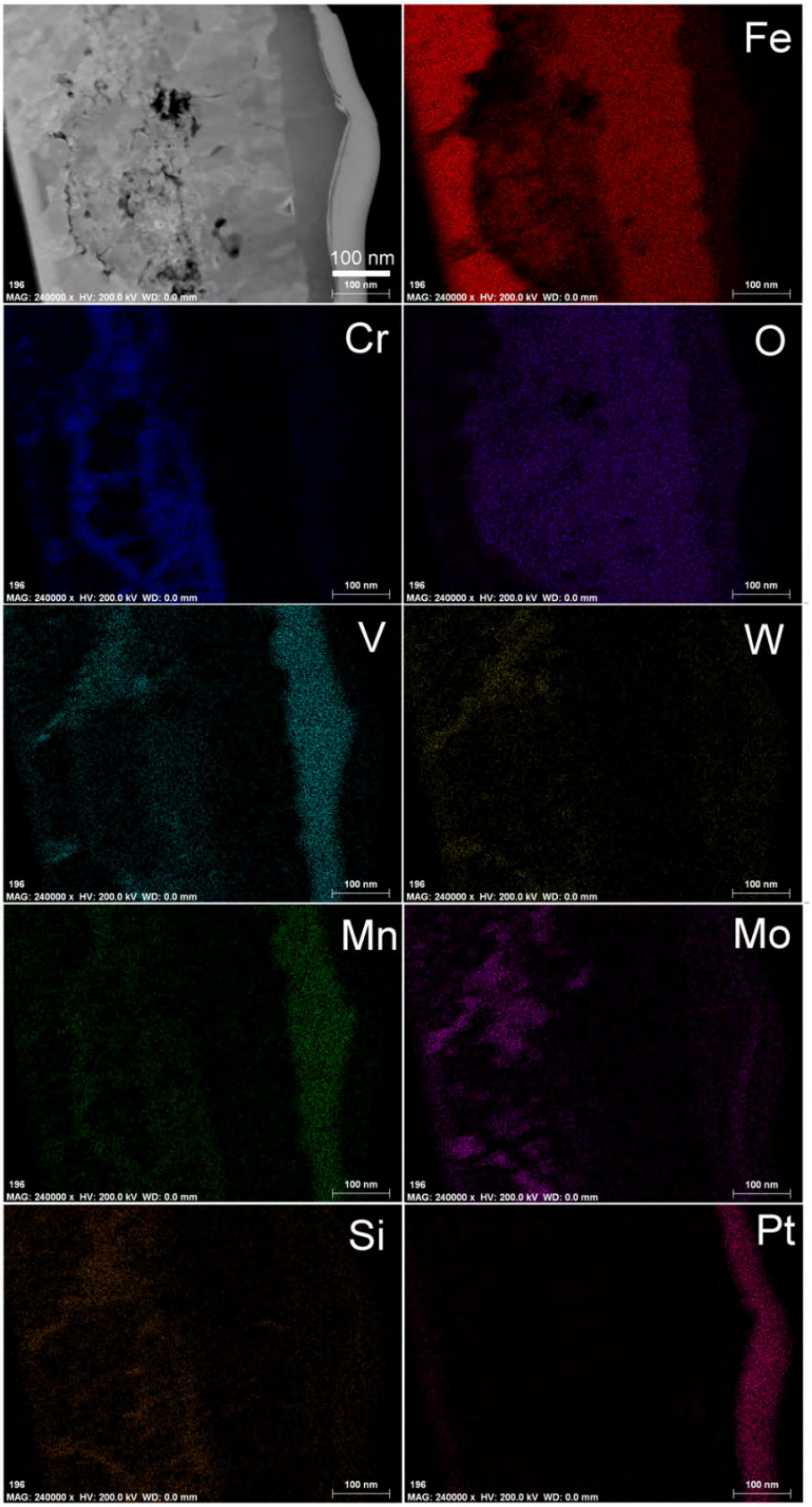

Fig. 4.30 TEM/X-ray mapping of the oxide scale formed at 650 ^{o}C after oxidation in dry air for 120 min.

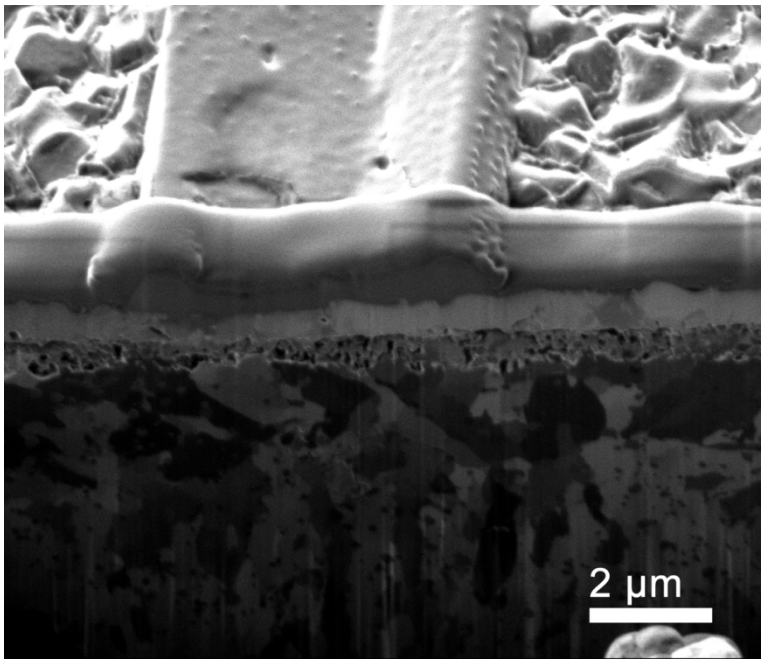

Fig. 4.31 An FIB cross section of an oxidised sample at 700 ^{o}C for 30 min in dry air. The sample is titled 52^{o}.

Fig. 4.31 shows the FIB cross section of oxide scale formed at 700 ^{o}C in dry air after 30 min of oxidation. This section was cut off from the matrix and can be clearly seen that the oxide scale has duplex-layer structure which is the same as those formed at lower temperatures. A vanadium oxide sitting on top of the oxide scale indicates that vanadium ions are more easily diffused to the metal/air interface during oxidation. The thickness of the oxide scale formed at 700 ^{o}C for 30 min in dry air was approximately 1.5µm, which is much thicker than those formed at lower temperatures, and indicates that the temperature has a significant influence on the oxidation behaviour of the HSS sample.

Table 4.2 compares the thickness of oxide scale formed at the V-rich MC carbides area and the carbides free matrix after oxidation at 600, 650, and 700 ^{o}C in dry air for 30 to 120 min. These results indicated that the carbides free matrix has a strong resistance to oxidation, which results in a thin oxide scale formed after oxidation. At 600 ^{o}C, the thickness of the oxide scale formed on the carbides free matrix had a less significant increase when the oxidation time was increased from 30 to 120 min., however the V-rich MC carbides area was easily oxidised and both the temperature

and oxidation time showed significant influences on the oxidation rate. The oxide scale formed at the V-rich MC carbides area after oxidation at 650 ^{o}C for 30 min was twice as thick as that formed at 600 ^{o}C, while the oxide scales formed on the carbides-free matrix only increases from 0.42 to 0.56µm. When the oxidation temperature reached 700 ^{o}C, severe oxidation occurred and the average thickness of oxide scale formed on HSS sample matrix reached 16 µm after 120 min oxidation.

Table 4.2 Comparison of Oxide scale thickness formed at the vanadium carbides area and carbides free area after oxidation at 600 and 650 ^{o}C in dry air for 30 to 120 min. The thicknesses were obtained by measuring from TEM and SEM images.

Temperature / ^{o}C	Oxidation time / min	Oxide scale thickness / µm	
		MC rich area	Carbides-free matrix
600	30	1.28	0.42
	120	3.18	0.65
650	30	2.31	0.56
	120	6.16	1.59
700	30	-	1.5
	120	-	16

4.2.5.2 Oxidation in 12.5% H_2O humid air

Fig. 4.32 shows the TEM bright field image of an FIB cross section of an oxidised sample at 550 ^{o}C for 30 min in 12.5% H_2O humid air. It can be seen clearly that a V-rich MC carbide is severely oxidised, where the maximum depth of oxidation on the MC carbide was more than 3µm (Fig. 4.32a). During oxidation the vanadium oxides spread to the surroundings and covered the top of the oxidised surface, as seen in Fig. 4.32b. The vanadium oxides are thicker than 300nm. Under the vanadium oxides a thin oxide scale (thicker than 300 nm) formed on the HSS matrix. Fig. 4.32c shows the oxidation frontier on the vanadium rich MC carbide and that columnar crystals grow on the oxide/MC carbide interface, indicating a strong diffusion of the vanadium element from carbide to the oxidation frontier.

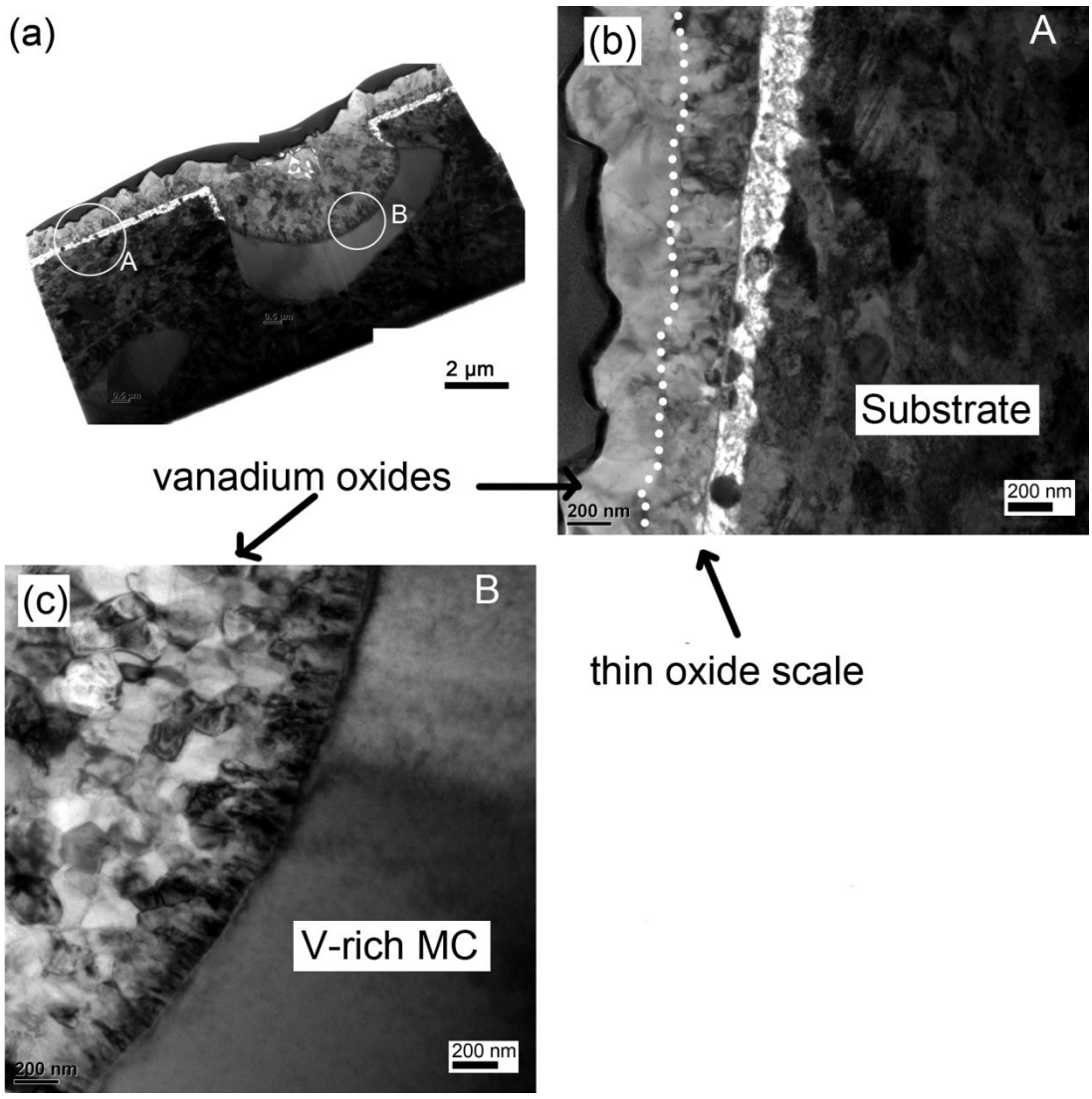

Fig. 4.32 a) Overview TEM bright field image of an FIB cross section of an oxidised sample at 550 ^{o}C for 30 min in 12.5% H_2O humid air; (b) Higher magnified TEM bright field image of area "A" labelled in (a), (c) Higher magnified TEM bright field image of area "B" labelled in (a).

Fig. 4.33 shows the TEM bright field image of an FIB cross section of the oxide scale formed at 600 ^{o}C for 120 min in 12.5% H_2O humid air where a continuous oxide scale formed on the sample surface after oxidation. At the carbides/matrix interfaces the oxidation was more severe than the matrix which leads to a thicker oxide scale forming at this place (Fig. 4.33a). The oxide scale consists of two sub-layers which is similar to that formed in dry air conditions. However, the grain sizes of oxides in the outer layer (Fig. 4.33b) were much finer than those formed in dry air (Fig. 4.25 and Fig. 4.26a). An EDS analysis of the outer layer (Fig. 4.33c)

confirmed that the outer layer consists of iron oxides. Figs. 4.33b and 4.33d indicate that the Mo-rich M_2C carbides (probably the combination of M_2C and M_7C_3) have a better oxidation resistance than the matrix.

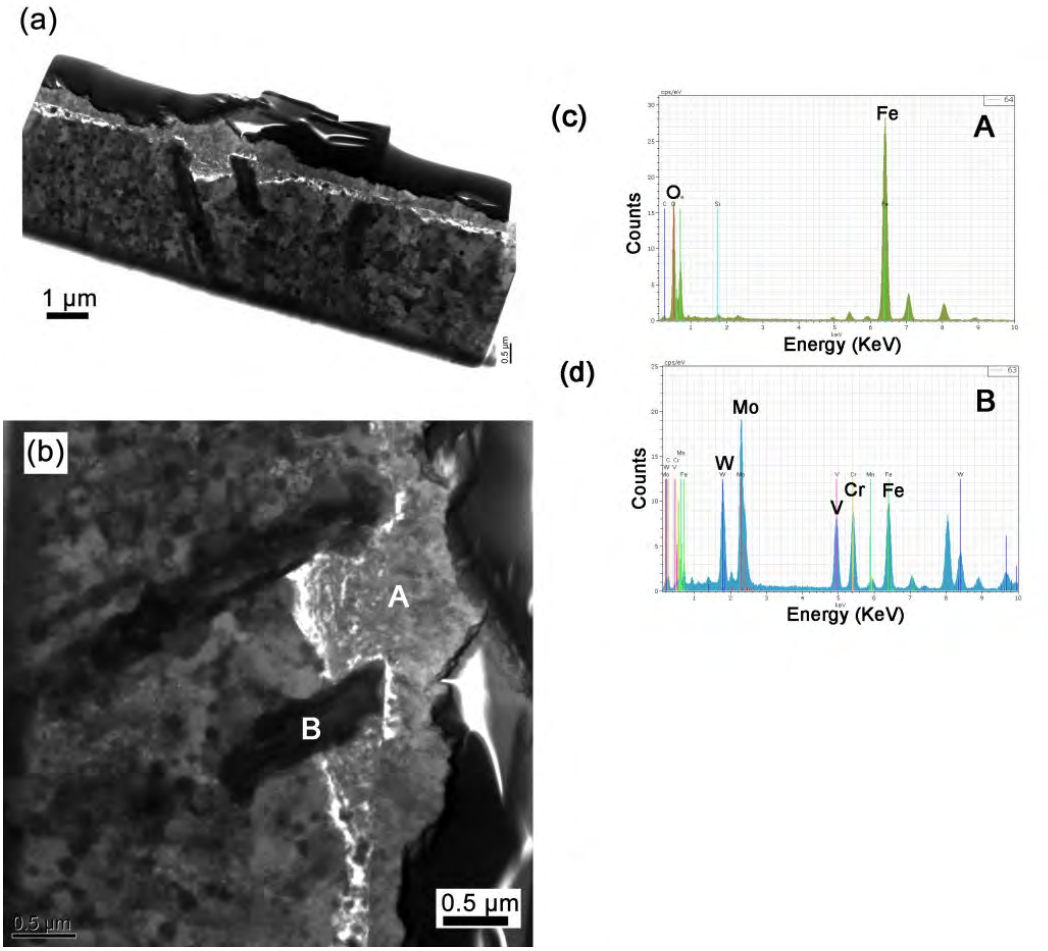

Fig. 4.33 (a) Overview TEM bright field image of an FIB cross section of an oxidised sample at 600 ^{o}C for 120 min in 12.5% H_2O humid air, (b) higher magnified TEM bright field cross sectional images of oxide scale, (c) EDS spectra of areas "A" and "B" labelled in (b).

Fig. 4.34 shows the TEM bright field image of an FIB cross section of oxide scale formed at 650 ^{o}C for 30 min in 12.5% H_2O humid air. The microstructure of oxide scale remains duplex layered, and the outer layer consists of large oxide crystals and the inner layer consists of fine oxides and an amount of pores. Its maximum thickness is approximately 3.4µm which is much greater than that formed in dry air (Fig. 4.28), and whose thickness was approximately 2.3µm.

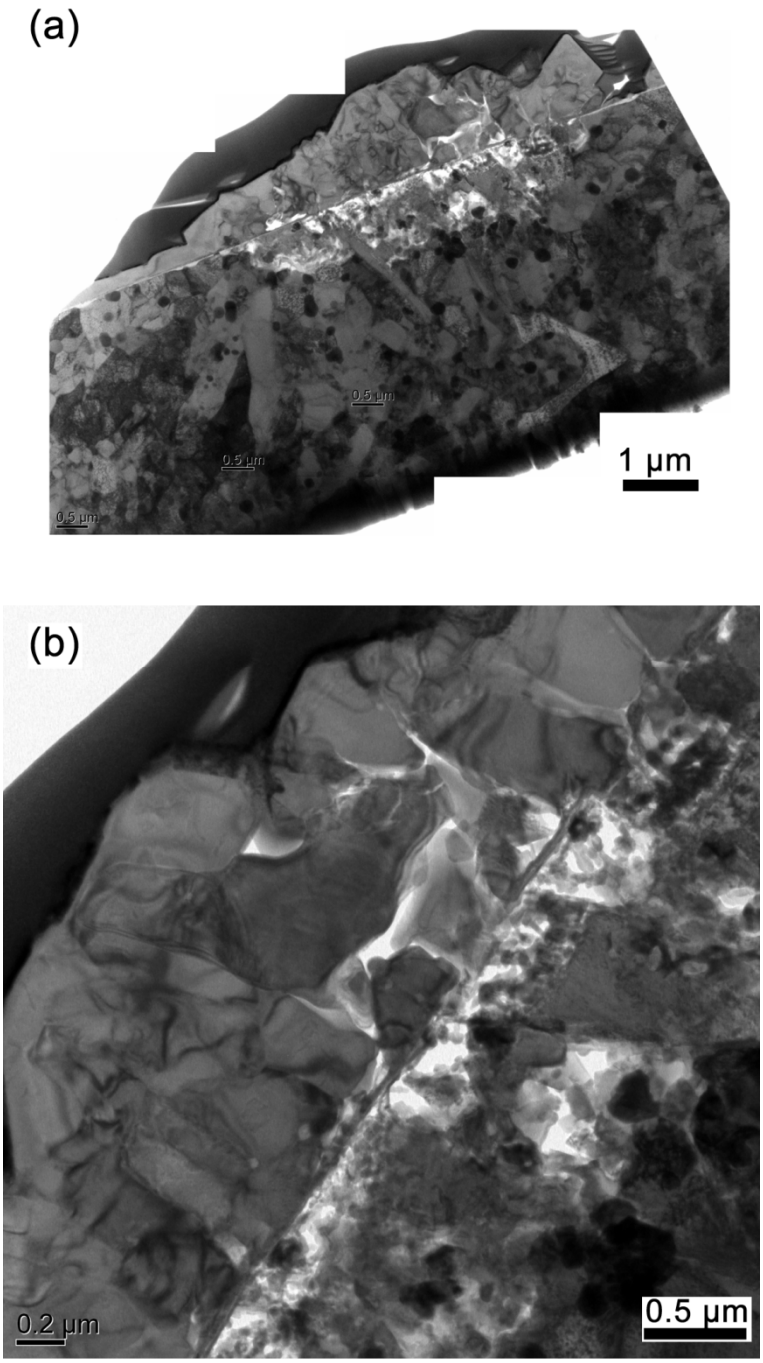

Fig. 4.34 (a) Overview TEM bright field image of an FIB cross section of the oxidised sample at 650 ^{o}C for 30 min in 12.5% H_2O humid air, (b) higher magnified TEM bright field cross sectional images of oxide scale.

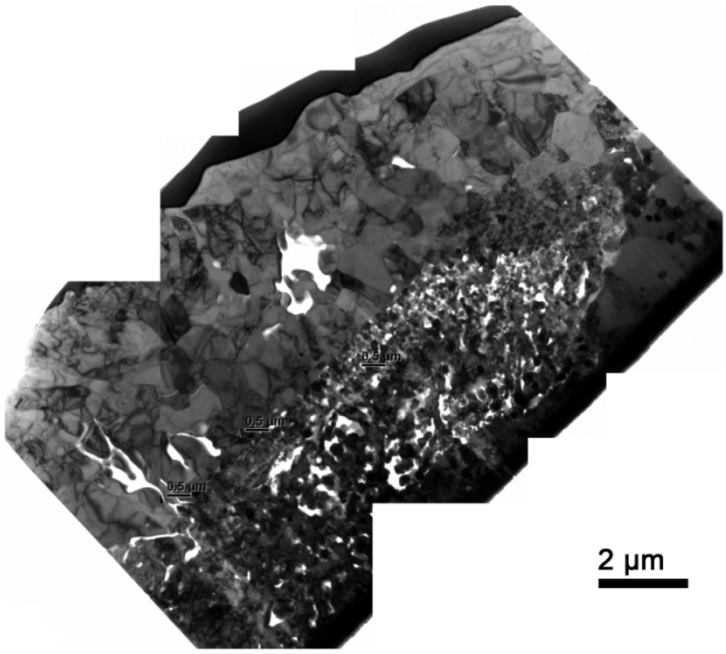

Fig. 4.35 TEM bright field image of FIB cross-section of oxidised sample at 650 ^{o}C for 120 min in 12.5% H_2O humid air.

Fig. 4.35 shows the TEM bright field image of an FIB cross section of an oxidised HSS sample at 650 ^{o}C for 120 min in 12.5% H_2O humid air. The micro-structure of the oxide scale remains the same compared with that formed in dry air at the same temperature (Fig. 4.29). The inner layer consists of fine oxides and a high concentration of pores and the outer layer of large columnar oxide crystals and larger, irregular pores. However, the oxide scale formed in humid air is thicker than that in dry air.

4.2.6 Surface topography after oxidation

Fig. 4.36 shows the AFM images of the surface topography of the samples after oxidation at different temperatures in dry air. The roughness of the surface increased significantly at higher temperatures, which suggests that the oxidation temperature has a great influence on the oxidised surface topography of HSS roll materials. The sample surface was mildly oxidised at 550 ^{o}C, leading to a relative smooth surface topography without any specific feature, as shown in Fig. 4.36a. At 600 ^{o}C, selective oxidation results in the V-rich MC carbides being oxidised faster than the matrix, and the locations of the carbides protrude from the surface after

oxidation, as shown in Fig. 4.36b. Increasing the temperature further (650 and 700 ^{o}C) resulted in an increase in the oxidation rate of both the carbides and the matrix. The oxidation rate of the carbides and matrix was still substantially different, which meant that the roughness of the sample surface increased with the oxidation temperature and was considerably greater than at 600 ^{o}C.

Fig. 4.37 shows the AFM images of the sample surface topography after oxidation at different temperatures in 12.5% H_2O humid air. The surface topographies at lower temperatures, 550 and 600 ^{o}C, oxidised in humid air, are similar to those in dry air. In contrast, the oxidised surface topographies at higher temperatures (i.e. 650 and 700 ^{o}C) in two various atmospheres are apparently different. The surface topographies after oxidation in humid air are far more uniform than those produced by oxidation in dry air.

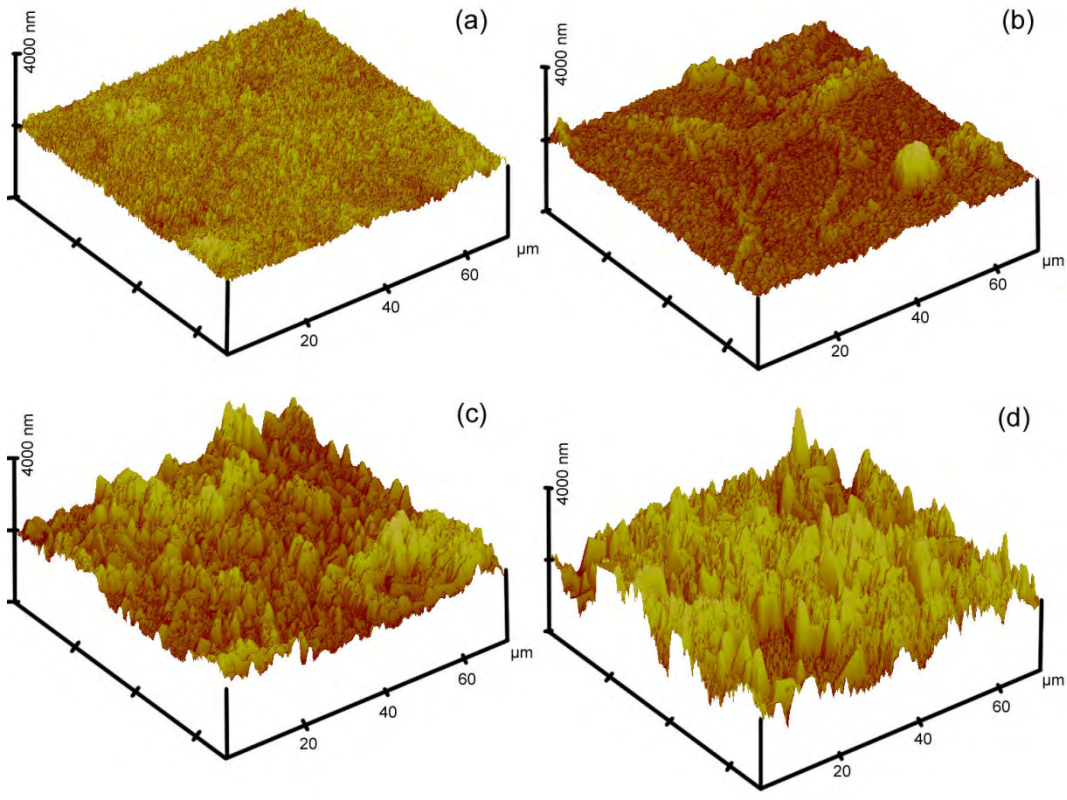

Fig. 4.36 AFM images of surface morphologies after oxidation at different temperatures in dry air: (a) 550 ^{o}C, (b) 600 ^{o}C, (c) 650 ^{o}C and (d) 700 ^{o}C.

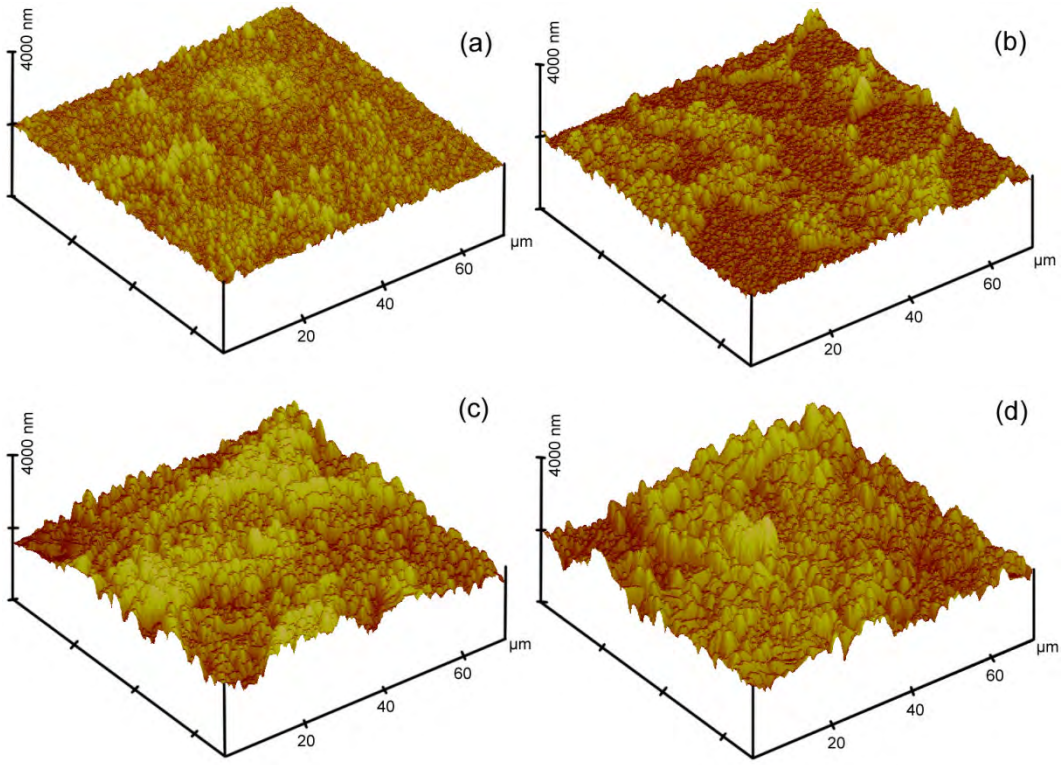

Fig. 4.37 AFM images of surface morphologies after oxidation at different temperatures in 12.5% H_2O humid air: (a) 550 ^oC, (b) 600 ^oC, (c) 650 ^oC and (d) 700 ^oC.

Fig. 4.38 compares the arithmetic mean roughness (Ra) of the sample surface after oxidation in dry air and 12.5% H_2O humid air. In both cases the roughness increased with higher temperatures, although the water vapour had less influence on the surface roughness at low temperatures such as 550 and 600 ^oC. When the oxidation temperature reached 650 and 700 ^oC the water vapour enhanced the oxidation rates of both carbides and the matrix, which reduced the differential oxidation behaviour of the carbides and matrix and hence the roughness of the oxidised surface decreased compared to that in dry air.

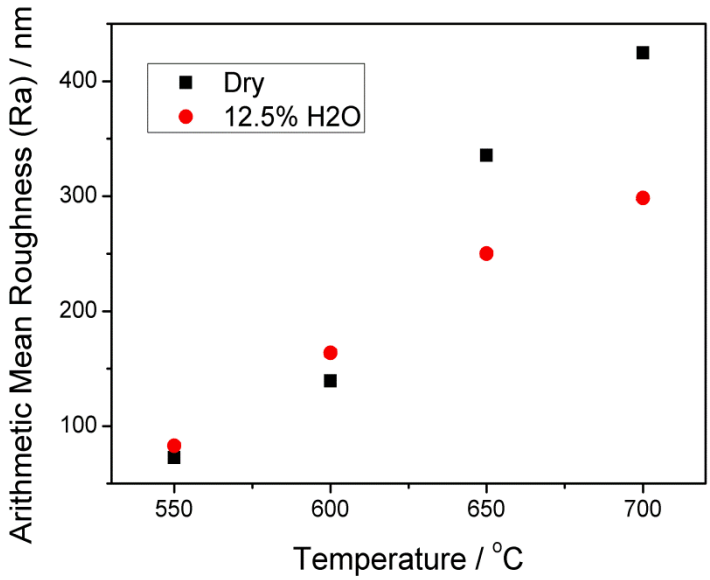

Fig. 4.38 Arithmetic mean roughness (Ra) of sample surfaces after 30 min oxidation at different temperatures in both dry and humid air.

4.3 Discussion

The surface morphology of the HSS samples changes greatly with temperature from 550 to 700 °C, which indicates that the temperature has a significant influence on the oxidation behaviour of the chosen HSS material. The HSS samples have very good oxidation resistance at low temperatures, i.e. 550 and 600 °C, but at 550 °C, there is a thin, compact chromium-iron layer of oxide covering on top of the HSS matrix. There are iron oxides growing among or on this layer as a result of Fe ions diffusing through the layer from the substrate. After oxidation at 650 °C, the sample surfaces were oxidised unevenly. Heavy oxidation occurred at the vanadium-rich MC carbides areas due to a low thermal stability of the vanadium-rich MC carbides and high free energy at the carbides/matrix interfaces [7, 107, 140]. At the same time the matrix shows a good oxidation resistance when covered with a thin, compact layer of Cr-Fe rich oxide.

Differential oxidation is expected to occur in the HSS samples due to a high level of alloying elements. Zhou et al. [93] indicated that alloy elements possess different levels of resistance to oxidation and preferably precipitate as different types of

carbides or dissolve in the matrix, leading to a different resistance to oxidation between the matrix and carbides. Kim et al. [2] pointed out that all kinds of carbides in the HSS material oxidised faster than the matrix because the formation of a protective Cr-rich oxide on the matrix results in a decrease in the oxidation rate. Molinari and Pellizzari [94] found that V-rich MC carbide and the matrix are heavily oxidised, Mo-rich M_2C carbide has intermediate oxidation behaviour, and Cr-rich M_7C_3 carbide is far less oxidised if it dissolved a high amount of chromium. The results of this study confirmed the previous research work [2, 94, 141], where the MC carbides are heavily oxidised even though MC carbides dissolve chromium, and M_7C_3 carbides have a very good resistance to oxidation.

Vanadium carbides have a great affinity for oxygen at high oxygen partial pressure [142]. Hence, during oxidation, vanadium ions (driven by the high partial pressure of oxygen) diffuse from the substrate and carbides across the thin oxide scale to feed the oxide layer formed on the outer layer. The development of vanadium rich oxide needles and parallelepiped crystals, as shown in Fig. 4.8 and Fig. 4.26, can be considered as evidence of the diffusion of vanadium ions. This also indicates that the diffusion rate of vanadium ions through the oxide scale is faster than iron ions. The possible oxidation reaction of vanadium carbides are listed as follows:

$$VC(s)+O_2(g)=VO(s)+CO(g)$$

$$2VC(s)+O_2(g)=V_2O_5(s)+2CO(g)$$

Due to the argument among many researchers regarding the oxidation products of the vanadium carbides under the hot rolling conditions, thermodynamic calculation of the Gibbs generation free energy was used to determine the most possible type of vanadium oxide in our experiments. Although the morphology of VO crystal is similar to V_2O_5 whose crystal structure is orthorhombic, thermodynamic calculations of the Gibbs free energy [143] that involved the reaction of vanadium carbide with oxygen to form vanadium oxide (VO) or vanadium oxide (V_2O_5) show that the formation of V_2O_5 (G=-1357 kJ/mol, 650 ^{o}C) is more favoured than the formation of VO (G=-457 kJ/mol, 650 ^{o}C).

The steel matrix has a good resistance to oxidation because chromium elements are distributed homogenously in it. It is well known that chromium is commonly added to steel to increase its resistance to oxidation [144]. Chromium has a greater affinity to oxygen than iron, and a Cr_2O_3 film is quickly formed at the base of the scale, which owes its protective character to a low ionic conductivity, and thickens slowly by the outward movement of cations. In the present work a complex layer composed of iron and chromium oxides at the matrix/oxides interface was formed. The formation of this layer may display a protective behaviour and reduce the oxidation rate, especially when $(Cr,Fe)_3O_4$ spinel are formed in the layer [145, 146]. The temperature has the most impact on the surface morphology when the HSS sample was oxidised at 700 ^oC. Despite massive V-rich carbides being oxidised into parallelepiped grains distributed on the top the surface, a continuous honeycomb-structural iron oxide scale formed across the whole surface after oxidation.

In spite of different oxidation behaviour in vanadium-rich carbides area and carbides-free matrix, the oxidation temperature has a significant influence on the kinetics of oxide scale growth (as shown in Table 4.2). The kinetics of oxide scale growth has been extensively studied and it is well interpreted into two growth laws (i.e. linear and parabolic laws) depending on the length of the oxidation time [20, 26, 30, 40, 41, 53-55]. As the oxidation time in the current study was limited due to the fact that the total oxidation time of hot roll surfaces in practical conditions is usually less than 2 hours, the linear rate is therefore more suited to describe the oxide growth which can be expressed as [20, ,26, 41]:

$$X=K_l t \qquad (4.1)$$

where X represents the thickness of the oxide layer measured throughout the oxidation time t and k_l is known as the linear rate constant a term that intrinsically includes the mobility of cations and electrons due to the gradients of chemical potential established across the oxide scale and the electrical conductivity of these

species. The constant K_l is strongly linked to the temperature of the environment and can be expressed by the Arrhenius expression [56, 57] such as:

$$K_l = Ae^{\left(\frac{-Q}{RT}\right)} \qquad (4.2)$$

where Q represents the activation energy needed to stimulate ionic motion for oxidation reactions to occur, T is the temperature in absolute units, R is the universal gas constant and A is a constant. Therefore, the rate of oxide growth normally increases with temperature. However, the growth rate of oxide scale is often influenced by the chemical composition and the purity of metal, the pressure of the system and the type and amount of defects and oxides phases present in the oxide layer. The compact thin oxide scale formed on the carbides-free matrix acts as a barrier reducing the ions diffusion (both metal ions and oxygen ions) through the scale resulting a low growth rate, while the porous oxide scale formed on the vanadium carbides rich area with complicate oxides phases and many defects cannot sufficiently act as a diffusion barrier which leads to a much higher growth rate of oxide scale in these areas.

Compared with oxidation in dry air, water vapour has a significant effect on increasing the oxidation rate of carbides, but less so on the matrix, at oxidation temperatures of 550 and 600 ^{o}C. The oxidation of sample surfaces at temperatures of 650 and 700 ^{o}C in 12.5% H_2O humid air (Figs. 4.37c and d) were far more apparent than corresponding cases in dry air (Figs. 4.36c and d). Water vapour in the oxidising atmosphere enhances the oxidation rates of both carbides and the matrix. After oxidation at 650 ^{o}C (Fig. 4.37c), V-rich MC carbides were significantly oxidised while the oxidised surface of the matrix in 12.5% H_2O humid air was not as even as in dry air. Some locations in the matrix were more heavily oxidised than other areas, leading to large iron oxide grains growing out of the surface. The oxidation kinetics of HSS is strongly influenced by the presence of water vapour in the atmosphere. The simplest explanation that can be given to this phenomenon is

that the rate of oxidation is higher when water vapour is present because the water provides a second source of oxygen needed for the oxidation reactions, apart from the fraction of oxygen that is already contained in the dry air. Thus, in addition to the simple oxidation reactions that involve the iron of the steel matrix to form magnetitie (Fe_3O_4) and hematite (Fe_2O_3) expressed by:

$$4Fe+3O_2=2Fe_2O_3 \qquad (4.3)$$

$$3Fe+2O_2=Fe_3O_4 \qquad (4.4)$$

, another oxidation reaction involving water vapour and iron to form magnetite was also present during the oxidation process expressed as [93, 12]:

$$3Fe+4H_2O=Fe_3O_4+4H_2 \qquad (4.5)$$

$$Fe_3O_4+H_2O=3Fe_2O_3+H_2 \qquad (4.6)$$

The surface morphology of an oxidised HSS sample at 700 ^{o}C in 12.5% H_2O humid air had a similar feature to that in dry air, however, the iron oxide scale seemed thicker and the iron oxide grains were smaller. And it is also noted that the V-rich MC carbides were severely oxidised and spread among the iron oxide scale instead of forming parallelepiped grains, as observed in dry air (Fig. 4.14). A similar morphology of iron oxide scale was obtained in Pujilaksono et al.'s research [35], where they reported that water vapour strongly influences the morphology of hematite (the outermost part of the scale) because the presence of water vapour increases the oxidation rate of iron resulting in a smaller grains in the hematite layer. The higher oxidation rate of the HSS material, due to water vapour in the oxidising atmosphere, found in this investigation confirms the results of previous studies [6, 93]. Monteiro and Rizzo [6] found that there is no protective chromium oxide layer formed on the oxide/alloy interface when HSS materials are oxidised in the presence of water vapour, while in dry air a protective chromium oxide scale is observed. Water vapour in the air significantly increases the oxidation rate of HSS

roll material at high temperatures of 650 and 700 ^{o}C, which makes the selective oxidation on surface morphology become less obvious after oxidation.

A cross sectional investigation indicates that differential oxidation produces a different growth mechanism of oxide scale. At 600 ^{o}C, vanadium-rich MC carbides were oxidised and decomposed, while (Mo, W) rich fine carbides were not oxidised and remained in their original shape. Because vanadium-rich MC carbides are easier to be oxidised than the carbides free HSS matrix, which has been discussed above, the oxide scale formed in these areas are much thicker than in the carbides free HSS matrix. The thickness of oxide formed on the vanadium-rich MC carbides area is more than twice thicker than that on the carbides free HSS matrix at 600 ^{o}C.

An FIB cross sectional observation indicates that the thickness of the oxide scale after oxidation for 120 min on the HSS matrix changed little compared to that for 30 min, but the oxide in the vanadium rich carbides areas are clearly getting thicker. After 120 min of oxidation at 650 ^{o}C, the carbides free HSS matrix area was covered with a thin, compact chromium-iron oxide layer with thickness of approximately 250nm thick, while heavy oxidation occurred in vanadium-rich MC carbides area where the oxide scale was more than 6μm thick after 30 min of oxidation. Both Fig. 4.25 and Fig. 4.28 show that the oxide scale formed in vanadium-rich MC carbides area has a duplex-layered structure. It is believed that the structure of oxide scale shown in Fig. 4.25 indicates the initial stage of oxide scale formation due to a lower oxidation temperature and shorter oxidation period.

The results of TEM/X-ray mapping of the cross section of oxide scale formed at 650 ^{o}C for 120 min indicate there was a fine grained structure deficient in iron and rich in chromium oxide layer next to the substrate and an outer layer consisting of columnar iron oxide crystals with vanadium oxides covering the top. These results are similar to Molinari et al.'s research [19] which indicated that the three sub-layers in the oxide scale after oxidation at 700 ^{o}C for 24 h are: i.) a thin α-Fe_2O_3 outer layer, ii.) a thick and porous α-Fe_2O_3 intermediate layer, and iii.) the inner M_3O_4 spinel

(M=Fe, Cr, V) produced by internal oxidation.

X-ray diffraction analysis showed that the oxide layer consists mainly of Fe_3O_4 (magnetite) and Fe_2O_3 (hematite). FeO (wustite) was not detected from X-ray diffraction analysis of the samples. The reason might be that although FeO (wusitite) is stable at 650 ^{o}C, its formation was suppressed by the existence of chromium in the steel, an element that increases the number of defects in the crystal structure of FeO (wusitite) and favours its transformation to magnetite or a chromium rich spinel structure [145, 148]. The absence of FeO (wustite) in the oxide layer agrees with the previous observations found in the oxidation studies of work rolls [2, 141, 149].

There is a clear interface between the inner and outer layer, which is also the initial metal surface. TEM/X-ray mapping indicated that chromium and silica accumulate at the interface. The accumulation of silica at the scale alloy interface of high temperature steels are frequently reported in the literature [107, 150]. It has been suggested that the formation of a silica sub-scale can significantly contribute to oxidation resistance, just like chromium does [151, 152], however, in this present case, the silica at the interface can hardly act as a diffusion barrier since it does not form a continuous film. We believe that this chromium and silicon rich band is a marker showing the original metal/gas interface. This implies that the inner layer grows mainly by inward oxygen diffusion while the outer layer grows by outward cation diffusion. There was high porosity in the inner layer which indicates that inner layer does not have much protection against oxidation. The formation of pores in the inner layer may be due to two possible reasons. First, Fe and V ions diffuse outwards, which leaves a vacancy, and second, the escape of CO produced by the reduction of carbides leave voids in the inner layer [153]. The columnar iron oxide outer layer is believed to be formed due to Fe ions diffusing outwards from the inner layer. The different oxidation behaviour between carbide-free matrix and vanadium-rich MC carbide areas leads to an inhomogeneous surface after oxidation.

This has an important influence on the contact friction and wear of hot rolls.

From our experimental results there are two mechanisms of oxidation behaviour happening at the V-rich MC carbides area and the carbides free matrix area, respectively. At the carbide free matrix area, the oxidation behaviour is similar to the behaviour of Fe-Cr alloy. At the beginning of the oxidation process both chromium and iron elements are oxidised, forming a thin oxide layer on the matrix surface. Then, a competitive process starts; as the chromium oxide is more stable than iron oxide, chromium diffuses to the metal/oxide interface and is oxidised in this region where the partial pressure of available oxygen is lower than that in the external oxidising gas. Furthermore iron diffuses across the internal chromium oxide layer to the external oxide/gas interface, reacting with oxygen and producing an outer growth of the scale [6, 25, 145]. In this way a layer of chromium oxide grows beneath the layer of iron oxide. This compact, chromium rich oxide inner layer effectively prohibits the iron elements from diffusing to the external interface of the oxide scale and reduces the oxidation rate significantly. At the V-rich MC carbides area, however, a continuous and compact chromium oxide sub-layer does not form on the original metal surface due to high free energy on the carbides/matrix interfaces and a great affinity that the V-rich MC carbides have for oxygen. The interfaces possess high free energy indicates that the interfaces can act like fast tunnels for transporting both oxygen ions and metal ions (Fe, Cr, V) to react, thereby increasing the oxidation rate. The aggressive oxidation in this region leads to a porous chromium oxide inner sub-layer which provides sufficient channels (micro-cracks, pores) for iron and vanadium elements to diffuse outwards and oxygen to diffuse inwards as well. As oxidation proceeds an outer iron oxide layer consisting of columnar crystals, forms due to a sufficient supply of iron elements from the substrate and the fast oxidation rate. Vanadium elements have a great affinity for oxygen at high oxygen partial pressure and hence, vanadium oxides appear on top of the oxide scale after oxidation. Water vapour in the oxidising atmosphere significantly increases the oxidation rate of HSS samples, although the

micro-structure of the oxide scale remains the same as in dry air. The possible reason is that the presence of water vapour intends to break down the formation of protective chromium oxide layer on the oxide/alloy interface, leading to a severe oxidation.

4.4 Conclusions

The oxidation behaviour of the HSS roll material was investigated in detail at temperatures ranging from 550 to 700 ^{o}C in both air and humid (12.5% H_2O) air up to 30 min. The following results were obtained in this work:

The in-situ observation by high temperature microscope indicates that oxidation initiates at the carbides/matrix interfaces and then spreads rapidly over the carbides, followed by a continuous growth over the whole surface in both dry and humid atmospheres. V-rich MC and Mo, W-rich M_2C carbides in HSS roll material oxidised faster than the matrix. Differential oxidation occurred during oxidation due to a highly alloyed component in the high speed steel (HSS). Vanadium rich carbide (MC) is easily oxidised because it has a great affinity for oxygen. Vanadium rich carbides areas were severely oxidised due to the low thermal stability of MC and high free energy at the carbides/matrix interfaces.

Duplex layer oxide scales with vanadium oxides on the top, formed after oxidation. The carbides free matrix shows a very good resistance to oxidation which may be due to the formation of a thin, compact $(Cr, Fe)_3O_4$ spinel which reduced the oxidation rate. At the vanadium rich MC carbides areas the oxide scale consists of porous, fine crystalline (Cr, Fe)-rich oxides in the inner layer and large columnar iron oxides in the outer layer. Due to the different oxidation behaviour between the carbide free matrix and V-rich MC carbide areas, the surface morphology becomes inhomogeneous.

Oxidation temperature has a significant influence on how oxidation behaved on the

HSS roll material in both dry and humid atmospheres. With an increasing temperature the oxidation rate increases. As the sample surface oxidised at 700 ^{o}C is most severe, the temperature of the roll should be controlled at a temperature lower than 650 ^{o}C to protect the roll surface.

Water vapour in an oxidising atmosphere increases the oxidation rate of HSS roll material and has a significant influence on the morphology of the oxidised surface. Water vapour in an oxidising atmosphere reduces the grain size and increases the porosity of the iron oxide. With an increasing temperature the roughness of the oxidised surfaces increases in both dry and humid atmospheres. The surface topography after oxidation in humid air is much smoother than in dry air when the temperature is over 650 ^{o}C, although the overall rate of oxidation in the humid air appeared to be greater.

Chapter 5
Mechanical properties of oxide scale on HSS surface

During hot rolling work rolls are subjected to thermal cycles which lead to oxidation on roll surface. The formation of a thin oxide scale on the roll surface plays an important role during hot rolling. It not only affects the performance of the work rolls, it also influences the tribological behaviour between the work rolls and strip. However the role of oxides in tribological behaviour is very complex and still not clear because it is influenced by the nature and physical properties of the oxide scales. It is therefore instructive to investigate the mechanical properties of the oxide scales formed on the work roll surface.

As oxide scales built up on the roll surface are very thin, it is difficult to use conventional techniques to measure their properties. Nano-indentation and nano-scratch techniques have successfully been used to investigate the properties of thin films [154, 155]. Recently, this technology has been developed by some scientists to measure the oxide scales formed on metals. Xie et al. [156] performed nano-indentation and nano-scratch tests on a thermal oxide layer formed on a FeAl alloy; Hosemann et al. [157] measured the properties of oxide layers formed in LBE on F/M steels by a nano-indentation test on the cross section of the oxide scale. In this chapter, a work roll grade high speed steel material was isothermally oxidised in both dry and 12.5% H_2O humid air. The oxidation experiments were followed by nano-indentation tests on the cross section of oxide layers.

5.1 Experimental methods

The oxidised high speed steel samples were prepared in the same way as previous oxidation tests (see Chapter 4). However, in order to obtain a thicker oxide scale on

the sample surface, a longer oxidation time (2 hours) was used. The oxidation temperature was set to 700 ^{o}C, which produces a faster oxidation rate than a lower temperature. After cooling the oxidised samples were hot mounted with DuroFast resin at 150 ^{o}C and under 20 MPa. The samples were then ground with SiC paper, polished, and finished with a 1μm diamond suspension.

Nano-indentation tests were performed on the cross section of oxide scale using the UMIS nano-indentation system with a Berkovich diamond indenter (radius of tip is around 160nm). There were three different loads, e.g. 5mN, 10mN and 20mN, chosen in the nano-indentation tests. A square root load control mode was selected where the load was gradually increased until it reached peak load and then it was decreased. The indentation load vs. displacement curves were continuously recorded by software with a resolution of 75nN in load and 0.05nm in depth. The hardness and modulus calculations were done according to the Oliver and Pharr method [158] using a tip shape correction. Before the test the UMIS system was calibrated on a standard fused silicon sample whose Young's modulus and hardness are 72.5GPa and 9.5GPa, respectively. The calibration data can be found in Appendix A. The Nano-indentation tests were performed on a matrix of 5 rows and 5 columns or 7 rows and 7 columns across the oxide layer from the HSS matrix to the resin, and a matrix of 10 rows and 10 columns on the HSS sample surface in order to obtain adequate data for analysis. Following the nano-indentation tests, samples were characterised by atomic force microscope (AFM), scanning electron microscope (SEM), and transmission electron microscope (TEM).

5.2 Results

5.2.1 Indentation on high speed steel sample

Fig. 5.1 shows the AFM images of nano-indents on the HSS matrix at three different maximum normal loads, i.e., 20, 10, and 5mN. It can be seen that the size of the indents decreased with a lower maximum normal load but at the same maximum load, the indent size varied considerably due to a complicated phase composition in

the HSS sample. The indents on the carbides or on the matrix very close to the carbides were much smaller than those on the carbide free matrix, as shown in Figs. 5.1b, 5.1d, and 5.1f. The backscattered electron (BSE) images shown as Fig. 5.2 clearly indicate that the indenters were distributed over three different areas, the MC carbides, M_2C/M_7C_3 carbides, and the carbides free steel matrix.

Fig. 5.3a shows the load-displacement curves of nano-indentation on the HSS sample, at a maximum load of 20mN in these three different regimes. It can be seen that the depth of the indentations on the MC carbides are the smallest while those on the carbides-free matrix are the deepest. And the depth of the indentations on the M_2C/M_7C_3 carbides is distributed between the other two regions. The deepest residue indentation depth on the MC carbides (approximately 0.125μm) is only half of that in the carbides-free matrix (approximately 0.225μm). Similar load-displacement curves can also be found at maximum loads 10 and 5mN. Fig. 5.3b and c show the values of Young's modulus and the hardness of these three different regimes calculated from the load-displacement curves, respectively. The MC carbide has the highest value of Young's modulus and hardness, while the mean values are 345.1GPa, and 20.7GPa, respectively. Table 5.1 displays the hardness and Young's modulus obtained from the nano-indentation tests at maximum loads 20, 10, and 5mN. It can be seen that the results obtained from different loads have a consistent tendency although there is a deviation in the value. The mechanical properties of HSS matrix obtained from the nano-indentation tests at different loads (i.e., 20, 10, and 5mN) are almost the same. As for the M_2C/M_7C_3 carbides area and MC carbides area, the hardness obtained at 20 and 10mN are close to each other and greater than that obtained at 5mN, while the Young's modulus obtained at 20, 10 and 5mN are close to each other.

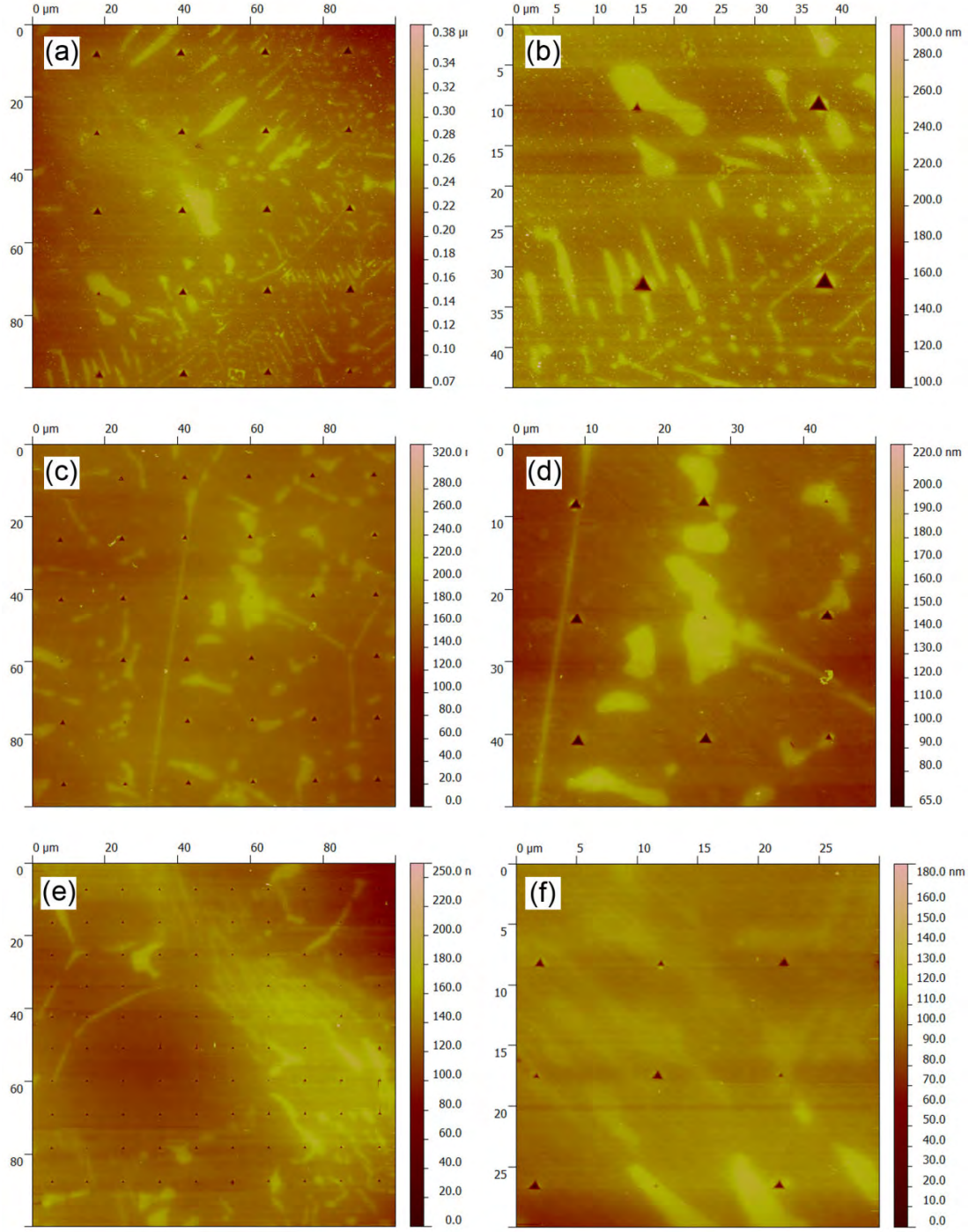

Fig. 5.1 AFM images of nano-indentations of a Berkovich indenter into a HSS sample surface at the maximum normal loads 20mN (a and b), 10mN (c and d) and 5mN (e and f). Higher magnification AFM images are shown on the right hand side.

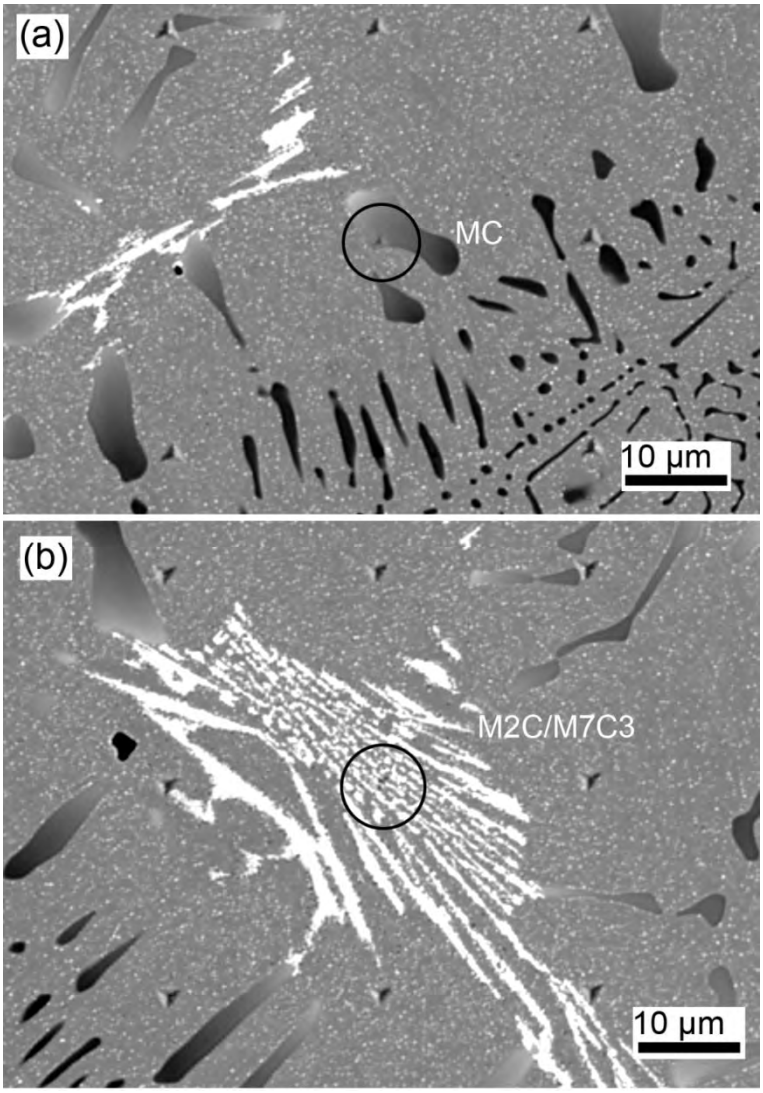

Fig. 5.2 Backscattered electron (BSE) images of nano-indentations on the HSS sample surface, the maximum indentation load is 20mN. (a) indenter on MC carbide, (b) indenter on M_2C/M_7C_3 carbides.

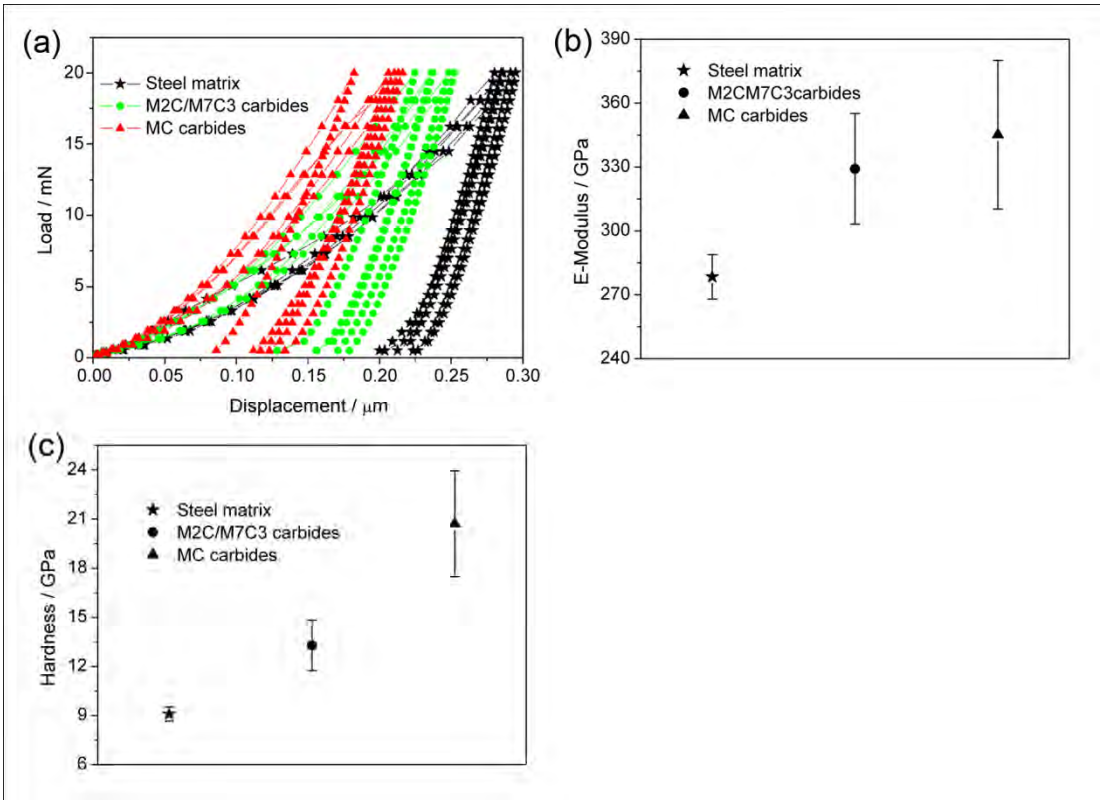

Fig. 5.3 (a) the load-displacement curves of indentations for three different regimes on a HSS sample surface, the maximum indentation load is 20mN,(b) a comparison of Young's modulus on three different regimes in a HSS sample, (c) comparison of nano-hardness on three different regimes in a HSS sample.

Table 5.1 Young's modulus and hardness obtained by nano-indentations at maximum loads 20, 10 and 5mN.

Indentation locations	Young's Modulus (GPa)		Hardness (GPa)	
	20mN			
	Mean	Standard deviation	Mean	Standard deviation
Steel matrix	222.1	3.7	9.0	0.4
M_2C/M_7C_3 carbides	308.7	7.8	13.2	1.5
MC carbides	358.4	19.6	20.7	3.2
	10mN			
	Mean	Standard deviation	Mean	Standard deviation
Steel matrix	221.7	8.4	9.4	0.7
M_2C/M_7C_3 carbides	305.4	5.9	13.0	1.3
MC carbides	354.3	5.7	21.8	1.4
	5mN			
	Mean	Standard deviation	Mean	Standard deviation
Steel matrix	231.7	8.8	9.0	0.3
M_2C/M_7C_3 carbides	296.6	13.2	11.3	1.0
MC carbides	373.4	9.7	17.3	2.5

5.2.2 Indentation on the cross section of oxide scale formed in dry air

Fig. 5.4 shows the backscattered electron microscope image of the cross section of oxide scale formed on the HSS sample after oxidation at 70 ^{o}C for 120 min in dry air, where a continuous oxide scale has formed on the sample surface after oxidation. A duplex oxide scale formed on the HSS sample matrix can easily be observed, as shown in Fig. 5.4b. At the carbides rich region, due to high free energy on the carbides/matrix interface and low thermal stability of V-rich MC carbides, a thick oxide scale has formed that appears like islands after oxidation (Fig. 5.4c).

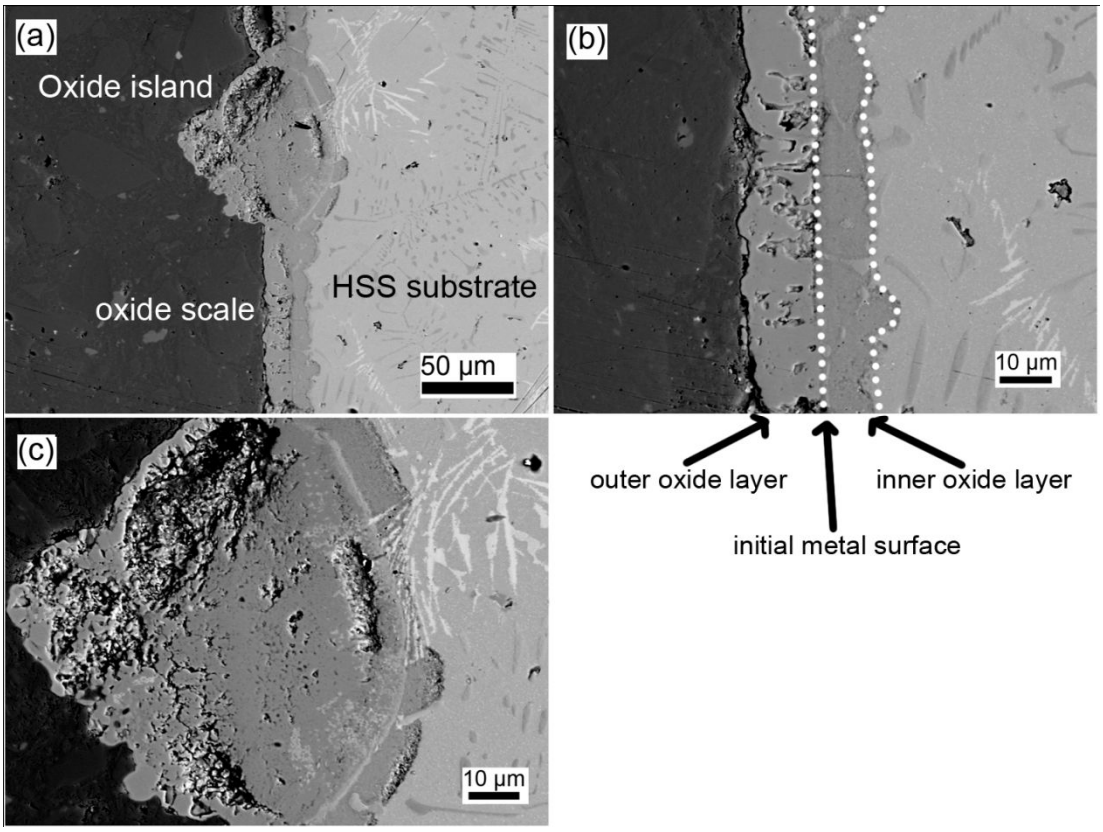

Fig. 5.4 Backscattered electron (BSE) image of oxide scale formed on a HSS sample after oxidation at 700 ^{o}C for 120 min in dry air. (a) an overview of oxide scale, (b) a higher magnified BSE image of oxide scale formed on the HSS sample matrix shown in (a), (c) a higher magnified BSE image of oxide island shown in (a).

Fig. 5.5a shows the AFM image of typical indents on the cross section of oxide scale at a maximum load 20mN. Figs. 5.5b, 5.5c, and 5.5d show the individual residual indent on the HSS matrix, and the inner and outer layers of oxide, respectively. It can be seen that the size of the indents decreased from the HSS matrix to inner

oxide layer and further to outer oxide layer. By comparing the two indents on the inner layer and outer layer, it can easily be seen that the indent on the outer layer is much smaller than that on the inner layer. Another significant feature is that the indent on the outer layer has curved edges, while the edges of the indent on the inner layer are straight.

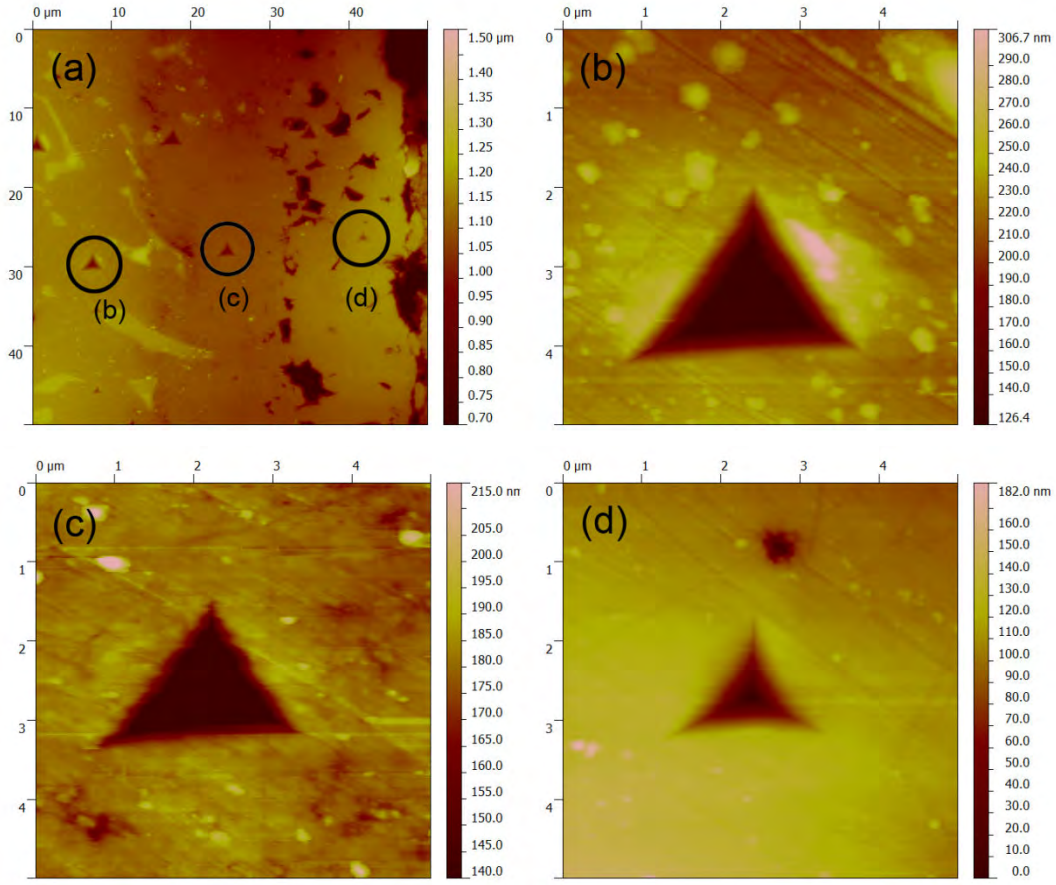

Fig. 5.5 (a) Typical AFM image of nano-indentations across the HSS substrate to oxide scale at 20mN, (b) Higher magnified AFM image of the residual indent on the HSS substrate, (c) Higher magnified AFM image of residual indent on the cross section of the inner oxide layer, (d) Higher magnified AFM image of residual indent on the cross section of the outer oxide layer.

Fig. 5.6 shows the plots of the indentation depths on the HSS matrix, the inner and the outer oxide layers. It can be seen that the pile up on the edge of the indent only appears significantly on the indentation on the HSS matrix. By disregarding the pile up, we found that the indent on the HSS matrix was approximate 0.22µm at 20mN. The indents on the oxide scale were smaller, about 0.17µm deep on the inner oxide

layer and 0.12µm deep on the outer layer.

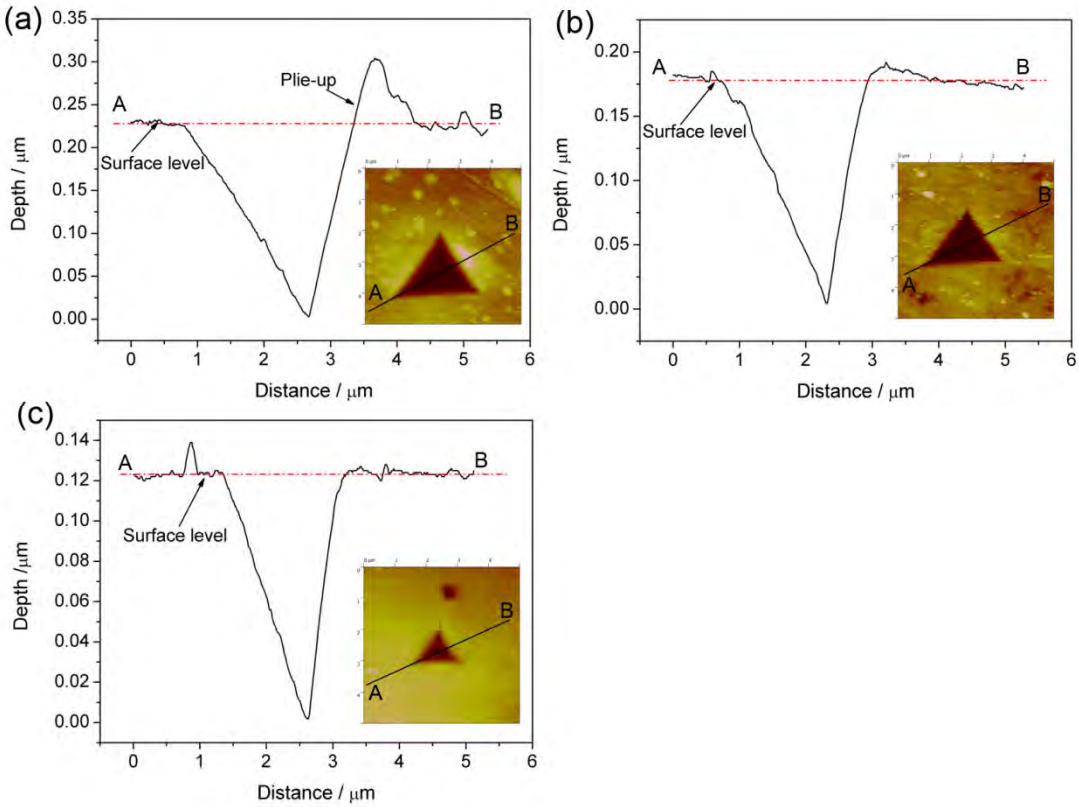

Fig. 5.6 (a) Indentation depth on HSS matrix at 20 mN; (b) indentation depth on the inner oxide layer at 20 mN; (c) indentation depth on the outer oxide layer at 20 mN.

Fig. 5.7a shows the plots of the load-displacement curves of the three nano-indentations shown in Fig. 5.5. It can be seen that the indent on the HSS matrix has the deepest indentation at peak load, followed by the indent on the inner layer. The indent on the outer oxide layer has the shallowest indentation. Fig. 5.5b shows that the HSS matrix has the largest Young's modulus of 285GPa, followed by the outer oxide layer of at 240GPa, and the inner oxide layer at 140GPa. Fig. 5.5c shows the hardness of these three different regions. The hardness of the oxide scale is greater here than the HSS matrix. The HSS matrix is less than 9GPa, the inner oxide layer is 9.64GPa, and the outer oxide layer is 16.22GPa. In order to study the difference between the inner and the outer oxide layers, two TEM thin-foils were taken out of the oxide scale by means of FIB. Fig. 5.8 shows the locations of the FIB operations on the oxide scale.

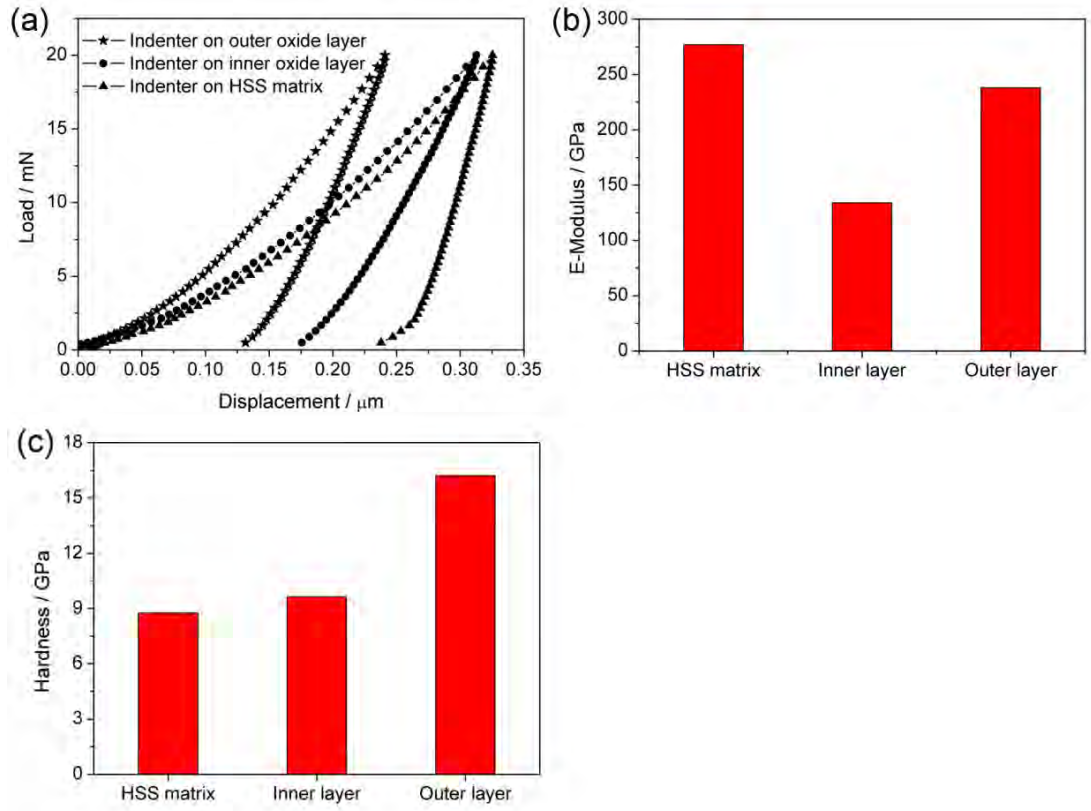

Fig. 5.7 (a) the plots of typical load-displacement curves of indentations on HSS substrate, inner and outer oxide layers at 20mN, (b) Young's modulus on the three different regions in a HSS sample, (c) nano-hardness on the three different regimes in a HSS sample.

Fig. 5.9a shows the TEM bright field image of the inner oxide layer where the inner layer consists of fine grained oxide crystals and fine pores. Fig. 5.9b shows the higher magnification image of the inner oxide layer showing that the oxide crystals are less than 200nm in size. Figs. 5.9c and 5.9d show the location of the nano-indentation on the inner oxide layer and diffraction patterns of the locations directly beneath the indent (mark "A") and far away from the indent (mark "B"). The diffraction patterns confirmed that the inner oxide layer consists of fine polycrystalline (Fe_3O_4, Cr_2O_3, (Fe, Cr)-rich oxides). And it also shows that two diffraction patterns are the same, which indicates that the nano-indentation test has not affected the crystal structure of the inner oxide layer.

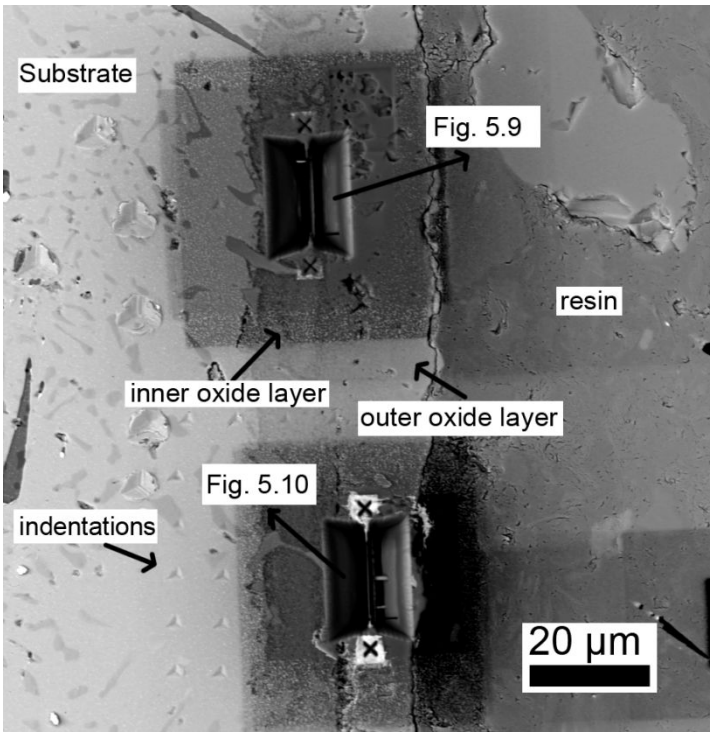

Fig. 5.8 Secondary electron (SE) image of cross-section of oxide scale which indicates the locations of FIB operation.

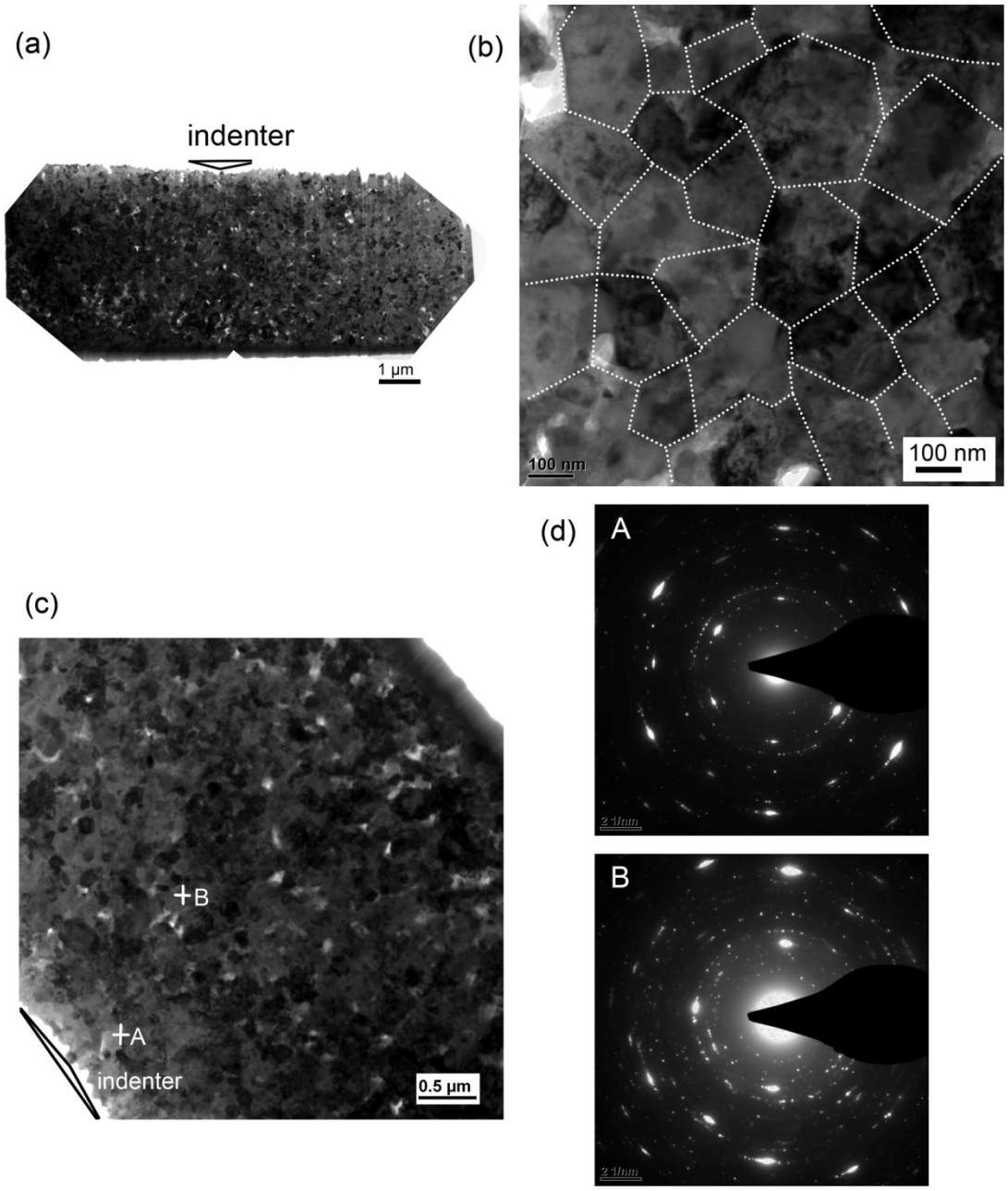

Fig. 5.9 (a) Overview of TEM bright field image of FIB cross-section of the inner oxide layer, (b) higher magnified TEM bright field image indicating the very fine crystalline structure of the inner oxide layer, (c) TEM bright field image of the region the inner oxide layer under the indent, (d) Diffraction patterns of locations “A” and “B” labelled in (c), “A” refers to the location directly underneath the indent, “B” refers to the location far away from the indent.

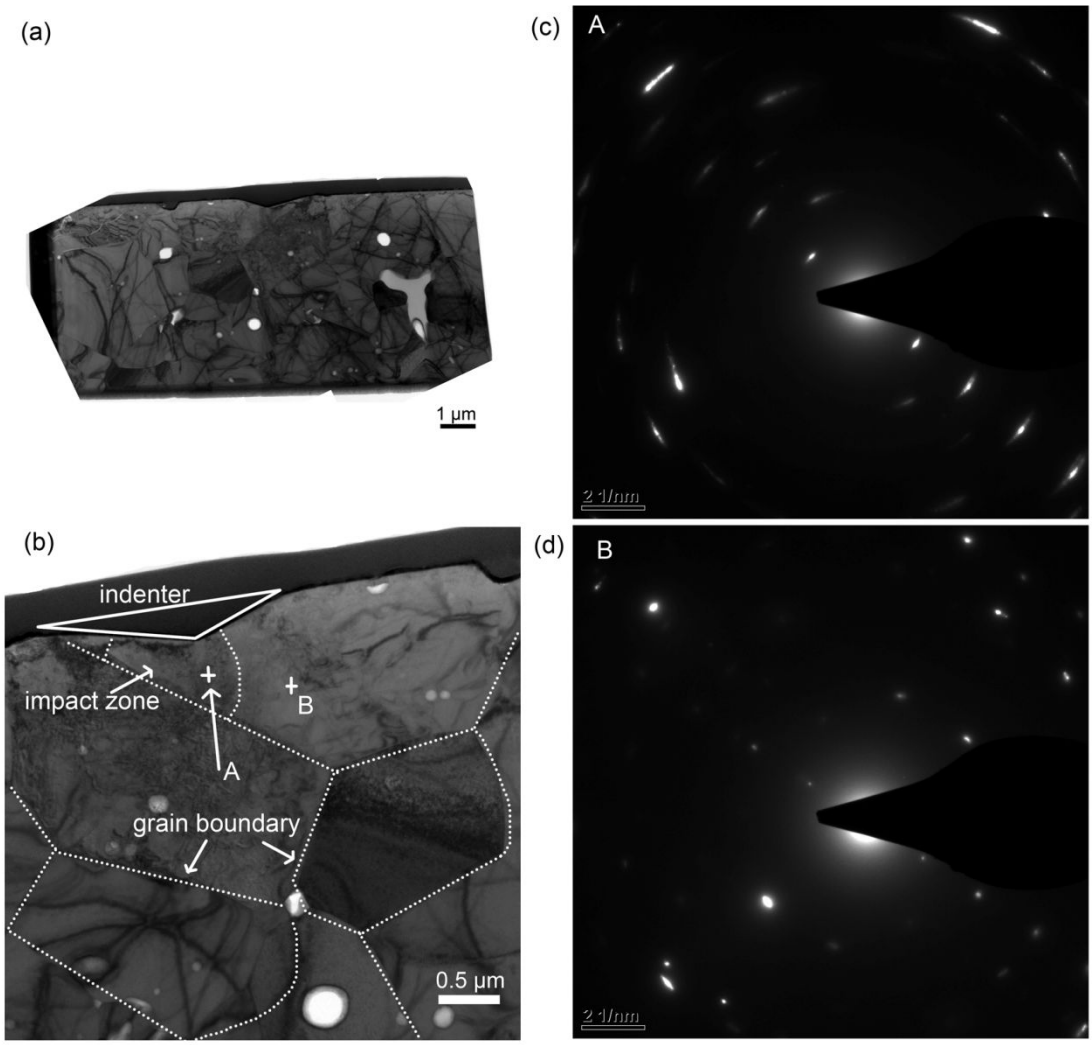

Fig. 5.10 (a) Overview of TEM bright field image of FIB cross-section of outer oxide layer, (b) higher magnified TEM bright field image indicating the large crystalline structure of the outer oxide layer and the location of the indent, (c) Diffraction patterns of locations "A" and "B" labelled in (b), "A" refers to the location directly underneath the indent, "B" refers to the location far away from the indent.

Fig. 5.10a shows the TEM bright field image of the outer oxide layer where the microstructure of the outer layer is quite dense although there are some large pores in the outer layer. Fig. 5.10b indicates the location of nano-indentation on the outer oxide layer and size of the oxide crystals (i.e. Fe_2O_3 grains). Compared to the oxides in the inner layer, the average size of the oxide crystals in the outer layer is over 2µm, which is approximately 10 times greater than in the inner layer. The figure indicates that the nano-indentation was actually performed on a specific oxide crystal in the outer oxide layer. Figs. 5.10c and 5.10d show the diffraction patterns of the

locations directly underneath the indent (cross “A”) and far away from the indent (cross “B”). The diffraction patterns show that locations “A” and “B” have the same crystal structure, which confirms that locations “A” and “B” are on the same oxide crystal. However, the elongated patterns shown in Fig. 5.10c indicating that a strain exists in location “A,” means that a plastic deformation has happened in this area on the oxide crystal.

Table 5.2 summarises the results of Young’s modulus and hardness of the inner and outer oxide layers obtained from the nano-indentation tests at 20mN. Generally the outer oxide layer has a higher Young’s Modulus and hardness than the inner layer, although there is a significant variation in the indentations on the outer oxide layer, as it can be seen that the minimum Young’s modulus and hardness was just 134.3GPa and 4.4GPa while the maximum Young’s modulus and hardness reached 239.1GPa and 16.2GPa, respectively.

Table 5.2 Young’s modulus and hardness of the inner and outer oxide layers (in dry air at 20mN).

	Young’s modulus / GPa	Hardness / GPa
Inner oxide layer	134.1	9.6
	178.1	9.6
	142	11.1
	133.4	10.8
	183.4	13.4
Outer oxide layer	238.1	16.2
	239.1	16.2
	219.2	13.1
	134.3*	4.4*
	194.1*	8.1*

The values with * correspond to the indentation locations on the pores in the oxide scale.

Fig. 5.11 shows the AFM image of nano-indentations on the HSS matrix/oxide scale interface where the residual indents on the interface are much larger than those on the HSS matrix, or the oxide scale. Fig. 5.11b shows the typical feature of a residual indent on the HSS matrix/oxide scale interface, indicating that cracks are

propagating from the indent. Fig. 5.12 shows the Young's Modulus and hardness of the HSS matrix/oxide scale interface obtained by the nano-indentation tests at 10mN. The results show that the hardness of the interface was approximately 2GPa, which is much lower than the HSS matrix and oxide scale (Table 5.1 and Table 5.3). Table 5.3 summarises the results of Young's modulus and the hardness of the inner and outer oxide layers obtained from the nano-indentation tests at 10mN. Compared to the results obtained at 20mN (Table 5.2), it can be seen that the results obtained at two different normal peak loads are consistent with each other.

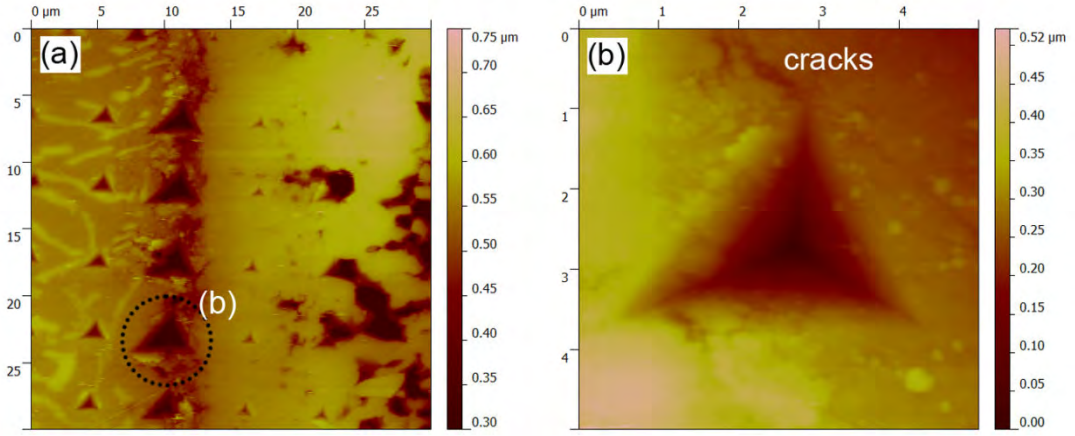

Fig. 5.11 (a) AFM image of nano-indentations from HSS matrix to cross sectional oxide scale at a maximum normal load of 10 mN; (b) higher magnified AFM of indent on the HSS matrix/oxide interface.

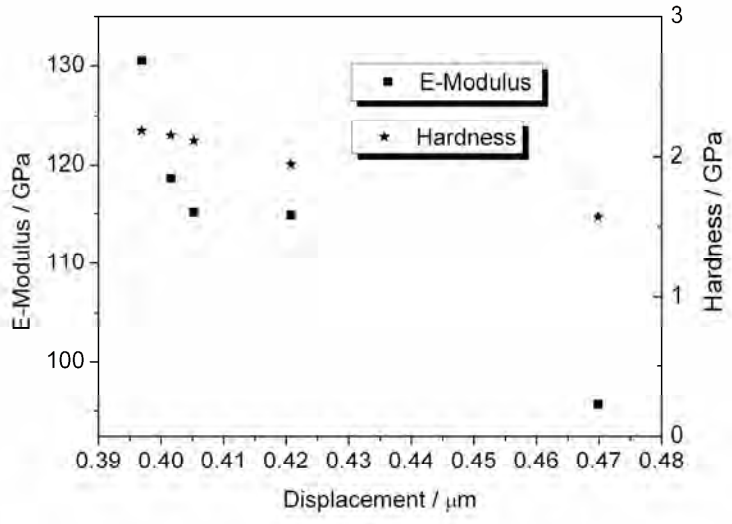

Fig. 5.12 Young's modulus and hardness of the HSS substrate/oxide interface obtained from the nano-indentation tests.

Table 5.3 Young's modulus and hardness of inner oxide layer and outer oxide layer (in dry air, at 10mN).

	Young's modulus / GPa	Hardness / GPa
Inner oxide layer	141.1	8.5
	189.2	11.7
	210.8	13.1
	180.4	10.7
	163.7	8.8
Outer oxide layer	213	14.1
	231.4	13.6
	189.9*	8.2*
	258.1	15.1
	234.6	16.4

The values with * correspond to the indentation locations on the pores in the oxide scale.

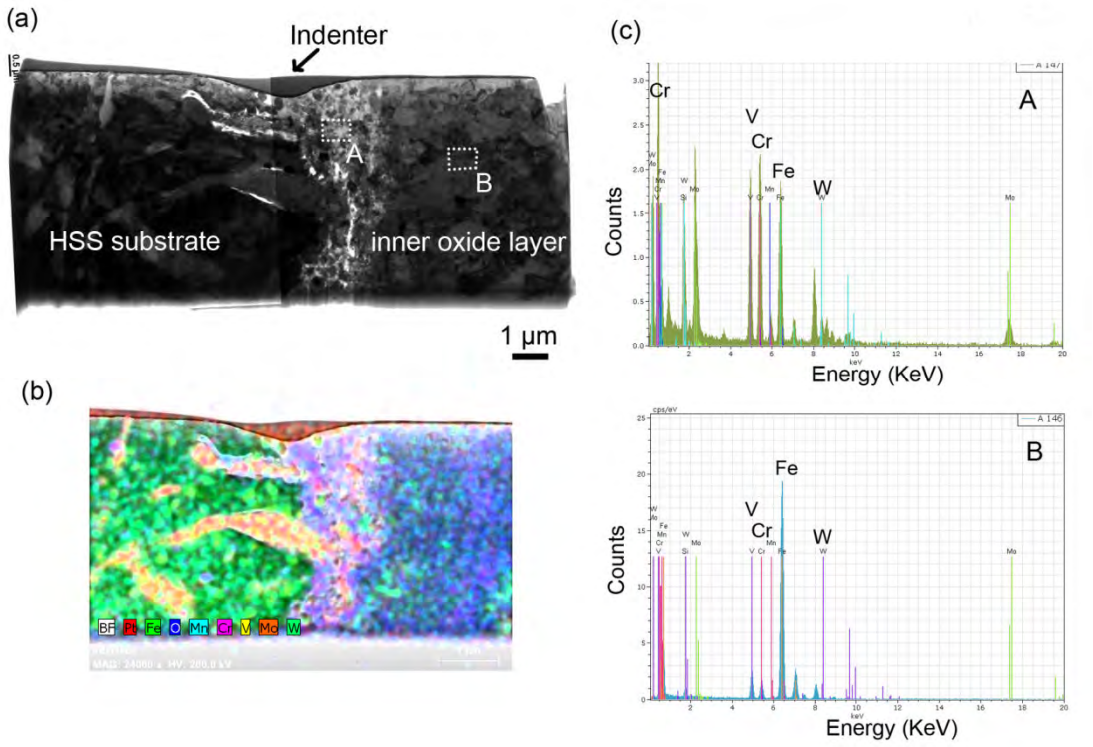

Fig. 5.13 (a) TEM bright field image of FIB thin-foil of HSS matrix/oxide interface; (b) TEM/X-ray mapping on the HSS matrix/oxide interface; (c) EDS spectra of areas "A" and "B" labelled in (a).

Fig. 5.13a shows the TEM bright field image of the cross section of the HSS matrix/oxide scale interface and location of the indentation on the interface where micro-cracks are visible on the interface. Fig. 5.13b shows the TEM/X-ray mapping of

the HSS matrix/oxide scale interface indicating that the Cr element in the interface is rich. Fig. 5.13c shows the EDS patterns of the HSS matrix/oxide scale and the inner oxide layer. The results show that the inner oxide layer and the interface consist of Cr-Fe oxides, and the concentration of Cr elements on the interface is much higher than in the inner oxide layer.

As shown in Fig 5.4, oxide islands existed on the original V-rich carbide region after oxidation. Fig. 5.14a shows the AFM image of nano-indentations on the oxide island at 5 mN. The AFM image reveals that the microstructure of the oxide island is similar to the oxide scale on the HSS matrix, and the inner oxide layer consists of fine-grained crystals and fine pores and the outer layer consists of large oxide crystals and large pores. Fig. 5.14b and 5.14c show the typical residual indents on the inner and outer oxide layers, respectively. It can be seen that the size of indent on the inner oxide layer is approximately 1.25μm and 0.7μm on the outer layer. The load-displacement curves of nano-indentations at 5mN on the inner oxide layer are shown in Fig. 5.15a and the Young's modulus and hardness obtained from the nano-indentations are shown in Fig. 5.15b. It can be seen that the maximum indentation depth on the inner oxide layer was kept at 0.15μm, although a few indentations approached 0.2μm. The Young's modulus of the inner oxide layer was 130 to 150GPa and its hardness was 8 to 9GPa. The maximum nano-indentation depth on the outer oxide layer was less than on the inner layer. The depth was approximately 0.11μm, Young's modulus was 210 to 230GPa, and the hardness from 13.5 to 16GPa. Compared to the results shown in Table 5.2, the oxide island has the same mechanical properties as oxide scale formed on the HSS matrix.

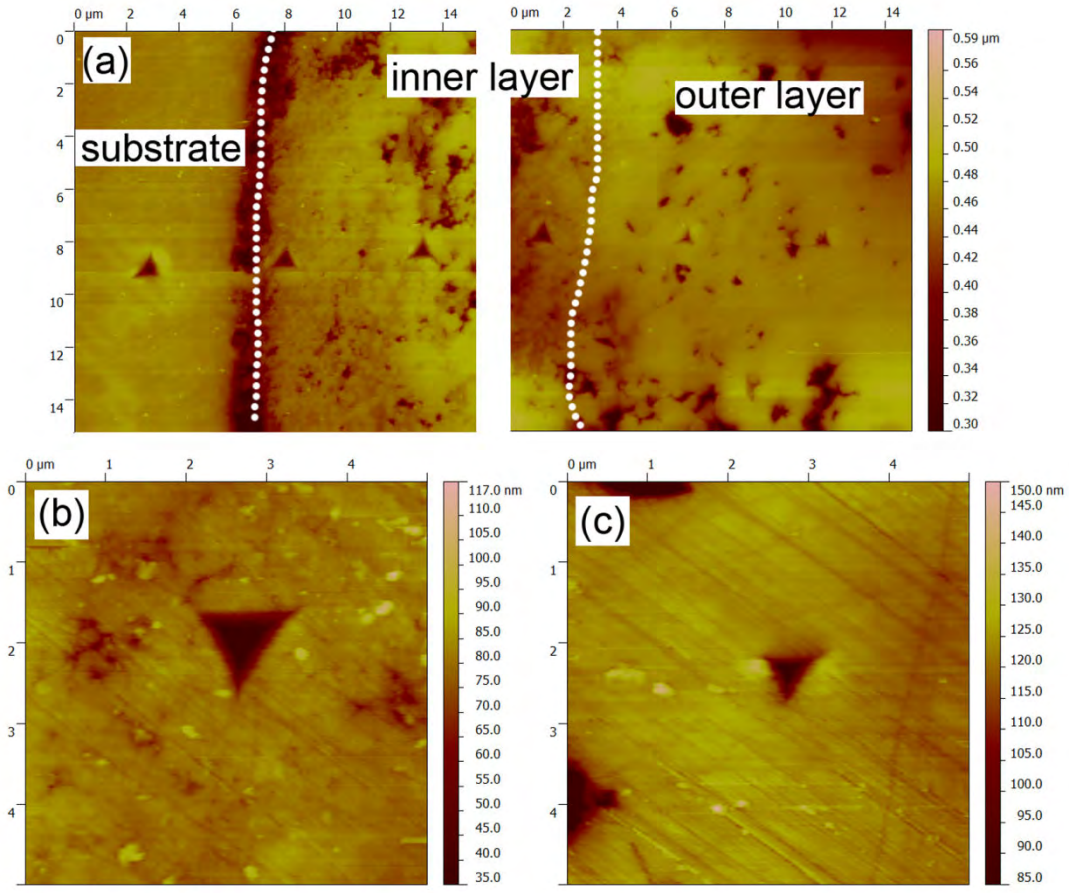

Fig. 5.14 (a) AFM images of nano-indentation from HSS matrix to oxide scale of oxide island at 5mN, (b) higher magnified AFM image of indent on the inner layer, (c) higher magnified AFM image of indent on the outer layer.

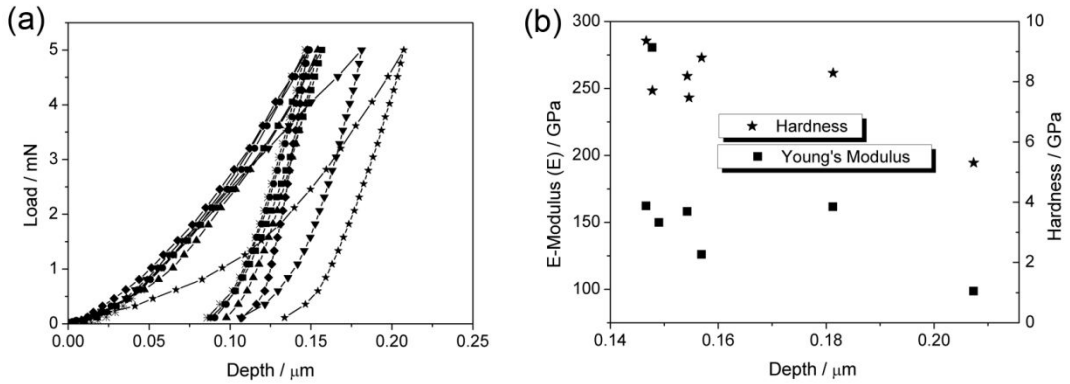

Fig. 5.15 (a) plots of load-displacement curves on inner oxide layer of oxide island at 5mN, (b) Young's modulus and hardness of inner oxide layer of the oxide island obtained by nano-indentation test at 5 mN.

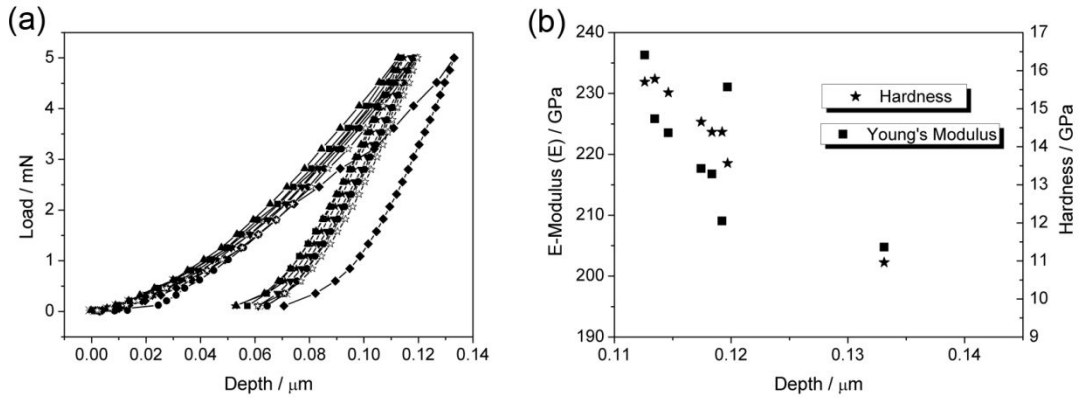

Fig. 5.16 (a) plots of load-displacement curves on inner oxide layer of oxide island at 5mN, (b) Young's modulus and hardness of inner oxide layer of the oxide island obtained by nano-indentation test at 5 mN.

5.2.2 Indentations on oxide scale formed in 12.5% H_2O humid air

Fig. 5.17 shows the AFM image of nano-indentations on the cross section of the oxide scale formed in 12.5% H_2O humid air. Although the previous investigation indicated that the oxide scale formed in 12.5% H_2O humid air had exactly the same microstructure as that formed in dry air, water vapour in the atmosphere increased the oxidation rate of the high speed steel. However, the microstructure of the oxide scale contained more defects such as cracks and pores than that in dry air. Table 5.4 shows the Young's modulus and hardness of the oxide scale formed in 12.5% H_2O humid air. It can be seen that the outer oxide layer generally has a higher Young' modulus and hardness than the inner layer has, although there are significant variations between the values. Compared to the oxide scale formed in dry air (Table 5.2, Table 5.3, Figs. 5.15, and 5.16), the mechanical properties of the oxide scale formed in the 12.5% H_2O humid air has lower values.

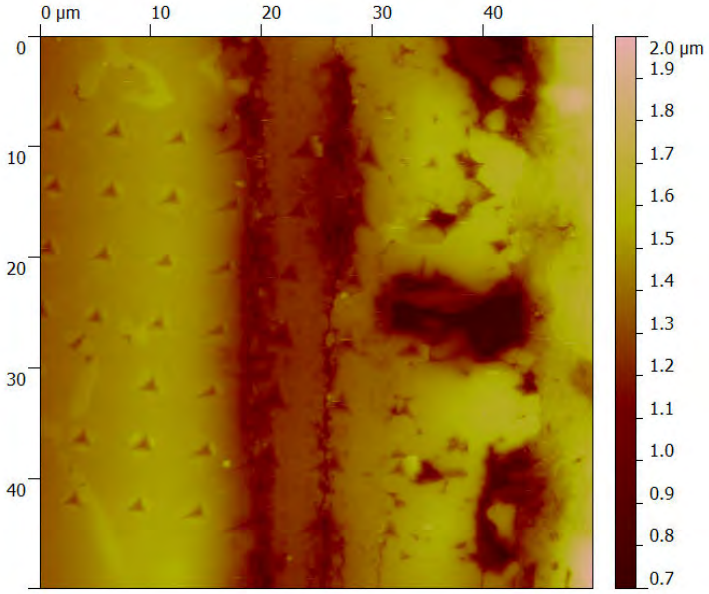

Fig. 5.17 AFM image of nano-indentations on the cross-section of the oxide scale formed in 12.5% H_2O humid air at 10mN.

Table 5.4 Young's modulus and hardness of inner oxide layer and outer oxide layer (in 12.5% H_2O humid air).

	Young's modulus / GPa	Hardness / GPa
Inner oxide layer	91.9	6.9
	115.4	8.9
	92.6	7.9
	76	3
	81.1	3.3
Outer oxide layer	170.1	7.2
	96.9*	3.5*
	142.2	5.2
	116.1*	5.3*
	205.5	8.8

The values with * correspond to the indentation locations on the pores in the oxide scale.

5.3 Discussion

The UMIS nano-indentation system was calibrated on a standard fused silicon sample at loads ranging from 2 to 30mN (as seen in Appendix A). After the calibration the obtained mechanical properties, i.e., Young's modulus and hardness, were consistent when the peak load was kept between 2 to 30mN. Therefore, it is

believed that the results obtained from the nano-indentation tests, and afterwards on the HSS samples, are reliable when the peak load is between 2 to 30mN.

The nano-indentation tests performed on the HSS sample revealed how carbides increased the hardness in the matrix. The hardness and Young's modulus obtained from the nano-indentation tests at three different maximum normal loads tended to be consistent, although the results varied due to the influence of a soft HSS matrix when a relative small indentation load was used. Young's modulus and hardness of the HSS matrix obtained from the nano-indentation tests in this study are approximately 270GPa and 9GPa (equal to 66HRC or 900HV), respectively. Compared with 210-230GPa and 61-65HRC (740-850HV) presented in previous research papers [159-162], the mechanical properties of the HSS matrix obtained in this work are a slightly higher. This was probably due to the Oliver and Pharr method (O & P method) used to calculate the Young's modulus and hardness in UMIS nano-indentation system. It should be noted that the Oliver and Pharr method was only developed for monolithic materials and the modified contact area function was only established for sink-in phenomenon [163]. From the indentation images (Fig. 5.1) and the plots of indents (Fig. 5.6), it can be confirmed that pile-up happened at the edge of the indent on the HSS matrix after nano-indentation. This resulted in an over estimation of the hardness and elastic modulus and an under estimation of the contact area. The hardness of MC and M_2C/M_7C_3 carbides in the HSS matrix obtained from the nano-indentation are around 21GPa and 13GPa, respectively (Table 5.1). Compared to the other previous works [159-161] which indicate that the hardness of MC is 25.5-30.6GPa and M_2C/M_7C_3 12.2-20.4GPa, the results here are smaller but still in a reasonable range. The reason why the carbides measured from the test are not as hard may be due to the soft, surrounding HSS matrix.

The nano-indentations on the cross section of the oxide scale formed on the HSS sample in dry air revealed the different mechanical properties between the inner and outer oxide layers. The results showed that the hardness of the both oxide layer

is higher than the HSS matrix and less than the carbides in the HSS samples, while Young's modulus of both layers is less than the HSS matrix and more less than the carbides.

From the oxidation investigation in Chapter 4, it has been known that the oxide scale formed on the HSS sample consists of two oxide sub-layers. The outer layer consists of large columnar grains of iron oxide (Fe_2O_3) and the inner layer consists of fine-grained Fe_3O_4, Cr_2O_3 and $(Fe, Cr)_2O_3$-spinel oxides. The microstructure of these two sub-layers can be observed in detail in Figs. 5.9 and 5.10. The residual indent size on the outer oxide layer at 20mN is around 1.5µm (Fig. 5.5d and Fig. 5.9b), while the average size grain of the iron oxides in the outer layer is more than 2µm (Fig. 5.9b). Hence, the indentations on this layer are more likely to land on a single grain of oxide, as shown in Fig. 5.18a. Although there is a large variation in the results of the nano-indentation on the outer oxide layer, as shown in Table 5.2, the Young's modulus and hardness of the outer oxide layer are between 200-240GPa and 13-16GPa, respectively. The results are similar to Schütze's work where he reported that Young's modulus of a single crystal of Fe_2O_3 is 220GPa [164]. The TEM image (Fig. 5.9a) also showed a number of large pores existing in the outer oxide layer. The nano-indentations on these locations are very close to these large pores (as seen in Fig. 5.18b), where the obtained results will be affected significantly. This is why some very low Young's modulus and hardness were obtained on the outer oxide layer (as shown in Table 5.2).

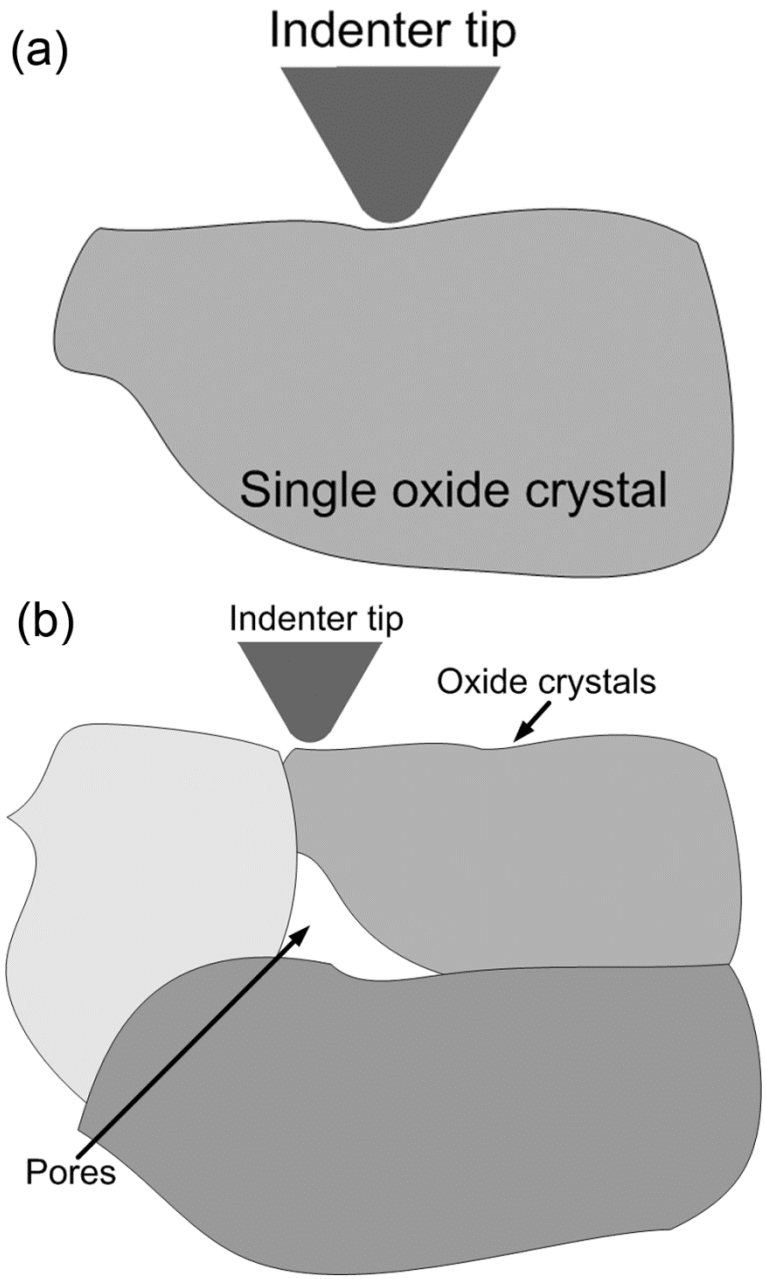

Fig. 5.18 Schematic illustration of nano-indentation on the outer oxide layer. (a) An indentation on a single oxide crystal, (b) an indentation on the location close to pores and grain boundary.

The Young's modulus and hardness of the inner oxide layer is between 130-180GPa and 9-11GPa, respectively. The residual indent size on the inner oxide layer at 20mN is approximate 2.5μm. Compared to the size of fine-grained oxides (<200 nm) in the inner oxide layer, the indentations on this layer are similar to indentations on sintered composites, as shown in Fig. 5.19. The results of the indentations are more sensitive to the porosity, grain size, grain boundaries, and binding energies among

the oxides. Young's modulus of a single crystal of Fe_3O_4, Cr_2O_3 and $FeCr_2O_4$ are 220, 280, and 233GPa, respectively [164]. But Young's modulus of the inner oxide layer is much lower than these values. It is believed that nano-indentation on the inner oxide layer well reveals the mechanical properties of the inner oxide scale instead of the single oxide crystals in [164].

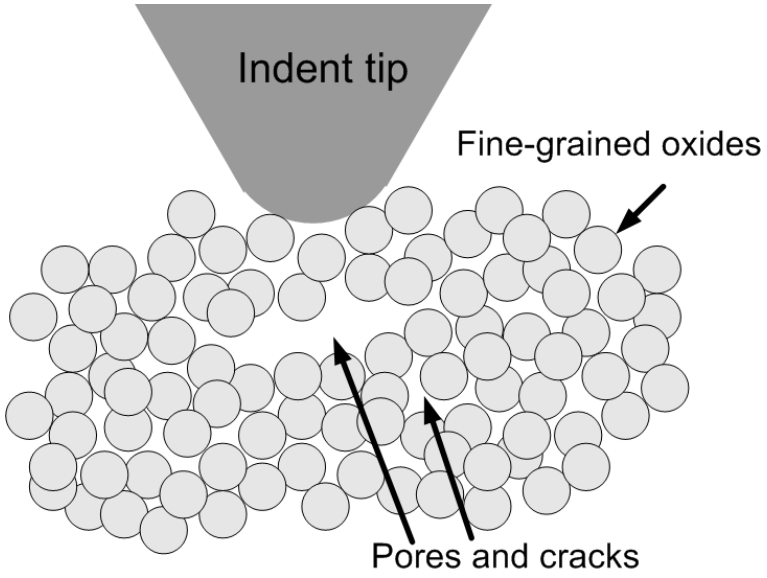

Fig. 5.19 Schematic illustration of nano-indentation on the inner oxide layer.

The difference in Young's modulus and hardness between the inner and outer oxide layers is not only because of the different oxide phase compositions, but more importantly due to the huge difference in the size of the oxide crystal (oxide grains in the outer layer is more than 10 times larger than those in the inner layer). The hardness of both the inner and outer oxide layer obtained by the nano-indentations is higher than the HSS matrix, which indicates that the oxide scale protects the material from wear. However, the results of nano-indentations on the HSS matrix/oxide scale interface (Figs. 5.11 and 5.13) indicate a weak binding between the oxide scale and the HSS substrate. This may cause the oxide scale to peel off from the HSS roll surface due to shear force during hot rolling.

The nano-indentations on the oxide scale formed in 12.5% H_2O humid air showed that the mechanical properties of the oxide scale are less than those of the oxide scale formed in dry air. The previous investigation indicated that the oxide scale

formed in humid air has exactly the same phase composition and microstructure as that formed in dry air. The water vapour in the atmosphere increases the oxidation rate of the HSS sample and promotes defects such as cracks and pores in the microstructure of the oxide scale. These defects significantly weaken the mechanical properties of the oxide scale.

5.4 Conclusions

Nano-indentation tests were successfully performed to investigate the mechanical properties of the HSS sample, and oxide scales formed in both dry and 12.5% H_2O humid air. The following conclusions were obtained in this work:

The nano-indentation tests on the HSS sample revealed that the hardness of MC carbides, M_2C/M_7C_3 carbides, and HSS matrix are approximate 21, 13, and 9GPa, respectively. The huge difference in hardness between the carbides and the HSS matrix indicated that adding carbides significantly enhance the wear resistance of the HSS sample.

The nano-indentation tests on the cross section of oxide scale well revealed the different mechanical properties of the inner and outer sub-layers. Young's modulus and hardness of the inner oxide layer is between 130-180GPa and 9-11GPa, respectively. Young's modulus of the outer oxide layer is from 200-240GPa and the hardness is from 13-16GPa. The difference in Young's modulus and hardness between the inner and outer oxide layers is due to the very different oxide phase composition and microstructures of these two sub-layers. The average size of the columnar iron oxide (Fe_2O_3) grains in the outer layer is more than 2μm while the fine-grained Fe_3O_4, Cr_2O_3 and $(Fe, Cr)_2O_3$-spinel oxides in the inner layer are less than 200nm. The nano-indentations on the outer oxide layer are more likely to land on a single crystal, while the nano-indentations on the inner oxide layer are more similar to indenting sintered fine-grained composites. The hardness of the HSS matrix/oxide scale interface (Figs. 5.10 and 5.11) is only 2GPa, which is much lower

than the HSS matrix and oxide scale, which indicates a weak binding between the oxide scale and the HSS substrate. The mechanical properties of the oxide scale formed in 12.5% H_2O humid air are less than those formed in dry air because there are more defects in the microstructure.

Chapter 6
Influence of oxides on tribological behaviour by a pin-on-disc test

In hot rolling, a superficial oxide scale forms on the work rolls due to the thermal cyclic working conditions. This oxide scale plays a major role in hot rolling because it allows for the starting and driving of metal sheet between the rolls [14, 164]. Under thermo-mechanical working conditions this scale grows to a critical thickness and then deteriorates and causes damage by inlaying and breaking down on the surfaces of rolled product and tools. The wear mechanisms of the work rolls in hot rolling are well known, i.e. thermal fatigue, abrasion, adhesion and oxidation. However, little attention has been given to the oxidation of rolling-mill roll surface and its effects on the tribological behaviour [112]. The tribological behaviour of oxides is very complex. It could be abrasive and therefore detrimental, or be lubricated and form a protection against wear, either way it is influenced by the nature and physical properties of the oxide scales into which it makes contact [109, 166-168].

Disc-on-disc configuration, one simulating the hot strip, the other one simulating the roll, has often been used to study the wear of the hot rolls [4, 8, 10, 12, 68, 99, 104-108]. However, the aim of this study is to identify the role of oxide scale on the tribological behaviour. The tribological properties are strictly system-dependent and have been clearly correlated to the ability of the contact surfaces towards the formation, accumulation, agglomeration and sintering of wear particles [108, 111]. From this point of view the choice of a conformal contact (pin-on-disc) rather than a non-conformal contact (disc-on-disc) is more suitable. In this chapter a pin-on-disc configuration was used to simulate the contact established between a HSS work roll and a hot strip material in hot rolling. This work only focus on the contact of oxide scale in the roll bite, therefore only the sliding part of the motion was considered

and the rolling part omitted. Although the operating conditions of tests are rather different from industrial rolling conditions, the testing temperature was close to the rolling temperature, the Hertzian pressure was similar to the contact pressure and the sliding speeds were close to those in the rolling bite. The coefficient of friction was monitored and recorded in-situ during the tribological tests. SEM and TEM techniques were used to characterise the morphologies and micro-structures of the contact zones on the surface of the pin.

6.1 Experimental

The pin-on-disc tests were carried out on the CETR tribometer. This device is not a hot rolling simulator, but this laboratory apparatus may give an understanding of the oxidational wear mechanism involved in hot rolling [110]. In a pin-on-disc configuration, the pin represents the HSS roll grade material (chemical composition listed in Table 4.1) and the disc represents a strip steel (Fig. 6.1). The pin is manufactured into a mushroom shape with a 3mm radius hemispherical end (Fig. 6.1). The chemical composition of the disc is given in Table 6.1.

Table 6.1 Chemical composition of the disc material (wt%, analysis by atomic emission spectroscopy).

C	P	Mn	Si	S	Ni	Cr	Mo	Cu	Al
0.215	0.015	0.79	0.34	0.029	0.006	0.020	<0.002	0.014	<0.003

The tribological tests were carried out in the following two steps:

(1) In the first step the disc was heated up to 900 ^{o}C in a heating chamber, while the pin was kept at room temperature outside the heating chamber. A K-type thermocouple was placed underneath the disc to monitor its temperature during the tribological test (Fig. 6.1).

(2) In the second step, when the temperature of the disc reached 900 ^{o}C, the pin was brought into contact with the disc and held for 20 min for pre-oxidation before starting to rotate the disc. The duration of the tribological test was 1 h. A K-type thermocouple was embedded into the pin, approximately 2mm vertical

distant away from the contact (shown in Fig. 6.1) to monitor its temperature during the test. The heating of the disc was not interrupted in order to maintain the high temperature (900 ^{o}C) during the sliding test. After each tribological test, the pin was pulled up out of the heating chamber and cooled in the air.

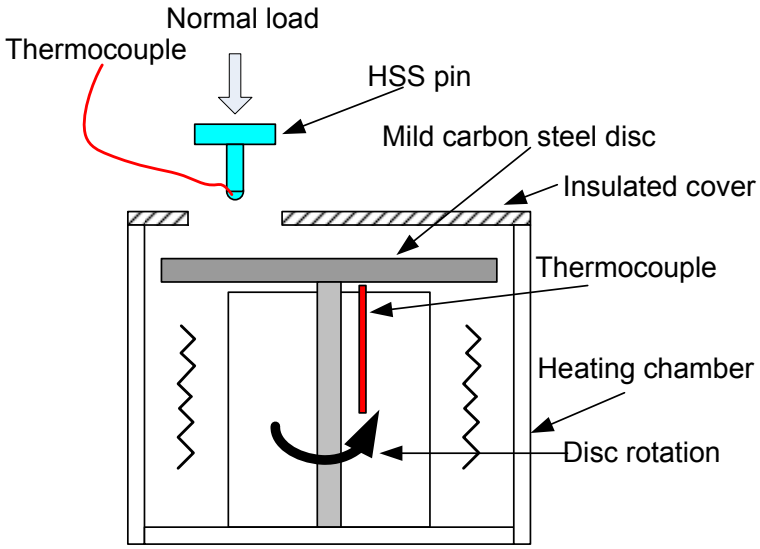

Fig. 6.1 Schematic illustration of a high temperature pin-on-disc test configuration.

Table 6.2 shows the operating conditions of the tribological tests. Test parameters such as the Hertzian pressure were chosen mild and close to the practical rolling conditions in order to observe the behaviour of the antagonistic oxide scales in the contact zone without destroying them too fast. The coefficient of friction was monitored and recorded in-situ during the test. Some interrupted tests were performed to understand the interaction of the oxides corresponding to the evolution of friction coefficient curve during the tests. After the tribological tests, SEM and TEM were used to characterise the morphologies, cross sections, and microstructures of the pin surface at both the contact and non-contact zones.

Table 6.2 Operating conditions of the tribological tests.

Normal load	Hertzian pressure	Sliding speeds	Disc temperature	Testing duration
5N 10 N	650 MPa 825 MPa	0.05 m/s, 0.2 m/s	900 ^{o}C	1 h

6.2 Results

6.2.1 The evolution of coefficient of friction during the test

Fig. 6.2 shows the evolution of temperatures of disc and pin during the tribological tests. It can be seen that the temperature of the disc remained stable at 900 ^{o}C throughout the whole test while the pin quickly reached 660 ^{o}C (less than 300 seconds) after making contact with the hot disc, and then kept at this temperature throughout the test. The pin was pre-oxidised at 660 ^{o}C for approximately 20 minutes before the test started. It should be noted that this monitored pin temperature refers to the location 2mm vertically away from the sliding contact zone.

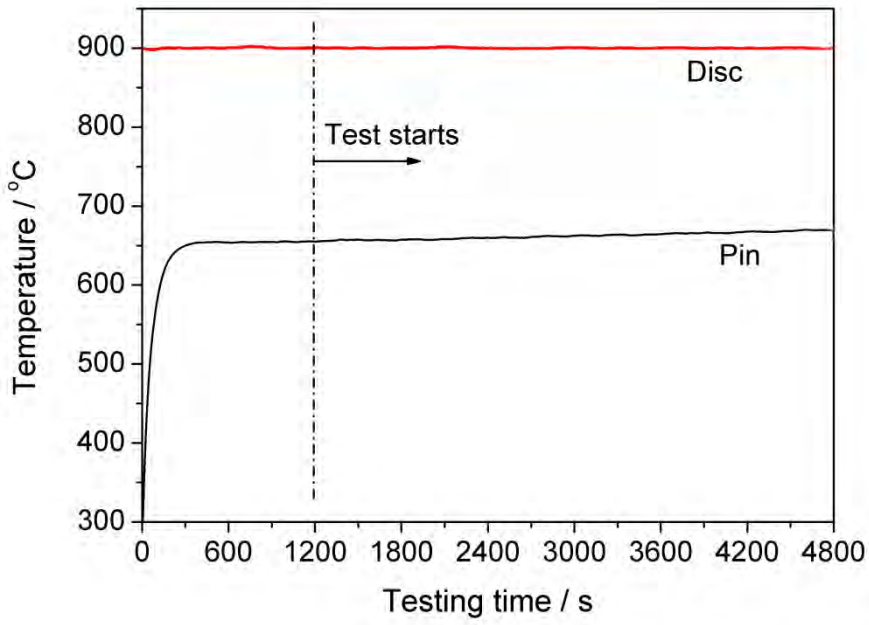

Fig. 6.2 Temperatures of disc and pin surface during a typical tribological test.

Fig. 6.3 shows the evolution of the coefficient of friction under different normal loads (i.e. 5 and 10N) at sliding speed 0.05 m/s. It can be seen that the coefficient of friction decreased from the start of the test and increased for a short time before stabilising for the remainder of the test. However, for the case of 5N, the value of coefficient of friction was gradually increasing from 0.26 to 0.28 during the

stabilising period until the end of the test. While for the case of 10 N, the coefficient of friction quickly stabled at 0.25. The evolution of the coefficient of friction remained similar when increasing the sliding speed from 0.05 m/s to 0.2 m/s, but the values of the coefficient of friction varied at the end of different tribological tests as shown in Table 6.3. It can be seen that a higher normal load leads to a lower coefficient of friction at the same sliding speed and a faster sliding speed leads to a higher coefficient of friction at the same normal load.

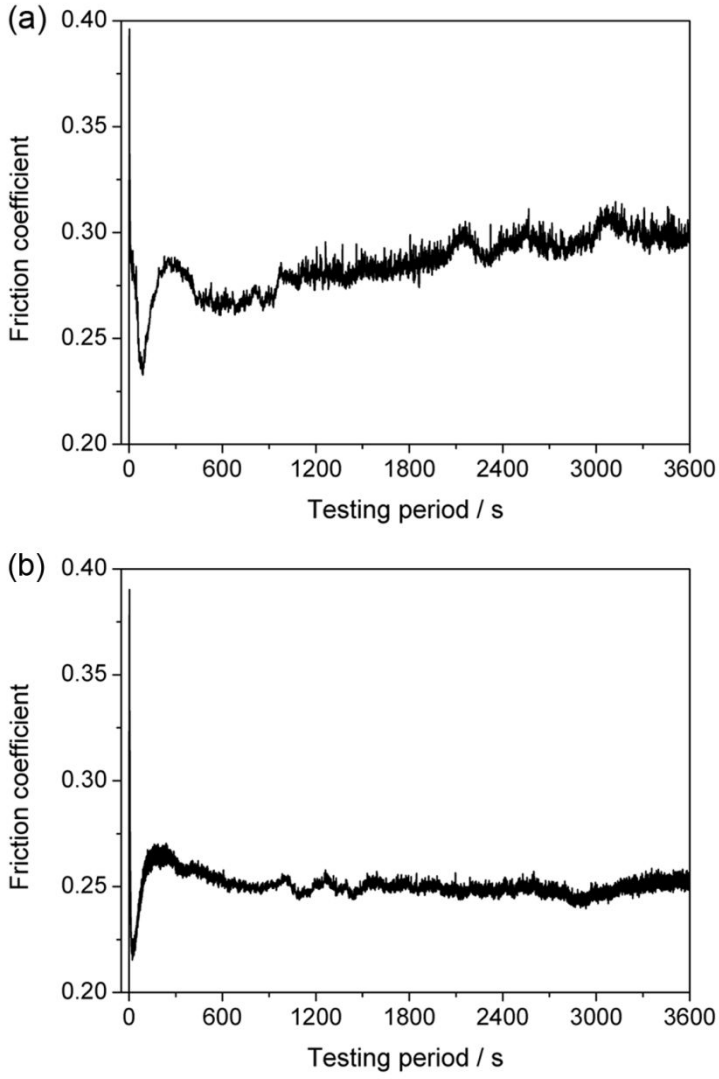

Fig. 6.3 Evolution of the coefficient of friction during the tribological tests. (a) Normal load 5N, and sliding speed 0.05 m/s, (b) normal load 10 N, and sliding speed 0.05 m/s.

Table 6.3 Friction coefficient at the end of the test.

Test conditions	Friction coefficient
Normal load 5N, sliding speed 0.05 m/s	0.280
Normal load 5N, sliding speed 0.2 m/s	0.326
Normal load 10N, sliding speed 0.05 m/s	0.250
Normal load 10N, sliding speed 0.2 m/s	0.306

Fig. 6.4a shows a friction coefficient curve of a typical tribological test under a normal load of 5 N and a sliding speed 0.05 m/s. It can be seen that the friction stabilises in a very short time (less than 300 seconds) from the start of the test and the coefficient of friction remained at approximately 0.26-0.28 for most of the test period. According to the friction coefficient curve, the tribological test can be divided into three stages, as shown in Fig. 6.4b. i) The first one, noted Stage I, corresponds to the start of the friction test when the coefficient of friction decreased, ii) The second one, noted Stage II, corresponds to an increase in the coefficient of friction after the minimum value, iii) the last one, noted Stage III, is the stabilisation step of the friction. To better understand tribological behaviour, two interrupted tribological tests, which have been labelled in Fig. 6.4b, were performed to investigate the evolution of tribological contact mechanisms during the test. The first interrupted test corresponds to the end of stage I (around 90 seconds from the start of the test), the second interrupted test refers to the middle of stage II (around 150 seconds from the start of the test).

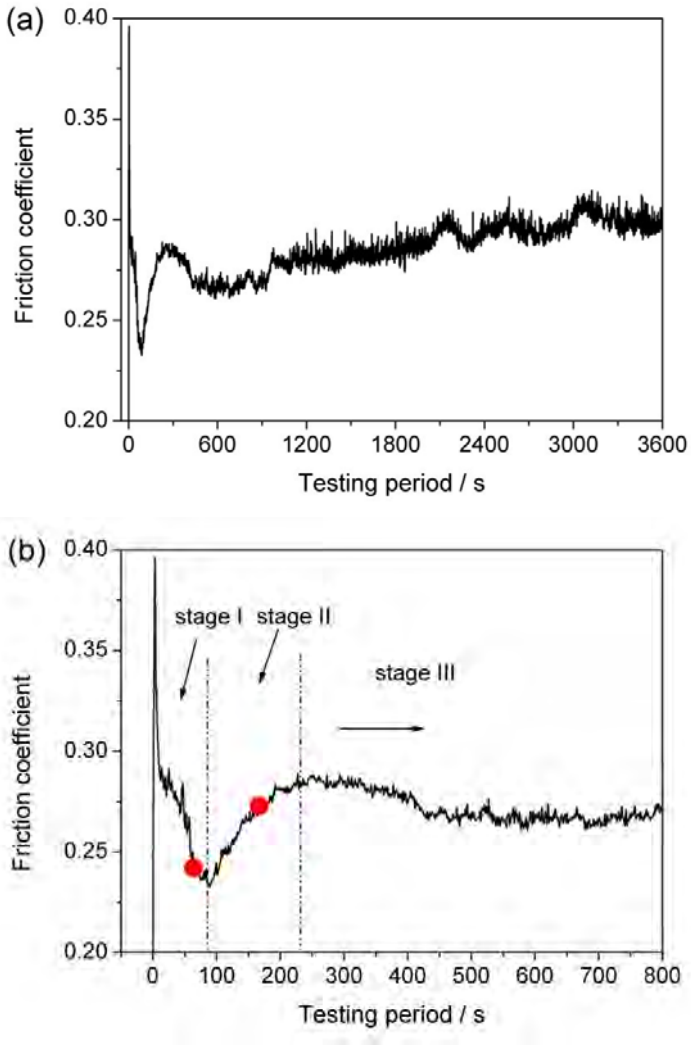

Fig. 6.4 (a) Evolution of friction coefficient during the tribological test with conditions of normal load 5N, and sliding speed 0.05 m/s (reproduced of Fig. 6.3a), (b) three tibological stages and two interrupted points considered in a typical tribological test.

6.2.2 SEM/TEM observations on pin wear track

Fig. 6.5a shows the wear track of the pin surface after the tribological test at a normal load of 5 N and a sliding speed 0.05 m/s for 90 seconds. According to the typical coefficient of friction curve shown in Fig. 6.3, it is near the end of stage I. It can be seen a compact and smooth “glaze” oxide scale covering was visible on the surface of the worn pin after the test (Fig. 6.5a). Fig. 6.5b shows the TEM bright field image of the cross section of the pin wear track where this “glaze” oxide scale was approximate 850 nm thick. The oxide scale was highly compressed because the microstructure of the scale is dense and free of pores. The interface between the

oxide scale and the HSS matrix can be clearly seen, although the bond between the oxide scale and HSS matrix must be good because there are no visible cracks and micro-pores at the interface. Underneath the oxide the HSS matrix has been deformed into the banding crystals in an array and direction consistent with a sliding direction.

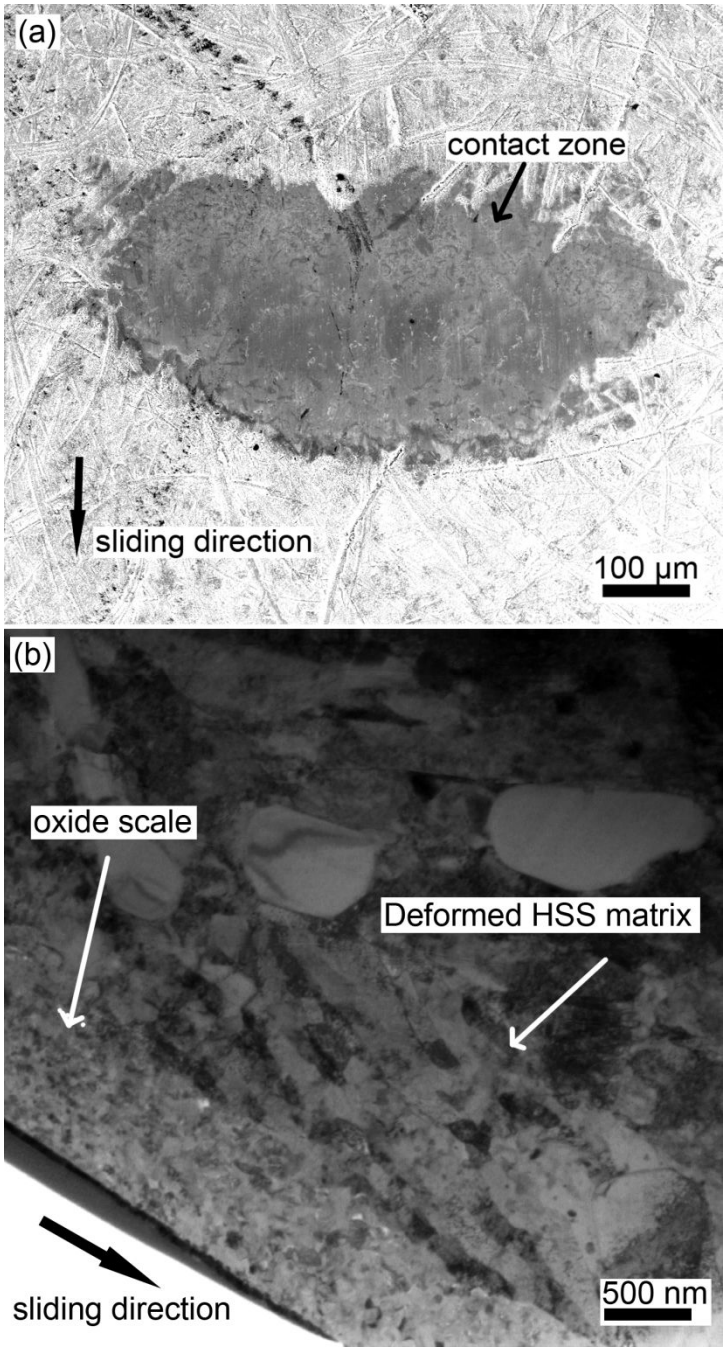

Fig. 6.5 (a) Secondary electron (SE) image of the pin wear track after the tribological test at normal load 5N and sliding speed 0.05 m/s for 90 seconds (in stage I), (b) TEM bright field image of the cross section of the pin wear track, FIB was used to prepare the cross section.

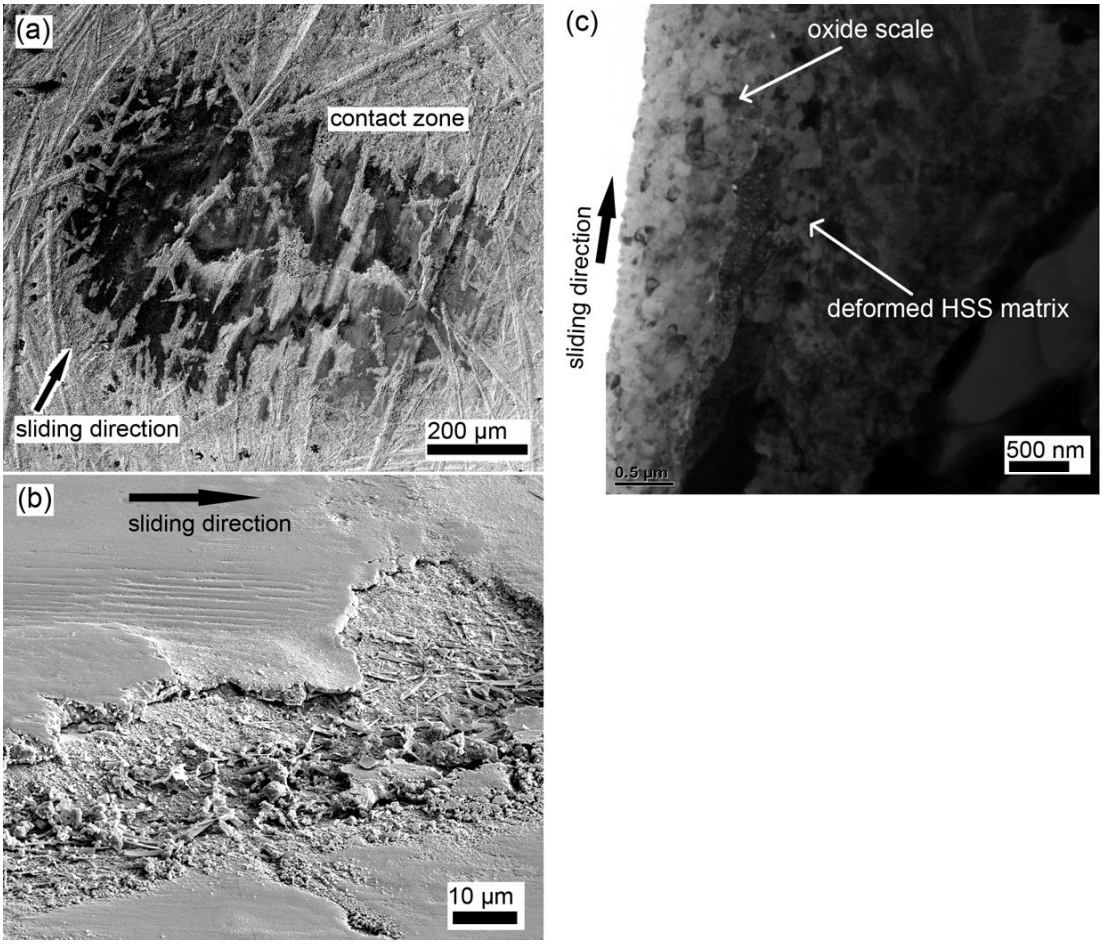

Fig. 6.6 (a) Secondary electron (SE) image of the pin wear track after the tribological test at normal load 5N and sliding speed 0.05 m/s for 150 seconds (in stage II), (b) higher magnified SE image of the pin wear track, the sample is titled 53°, (c) TEM bright field image of the cross section of the pin wear track, FIB was used to prepare the cross section.

Fig. 6.6a shows the wear track of the pin surface after the tribological test at a normal load of 5 N and a sliding speed of 0.05 m/s for 150 seconds (in stage II). The morphology of the surface of the pin is quite different from that at the stage I. A discontinuous "glaze" oxide scale covers the worn surface of the pin. A higher magnification SEM observation on the wear track indicates that the discontinuity of the "glaze" oxide scale was due to the oxide scale spalling in some areas of the sliding contact zone of the pin surface (Fig. 6.6b). In this spallation area the sub-surface of the pin was oxidised again because it had no protection from the oxide scale. Fig. 6.6c shows the TEM bright field image of the cross section of the contact zone (non-spallation area) of the pin showing a compact oxide scale of approximately 800 nm covering the pin surface. The bonding of the oxide scale and

the HSS matrix was also very good because there are no visible cracks and micro-pores at the interface.

Fig. 6.7a shows the morphology of the surface of the pin outside the wear track, but very close, after the test at a normal load of 5 N and a sliding speed of 0.05 m/s for 150 seconds. The surface of the pin is covered by iron oxides and large parallelepiped vanadium oxides, which is similar to the oxidation test shown in Fig. 4.15 in Chapter 4. Fig. 6.7b shows the TEM bright field image of the cross section of the non-contact surface of the oxidised pin where the oxide scale consists of a large crystalline outer layer of iron oxide (Fe_2O_3) and a fine-grained inner oxide layer of Fe_3O_4, Cr_2O_3 and $(Fe, Cr)_2O_3$-spinel oxides. There is a porous and clear interface between the oxide scale and the HSS matrix. The oxide layer is approximately 1µm thick. The surface of oxidised pin has become rough due to protrusions of iron oxides and vanadium oxides.

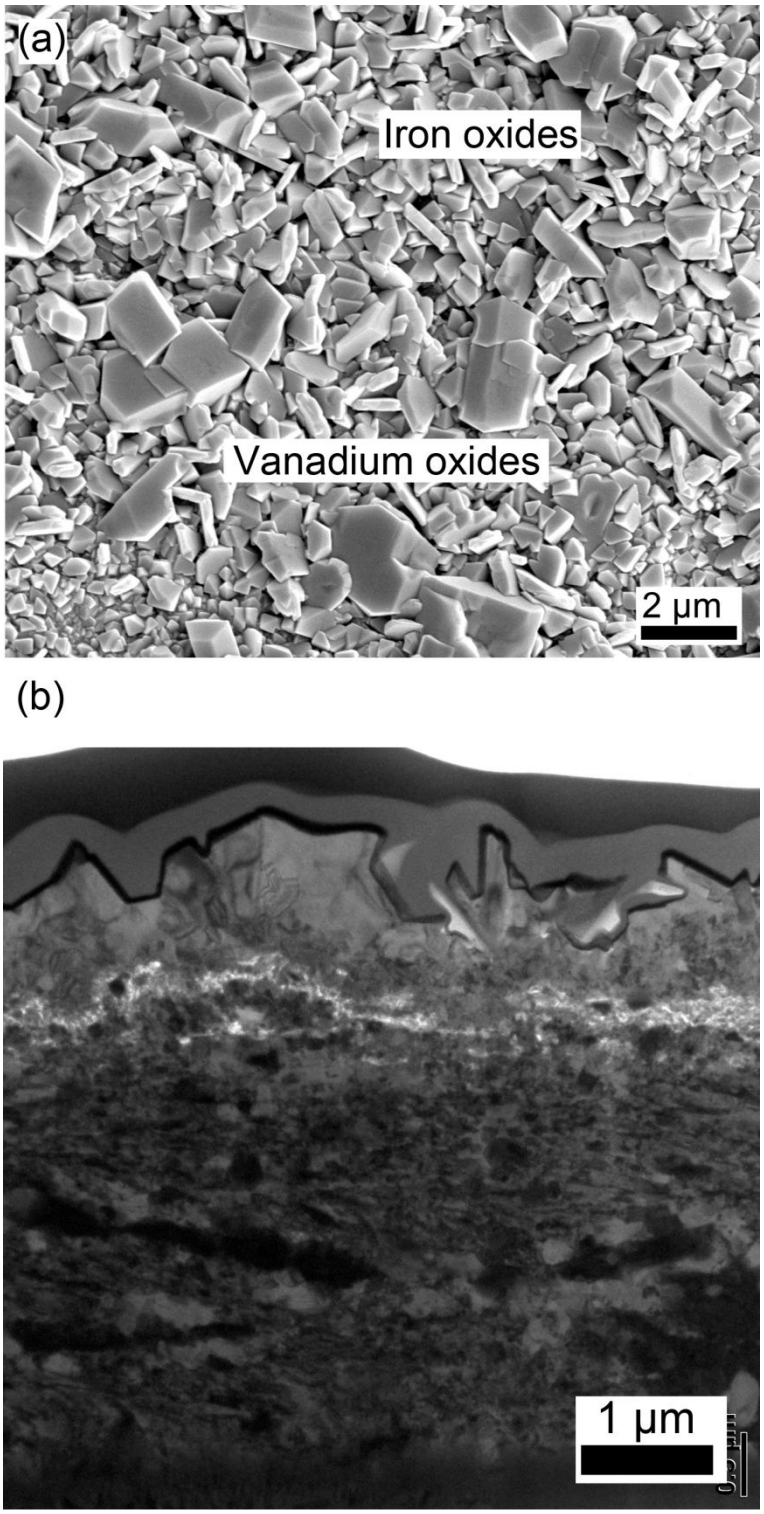

Fig. 6.7 (a) Secondary electron (SE) image of non-contact pin surface after the tribological test at normal load 5N and sliding speed 0.05 m/s for 150 seconds (in stage II), (b) TEM bright field image of the cross section of the non-contact zone, FIB was used to prepare the cross section.

Fig. 6.8 shows the wear track of the pin after the tribological test at a normal load of 5 N and a sliding speed of 0.05 m/s for 3600 seconds (end of stage III). It can be seen

that the morphology of the wear track at stage III is similar to stage II. The contact zone of the pin surface is covered by a discontinuous “glaze” oxide scale, however, the adherent no-spallation “glaze” oxide scale seems much thicker compared with that at stage II, as shown in Fig. 6.6. There is a clear interface between the sliding contact zone and non-contact area (as shown in Figs. 6.8b and 6.8c), and oxide debris were only found in the contact region, not around the interface between the sliding contact zone and non-contact area. In the sliding contact zone there was oxide spallation, as shown in Fig. 6.6 at Stage II, and also crack propagation and oxide debris from oxide scale in the same area, as shown in Fig. 6.8d.

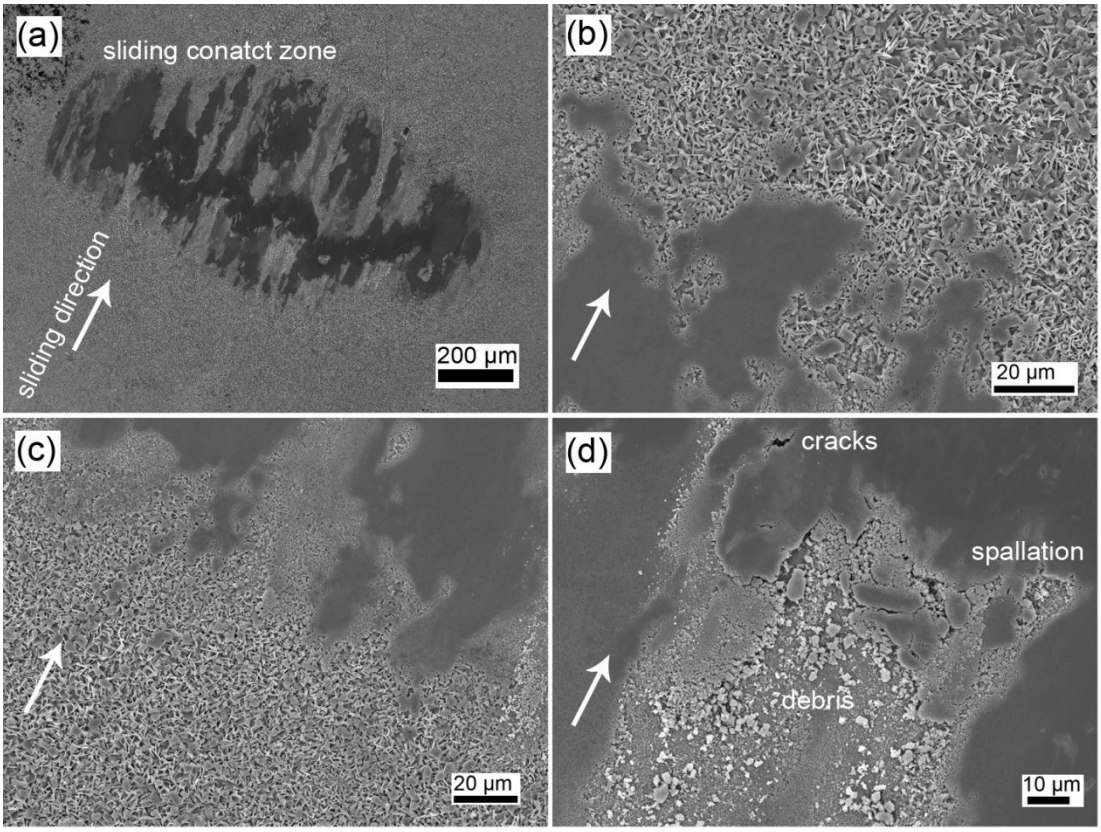

Fig. 6.8 (a) Secondary electron (SE) image of the pin wear track after the tribological test at normal load 5N and sliding speed 0.05 m/s for 3600 seconds (end of stage III), (b) morphology of the wear track front, (c) morphology of the wear track tail, (d) spallation and wear debris at the wear track.

Fig. 6.9a shows the SE and TEM bright field images of the cross section of wear track after a tribological test at a normal load of 5 N and a sliding speed of 0.05 m/s for 3600 seconds (end of stage III). It can be seen that the pin wear track is covered by

an oxide scale of non-uniform thickness and at the centre of the wear track, a small piece of material has been rubbed off and cracks underneath propagated into the material. It is possible that this material rubbed off is vanadium MC carbide. Fig. 6.9b shows the detailed microstructure of the cross section of the pin wear track where “glaze” oxide scale is adhering to the substrate and after the tribological test, a thick oxide scale has developed in the contact zone. The total thickness of the adherent no-spallation oxide scale was approximately 9.5μm. From a top down view the “glaze” oxide scale seems to be compact and smooth, but there are two large cracks inside the oxide scale parallel to the surface, which actually divides the oxide scale into three sub-layers (Fig. 6.9b). Fig. 6.9c shows very fine-grained oxides (less than 200nm in size) where the outside part consists mostly of oxide scale, while inside the oxide scale the oxides are a little larger, at about 400nm (Fig. 6.9d). Fig. 6.10 shows the TEM/X-ray mapping of the inner part of the oxide scale and its interface between the oxide scale and HSS matrix. The results indicated that the adherent oxide scale mainly consists of iron oxides (Fe_2O_3). Chromium oxides and vanadium oxides only appeared in the most inner part of the oxide scale and at the interface between the oxide scale and HSS matrix.

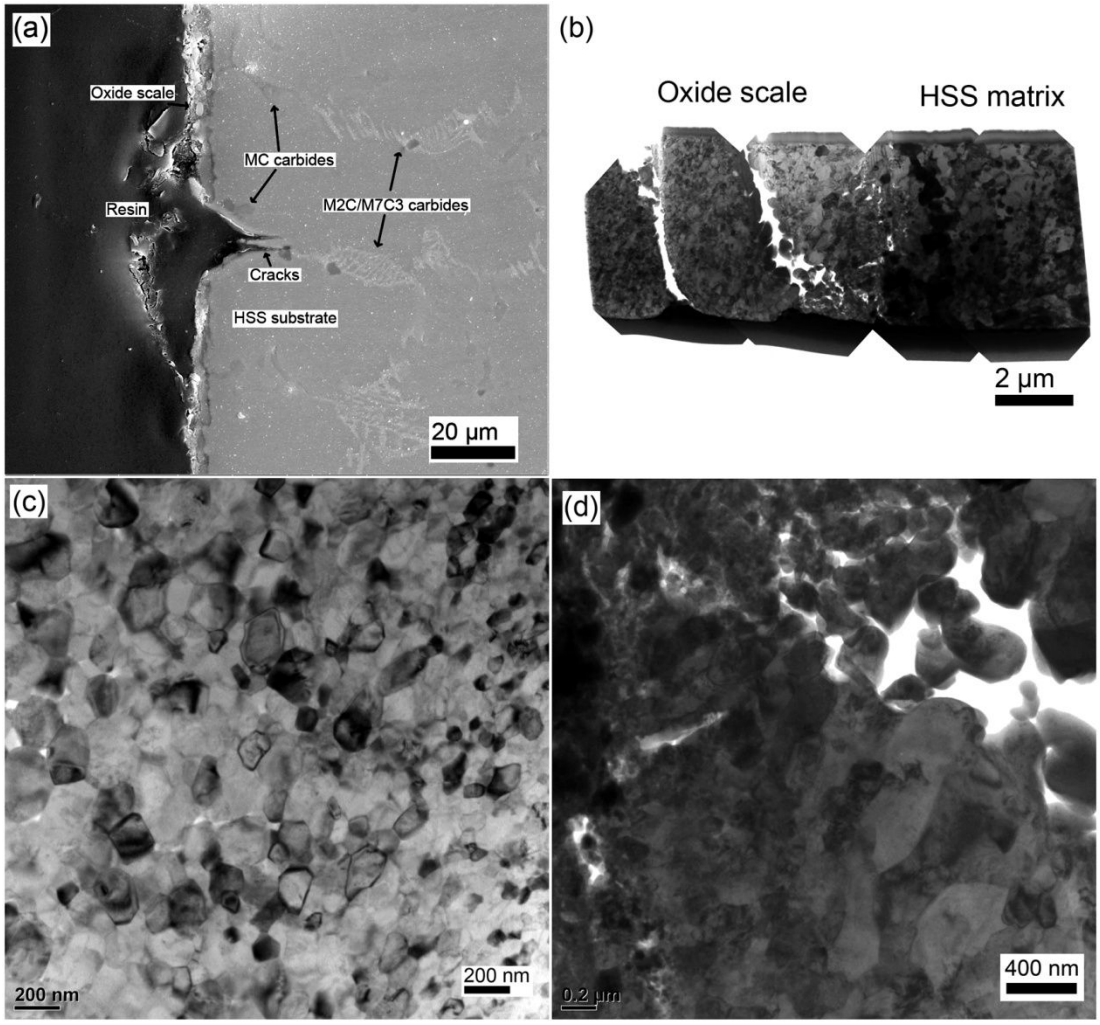

Fig. 6.9 (a) Secondary electron (SE) image of the cross-section of the pin wear track after tribological test at normal 5N and sliding speed 0.05 m/s for 3600 seconds (end of stage III), (b) TEM bright field image of cross-section of the wear track, (c) higher magnified TEM bright field image of the oxide scale at the contact frontier, (d) higher magnified TEM bright field image of the oxide scale near the interface of oxide scale and the HSS matrix.

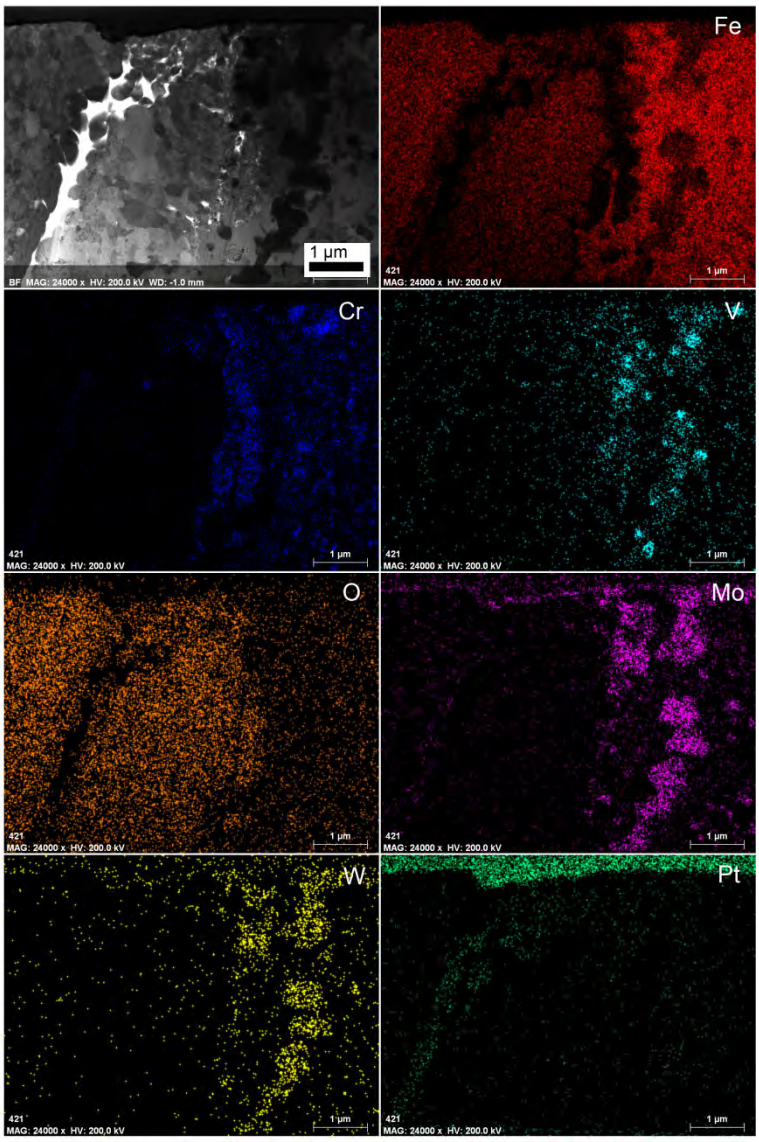

Fig. 6.10 TEM/X-ray mapping of the cross-section pin wear track after tribological test at normal 5N and sliding speed 0.05 m/s for 3600 seconds (inner part of the oxide scale and the HSS matrix).

Fig. 6.11a shows the morphology of the non-contact area of the pin, very close to the sliding contact zone. It can be seen that the surface is covered by a continuous porous oxide scale with iron oxide whiskers and parallelepiped vanadium oxides protruding from the scale, which is similar to the oxidation test shown in Fig. 4.15 in Chapter 4. Fig. 6.11b clearly shows the morphology of the oxide scale in a cross sectional view. TEM/X-ray mapping of the cross section of the oxide scale confirmed that the scale consists of two sub-layers, with the outer layer being mainly large columnar iron oxide (Fe_2O_3) and the inner layer a mixture of fine iron oxides and

chromium oxides (Fe_3O_4, Cr_2O_3 and (Fe, Cr)$_2O_3$-spinel oxides). The parallelepiped vanadium oxides are protruding from the oxide scale (Fig. 6.11c). The oxide scale outside of the contact area was around 2.8µm thick after a 1h tribological test (the protruding vanadium oxides were not included).

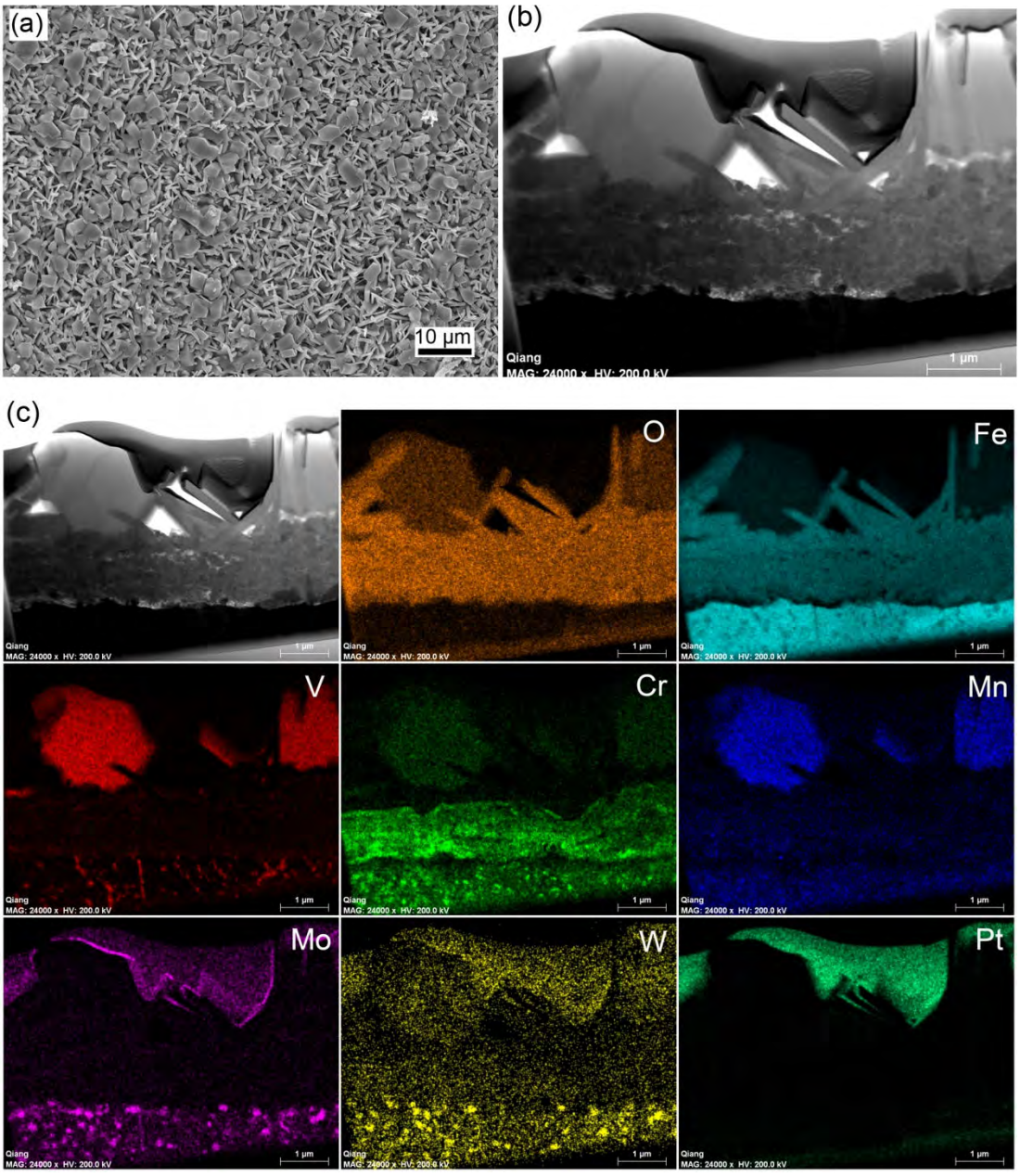

Fig. 6.11 (a) Secondary electron (SE) image of pin surface morphology at the non-contact area after a pin-on-disc test, (b) TEM bright field image of the cross section of the non-contact area, (c) TEM/X-ray mapping of the cross section of the non-contact area.

Fig. 6.12a shows the pin wear track after a tribological test at a normal load of 5N and a sliding speed of 0.2 m/s for 3600 seconds. The wear track is also covered by a

discontinuous “glaze” oxide scale. However, compared to the morphology of the wear track after a test at a normal load of 5N and a sliding speed 0.05 m/s, the adherent “glaze” oxide scale seemed to be much thicker. A lot of oxide debris has spread out of the pin wear track due to a relative high sliding speed (Figs. 6.12b and 6.12c). In the sliding contact zone there was spallation of small pieces of oxide scale, as shown in Fig. 6.12d.

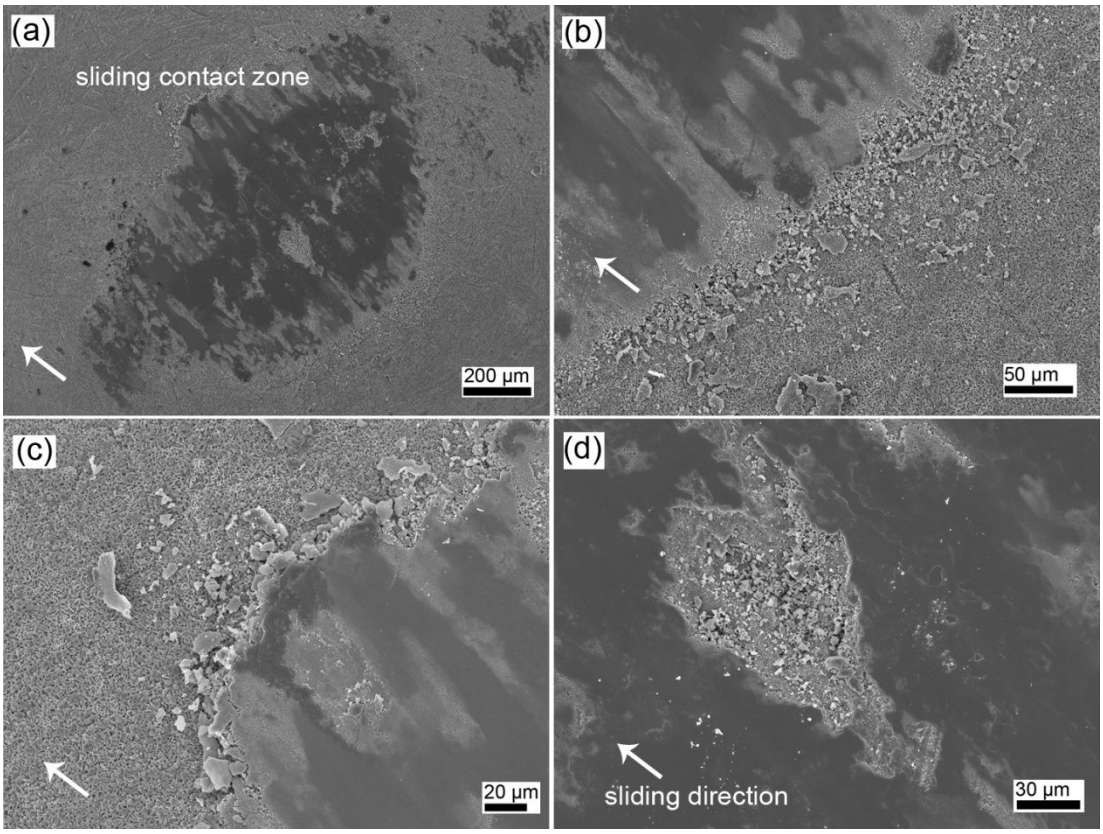

Fig. 6.12 (a) Secondary electron (SE) image of the pin wear track after a tribological test at normal load 5N and sliding speed 0.2 m/s for 3600 seconds, (b) morphology of the wear track front, (c) morphology of the wear track tail, (d) spallation and wear debris in the wear track.

Fig. 6.13a shows the detailed microstructure of the cross section of the pin wear track after a tribological test at a normal load of 5N and a sliding speed 0.2 m/s for 3600 seconds. The microstructure of the “glaze” oxide scale is similar to that formed under a normal 5N load and sliding speed of 0.05 m/s (Fig. 6.9b). There are two cracks inside the oxide scale, parallel to the worn surface of the pin which divided the oxide scale into three sub-layers. A clear interface (just like another crack) exists at the interface between the oxide scale and HSS matrix, which severely weakens

the bonding between the oxide and matrix. The oxide scale in the contact area is approximately 11µm thick. Fig. 6.13b shows detailed microstructure of the outside part of the "glaze" oxide scale where this sub-layer consists of very fine grained oxides ranging in size from 50-100nm. As for the inner part of the oxide scale, the sintered oxides are around 200nm in size (Fig. 6.13c). The results of TEM/X-ray mapping (Fig. 6.14) indicated that the outside part of the "glaze" oxide scale (contact frontier) consisted of pure iron oxides. Chromium oxides are rich at the interface between the oxide scale and HSS matrix, and at some locations on the inner part of the oxide scale. Vanadium oxides were hardly detected in the oxide scale.

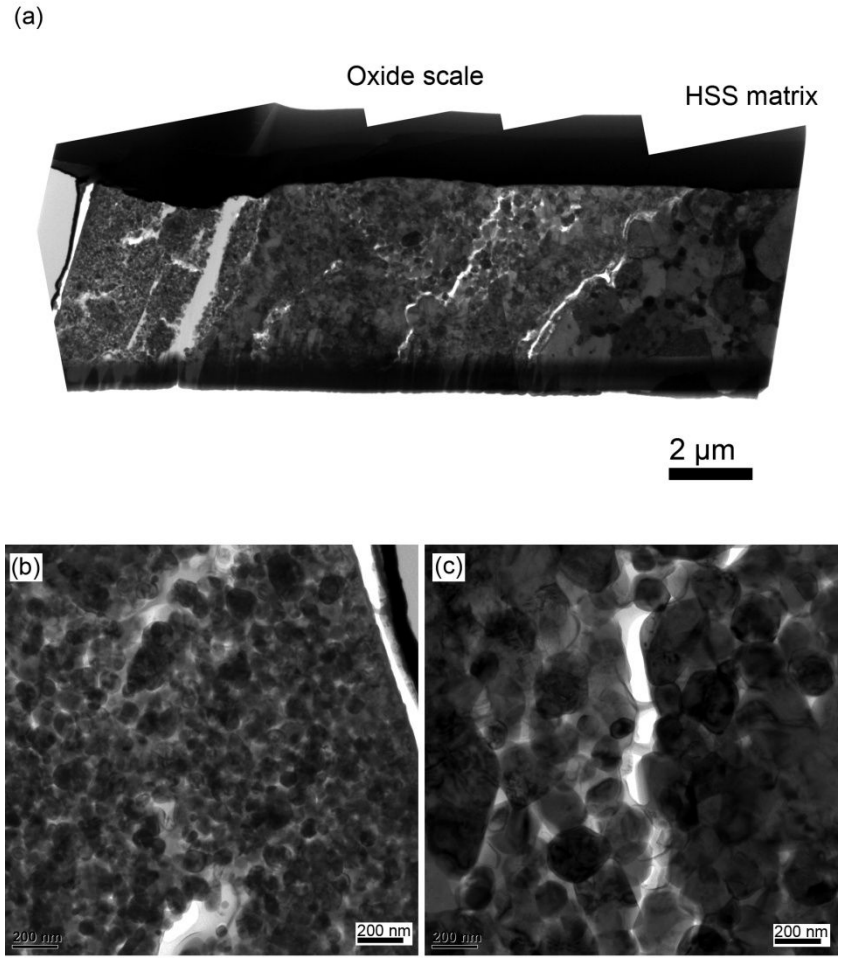

Fig. 6.13 (a) TEM bright field image of the cross-section of the pin wear track after the tribological test at normal load 5N and sliding speed 0.2 m/s for 3600 seconds, (b) higher magnified TEM bright field image of the oxide scale at the contact frontier, (c) higher magnified TEM bright field image of the inner part oxide scale.

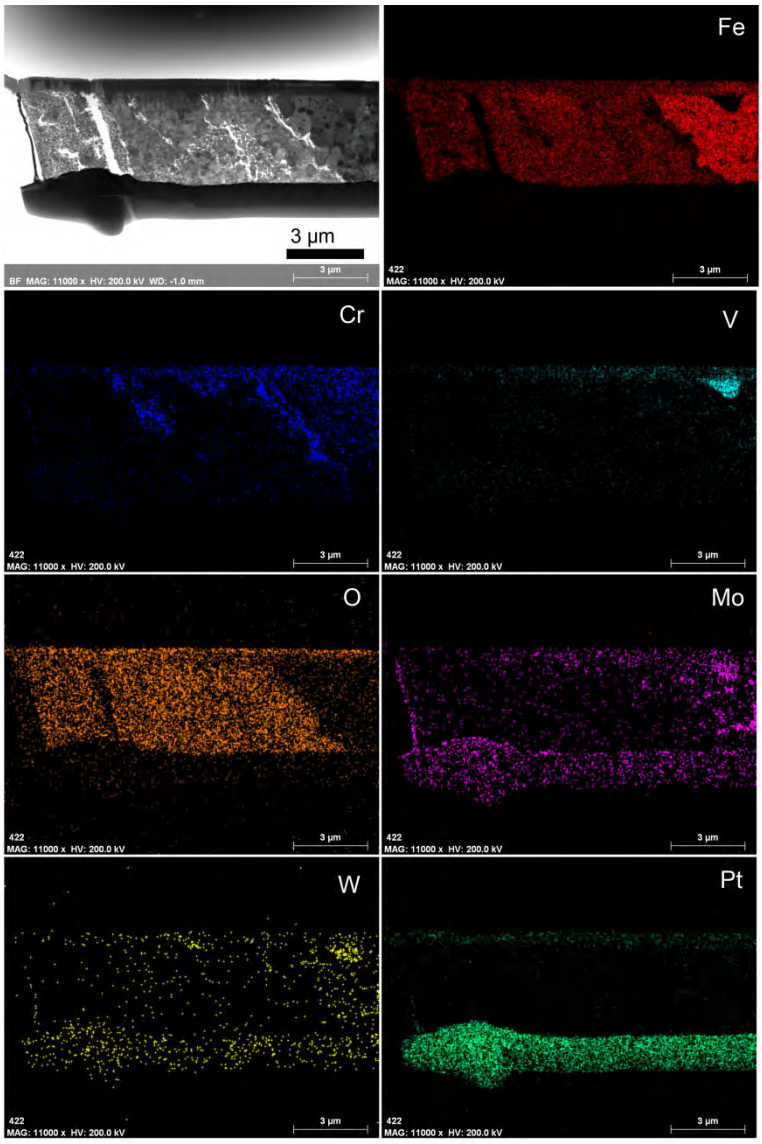

Fig. 6.14 TEM/X-ray mapping of the cross section of the pin wear track after a tribological test at a normal load of 5N and a sliding speed 0.2 m/s for 3600 seconds.

Fig. 6.15 shows the SE images of the cross section of oxide scale formed on the mild carbon steel disc after a 1 h tribological test at 900 ^{o}C. The oxide scale was around 70µm thick after the test. The oxide scale consists of three sub-layers; the outer layer should be hematite (Fe_2O_3) approximate 4.7µm thick, the columnar crystalline middle layer is magnetite (Fe_3O_4) approximate 19µm thick, and the large-grained inner layer is wüstite (FeO) approximate 46µm thick.

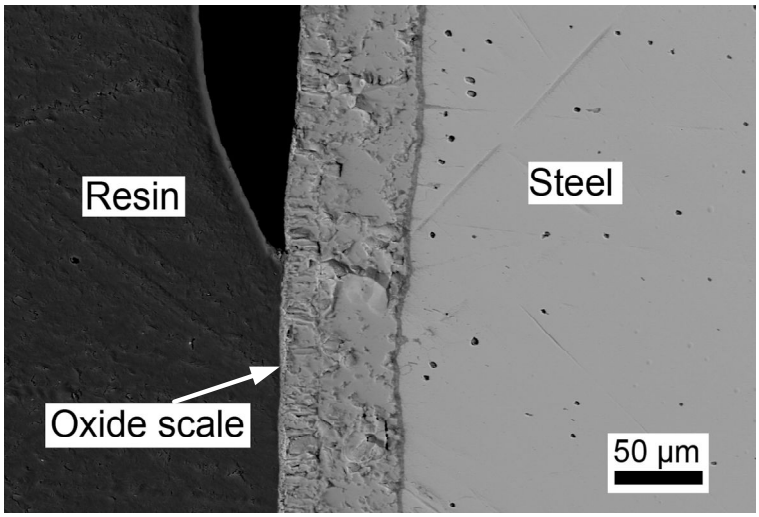

Fig. 6.15 Secondary electron (SE) image of the cross section of oxide scale on the surface of the disc after a 1 h tribological test (outside the wear track).

6.3 Discussion

The temperature of the disc and pin were well controlled during the tribological tests (Fig. 6.2). The surface temperature of the disc was kept at 900 ^{o}C, with fluctuations less than 2 ^{o}C. The surface temperature of the pin reached 660 ^{o}C in a very short time (less than 300 seconds) after making contact with the disc due to thermal conduction and radiation. The temperature of the pin was monitored from a position located 2 mm above the contact zone. However, after comparing the morphology of pin close to the contact zone (Figs. 6.7 and 6.11) with the oxidation results obtained in Chapter 4, the temperature of the pin at the contact zone was probably around 700 ^{o}C. During hot rolling the temperature of strip ranges from 800-1200 ^{o}C, and the temperature of the surface of a work roll can reach up to 650 ^{o}C, or even up to 800 ^{o}C due to heat generated by plastic deformation and friction [2, 13, 62, 73-75]. Therefore, the tribological tests reproduced the temperatures of hot rolling very well. From Fig. 6.2 it can be known that the pin was oxidised at 660 ^{o}C for nearly 20 min before the tribological test began, and therefore the contact mechanism between the pin and the disc must be oxide-to-oxide.

The coefficient of friction obtained from the tests (Table 6.3) indicated that the sliding speed has a significant influence on the tribological behaviour. The

coefficient of friction increased when the sliding speed was increased from 0.05 m/s to 0.2 m/s. An interesting result should be noticed when increasing the normal load from 5N to 10N, the coefficient of friction at the stable stage of the tests decreases both at the sliding speeds 0.05 m/s and 0.2 m/s. It seems controversial, but it should be noted that mild testing conditions (small Hertzian contact pressures) were used in this study to investigate the role of oxides in tribological behaviour in the contact zone. The normal loads 5N chosen (equals a Hertzian contact pressure of approximately 650MPa) and 10N (825MPa) will not destroy the antagonist oxide scales too fast during the tests, but increasing the normal load from 5N to 10N results in a more compact and smoother antagonist oxide scale because it can be deformed at high temperatures. The smoother the antagonistic surfaces, the lower the coefficient of friction.

The tribological test conditions of a normal load of 5N and a sliding speed of 0.05 m/s is close to the tribological conditions in the roll bite during hot rolling. Three stages were identified after analysing friction coefficient curve: Stage I where the coefficient of friction decreased dramatically from around 0.4 to 0.23 (minimum value) in a very short time (less than 100 seconds). Stage II where the coefficient of friction increased from a minimum value to approximately 0.29 in a short time (about 150 seconds), and Stage III, where the coefficient of friction remained at about 0.27 for the remainder of the test. The results were similar to the work of Vernge et. al.s work [109] where Vernge defined the period before the friction stabilised as a running-in period. In this work the running-in period consisted of Stages I and II, and Stage III corresponds to the friction stabilisation period.

Table 6.4 summarises the morphology of pin wear at different stages during the tribological tests. SEM and TEM investigations showed that a thin, compact, and smooth “glaze” oxide scale around 800-850nm formed on the pin during the running-in period of Stages I and II. Compared to the thickness of the oxide scale formed at the non-contact zone (approximate 1μm) in the period, the “glaze” oxide

scale has been compressed and it is believed that no oxides transferred from the disc to the pin. Therefore the adhesive oxide scale consists of iron oxides (Fe_2O_3 and Fe_3O_4), (Fe, Cr) oxides and some vanadium oxides (V_2O_5). This "glaze" oxide scale has a good adhesion to the HSS matrix, as seen in Figs. 6.5b and 6.6b, and the interface between the oxide scale and HSS matrix was very compact and free from pores and cracks. The formation of the "glaze" oxide scale protects the pin from surface wear, which can be reflected from the coefficient of friction whose value in the running-in period was lower than the rest of the tribological test. From the beginning of Stage I, the pin began to slide from static to dynamic, with an oxide to oxide contact configuration. The oxide on an HSS pin was deformed from 1 μm to 850 nm and a continuous and complete "glaze" oxide scale (Fig. 6.5a) covered the whole contact area to act as a solid lubricant and leading to the minimum friction. However, this protection did not last long, at the Stage II running in period the oxide scale spalled from the shear stress generated by sliding friction, from oxide scale growing, from thermal impact, and from stress growing inside the oxide scale, and so forth (seen in Fig. 6.6c). The contact surface became rougher due to the oxide spallation, hence the coefficient of friction quickly increased from its minimum value. However, there was no debris or cracks on the contact surface of the pin at this stage. Therefore the main wear mechanism of the pin in the running in period is adhesive wear.

As the test proceeded, friction between the pin and the disc stabilised (stage III), while the wear mechanisms became complicated. Local spallation of the oxide scale kept happening during the rest of the test and oxide debris generated on the wear track because the disc was horizontal and the sliding speed was quite slow. On one hand, spallation of the oxide scale may cause superficial damage and increase the rate of oxidation on the HSS pin. On the other hand, oxide debris on the wear track may act as free third bodies abrading the antagonistic surfaces [169]. Vanadium MC carbides have been rubbed off the surface due to the relative weak binding energy between them (Fig. 6.9a). The adhesive non-spallation oxide scale in the contact region was around 9.5μm thick after a 1h tribological test, whereas the oxide scale

at the non-contact zone was only 2.8μm thick. A much thicker non-spallation oxide in the contact region is only possible from oxidation by the HSS pin itself. It is believed that oxides transferring from the disc to the pin thicken the adhesive oxide scale. Because the external oxide scale on the surface of the HSS pin consisted mainly of iron oxides (Fe_2O_3 and Fe_3O_4), as shown in Fig. 6.14, which was the same phase composition of oxide on the disc surface, it provided further evidence that oxide transferred from the disc to the pin. The dense, fine-grained and equiaxed oxides (mainly Fe_2O_3) found in the contact zone is the result of the combination of compression, sliding, oxidation, accumulation, agglomeration and sintering of wear particles during the high temperature pin-on-disc testing. Although the unbroken adhesive oxide seemed compact and smooth from a top view, there were large cracks inside the oxide scale. Bonding between the oxide scale and the HSS matrix also weakened because cracks and pores appeared at the interface. It could be predicted that catastrophic spalling might happen under certain circumstances, which may be the possible mechanism for why the “banding” phenomenon [134, 170] occurred during hot rolling.

When the sliding speed was increased from 0.05 m/s to 0.2 m/s, the adhesive oxide scale (approximate 11μm) was thicker, which meant that this action caused the transfer of oxides from the disc to the pin to accelerate. The TEM observation shows that more cracks appeared inside the oxide scale and a large crack appeared at the interface between the oxide scale and HSS matrix. This indicates that increasing the sliding speed accelerated the failure of the oxide scale during the test. A large amount of wear debris found at the non-contact zone surrounding the wear track also indicates that increasing the sliding speed increases the free third body abrasion. The more the oxide scale fails and the more amount of wear debris due to the higher sliding speed cause an increase of the friction coefficient at the lower sliding speed.

The influence of the disc surface has not been considered in this study because an

SEM observation (Fig. 6.15) indicated that a quite thick and uniform oxide scale formed on the disc during the test, which ensured that the contact was always oxide-on-oxide. However, it is difficult to measure the mass loss of the disc after the tests because the pin-on-disc tests were carried out under a high temperature (the disc temperature was 900 ^{o}C) and oxidation continually occurred during the tests.

Table 6.4 Summary of the morphology of the pin wear track at different friction stages during the tribological tests.

Test conditions	Evolution of friction coefficient	Contact zone	Non-contact zone
Normal load 5 N, sliding speed 0.05 m/s	Stage I	A continuous and compact "glaze" oxide scale forms. Thickness of the oxide scale is approximate 850nm. No oxide scale spallation. Good bonding between the oxide scale and the substrate.	Similar to Stage II.
	Stage II	A discontinuous but compact "glaze" oxide scale forms. Thickness of no-spallation oxide scale is approximate 800nm. Oxide scale spallation happens. No wear debris in the wear track. Good bonding between the oxide scale and the substrate.	A duplex-layered oxide scale forms, outer layer is large Fe_2O_3 oxides, inner layer fine-grained (Fe, Cr) oxides and many micro-pores. Thickness of the oxide scale is approximate 1µm. A porous interface can be observed.
	Stage III (End of the test)	A discontinuous "glaze" oxide scale forms. Thickness of no-spallation oxide scale is approximate 9.5µm. Oxide scale spallation happens, wear debris accumulate on the wear track, cracks propagate on the surface. Two large cracks exist inside the oxide scale. Micro-pores and cracks appear at the interface of the oxide scale and the substrate.	The microstructure of the oxide scale is similar to that at the Stage II. Thickness of the oxide scale is approximate 2.8µm. A porous interface can be observed.
Normal load 5 N, sliding speed 0.2 m/s	stage III (End of the test)	A discontinuous "glaze" oxide scale forms. Thickness of no-spallation oxide scale is approximate 11µm. Oxide scale spallation happens, wear debris accumulate on the wear track, cracks propagate on the surface. Two large cracks exist inside the oxide scale. A large crack appears at the interface of oxide scale/substrate.	Similar to above (Stage III) More wear debris is spinned out of the wear track and sticked on the non-contact pin surface due to a relative high sliding speed.

6.4 Conclusions

Pin-on-disc high temperature tribological tests have been successfully carried out to simulate the tribological behaviour of the oxide scale in the role bite. The pin represents hot work rolls and the disc represents the hot steel strip. Contact between the pin and the disc is actually oxide-on-oxide because both antagonistic surfaces were oxidised under a high temperature before the test started. The results of the coefficient of friction show that the sliding speed has a significant influence on the tribologcial behaviour. It takes much longer for the coefficient of friction to stabilise when the sliding speed was increased from 0.05 m/s to 0.2 m/s, and the coefficient of friction increased in value with the sliding speed. Increasing the normal load from 5N to 10N lowered the coefficient of friction and resulted in a more compact and smoother “glaze” oxide scale forming under a higher normal load.

A typical tribological tests has been analysed; and based on the evolution of the friction coefficient, it can be divided into three stages: i) Stage I corresponds to the start of the friction curve when the coefficient of friction decreased, ii) Stage II corresponds to an increase in the coefficient of friction after the minimum value, and iii) Stage III is the stabilisation step of the friction. Stages I and II can be summarised as a running-in period which lasts less than 300 seconds from the start of the test. The interrupted tests indicated that adhesive wear dominated the wear mechanisms of the pin in this period. A thin, continuous, compact and smooth “glaze” oxide scale formed on the pin at the Stage I, acted like a solid lubricant and lead to a sharp decrease in friction. At Stage II of the running-period, oxide scale spallation occurred at the contact zone due to shear stress generated by friction, oxide scale growing, thermal impact, stress growth inside the oxide scale, so the contact surface became rougher and the coefficient of friction quickly increased from its minimum value.

At Stage III, friction stabilised while the wear mechanism on the pin becomes complicated. In addition to oxidation on the HSS pin, the oxides transfers from the disc to the pin which significantly thicken the oxide scale on the pin. Large cracks and pores can be found inside the oxide scale, indicating that the severe “banding” phenomena could happen when the oxide scale reaches a critical value. A large amount of wear debris observed on the pin wear track confirms that abrasive wear happens at this stage. By increasing sliding speed, more cracks and pores are generated inside the oxide scale and more wear debris is distributed on the pin wear track which causes the increase the coefficient of friction. The wear mechanism at this stage is a balance between adhesion, abrasion, and oxidation.

Chapter 7
Oxidation and tribology tests on Gleeble 3500 system

The aim of this chapter is to perform preliminary rolling experiments to simulate the contacts between the HSS rolls and the heated steel strip. Oxidation and tribology experiments were carried out on a Gleeble 3500 thermo-mechanical simulator. By using Gleeble system, the influence of high water vapour content (up to 46.5% H_2O) on the oxidation rate of the high speed steel roll material can be successfully investigated. The surface characteristics after oxidation were characterised by scanning electron microscope (SEM) and X-ray diffraction (XRD) analysis. It is reported here for the first time that a simulation of the hot rolling process has been carried out on a mini rolling mill that has been adapted within the Gleeble 3500 thermo-mechanical simulation system. Two types of roll surface were investigated in the simulation of the hot rolling process, one is a fresh metallic surface (virgin surface) and the other is a pre-oxidised surface in dry air. Test parameters such as rolling force, surface roughness of the strip and rollers were measured at different temperatures and reductions to investigate the tribological behaviours after a number of simulated rolling passes.

7.1 Oxidation tests

7.1.1 Experimental methods

The samples were oxidised isothermally at 700 ^{o}C for 30-120 min in dry air, 12.5% and 46.5% H_2O moist air. Compressed industrial air was used as the dry air. In the case of moist air, controlled moisture was obtained by passing industrial air through a distilled water tank which was maintained at a constant temperature. Moist air with 12.5% and 46.5% water vapour can be obtained by controlling the water temperature at 50 and 80 ^{o}C, respectively. Fig. 7.1 shows the water vapour content

The content of this chapter has been published in *Wear 2011 (273): 43-48.*

in the atmosphere according to the water temperature. The gas tube connecting the water tank and Gleeble chamber was pre-heated to prevent the condensation of water on the inside wall of the tube. The following procedure was used for each of the oxidation experiments:

(1) The sample was heated to 700 ^{o}C in an Argon protective atmosphere at a heating rate of 100 ^{o}C/min;

(2) When the temperature reached 700 ^{o}C, Argon was switched off and the oxidising gas introduced;

(3) After oxidation, the sample was cooled down to room temperature in the Argon atmosphere.

A JEOL JSM 64900 scanning electron microscope (SEM) equipped with energy-dispersive X-Ray (EDX) analysis was employed to investigate the surface morphology of the samples before and after oxidation and the microstructures of the oxide scale formed on the sample surface. An X-ray diffraction (XRD) using a GBC MMA diffractometer with monochromated Cu Kα radiation was used to analyse the phase composition of the oxide scale. In order to measure the thickness of the oxide scale, oxidised samples were cold mounted in EpoFix resin and then cut through the corss-sections. A Leica DMRM optical microscope was used to measure the thickness of oxide scale formed on the HSS sample surface.

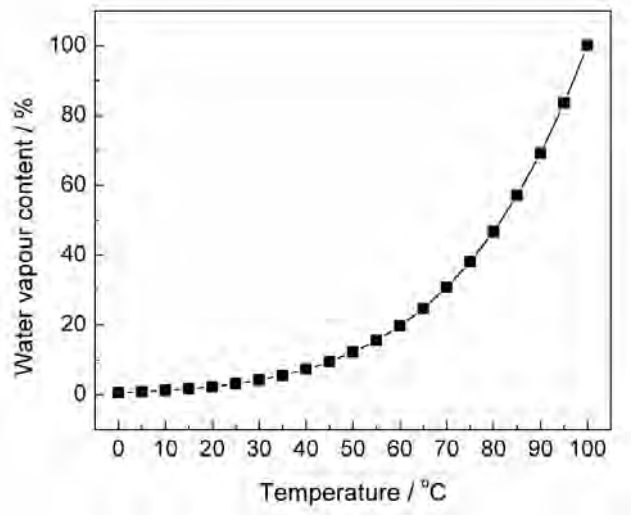

Fig. 7.1 Water vapour constitutions in the air corresponding to water temperatures. [171]

7.1.2 Results and discussion

Fig. 7.2a shows the original topography of the high speed roll surface. The grinding marks can be seen clearly. Figs. 7.2b, 7.2c, and 7.2d show the topographies of oxidised HSS sample surfaces after oxidation at 700 ^{o}C for 120 min in dry air, and at 12.5% and 46.5% H_2O moisture, respectively. The oxide scale formed in different atmospheres shows a significant difference in morphology. The oxide scale formed in dry air is dense and iron oxide crystals grow well. Oxidised V-rich MC carbides can be found on top of the oxide scale. Because water vapour exists in a moist atmosphere, the oxygen partial pressure is decreased compared to the dry air, so the size of iron oxide is limited. With increasing water content in an oxidising atmosphere, the oxide scale is becoming more and more porous and the iron oxide crystals finer. The morphology of oxide scale formed in a moist atmosphere shows a sponge like structure, and V-rich MC carbides are oxidised more severely and spread among the oxide scale without a clear crystal shape, as shown in Figs. 7.2c and 7.2d.

Fig. 7.3 shows the XRD results of oxidised HSS sample surfaces after oxidation at 700 ^{o}C for 120 minutes in different atmospheres. The results indicate that the main phases found in oxide scale are Fe_3O_4 and Fe_2O_3. Because the XRD tests were conducted directly on the oxidised surface, the Fe phase appearing in the XRD result indicates that the oxide scale formed in dry air after oxidation is not thick enough to prevent the X-ray penetrating through the oxide scale and detect the metallic part underneath. As the water content increases in the oxidising atmosphere the Fe_3O_4 phase decreases and the Fe_2O_3 phase increases in the oxide scale. This phenomenon can be explained as follows: as discussed above, the microstructure of the oxide scale become more and more porous as the water vapour increases in an oxidising atmosphere, so it is much easier for oxygen to diffuse inward through a more porous oxide scale and further react with Fe_3O_4 to form Fe_2O_3.

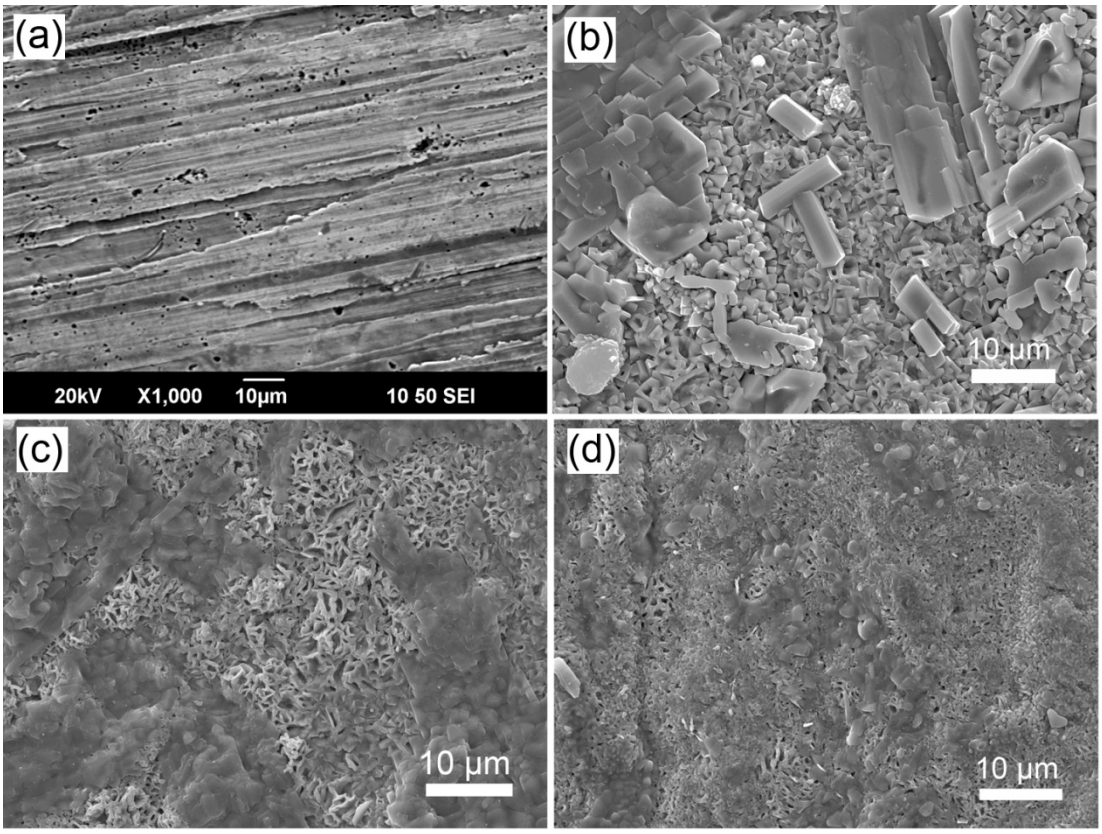

Fig. 7.2 Morphologies of HSS sample surface. (a) Original surface; (b) oxide scale formed in dry air for 120 min oxidation at 700 ^{o}C, (c) oxide scale formed in 12.5% H_2O moisture air for 120 min oxidation at 700 ^{o}C and (d) oxide scale formed in 46.5% H_2O moisture air for 120 min oxidation at 700 ^{o}C.

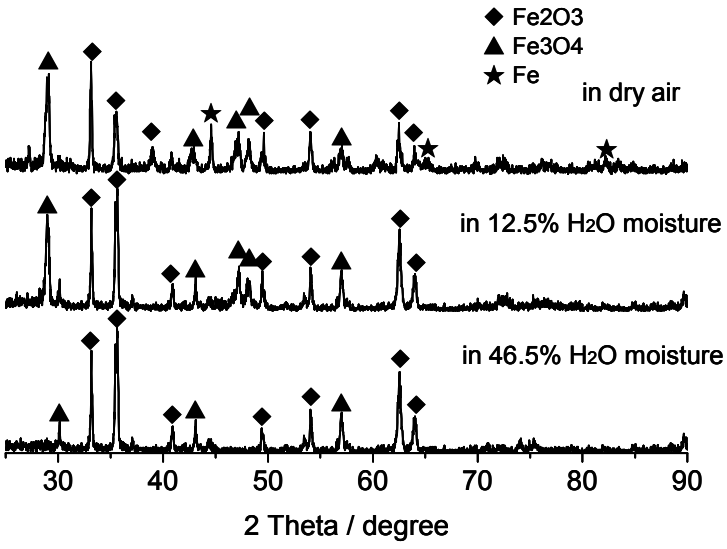

Fig. 7.3 XRD results of oxidized surfaces of HSS samples at 700 ^{o}C for 120 min in different atmospheres.

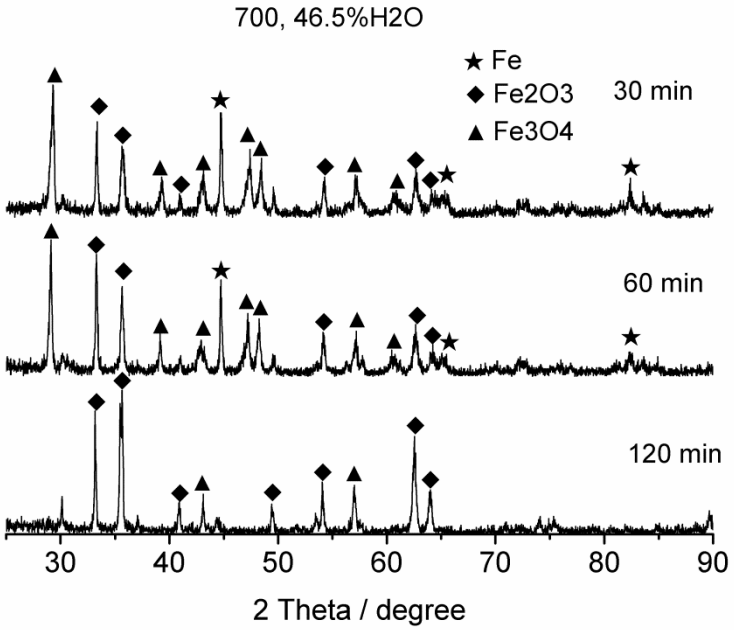

Fig. 7.4 XRD patterns of oxidized surface at 700 ^{o}C in 46.5% H_2O humid air for 30, 60 and 120 min.

Fig. 7.4 shows the XRD results of oxidised surfaces at 700 ^{o}C in 46.5% H_2O moist air for different oxidation times. It can be seen that the oxide scale consists mainly of Fe_3O_4 and Fe_2O_3, although the constitution of Fe_2O_3 increases with oxidation time. It can be explained that the oxide scale formed under moist conditions is porous, as shown in Fig. 7.2, so it is much easier for oxygen to diffuse inward through the oxide scale and react further with Fe_3O_4 to form Fe_2O_3.

Fig. 7.5 shows the evolving thickness of oxide scale formed at 700 ^{o}C in different atmospheres. It is evidenced that the growth of oxide scale on HSS surface follows the parabolic law in both dry and moist atmosphere. The oxide scales formed in a moist atmosphere are always thicker than in dry air. The growth rate of oxide scale seems similar for dry air and 46.5% H_2O moisture. However, it is different with 12.5% H_2O moisture where the growth in thickness is lower in the first 30 minutes, but rise at the end. This indicates that the water content in an oxidising atmosphere has a significant effect on the oxidation rate of high speed steel material. But a much higher water content in the atmosphere decreases the oxidation rate for a long period due to a significant reduction of oxygen partial pressure.

It was proposed in [172] that increased oxidation in the presence of water vapour was due to a dissociation reaction in the pores/cracks of the oxide which contained H_2O and H_2. Reduction of the oxide occurs at the outer edge of the pore/crack and oxidation of iron ions or metal at the inner surface, thereby transporting oxygen inwards to accelerate the reaction. The HSS material, which contains around 5% chromium, can be considered as a Fe-Cr alloy. Extensive studies about the oxidation behaviour of Fe-Cr alloys indicate that the presence of water vapour may increase the oxidation rate of the alloys due to the formation of volatile $CrO_2(OH)_2$ and $Cr(OH)_3$ [173-181]. The effect of evaporation of the volatile $CrO_2(OH)_2$ and $Cr(OH)_3$ compound may affect the rate of oxidation if the supply of chromium from the substrate is rate limiting. Ehlers et al. [182] in their study of the oxidation of 9% Cr steel suggest that volatile $Fe(OH)_2$ forms at low oxygen partial pressure in the inner layers of the scale and is then converted to haematite or magnetite in the outer layers of the scale so contributing to the higher rates of oxidation observed.

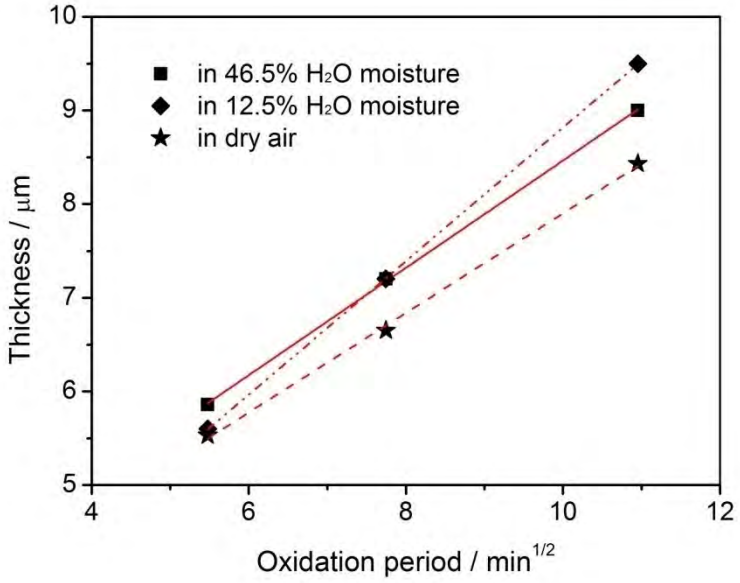

Fig. 7.5 Thickness evolution of oxide scales formed at 700 ^{o}C in different atmospheres.

7.2 Tribology tests

7.2.1 Experimental methods

The experiments were carried out on a Gleeble 3500 thermal-mechanical simulator

with a mini-mill fixed inside its chamber. The mini-mill is called a Lateral-setting Test System (LST) which is different to the upsetting rolling test (URT) [12]. Fig. 7.6 shows the assembly of the LST in the Gleeble chamber. To accomplish the proposed experiments the mini-mill must be fitted accurately into the space within the Gleeble chamber and be easy to assemble and disassemble the samples. In addition, each part of the mill must be strong enough to withstand the rolling process. The rolling distance was designed as 25mm due to limitations with the Gleeble chamber. Fig. 7.7 shows the details of theLST mini-roll. There are two load cells mounted on the top of the upper roller shaft, so the rolling force can be measured directly while simulating hot rolling. By adjusting the thickness of four spacers, a different reduction can be obtained. Rolling simulation is obtained by the Gleeble digital control system driving the sample strip. The strip is clamped with high thermal conductivity grips and driven into the roll gap. Before simulation, the strip is heated to the desired temperatures by introducing the electric current through the sample. The samples are mild carbon steel with a chemical composition listed in Table 7.1. There are three thermocouples welded on the strip, as shown in Fig. 7.8. The middle one is the control thermocouple and the other two are for monitoring. By controlling the heating rate according to feedback from the control thermocouple, a uniform distribution of temperature can be obtained on the rolling zone of the strip sample. The whole experiment was conducted in an Argon atmosphere in order to prevent the strip from oxidising.

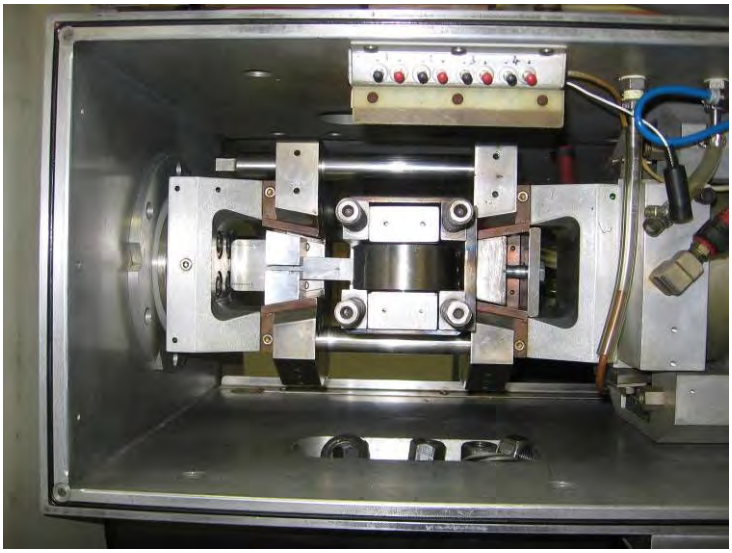

Fig. 7.6 LST mill assembled in the Gleeble 3500 chamber.

Table 7.1 Chemical composition of the mild carbon steel strip sample (wt%).

C	Si	Mn	P	S	Cr	Ni	Cu	Mo	Al	Ti
0.15	0.15	0.51	0.008	0.018	0.071	0.070	0.23	0.24	0.003	0.001

Two different surface morphologies of high speed steel rolls were investigated in this study. One is a relatively fresh metallic surface, and the other is a surface that was pre-oxidised at 700 ^{o}C for 80 min in dry air (oxide was 7µm thick). The strip was first heated to 700 or/and 850 ^{o}C in an Argon atmosphere and then hot rolled at a rolling speed of 15 mm/s. During the experiments the rolling force was recorded in-situ by load cells, and the effect of both the strip, the original surface roughness of the roll, and the pass reduction were considered. A stylus type Hommel Tester T1000 profilometer with ISO11562 filter was used to measure the surface roughness of the sample. A JEOL JSM 6490 Scanning Electron Microscope (SEM) equipped with energy-dispersive X-ray analysis (EDX) was used to investigate the surface morphology of these two different rollers.

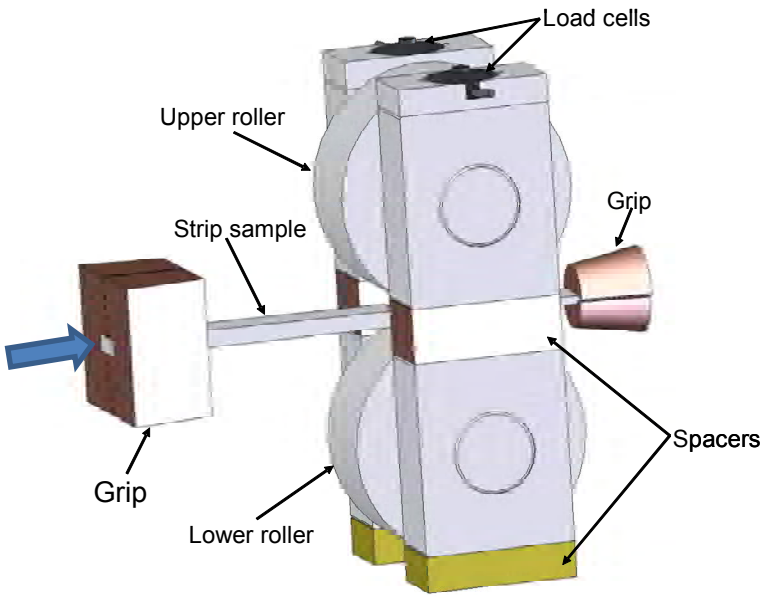

Fig. 7.7 Schematic illustration of mini two–high LST mill.

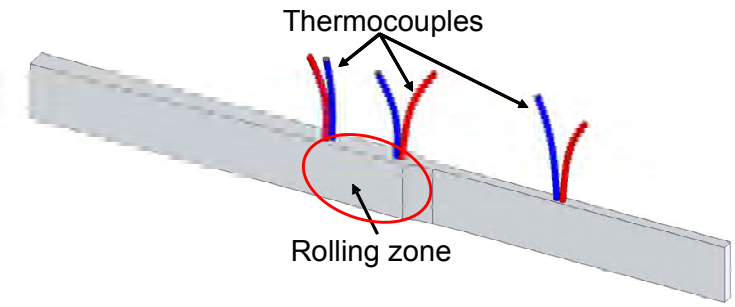

Fig. 7.8 Schematic illustration of strip sample welded with three thermocouples.

7.2.2 Results and discussion

The surface morphologies of the two rollers are shown in Fig. 7.9. Grinding marks can be seen on the fresh metallic surface (Fig. 7.9a) and there are many voids appearing on the surface where some hard carbide particles were detached during grinding. The average roughness of the fresh metallic surface was 0.2-0.3µm. Fig. 7.9b shows the morphology SEM image of the surface of the mini-roll after oxidation at 700 ^{o}C for 80 min in dry air. It can be seen that the surface has been totally changed; the grinding marks are not visible and the roll is covered with a

layer of continuous oxide scale. Fig. 7.10 shows the SEM/X-ray mapping analysis of oxide scale where the oxide scales not only consists of iron oxides but also the oxidation products of carbides due to high speed steel contains a high volume fraction of various carbides. In the as-received HSS roller, the volume fraction of the carbides occupies around 13%, which consists of 9% V-rich MC carbides and 4% Mo-rich M_2C and Cr-rich M_7C_3 carbides (in Chapter 4). These carbides have oxidised much more than the steel matrix and protruding oxide scale. The average roughness (Ra) of the pre-oxidised roll surface is around 1.5µm.

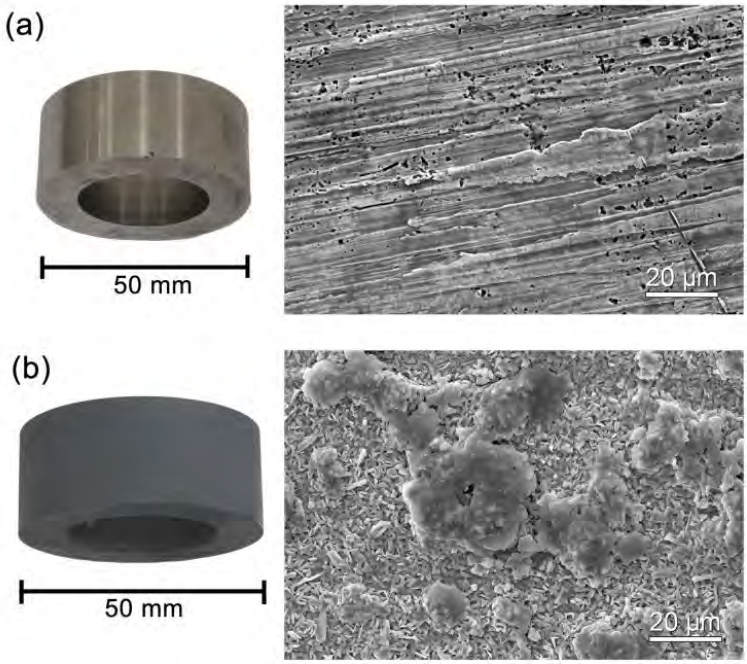

Fig. 7.9 Surface morphologies of HSS mini-rolls. (a) fresh metallic roll surface, (b) pre-oxidized roll surface after oxidation at 700 ^{o}C in dry air for 120 min.

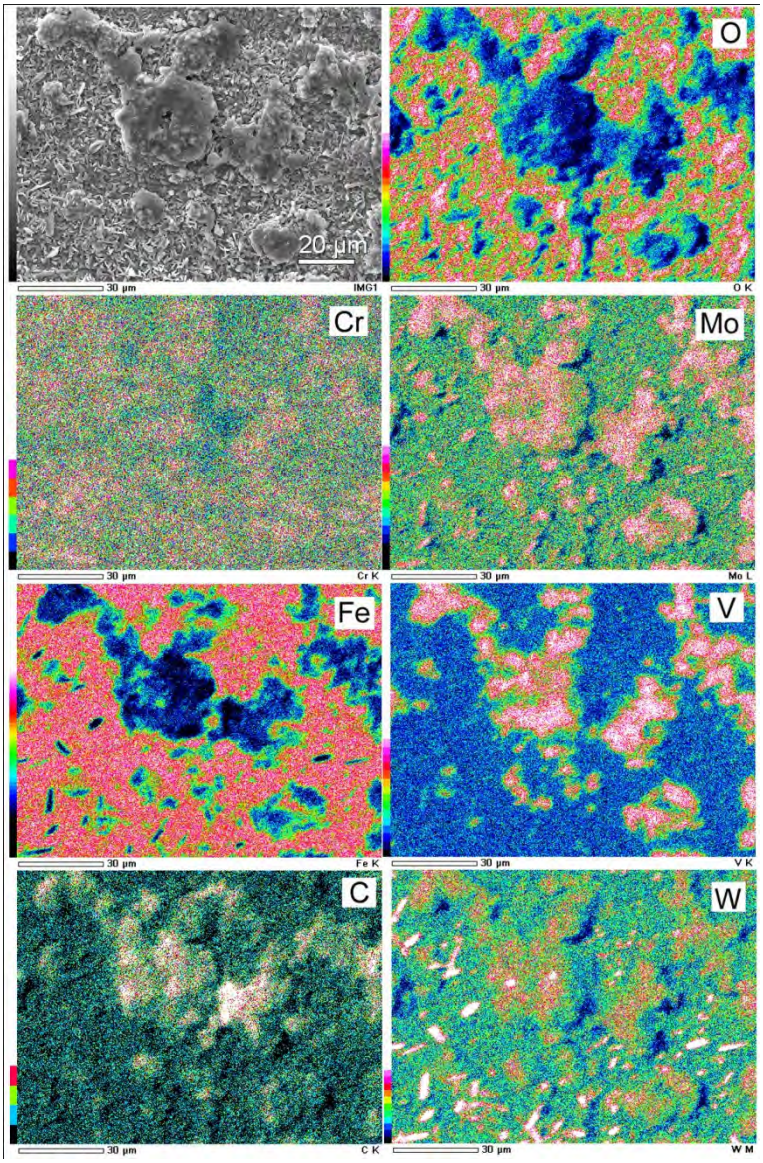

Fig. 7.10 SEM/X-ray mapping of the pre-oxidised roll surface.

Fig. 7.11 shows the distribution of temperature along the rolling zone of the strip before the hot rolling simulation. The rolling zone was designed to start from "A" and end at "B" with the distance AB being 25mm. There are two thermocouples welded at each end of the rolling zone to monitor the temperatures. A thermal gradient exists between position "A" and "B". A larger thermal gradient can be obtained by increasing the rolling temperature. A thermal gradient is inevitable because the local heating method used by the Gleeble system cannot produce a completely uniform temperature distribution. However, by adjusting the heating control according to feedback from the controlling and monitoring thermocouples,

the thermal gradient can be reduced as small as possible, which is crucial in simulating hot rolling.

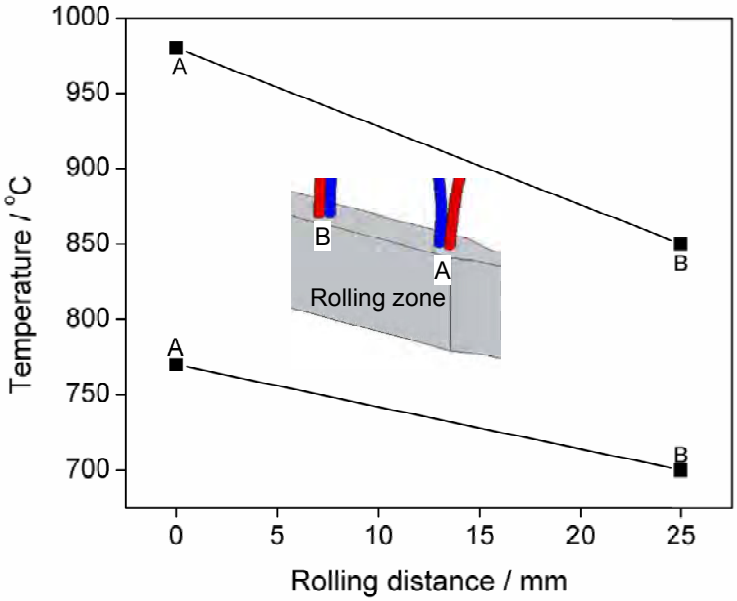

Fig. 7.11 Temperature distribution of rolling zone of strip sample.

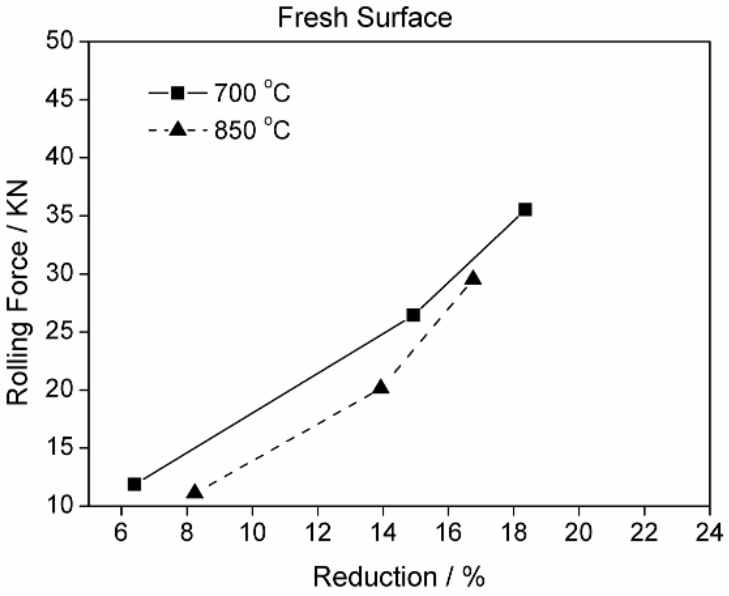

Fig. 7.12 Effect of reduction on rolling force (virgin roll surface).

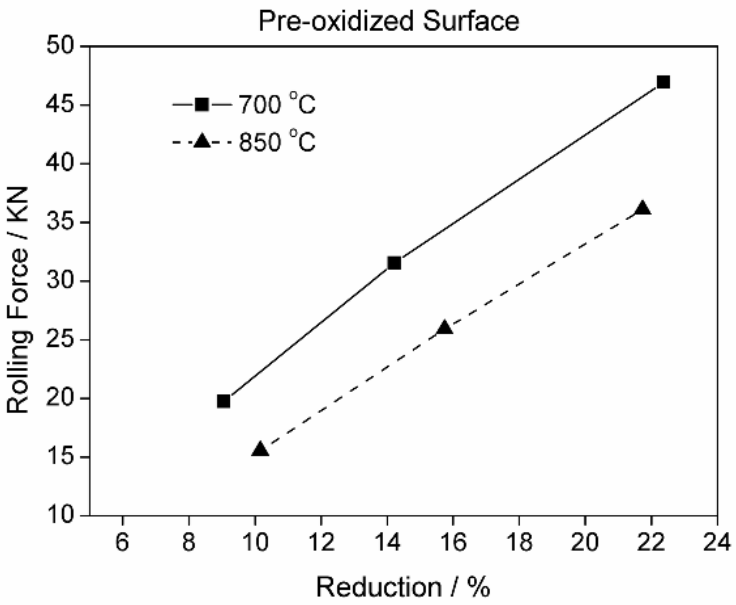

Fig. 7.13 Effect of reduction on rolling force (pre-oxidised roll surface).

Figs. 7.12 and 7.13 indicate the respective effects of a reduction in thickness of the rolling force for two different roll surface conditions and rolling temperatures. The figures show that the rolling force increases with lower rolling temperatures and higher reductions. The rolling force of the pre-oxidised surface roll is higher than the metallic surface roll. The roughness (Ra) of the pre-oxidised surface is about 1.50µm, while the roughness (Ra) of a metallic surface is between 0.2 and 0.3µm.

The coefficients of friction are estimated from the rolling force and push force. For a thickness reduction of 14-16% at 850 ^{o}C, the average coefficient of friction of the pre-oxidised roll was calculated as 0.292 compared with 0.268 for the non-oxidised surface. At 700 ^{o}C the respective coefficients of friction are 0.302 and 0.297. The rougher surface of the pre-oxidised roll produces a higher coefficient of friction and rolling force than the virgin roll surface. The amplitude of friction and its change with temperature are similar to those by Munther and Lenard [43].

Figs. 7.14 and 7.15 respectively indicate the changes of average roughness (Ra) of the strip with two types of roller surfaces after a single rolling pass. The original roughness of the strip surface is approximately 1.8-2.0µm. The surface of the strip was oxidised during heating although the Gleeble chamber was filled with argon gas

throughout the experiment. With the surface of the virgin roll, the oxide scale formed on the strip was pressed, and remained there even after rolling at 700 and 800 ^{o}C for all reductions. As shown in Fig. 14, the strip roughness decreases significantly with reduction. For low reductions (6-14%), the lower strip roughness value corresponds to the high temperature. At higher reductions (16-18%), the strip roughness after rolling is close to the roll surface roughness (Ra of the roll surface after rolling is 0.2-0.3µm).

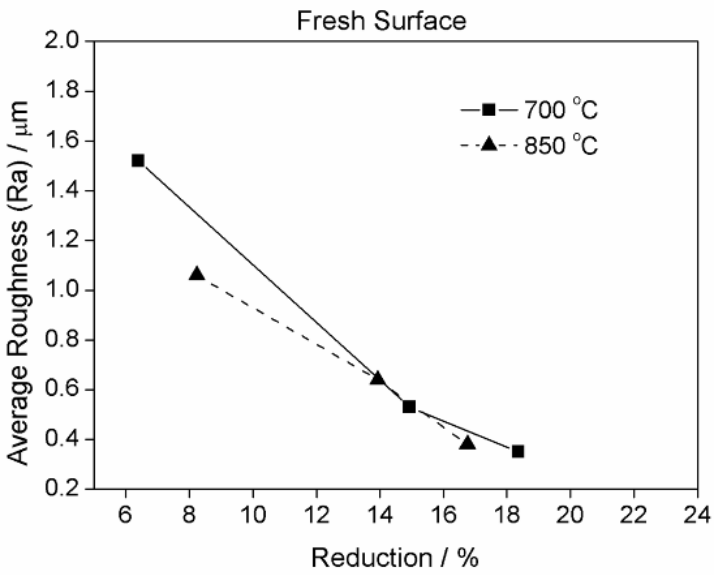

Fig. 7.14 Effect of thickness reduction on strip surface roughness (virgin roll surface). (Reduction of thickness is % reduction times 6 mm).

For the case of pre-oxidised roll surface, the oxide scale peels off from the strip surface, and the rolled strip sample presents a clear metallic surface after rolling when the reduction is higher than 12%, at both 700 and 850 ^{o}C. As shown Fig. 7.16, the oxide scale was pressed and remained on the strip surface after deformation at lower reductions (<10%) at 700 ^{o}C. However at 850 ^{o}C the oxide scale on the strip, thicker than at 700 ^{o}C, was broken, peeled off and sticked onto the roll surface. For a reduction of less than 10% at 700 ^{o}C, the remaining oxide scale has a smoother surface. This explains why the value of the strip roughness after rolling at 700 ^{o}C is much lower than that at 850 ^{o}C for 10% thickness reduction, as shown in Fig. 7.16. For both temperatures 700 and 850 ^{o}C, the strip roughness is getting closer to the

roller surface roughness when the reduction is higher than 12% after rolling. It can be stated that the roughness of the roller surface has a major effect on the strip roughness.

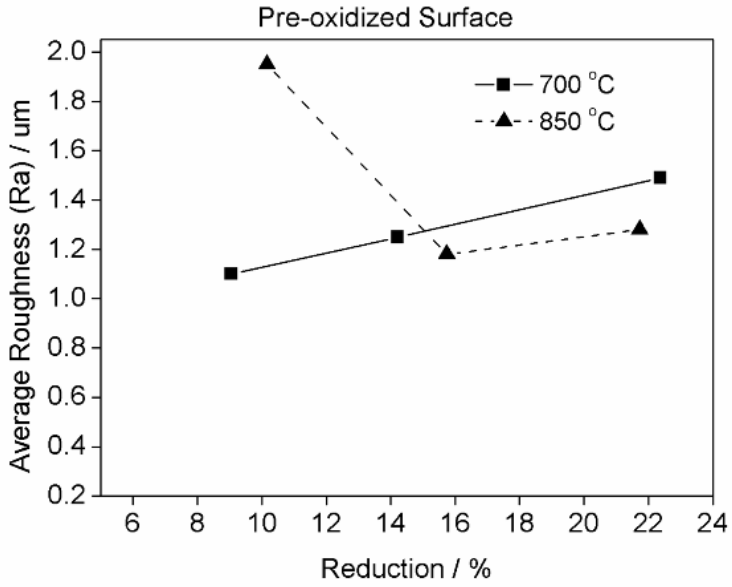

Fig. 7.15 Effect of thickness reduction on strip surface roughness (pre-oxidised roll surface). (Reduction of thickness is % reduction times 6 mm).

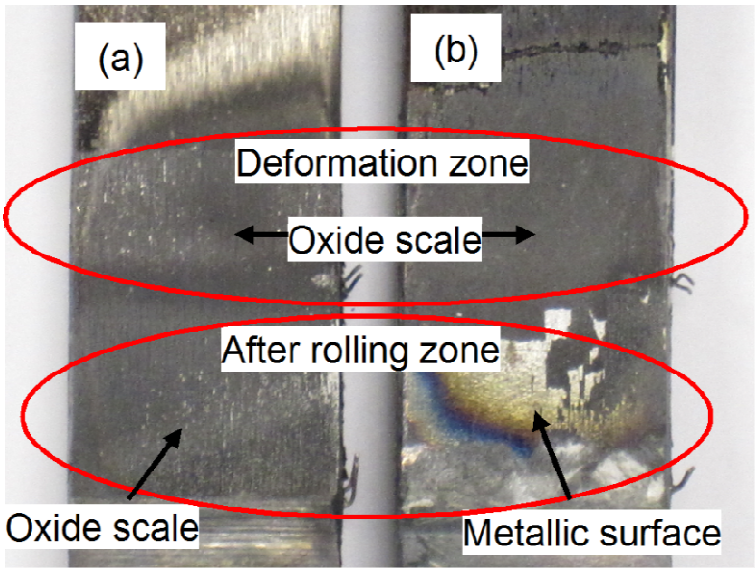

Fig. 7.16 Digital photos of surface images of strip samples after hot rolling simulation. (a) With 9% reduction at 700 °C and (b) with 10% reduction at 850 °C.

Table 7.2 Relevant roughness parameters of the roller surface for two types of roll surfaces (thickness reduction 22% at 850 ^{o}C).

Roll surface	Conduction	Ra	Rq	Rsk	Rku
Virgin surface	Before rolling	0.25	0.32	-0.189	3.581
	After 5 passes	0.20	0.24	-0.02	0.635
Pre-oxidised surface	Before rolling	1.55	2.07	-0.356	4.284
	After 5 passes	0.85	1.16	-0.033	3.996

For the thickness reduction of 22% at 850 ^{o}C, the surface roughness parameters of the two roller surfaces are tabulated in Table 7.2. The change of average roughness after 5 passes is much more significant with the pre-oxidised roll. The initial negative skewness indicated more plateau-like bearing surfaces, but after 5 passes the skewness decreases towards zero, which indicates a reduction of the bearing area. The initial Kurtosis value was more than 3 from both original surfaces, which indicates sharp peaks and valleys but it was reduced after 5 passes. However, for the virgin surface, the Kurtosis values changed much more than the pre-oxidised roll. In this case the Kurtosis changed significantly from 3.581 to 0.653 after 5 passes, which indicates that the fewer original sharp peaks and valleys become more in number of relatively smaller peaks and valleys. The results obtained so far have been for pre-oxidised rolls in dry air. As the oxide layers in moist air are non-uniform and more porous, it is expected that changing the roughness parameters of the roll and strip for the case of moist air will be more dramatic than the above case with dry air.

A large number of stalled hot rolling experiments will need to be carried out to investigate the evolution of roll surface morphology and roughness in moist air, and eventually the wear mechanics of HSS rolls. The testing program is extensive and is beyond the scope of this chapter. The mini rolling mill on the Gleeble thermal mechanical simulator has demonstrated that this can be carried out in the future.

7.3 Conclusions

7.3.1 Oxidation experiments

The following conclusions can be made according to the oxidation experiments under dry and moist air (12.5% and 46.5% H_2O) on the Gleeble 3500 thermal mechanical simulator:

(1) The oxide scale consists mainly of Fe_3O_4 and Fe_2O_3. The influence of water vapour content on the oxidation behaviour of high-speed steel roll material is significant. The moist atmosphere not only increases the oxidation rate of the high speed steel, it also influences the microstructure and morphology of the oxide scale. The oxide scale formed, is non-uniform and more porous and fractured than the compact and uniform layer formed in dry air. With an increasing content of water vapour, more porous oxide scale forms, and more Fe_2O_3 phase formed in the oxide scale.

(2) The oxidation rate of the HSS sample in 12.5% H_2O moisture is higher than those in dry air and 46.5% H_2O moisture. The water moisture has a significant effect on the oxidation rate of high speed steel material, but higher water vapour content during a long experiment time decreases the oxidation rate.

7.3.2 Tribology tests

A mini-rolling mill was successfully incorporated into the Gleeble 3500 thermal mechanical simulator to simulate stalled hot rolling. Two types of roller surfaces, e.g. a relatively virgin surface and a pre-oxidised surface were investigated. The experimental results reveal that the two types of roller surfaces exhibit quite different tribological behaviours. The rolling force and friction of pre-oxidised rolls is always higher than that of fresh rolls for different reductions and temperatures. With the pre-oxidised roll, a high rolling temperature can cause the oxide scale to peel off from the strip and stick onto the roll surface.

The tribological experiment indicates that the original surface profile of work roll plays an important role on the contact behaviour between the roll and strip, and in particular, strip roughness. Compared with the virgin surface, the pre-oxidised roller shows more significant changes to its roughness parameters after 5 rolling passes, except for the Kurtosis where the change is small.

Chapter 8
Conclusions and recommendations

8.1 Conclusions

Detailed conclusions have been described in each Chapter 4, 5, 6 and 7. The general conclusions are outlined as following.

8.1.1 Oxidation behaviour of the HSS material

- The in-situ observations by a high temperature microscope indicated that the oxidation of the HSS sample initiates at the carbides/matrix interfaces, and then spread rapidly over the carbides, followed by a continuous growth over the whole surface, in both dry and 12.5% H_2O humid air.

- Chromium rich carbide (M_7C_3) has the greatest resistance to oxidation among the carbides, followed by (Mo, W)-rich carbides (M_2C). Vanadium rich carbide (MC) is easiest to oxidise because it has a great affinity for oxygen.

- Duplex-layer oxide scales formed in vanadium rich carbide (MC) areas after oxidation, consisting of fine, porous crystalline (Cr, Fe)-rich oxide inner layer and a large columnar iron oxide outer layer with vanadium oxides on the top. The carbides-free matrix also shows a very good oxidation resistance which may be due to the formation of a thin, compact $(Cr, Fe)_3O_4$ spinel that reduces the oxidation rate.

- Temperature has a significant influence on the oxidation behaviour of the HSS roll material in both dry and humid air; as the temperature increased, so too does the rate of oxidation. As the sample surface oxidised at 700 ^oC is the most severe, the temperature of the roll surface should be kept lower than 650 ^oC to protect the surface.

- Water vapour in air increases the oxidation rate of HSS roll material and has a significant influence on morphology of the oxidised surface. The presence of water vapour reduces the grain size and increases the porosity of iron oxide.

8.1.2 Mechanical properties of the oxide scale

- The nano-indentation tests on the HSS sample successfully revealed the mechanical properties of MC carbides, M_2C/M_7C_3 carbides, and HSS matrix. The huge difference in hardness between the carbides and HSS matrix indicate that adding carbides significantly enhanced the wear resistance of the HSS sample.

- The nano-indentation tests on the cross section of oxide scale well revealed the different mechanical properties of the inner and outer sub-layers. The difference in Young's modulus and hardness between the inner and outer oxide layers is mainly due to the very different microstructures of these two sub-layers. The nano-indentations on the outer oxide layer are more likely to land on a large single crystal, while the nano-indentations on the inner oxide layer are more similar to indenting sintered fine-grained composites.

8.1.3 Influence of oxide scales on tribological behaviour

- Pin-on-disc high temperature tribological tests have been successfully carried out to simulate the tribological behaviour of oxide scale in the role bite. The results indicate that both normal load and sliding speed have a significant influence on the coefficient of friction.

- The evolution of the coefficient of friction in a typical tribology test can be divided into three stages. Stages I and II can be summarised as the running-in period which lasts less than 300 seconds from the test commencing. Adhesive wear on the pin is the dominant mechanism in this period. At Stage III the wear mechanism on the pin becomes complex. It is a balance between adhesion, abrasion, and oxidation.

8.1.4 Oxidation and tribology tests on Gleeble 3500

- Oxidation tests in the Gleeble 3500 indicated that the water content in an oxidising atmosphere influences the morphology and phase composition of the oxide scale. By increasing the water content in air, more porous oxide scale forms and more Fe_2O_3 oxides are formed in the oxide scale.

- A mini-rolling mill has been successfully incorporated in the Gleeble 3500 thermal mechanical simulator to simulate stalled, hot rolling. Two types of roller surfaces, a relatively virgin surface and a pre-oxidised surface were investigated. The results showed that the two types of roller surfaces exhibited quite different tribological behaviours. The tribological experiment indicated that the original surface profile of the work roll plays an important role on the contact behaviour between the roll and strip, and in particular, the strip roughness.

8.2 Recommendations for future work

- The experimental technique developed in the current work has proved to be very effective. The in-situ observation of initial oxidation nucleation and growth is a powerful technique and it is strongly recommended that this type of observations be extended to study the oxidation of other steel compositions. As for the high speed steel materials, how the chromium elements and morphologies of the various carbides and their distribution in the material, influences the behaviour of oxidation should be investigated in order to gain a better understanding of the oxidation of the high speed steel series.

- The work rolls actually is subjected to thermal cycling during hot rolling. The drastic thermal cycling leads to very different oxidation kinetics and oxidation behaviour of work rolls because they are sensitive to the temperature. Cyclic oxidation experiments will be carried out in order to simulate a closer thermal condition to the hot rolling.

- Nano-indenation has successfully revealed the mechanical properties of the oxide scale formed on the HSS sample surface. More nano-indentation tests and nano-scratch tests need to be done to investigate how the thin oxide scale influences the surface properties of high speed steel, such as hardness, wear resistance, and adhesion between the oxide scale and substrate.

- A large number of stalled, hot rolling experiments in Gleeble 3500 will need to be carried out to investigate in depth the evolution of roll surface morphology and roughness in humid air, and eventually the wear mechanics of HSS roll.

References

[1] K.C. Huang, S. Lee, H.C. Lee, Effects of elements on microstructure and fracture properties of cast high speed steel rolls, Mater. Sci. Eng. A 254 (1998) 282-295.

[2] H.H. Kim, J.W. Lim, J.J. Lee, Oxidation behavior of high-speed steels in dry and wet atmospheres, ISIJ Int. 43 (2003) 1983-1988.

[3] D.N. Hanlon, W.M. Rainforth, The rolling sliding wear response of conventionally processed and spray formed high speed steel at ambient and elevated temperature, Wear 255 (2003) 956-966.

[4] Y. Sano, T. Hattori, M. Haga, Characteristics of high-carbon high speed steel rolls for hot strip mill, ISIJ Int. 32 (1992) 1194-1201.

[5] K. Goto, Y. Matsuda, K. Sakamoto, Y. Sugimoto, Basic characteristics and microstructure of high-carbon high speed steel rolls for hot rolling mill, ISIJ Int. 32 (1992) 1184-1189.

[6] M.J. Monteiro, F.C. Rizzo, Effect of chromium content on the oxidation behaviour of high-speed steels under dry and moist air environments, Mater. Sci. Forum 522-523 (2005) 171-180.

[7] C. Rodenburg, W.M. Rainforth, A quantitative analysis of the influence of carbides size distributions on wear behaviour of high-speed steel in dry rolling/sliding contact, Acta Mater. 55 (2007) 2443-2454.

[8] Y.J. Kang, J.C. Oh, H.C. Lee, S. Lee, Effects of carbon and chromium additions on the wear resistance and surface roughness of cast high-speed steel rolls, Metall. Mater. Trans. A 32A (2001) 2515-2525.

[9] A.M. El-Rakayby, B. Mills, The role of primary carbides in the wear of high speed steel, Wear 112 (1986) 327-340.

[10] J.W. Park, H.C. Lee, S. Lee, Composition, microstructure, hardness, and wear properties of high-speed steel rolls, Metall. Mater. Trans. A 30A (1999) 399-409.

[11] E. Badisch, C. Mitterer, Abrasive wear of high speed steels: Influence of abrasive particles and primary carbides on wear resistance, Tribology Int. 36 (2003) 765-770.

[12] O. Kato, H. Yamamoto, M. Ataka, K. Nakajima, Mechanisms of surface deterioration of roll for hot strip rolling, ISIJ Int., 32 (1992) 1216-1220.

[13] S. Spuzic, K.N. Strafford, C. Subramanian, G. Savage. Wear of hot rolling mill rolls: an overview. Wear 176 (1994) 261-271.

[14] C. vergne, C. Boher, C. Levaillant, R. Gras, Analysis of the friction and wear behaviour of hot work tool scale: Application to the hot rolling process, Wear 250 (2001) 322-333.

[15] C.S. Li, J.Z. Xu, X.M. He, X.H. Liu, G.D. Wang, Formation and control of strip scale pores in hot rolling, J. Mater. Process. Technol. 116 (2001) 201-204.

[16] W.S. Dai, M. Ma, J.H. Chen, The thermal fatigue behaviour and cracking characteristics of hot-rolling material, Mater. Sci. Eng. A 448 (2007) 25-32.

[17] R. Colas, J. Ramírez, I. Sandoval, J.C. Morales, L.A. Leduc, Damage in hot rolling work rolls, Wear 230 (1999) 56-60.

[18] V. Lanteri, C. Thomas, J. Bocqet, Black oxide film generation on work rolls and its effects on hot-rolling tribological characteristics, in: Proceedings of the 7th International Conference on Steel Rolling (Steel Rolling'98), Chiba, Japan, 1998, 423-428.

[19] A. Molinari, G. Straffelini, A. Tomasi, A. Biggi, G. Corbo, Oxidation behaviour of ledeburitic steels for hot rolls, Mater. Sci. Eng. A 280 (2000) 255-262.

[20] O. Kubaschewski, B.E. Hopkins, Oxidation of metals and alloys, Butter Worths, London, Second Edition, 1962.

[21] E. Rabinowicks, Friction and Wear of Materials, John Willey and Sons, New York, 1965.

[22] L. Caithness, S. Cox, S. Emery, Surface behaviour of HSS in hot strip mills, in: Proceedings of Rolls 2000+ Conference of Advances in Mill Roll Technology, Birmingham UK, 1999, 111-120.

[23] D. Caplan, M. Cohen. Effect of cold work on the oxidation of iron from 400-650 ^{o}C. Corros. Sci. 6 (1966) 321-335.

[24] P. Kofstad. High-temperature oxidation of metals. John Wiley & Sons, Inc., New York and London and Sydney, 1966.

[25] P. Kofstad. High temperature corrosion. Elsevier Applied Science Publishers Ltd, London and New York, 1988.

[26] N. Birks, G.H. Meier, Frederick S. Pettit. Introduction to the high-temperature oxidation of metals. Second Edition, Cambridge University Press, New York, 2006.

[27] L. Suárez, P. Rodríguez-Calvillo, Y. Houbaert, R. Colás, Oxidation of ultra low carbon and silicon bearing steels, Corros. Sci. 52 (2010) 2044-2049.

[28] R.M. Cornell, U. Schwertmann. The iron oxides: Structure, properties, occurrences and uses. Wiley-VCH, Weinheim, 2003.

[29] N. Bertrand, C. Desgranges, D. Poquillon, M.C. Lafont, D. Monceau, Iron oxidation at low temperature (260-500 ^{o}C) in air and the effect of water vapour, Oxid. Met. 73 (2010) 139-162.

[30] R.M. Cornell, U. Schwertmann, The Iron Oixdes, VCH Publishers, New York, 1996.

[31] J. Païdassi, The kinetics of the air oxidation of iron in the range 700-1250 °C. Acta Metall. 6 (1958) 184-194.

[32] V.B. Ginzburg, Steel rolling technology, Marcel Dekker, New York, 1989.

[33] I. Iordanova, M. Surtchev, K.S. Forcey, V. Krastev. High-temperature surface oxidation of low-carbon rimming steel. Surf. Interface Anal. 30 (2000) 158-160.

[34] T. Jonsson, B. Pujilaksono, S. Hallström, J. Ågren, J.-E. Svensson, L.-G. Johansson, M. Halvarsson, An ESEM in situ investigation of the influence of H_2O on iron oxidation at 500 ^{o}C, Corros. Sci. 51 (2009) 1914-1924.

[35] B. Pujilaksono, T. Jonsson, M. Halvarsson, J.-E. Svensson, L.-G. Johansson, Oxidation of iron at 400-600 ^{o}C in dry and wet O_2, Corros. Sci. 52 (2010) 1560-1569.

[36] J. Tominaga, K. Wakimoto, T. Mori, M. Murakami, T. Yoshimura, Manufacture of wire rods with good descaling property, Trans. ISIJ 8 (1982) 646-656.

[37] L.W. Pinder, K. Dawson, G.J. Tatlock, High temperature corrosion of low alloy steels, Shreir's Corrosion, Elsevier.

[38] H.F. Marston, P.H. Bolt, G. Leprince, M. Roder, R. Klima, J. Niska, M. Jarl, Challenges in the modelling of scale formation and decarburisation of high carbon, special and general steels, Ironmak. Steelmak. 31 (2004) 57-65.

[39] F. Friedel, H. Bolt, X. Cornet, G. Bourdon, X. Vanden, E. Zeimetz, S. Ehlers, F. Steinert, Investigation of the formation, constitution and properties of scale formed during the finishing, rolling, cooling and coiling of thin hot strips, ECSC Research Project 7210.PR/153, 2004.

[40] R.Y. Chen, W.Y.D. Yuen, Review of the high-temperature oxidation of iron and carbon steels in air or oxygen, Oxid. Met. 59 (2003) 433-468.

[41] A.T. Fromhold, Theory of metal oxidation (Volume I-Fundamentals), New York, 1972.

[42] W.W. Smeltzer, The kinetics of wustite scale formation on iron, Acta Metall. 8 (1960) 377-383.

[43] P.A. Munther, J.G. Lenard, The effect of scaling on interfacial friction in hot rolling of steels, J. Mater. Proces. Technol. 88 (1999) 105-113.

[44] K. Hauffe, Oxidation of metals, Plenum Press, New York, 1965.

[45] J.J. Senkevich, D.A. Jones, I. Chatterjee, Measuring the growth of oxide films on low carbon steel at 500 ^{o}C by impedance spectroscopy, Corros. Sci. 42 (2000) 201-210.

[46] W. Gao, H. Gong, J. He, A. Thomas, L. Chan, S. Li, Oxidation behaviour of Cu thin films on Si wafer at 175-400 ^{o}C, Mater. Lett. 51 (2001) 78-84.

[47] F. Pettit, R. Yinger, J.B. Wagner Jr, The mechanism of oxidation of iron in carbon monoxide carbon dioxide mixtures, Acta Metall. 8 (1960) 617-623.

[48] I. Iordanova, K.S. Forcey, R. Harizanova, Y. Georgiev, M. Surtchev, Investigation of structure and composition of surface oxides in a high chromium martensitic steel, J. Nucl. Mater. 257 (1998) 126-133.

[49] D.T. Hoelzer, B.A. Pint, I.G. Wright, A microstructural study of the oxide scale formation on ODS Fe-13Cr steel, J. Nucl. Mater. 283-287 (2000) 1306-1310.

[50] W.L. Roberts, Hot rolling of steel, Marcel Dekker, New York, 1983.

[51] N. Babu, R. Balasubramaniam, A. Ghosh, High-temperature oxidation of Fe_3Al-based iron aluminides in oxygen, Corros. Sci. 43 (2001) 2239-2254.

[52] R. Haugsrud, High-temperature oxidation of Cu- 10wt% Ni and Cu- 15wt% Ni at 900-1050 ^{o}C, Corros. Sci. 42 (2000) 383-399.

[53] F.S. Pettit, J.B. Wagner, Transition from the linear to the parabolic rate law during the oxidation of iron to wustite in CO-CO_2 mixtures, Acta Metall. 12 (1964) 35-40.

[54] M. Kkrzyzanowski, J.H. Beynon, Modelling the boundary conditions for thermo-mechanical processing—oxide scale behaviour and composition effects, Modell, Simul. Mater. Sci. Eng. 8 (2000) 927-945.

[55] J.S. Sheasby, W.E. Boggs, E.T. Turkdogan, Scale growth on steels at 1200 ^{o}C: rationale of rate and morphology, Metal. Sci. 18 (1984) 127-136.

[56] G.J.W. Kor, E.T. Turkdogan, Sulfides and oxides in Fe-Mn alloys: Part II. Precipitation of solid sulfides and liquid oxysulfides during oxidation of iron alloys, Metall. Mater. Trans. B 2 (1971) 1571-1578.

[57] W.W. Smeltzer, D.J. Young, Oxidation properties of transition metals, Progress in Solid-State Chemistry 10 (1975) 17-54.

[58] J. Païdassi, Sur l'oxydation du fer dans l'air dans l'intervalle 400–700 ^{o}C, Acta Metall. 4 (1956) 227-229.

[59] J.K. Stanley, J. von Hoene, J.T. Huntoon, The oxidation of pure iron, Trans. Amer. Soc. Metals. 43 (1951) 426-453.

[60] W.M.C. Melfo, Analysis of hot rolling events that lead to ridge-buckle defect in steel strips, PhD thesis, the univeristy of wollongong, 2006.

[61] J. Tiley, Y. Zhang, J.G. Lenard, Hot compression of mild steel industrial reheat furnace scale, Steel Res. 70 (1999) 437-440.

[62] Y. Yu, J.G. Lenard. Estimating the resistance to deformation of the layer of scale during hot rolling of carbon steel strips. J. Mater. Proces. Technol. 121 (2002) 60-68.

[63] F.J. Belzunce, A. Ziadi, C. Rodriguez, Structural integrity of hot strip mill rolling rolls, Eng. Fail. Anal. 11 (2004) 789-797.

[64] M. hashimoto, T. Koie, Evolution of hot rolling mill rolls with CPC type high speed steel rolls, in: 44th Mechanical Working and Steel Processing Conference Proceedings, Vol. XL, 2002, 81-90.

[65] B. Feistritzer, K.H. Schroder, M. Windhager, K.H. Ziehenberger, Indefinite chill: upgrading an old HSM work roll grade, in: 41st Mechanical Working and Steel

Processing Conference Proceedings, Vol. XXXVII, 1999, 103-108.

[66] J. Asensio, J.A. Pero-Sanz, J.I. Verdeja, Microstructure selection criteria for cast irons with more than 10 wt% chromium for wear applications, Mater. Charact. 49 (2003) 83-93.

[67] J. Asensio-Lozano, J.F. Álvarez-Antolín, G.F. Vander Voort, Identification and quantification of active manufacturing factors for graphite formation in centrifugally cast Nihard cast irons, J. Mater. Proces. Technol. 206 (2008) 202-215.

[68] M. Pellizzari, A. Molinari, G. Straffelini, Tribological behaviour of hot rolling rolls, Wear 259 (2005) 1281-1289.

[69] B.T.C. Nycen, T.P. Adams, Cast iron indefinite roll produced by the addition of Nb, US Patent 6013144, US, 2000.

[70] I. Fernandez, F.J. Belzunce, Wear and oxidation behavior of high-chromium white cast irons, Mater. Charact. 59 (2008) 669-674.

[71] D. Li, L. Liu, Y. Zhang, C. Ye, X. Ren, Y. Yang, Q. Yang, Phase diagram calculation of high chromium cast irons and influence of its chemical composition, Mater. Des. 30 (2009) 340-345.

[72] M. Boccalini, H. Goldenstein, Solidification of high speed steels, International Mater. Reviews 46 (2001) 92-115.

[73] V. Vitry, S. Nardone, J.-P. Breyer, M. Sinnaeve, F. Delaunois, Microstructure of two centrifugal cast high speed steels for hot strip mills applications, Mater. Des. 34 (2011) 372-378. [73] M.P. Guerrero, C.R. Flores, A. Pérez, R. Colás. Modelling heat transfer in hot rolling work rolls. J. Mater. Proces. Technol. 94 (1999) 52-59.

[74] A.A. Tseng, F.H. Lin, A.S. Gunderia, D.S. Ni. Roll cooling and its relationship to roll life. Metall. Trans. A 20A (1988) 2305-2320.

[75] A. Tudball, S.G.R. Brown. Practical finite element heat transfer modelling for hot rolling of steels. Ironmak. Steelmak. 33 (2006) 61-66.

[76] P. Kotrbacek, M. Raudensky, J. Horsky, M. Pohanka. Experimental study of heat transfer in hot rolling. Revue De Metallurgie-Cahiers D Informations Techniques, 103 (2006) 333-341.

[77] X. Li, M. Wang, F. Du. A coupling thermal mechanical and microstructural FE

model for hot strip continuous rolling process and verification. Mater. Sci. Eng. A, 408 (2005) 33-41.

[78] S.M. Hwang, C.G. Sun, S.R. Ryoo, W.J. Kwak, An integrated FE process model for precision analysis of thermo-mechanical behaviours of rolls and strip in hot strip rolling, Comput. Methods Appl. M. 191 (2002) 4015-4033.

[79] A.A. Tseng, Thermal modelling of roll and strip interface in rolling processes: part 1-review. Numer. Heat Tr. A-Appl. 35 (1999) 115-133.

[80] A.A. Tseng, Thermal modelling of roll and strip interface in rolling processes: part 2-simulation. Numer. Heat Tr. A-Appl. 35 (1999) 135-154.

[81] C.G. Sun, J.W. Kim, S.M. Hwang, Investigation of the thermo-mechanical behaviour of type 304 stainless slab in hot charge rolling condition by the finite element method, ISIJ Int. 43 (2003) 1773-1780.

[82] R. Colás, Modelling heat transfer during hot rolling of steel strip, Model. Simul. Mater. Sc. 3 (1995) 437-453.

[83] U. Wankhede, I.V. Samarasekera, Thermal behaviour of high speed steel work rolls in the finishing stands of a hot strip mill, Ironmak. Steelmak. 24 (1997) 55-60.

[84] Y.H. Li, C.M. Sellars, Evaluation of interfacial heat transfer and its effects on hot forming processes, Ironmak. Steelmak. 23 (1996) 58-61.

[85] Y.H. Li, C.M. Sellars, Comparative investigations of interfacial heat transfer behaviour during hot forging and rolling of steel with oxide scale formation, J. Mater. Proces. Technol. 80-81 (1998) 282-286.

[86] C.G. Sun, C.S. Yun, J.S. Chung, S.M. Hwang, Investigation of thermomechanical behaviour of a work roll and of roll life in hot strip rolling, Metall. Mater. Trans. A 29A (1998) 2407-2424.

[87] C. Devadas, I.V. Samarasekera. Heat transfer during hot rolling of steel strip, Ironmak. Steelmak. 13 (1986) 311-321.

[88] R.L. Corral, R. Colás, A. Pérez. Modeling the thermal and thermoelastic responses of work rolls used for hot rolling steel strip, J. Mater. Proces. Technol. 153-154 (2004) 886-893.

[89] S. Sikdar, S. John. Simulation of thermal history of work rolls of finishing stand in

hot strip mill: a numerical approach, Ironmak. Steelmak. 33 (2006) 493-499.

[90] C.S. Li, X.H. Liu, G.D. Wang, X.M. He, Three-dimensional FEM analysis of work roll temperature field in hot strip rolling, Mater. Sci. Technol. 18 (2002) 1147-1150.

[91] C.S. Li, J.Z. Xu, X.M. He, X.H. Liu, G.D. Wang, Formation and control of strip scale pores in hot rolling. J. Mater. Proces. Technol. 116 (2001) 201-204.

[92] L. Zhou, F. Liu, C.S. Liu, D.L. Sun, L.S. Yao, High temperature oxidation behaviour of high speed steel for hot rolls material, J. Univ. Sci. Technol. B. 12 (2005) 166-171.

[93] L. Zhou, F. Liu, C.S. Liu, D.L. Sun, High temperature oxidation behaviour of high speed steel for roll in water vapour, Trans. Mater. Heat Treat. 25 (2004) 135-138.

[94] A. Molinari, M. Pellizzari, Primary carbides in spincast HSS for hot rolls and their effect on the oxidation behaviour. In: 6th International Tooling Conference, 2005, pp. 437-452.

[95] M.J. Monteiro, S.R.J. Saunders, F.C. Rizzo, The effect of water vapour on the oxidation of high speed steel, kinetics and scale adhesion, Oxid. Met. 75 (2011) 57-76.

[96] N.F. Garza-Montes-de-Oca, R. Colas, W.M. Rainforth, Failure modes of the oxide scale formed on a work roll grade high speed steel, Oxid. Met. (2011) Doi:10.1007/s11085-011-9243-9.

[97] R.V. Williams, G.M. Boxall, Roll surface deterioration in hot strip mills, J. Iron and Steel I. 4 (1965) 369-377.

[98] P.G. Stevens, K.P. Ivens, P. Harper, Increasing work-roll life by improved roll-cooling practice, J. Iron and Steel I. 1 (1971) 1-11.

[99] J.H. Lee, J.C. Oh, J.W. Park, H.C. Lee, S. Lee, Effects or tempering temperature on wear resistance and surface roughness of a high speed steel roll, ISIJ Int. 41 (2001) 859-865.

[100] A. Pellizzari, A. Molinri, G. Straffelini, Tribological behaviour of hot rolling rolls, Wear 259 (2005) 1281-1289.

[101] M.R. Green, W.M. Rainforth, M.F. Frolish, J.H. Beynon, The effect of microstructure and composition on the rolling contact fatigue behaviour of cast bainitic steels, Wear 263 (2007) 756-765.

[102] D.N. Hanlon, W.M. Rainforth, C.M. Sellars, The effect of processing route, composition and hardness on the wear response of chromium bearing steels in a rolling-sliding configuration, Wear 203-204 (1997) 220-229.

[103] J.C. Mascia, O.C. marini, E. Ubici, Reduction of work roll wear by controlling tertiary scale growth, Iron Steel Eng. 75 (1998) 48-51.

[104] G. Savage, R. Boelen, A. Horti, H. Morikawa, Y. Tsujimoto, Hot wear testing of roll alloys, in: Proceedings of 37thMWSP Conference, ISS, vol. XXXIII, 1996, pp.333–337.

[105] S. Lundberg, T. Gustafsson, The influence of rolling temperature on roll wear, investigated in a new high temperature test rig, J. Mater. Process. technol. 42 (1994) 239-291.

[106] D.N. Hanlon, W.M. Rainforth, C.M. Sellars, The rolling-sliding wear response of conventionally processed and spray formed high chromium content cast iron at ambient and elevated temperature, Wear 225-229 (1999) 587-599.

[107] D.N. Hanlon, W.M. Rainforth, The rolling sliding wear response of conventionally processed and spray formed high speed steel at ambient and elevated temperature, Wear 255 (2003) 956-966.

[108] M. Pellizzari, D. Cescato, M.G. De Flora, Hot friction and wear behaviour of high speed steel and high chromium iron for rolls, Wear 267 (2009) 467-475.

[109] C. Vergne, C. Boher, R. Gras, C. Levaillant, Influence of oxides on friction in hot rolling: experimental investigations and tribological modelling, Wear 260 (2006) 957-975.

[110] O. Joos, C. Boher, C. Vergne, C. Gaspard, T. Nylen, F. Rezai-Aria, Assessment of oxide scales influence on wear damage mechanisms of HSM work rolls, Wear 263 (2007) 198-206.

[111] F.H. Stott, M.P. Jordan, The effects of load and substrate hardness on the development and maintenance of wear protective layer during sliding at elevated temperatures, Wear 250 (2001) 391-400.

[112] J.C.G. Milan, M.A. Carvalho, R.R. Xavier, S.D. Franco, J.D.B. DeMello, Effect of temperature, normal load and pre-oxidation on the sliding wear of multicomponent

ferrous alloys, Wear 259 (2005) 412-423.

[113] J.D.B. De Mello, Tribological behavior of multi-component ferrous alloys, in: A. Sinatora, M. Boccalini Jr., M.E. Hara (Eds.), Proceedings of International Conference on Abrasion 2005, Abrasion Wear Resistant Alloyed Cast Irons for Rolling and Pulverizing Mills, Sao Paolo (Brazil), 14–17 August, 2005, pp. 19-45.

[114] N.F. Garza-Montes-de-Oca, W.M. Rainforth, Wear mechanisms experienced by a work roll grade high speed steel under different environmental conditions, Wear 267 (2009) 441-448.

[115] W. Sun, A.K. Tieu, Z.Y. Jiang, C. Lu, H.T. Zhu, Surface characteristics of oxide scale in hot strip rolling, J. Mater. Proces. Technol. 140 (2003) 76-83.

[116] W. Sun, A.K. Tieu, Z.Y. Jiang, H.T. Zhu, C. Lu, Oxide scale growth of low carbon steel at high temperatures, J. Mater. Proces. Technol. 155-156 (2004) 1300-1306.

[117] W. Sun, A.K. Tieu, Z.Y. Jiang, C. Lu, High temperature oxide scale characteristics of low carbon steel in hot rolling, J. Mater. Proces. Technol. 155-156 (2004) 1307-1312.

[118] W. Sun, A.K. Tieu, Z.Y. Jiang, H.T. Zhu, Effect of hot rolling conditions on deformation behaviour of oxide scale at high temperatures, Key Eng. Mat. 274-276 (2004) 511-516.

[119] Z.Y. Jiang, A.K. Tieu, W.H. Sun, J.N. Tang, D.B. Wei, Characterisation of thin oxide scale and its surface roughness in hot metal rolling, Mater. Sci. Eng. A 435-436 (2006) 434-438.

[120] F.J. Pérez, martínez, M.P. Hierro, C. Gómez, A.L. Portela, G.N. Pucci, D. Duday, J. Lecomte-Beckers, Y. Greday, Corrosion behaviour of different hot rolled steels, Corros. Sci. 48 (2006) 472-480.

[121] J. Tang, A.K. Tieu, Z.Y. Jiang, Modelling of oxide scale surface roughness in hot metal forming, J. Mater. Proces. Technol. 177 (2006) 126-129.

[122] Y. Yun, J.G. Lenard, Estimating the resistance to deformation of the layer of scale during hot rolling of carbon steel strips, J. Mater. Proces. Technol. 121 (2002) 60-68.

[123] A.W. Batchelor, G.W. Stachowiak, Tribology in materials processing, J. Mater.

Proces. Technol. 48 (1995) 503-515.

[124] G.W. Stachowiak, A.W. Batchelor, Corrosive and oxidative wear, in: Engineering Tribology (Third version), Elsevier, on-line, 2005. http://www.sciencedirect.com.ezproxy.uow.edu.au/science/book/9780750678360.

[125] S. Iwadoh, T. Mori, Effect of work roll materials and progress of manufacturing on cold rolling and future development in Japan, ISIJ Int. 32 (1992) 1224-1231.

[126] R.D. Arnell, P.B. Davies, J. Halling, T.L. Whomes, Tribology, principles and design applications, Macmillan, London, 1991.

[127] P.J. Blau, Fifty years of research on the wear of metals, Tribol. Int. 30 (1997) 321-331.

[128] C.R. Gagg, P.R. Lewis, Wear as a product failure mechanism – overview and case studies, Engineering Failure Analysis 14 (2007) 1618-1640.

[129] J.H. Beynon, Tribology of hot metal forming, Tribol. Int. 31 (1998) 73-77.

[130] M. Boccalini, A. Sinatora, Microstructure and wear resistance of high speed steels for rolling mill rolls, in: Proceedings of the 6th International Tooling Conference, Karlstadt University, September, 2002, 425-437.

[131] M. Schütze, Mechanical properties of oxide scales, Oxid. Met. 44 (1995) 29-61.

[132] R. Colás, J. Ramyírez, I. Sandoval, J.C. Morales, L.A. Leduc, Damage in hot rolling works rolls, Wear 230 (1999) 56-60.

[133] M. Vardavoulias, The role of hard second phases in the mild oxidational wear mechanism of high-speed steel-based materials, Wear 173 (1994) 105-114.

[134] K. Hokkirigawa, T. Kato, T. Fukuda, M. Shinooka, Analysis of sliding wear mechanism of oxide films on hot roll surfaces base on in-situ observation of wear process by the CCD microscope tribosystem, J. Jpn. Soc. Tribologis. 42 (1997) 777-784.

[135] W.M. Melfo, R.J. Dippenaar, In situ observations of early oxide formation in steel under hot-rolling conditions, J. Microsc. 225 (2007) 147-155.

[136] D.J. Phelan, M.H. Reid, R.J. Dippenaar, Experimental and modelling studies into high temperature phase transformations, Comput. Mater. Sci. 34 (2005) 282-289.

[137] MultiMode SPM Instruction Manual, version 3.0, Digital Instruments, Veeco

Metrology Group (2000).

[138] X.D. Zhang, W. Liu, D.L. Sun, Y.G. Li, The transformation of carbides during austenization and its effect on the wear resistance of high speed steel rolls, Metall. Mater. Trans. A 38 (2007) 499-505.

[139] K.C. Hwang, S. Lee, H.C. Lee, Effects of alloying elements on microstructure and fracture properties of cast high speed steel rolls Part I: Microstructural analysis, Mater. Sci. Eng. A 254 (1998) 282-295.

[140] A. Molinari, G. Straffelini, A. Tomasi, A. Bigi, G. Corbo, Influence of microstructure and chromium content on oxidation behaviour of spin cast high-speed steels, Mater. Sci. Technol. 17 (2001) 425-430.

[141] Q. Zhu, H.T. Zhu, A.K. Tieu, M. Reid, L.C. Zhang, In-situ investigation of oxidation behaviour in high-speed steel roll material under dry and humid atmospheres, Corros. Sci. 52 (2010) 2707-2715.

[142] C. Santafé, C. Borgianni, Study of the oxidation kinetics of vanadium carbide, Oxid. Met. 9 (1975) 415.425.

[143] JANAF, Thermochemical tables, Office of standard reference data, Natural Bureau of Standards, Washington D.C., USA, 1971.

[144] Ulick R. Evans, The corrosion and oxidation of metals, second supplementary volume, Edward Arnold, 1976.

[145] A.S. Khanna, Introduction to high temperature oxidation and corrosion, ASM International, 2002.

[146] I. Kvernes, M. Oliveira, P. Kofstad, High temperature oxidation of Fe-13Cr-xAl alloys in air/H2O vapour mixtures, Corros. Sci. 17 (1977) 237-252.

[147] D. Laverde, T. Gómez-Acebo, F. Castro, Continuous and cyclic oxidation of T91 ferritic steel under steam, Corro. Sci. 46 (2004) 613-631.

[148] Y.N. Chang, F.I. Wei, High temperature oxidation of low alloy steels, J. Mater. Sci. 24 (1989) 14-22.

[149] V. Gonzálze, R. Rodríguez, Z. Haduck, R. Colás, Modelling oxidation of hot rolling work rolls, Ironmak. Steelmak. 28 (2001) 470-473.

[150] L. Mikkelsen, S. Linderoth, J.B. Bilde-Sørensen, The effect of silicon addition on

the high temperature oxidation of a Fe-Cr alloy, Mater. Sci. Forum, 461-464 (2004) 117-122.

[151] Y. Wouters, G. Bamba, A. Galerie, M. Mermous, J.-P. Petit, Oxygen and water vapour oxidation of 15Cr ferritic stainless steels with different silicon, Mater. Sci. Forum, 461-464 (2004) 839-846.

[152] C. Pettersson, T. Jonsson, C. Proff, M. Halvarsson, J.-E. Svensson, L.-G. Johansson, High temperature oxidation of the austenitic (35Fe27Cr31Ni) alloy sanicro 28 in O_2 + H_2O environment, Oxid. Met. 74 (2010) 93-111.

[153] R.Y. Chen, W.Y.D. Yuen, Review of the high-temperature oxidation of iron and carbon steels in air or oxygen, Oxid. Met. 59 (2003) 433-468.

[154] X.J. Zheng, Y.C. Zhou, J.Y. Li, Nano-indentation fracture test of Pb(Zr0.5Ti0.48)O3 ferroelectric with thin films, Acta Mater. 51 (2003) 3985-3997.

[155] A.K. Nanka Kumar, M.D. Kannan, S. Jayakumar, K.S. Rajam, V.S. Raju, Investigations on the mechanical behaviour of rough surfaces of TiNi thin films by nanoinden studies, Surf. Coat. Technol. 201 (2006) 3253-3259.

[156] J. Xie, C.X. Li, H. Dong, T. Bell, Nanoindentation and nanoscratch of a thermal oxide layer on a FeAl alloy, J. Mater. Res. 19 (2004) 291-300.

[157] P. Hosemann, J.G. Swadener, J. Welch, N. Li, Nano-indentation measurement of oxide layers formed in LBE on F/M steels, J. Nucl. Mater. 377 (2008) 201-205.

[158] W.C. Oliver, G.M. Pharr, An improved technique for determining hardness and elastic modulus using load and displacement sensing indentation experiments, J. Mater. Res., 7 (1992) 1564-1583.

[159] T. Antretter, F.D. Fischer, Critical shapes and arrangements of carbides in high-speed tool steel, Mater. Sci. Eng. A 237 (1997) 6-11.

[160] N. Lippmann, A. Lehmann, Th. Steinkopff, H.-J. Spies, Modelling the fracture behaviour of high speed steels using finite element method, Comput. Mater. Sci. 7 (1996) 123-130.

[161] F.G. Rammerstorfer, A.F. Plankensteiner, F.D. Fischer, T. Antretter, Hierarchical models for simulating the mechanical behaviour of heterogeneous materials: an approach to high speed tool steel, Mater. Sci. Eng. A 259 (1999) 73-84.

[162] Y.J. Kang, J.C. Oh, H.C. Lee, S. Lee, Effects of carbon and chromium additions on the wear resistance and surface roughness of cast high-speed steel rolls, Metall. Mater. Trans. A 32 (2001) 2515-2525.

[163] S.H. Chen, L. Liu, T.C. Wang, Small scale, grain size and substrate effects in nano-indentation experiment of film-substrate systems, Int. J. Solids Struct. 44 (2007) 4492-4504.

[164] M. Schütze, Mechanical properties of oxide scales, Oxid. Met. 44 (1995) 29-61.

[165] E. Flder, Modes of wear and damage of hot rolling rolls. Relationships with thermomechanical characteristics of calamines, Cahiers d'Informations Techniques - Revue de Metallurgie 81 (1984) 931-942.

[166] F.H. Stott, J. Glascott, G.C. Wood, Factors affecting the progressive development of wear-protective oxides on iron-base alloys during sliding at elevated temperatures, Wear 97 (1984) 93-106.

[167] J. Jiang, F.H. Stott, A mathematical model for sliding wear of metals at elevated temperatures, Wear 181-183 (1995) 20-31[4, 166] J. Jiang, F.H. Stott, A mathematical model for sliding wear of metals at elevated temperatures, Wear 181-183 (1995) 20-31.

[168] M.B. Peterson, S.J. Calabrese, S. Li, X. Jiang, Friction of alloys at high temperature, J. Mater. Sci. Technol. 10 (1994) 313-320.

[169] N. Chelliah, S.V. Kailas, Synergy between tribo-oxidation and strain rate response on governing the dry sliding wear behaviour of titanium, Wear 266 (2009) 704-712.

[170] L.C. Erickson, S. Hogmark, Analysis of banded hot rolling rolls, Wear 165 (1993) 231-235.

[171] http://www.engineeringtoolbox.com/moist-air-specific-volume-d_25.html.

[172] S.R.J. Saunders, M. Monteiro, F. Rizzo, The oxidation behaviour of metals and alloys at high temperatures in atmospheres containing water vapour: A review, Prog. Mater. Sci. 53 (2008) 775-837.

[173] M. Schutze, D. Renusch, M. Schorr, Chemical-mechanical failure of oxide scales on 9% Cr steels in air with H_2O, Mater. High Temp. 22 (2005) 113-120.

[174] X. Peng, J. Yan, Y. Zhou, F. Wang, Effect of grain refinement on the resistance of 304 stainless steel to breakaway oxidation in wet air, Acta Mater. 53 (2005) 5079-5088.

[175] H. Asteman, J-E. Svensson, L-G. Johansson, Evidence for chromium evaporation influencing the oxidation of 304L: the effect of temperature and flow rate, Oxid. Met. 57 (2002) 193-216.

[176] H. Asteman, J-E. Svensson, M. Norell, L-G. Johansson, Influence of water vapour and flow rate on the high-temperature oxidation of 304L: Effect of chromium oxide hydroxide evaporation, Oxid. Met. 54 (2000) 11-26.

[177] M. Halvarsson, J.E. Tang, H. Asteman, J.-E. Svensson, L.-G. Johansson, Microstructural investigation of the breakdown of the protective oxide scale on a 304 steel in the presence of oxygen and water vapour at 600 ^{o}C, Corro. Sci. 48 (2006) 2014-2035.

[178] H. Asteman, J.-E. Svensson, L.-G. Johansson, Oxidation of 310 steel in H_2O/O_2 mixtures at 600 ^{o}C: the effect of water-vapour-enhanced chromium evaporation, Corro. Sci. 44 (2002) 2635-2649.

[179] K. Segerdahl, J.-E. Svensson, M. Halvarsson, I. Panas, L.-G. Johansson, Breakdown of the protective oxide on 11% Cr steel at high temperature in the presence of water vapor and oxygen, the influence of chromium vaporization, Mater. High Temp. 22 (2005) 69-78.

[180] A. Yamauchi, K. Kurokawa, H. Takahashi, Evaporation of Cr_2O_3 in atmospheres containing H_2O, Oxid. Met. 59 (2003) 517-527.

[181] Elizabeth J. Opila, Volatility of common protective oxides in high-temperature water vapor: current understanding and unanswered questions, Mater. Sci. Forum 461-464 (2004) 765-774.

[182] J. Ehlers, D.J. Young, E.J. Smaardijk, A.K. Tyagi, H.J. Penkalla, L. Singheiser, W.J. Quadakkers, Enhanced oxidation of the 9%Cr steel P91 in water vapour containing environments, Corro. Sci. 48 (2006) 3428-3454.

Appendix A
Calibration of nano-indentations

The UMIS/IBIS nano-indentation system mounted with a Berkovich diamond tip (radius 160nm) was calibrated on a standard sample of fused silicon from 1mN to 400mN before the nano-indentation tests. After calibration, a series of indentations were performed on the standard sample of fused silicon to verify the calibration. Fig. A.1a shows the load-displacement curves. The loading force started from 2mN to 30mN at increments of 2mN. It can be seen that the load-displacement curves increased smoothly while increasing the load which means the loading force was controlled well by the system. Figs. A.1b and A.1c show Young's modulus and nano-hardness of the standard sample of silicon obtained from the verification test. It can be seen that Young's modulus was from 72-74GPa, and the nano-hardness from 9-10.5GPa. Comparing the measured data to Young's modulus and Hardness of the standard sample of fused silicon were 72.5GPa and 9.5GPa respectively, so the measured results are reliable. Therefore, it can be concluded that the results obtained from the nano-indentations in the loading force range from 2 to 30mN after the calibration are reasonable and reliable.

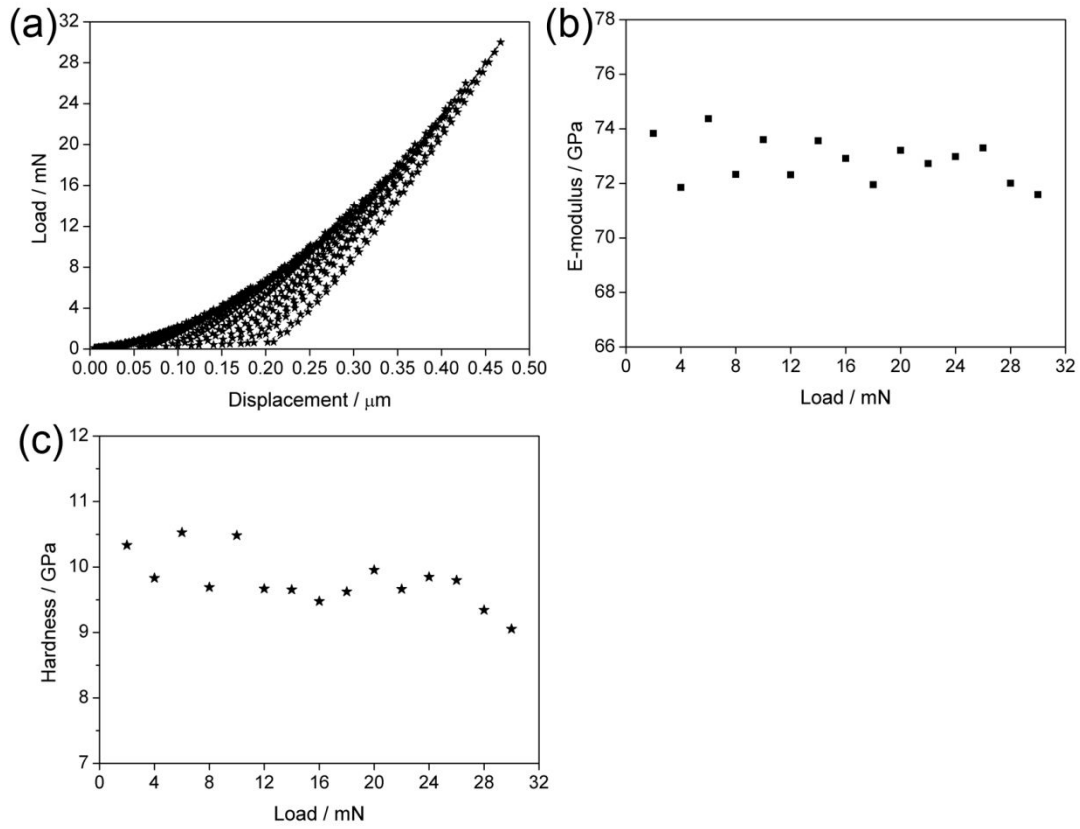

Fig. A.1 (a) Load-displacement curves on a standard fused silicon sample in loading force range 2 to 30mN, (b) the obtained Young's modulus, (c) the obtained nano-hardness.